A Study of GaSb Quantum Ring Vertical-Cavity Surface-Emitting Devices at Telecommunications Wavelengths

Samuel Oliver Jones
Department of Physics
Lancaster University

November 2024

This work was supported by an EPSRC ICASE studentship (EP/T517392/1) with IQE plc.

This thesis is submitted in partial fulfilment of the requirements for the degree of *Doctor of Philosophy* at Lancaster University.

Declaration

I hereby declare that, except where specific reference is made to the work of others, the content of this thesis is my own work and has not been submitted in substantially the same form for the award of higher degree elsewhere.

Samuel Jones, November 2024

Abstract

This work presents the results of studies that were conducted in the context of gallium antimonide (GaSb) quantum ring (QR) vertical-cavity surface-emitting lasers (VCSELs). The aim of this project was to produce GaSb QR VCSELs operating at telecoms-wavelengths for applications in data transfer and in mobile device sensing.

Simulations of the optical and electrical properties of distributed Bragg reflectors (DBRs) and VCSELs were performed in order to inform and optimise the design of several generations of QR VCSELs. Numerous experimental techniques were used to characterise and provide insight into the optical, electrical and material properties of samples produced throughout the duration of this project, and to enable comparison of designs, models and experiments. Characterisation techniques included optical transmittance and reflectance measurements, electrical characterisation, photoluminescence and time-resolved photoluminescence (PL and TRPL), electroluminescence (EL), scanning electron and transmission electron microscopy (SEM and TEM), energy-dispersive X-ray spectroscopy (EDS), beam-exit cross-sectional polishing in conjunction with atomic force microscopy (BEXP+AFM) and X-ray photoelectron spectroscopy (XPS). Epitaxial growth was performed in-house using molecular beam epitaxy (MBE), and externally using an industrial metal organic chemical vapour deposition (MOCVD) reactor. Device fabrication and processing studies were conducted in the Lancaster Quantum Technology Centre (QTC).

A study into the annealing of Au/Ni/Au contacts to p-type GaAs yielded a new ohmic contact scheme with specific contact resistance as low as $(1.6 \pm 0.2) \times 10^{-5}\,\Omega\,\mathrm{cm}^2$. An in-house reflectance monitoring setup was shown to provide accurate measurements of layer thickness for GaAs and AlAs layers grown by MBE and demonstrated that the approach is suitable for the calibration of group-III growth rates for future GaSb QR VCSEL growth runs.

DBRs with a step-graded interface between GaAs/$Al_{0.9}Ga_{0.1}$As layers and grown by MBE show improved electrical resistance when compared to ungraded structures. The step-graded structures are p-doped with beryllium as highly as $5 \times 10^{18}\,\mathrm{cm}^{-3}$ without detriment due to the low optical absorption at 1300 nm. A set of continuously-graded DBRs were grown by IQE using MOCVD and demonstrated comparable electrical performance to conventional Al_xGa_{1-x}As-based DBRs. The peak reflectance of such structures approached that of the conventional DBRs; however, the conventional structures exhibited a broader stopband.

TRPL measurements provided new insight into the carrier recombination lifetimes of QR structures in the presence of an optical cavity and stimulate further interest in the area.

QR VCSEL devices are shown to operate within the telecoms 'O'-band but are plagued by background emission. Low temperature (77 K) operation of the devices reveals interesting device physics associated with the quenching of the output emission when driven at high biases. Improvements to the QR VCSELs are presented as well as avenues in need of further investigation regarding the fundamental device physics and the measurement of device performance.

Acknowledgements

I thank Professor Manus Hayne for his indispensable support and guidance throughout the course of my studies. I also thank Dr J. Iwan Davies from IQE for enabling this opportunity and for providing me with valuable insights, experience and interesting discussions surrounding the growth of compound semiconductors in the UK industry.

A special thank you to Dr Peter Hodgson for the many hours spent in the evenings, early mornings and at weekends for the MBE-growth of samples in this work and our shared discussions and anticipation as new measurements were taken. Thank you to Salem Aeyed for leading the growth of the MOCVD-grown samples in this work and welcoming me during my visit to IQE.

I extend a huge thank you to Garry Vernon, without whom there would have been endless headaches due to cleanroom-equipment downtime!

Thank you to the staff and students at Lancaster University and our collaborators for their support in this work including Dr Lefteris Danos for providing access to the spectrophotometer and his support with the time-resolved photoluminescence setup, Dr Sam Jarvis and Elizabeth Bancroft for their XPS imaging, Dr Alex Robson for BEXP+AFM measurements and Francisco Alvarado for TEM imaging.

Finally, last but certainly not least, I thank my parents and close friends for their support throughout the years of my PhD. Not to mention making the most of any sunshine Lancaster has to offer with our numerous climbing trips!

This work was made possible by the funding of IQE and the EPSRC through ICASE studentship EP/T517392/1.

Publications and Presentations

Publications

Au/Ni/Au as a Contact for p-Type GaAs *IOP Semiconductor Science and Technology*, S. O. Jones, E. Bancroft, S. P. Jarvis and M. Hayne (2024). Semicond. Sci. Technol. **39** 125011.

GaSb Quantum-Rings for Vertical-Cavity Surface-Emitting Lasers Emitting at Telecommunications and Mobile Sensing Wavelengths *SPIE Photonics West, Conference Proceedings,* S. O. Jones, P. D. Hodgson and M. Hayne (2024). Proc. SPIE **12904**, Vertical-Cavity Surface-Emitting Lasers XXVIII, 129040J.

Towards GaSb/GaAs Quantum-Ring Single-Photon LEDs: Recent Progress and Prospects *SPIE Photonics West, Conference Proceedings,* Gizem Acar, Lucie Leguay, Samuel Jones, Peter Hodgson, Andrei Schliwa, and Manus Hayne (2024). Proc. SPIE **12906**, Light-Emitting Devices, Materials, and Applications XXVIII, 1290609.

Conference Presentations and Posters

GaSb Quantum-Rings for Vertical-Cavity Surface-Emitting Lasers Emitting at Telecommunications and Mobile Sensing Wavelengths SPIE Photonics West, *San Francisco, USA,* Oral Presentation (2024).

GaSb Quantum Rings as Active Regions for Telecoms-Wavelength Vertical–Cavity Surface-Emitting Lasers International Conference on Quantum Dots, *Munich, Germany,* Poster (2024).

GaSb Quantum-Ring Vertical-Cavity Surface-Emitting Lasers Emitting at 1.3 μm UK Semiconductors Conference, *Sheffield, UK,* Oral Presentation (2024).

GaSb/GaAs Quantum Ring Vertical Cavity Surface Emitting Lasers Approaching 1.3 μm Emission Semiconductor Integrated Opto-Electronics Conference, *Cardiff, UK,* Oral Presentation (2024).

GaSb/GaAs Quantum-Rings in Vertical-Cavity Surface-Emitting Lasers for Communication and Sensing WOCSDICE EXMATEC, *Palermo, Sicily,* Oral Presentation (2023).

GaSb/GaAs Quantum-Rings in Vertical-Cavity Surface-Emitting Lasers for Communication and Sensing iNOW 2023 - International Nano-Optoelectronics Workshop, *Würzburg, Germany,* Poster (2023).

The Current Status of GaSb/GaAs Quantum Ring Vertical Cavity Surface Emitting Lasers UK Semiconductors Conference, *Sheffield, UK,* Oral Presentation (2023).

GaSb/GaAs Quantum Ring Vertical Cavity Surface Emitting Lasers for Telecommunications and Sensing Semiconductor Integrated Opto-Electronics Conference, *Cardiff, UK,* Oral Presentation (2023).

Experimental Comparison of GaAs/AlGaAs DBRs and Ohmic Contacts for Improved Electrical Injection in GaSb Quantum-Ring VCSELs UK Semiconductors Conference, *Sheffield, UK,* Oral Presentation (2022).

Electrical Properties of GaAs/AlGaAs DBRs and Ohmic Contacts for GaSb/GaAs Quantum-Ring VCSELs Semiconductor Integrated Opto-Electronics Conference, *Cardiff, UK,* Oral Presentation (2022).

A Comparison of GaAs/$Al_xGa_{1-x}As$ P-Type Distributed Bragg Reflectors Semiconductor Integrated Opto-Electronics Conference, *Cardiff, UK,* Oral Presentation (2021).

Contents

1 Introduction **1**
1.1 Synopsis of Chapters . . . 3

2 Background Theory **5**
2.1 Multi-Layer Optics at Normal Incidence . . . 6
2.2 Electrical Properties of Semiconductors . . . 10
2.2.1 Doping and Carrier Density . . . 13
2.2.2 Heterojunctions . . . 14
2.2.3 Metal-Semiconductor Interfaces . . . 17
2.3 Quantum Tunnelling Through a Triangular Barrier . . . 17
2.4 Distributed Bragg Reflectors . . . 19
2.5 GaSb Quantum Rings Background . . . 22
2.6 VCSELs . . . 25

3 Simulations **29**
3.1 Nextnano++ . . . 30
3.2 TFCalc . . . 30

4 Characterisation Techniques **33**
4.1 Spectrophotometer Transmittance and Reflectance Measurements . . . 34
4.2 Electrical Characterisation . . . 38
4.3 Photoluminescence and Time-Resolved Photoluminescence . . . 40
4.4 Electroluminescence . . . 42
4.5 Electron Microscopy . . . 42
4.6 BEXP+AFM . . . 44
4.7 X-ray Photoelectron Spectroscopy . . . 46

5 Epitaxial Growth **49**
5.1 Molecular Beam Epitaxy . . . 50
5.1.1 Growth Rates in MBE . . . 52
5.2 Metal Organic Chemical Vapour Deposition . . . 52

6 Device Fabrication Techniques **55**
6.1 Lithography . . . 56
6.2 Metal Deposition Techniques . . . 59
6.3 Plasma Enhanced Chemical Vapour Deposition of Dielectric Materials . . . 62
6.4 Plasma Etching Systems . . . 62
6.5 Rapid Thermal Annealing . . . 64
6.6 In-House Mask Fabrication . . . 65

6.7 GaSb QR VCSEL Fabrication Flow 66

7 Ohmic-Contacts to p-Type GaAs 71
7.1 Declaration 72
7.2 Au/Ni/Au as a Contact for p-Type GaAs 72

8 Reflectance Monitoring for Growth and Etching 81
8.1 Principles of In-Situ Reflectance Monitoring for Molecular Beam Epitaxy and Inductively-Coupled Plasma Etching 82
8.2 In-Situ Monitoring for ICP 85
8.3 In-Situ Monitoring for MBE 87
8.4 Summary of Reflectance Monitoring 96

9 Distributed Bragg Reflectors 97
9.1 Reduced DBR Resistance using Tailored Interfaces 98
9.2 Optical Absorption at Telecoms Wavelengths 105
9.3 Spiky DBRs 109
9.4 Summary of DBR Studies 119

10 Photoluminescence and Time-Resolved Photoluminescence of GaSb Quantum Rings 121

11 GaSb Quantum Ring VCSELs 127
11.1 VCSEL Design and Modelling 128
11.2 Prior Work 130
11.3 This Work 134
11.3.1 First-Generation Stepped-Interface VCSEL - V1 134
11.3.2 Second-Generation Stepped-Interface VCSELs - V2 and V3 . . . 139
11.3.3 Third-Generation Stepped-Interface VCSEL - V4 143
11.3.4 Discussion of $\lambda/2$ and $3\lambda/2$ Cavity VCSELs 151
11.3.5 Future Work 154

12 Conclusions and Future Work 155

References 159

A Recipes 173
A.1 SiNx Deposition by ICP-PECVD 173
A.2 SiNx Etch by RIE 178
A.3 Mesa-Etch by ICP 180
A.4 Ti-Etch by ICP for Mask Fabrication 183

List of Figures

1.1 Room-temperature photoluminescence of GaSb quantum-rings (black line) with comparison to the measured electroluminescence spectrum (red line) of mesa-less GaSb QR VCSEL material (sample V1, see Table 11.1 and section 11.3.1). The telecoms 'C'-band and 'O'-band are indicated by the shaded regions whilst the lower-cutoff for below-screen applications is indicated by the vertical blue line. 3

2.1 Normal-incidence transmittance (a) and reflectance (b) as a function of refractive index n at the interface between two regions of material 1 and material 2. 8

2.2 Components of plane wave of the form $\tilde{\mathbf{E}}_\mathbf{1} = A_1 e^{ik_1 z} + B_1 e^{-ik_1 z}\hat{\mathbf{x}}$ moving in the z direction towards an interface between two materials, medium 1 and medium 2, and the components of the plane wave $\tilde{\mathbf{E}}_\mathbf{2} = A_2 e^{ik_2 z} + B_2 e^{-ik_2 z}\hat{\mathbf{x}}$ after the interface. 8

2.3 Components of plane wave of the form $\tilde{\mathbf{E}}_\mathbf{0} = A_0 e^{ik_1 z} + B_0 e^{-ik_1 z}\hat{\mathbf{x}}$ moving in the z direction towards a multi-layer material stack after the interfaces. 9

2.4 Representation of the conduction and valence band edges for a direct gap (left) and indirect gap (right) semiconductor. 11

2.5 A sketch of the Brillouin zone for a face-centred cubic lattice indicating the points of symmetry referred to as X, L, and Γ. 12

2.6 Representation of the conduction and valence band offsets for type-I (a), type-II (b) and type-III (c) semiconductor interfaces. The red shaded region represents the forbidden gap between the conduction (E_c) and valence (E_v) bands. The conduction and valence bands are represented by the grey shaded regions and labelled accordingly. The vertical dashed lines represent the interface between a wider bandgap semiconductor material on the left and narrower bandgap on the right. 15

2.7 Schematic of the heterojunction between separate (left) and contacted (right) lightly n-doped (a) / p-doped (b) and heavily N-doped (a) / P-doped (b) materials in a type-I heterojunction. The positions of the conduction band, E_c, valence band, E_v, and Fermi level, E_{fl}, are indicated and the depletion region with net charge is indicated across the interface. The arrow indicates the charge carrier migration across the interface that gives rise to the net charge. 16

2.8 Schematic of the band structure of a separate (left) and a contacted (right) metal-semiconductor interface. The Fermi level, E_{fl}, is indicated and the positions of the conduction band, E_c, and valence band, E_v, are indicated for the semiconductor. The work function of the metal, Φ_m, and the electron affinity of the semiconductor, χ, are indicated on the left hand side of the diagram and the barrier at the metal semiconductor interface, Φ_{ms}, is shown for the contacted case. 17

2.9 Representation of an electron with energy, E, tunnelling through a triangular potential-energy barrier, $V(x)$, of height, V_0, and width, t. 18

2.10 The reflectance spectrum for an undoped GaAs/$Al_{0.9}Ga_{0.1}As$ first-order DBR consisting of 35 pairs on a thick GaAs substrate with a target wavelength of 1300 nm. 20

2.11 The conduction (a) and valence (b) band edges for n-type and p-type GaAs/$Al_{0.9}Ga_{0.1}As$ DBRs doped to $1 \times 10^{18}cm^{-3}$ have large barriers to their respective charge carriers at the material interfaces, as seen by the offset of the bands with respect to the Fermi level. In both cases the Fermi level (indicated by the horizontal lines) sits further from the band edge within the $Al_{0.9}Ga_{0.1}As$ layer. 21

2.12 Transmission electron microscope image of cross-sectioned GaSb quantum-rings within the GaAs cavity of a VCSEL (sample P3, see Table 11.1 and section 11.2). 23

2.13 An artistic interpretation of the cross-section for growth of GaSb quantum dots on GaAs by the Stranski-Krastanow (SK) method before capping with a carefully controlled GaAs layer results in the formation of rings through As-Sb exchange. Stage 1 represents a GaAs surface, upon which the wetting layer and SK GaSb QDs are grown (stage 2). The final stage involves the growth of a cold-cap GaAs layer (upper blue layer in stage 3) and As-Sb exchange which results in the ring geometry. The final cross-section indicates the lobes of a cross-sectioned ring. 24

2.14 The broad room-temperature photoluminescence spectrum of GaSb quantum rings. The blue section represents the telecoms O-band, the red shaded region shows the telecoms C-band, and the orange dotted line represents the transparent region for below-screen applications. 24

2.15 Schematic of a generic top-emitting VCSEL. The active region is contained within a short optical cavity defined by a pair of semiconductor-based DBRs. An oxidation ring is used in the vicinity of the cavity for both optical and electrical confinement. 26

3.1 Schematic of the TFCalc simulation environment. Light is incident on the front layers and detected in the exit medium. Simulations are treated in one dimension so the detector collects all light in the exit medium. . . . 31

4.1 Measured and modelled reflectance for a VCSEL with a $3\lambda/2$ cavity length designed for operation at 1270 nm (sample V4, see Table 11.1 and section 11.3.3). The mismatch between the reflectance of the designed and grown structures indicates a deviation from the design. The DBR is shifted to shorter wavelengths and the cavity resonance shifted to the longer-wavelength side of centre in the stopband. 35

4.2 The Cary 5000 solid sample stage transmission measurement uses two beams passing through a pair of apertures. Beam 1 is used as a reference to minimise the impact of instrument fluctuations. The sample is placed flush against the aperture in the path of the measurement beam. 36
4.3 Reflectance and transmittance measurements for a VCSEL (sample V3, see Table 11.1 and section 11.3.2), indicating a resonance in the region of 1280 nm. A magnified view of the transmittance (right) demonstrates better wavelength-resolution of the cavity but much weaker response compared to the reflectance measurement. Fast scans correspond to an integration time of 0.5 seconds per point, and 10 seconds per point for a slow scan. 36
4.4 The Cary 5000 diffuse reflectance accessory measures the combined specular (beam 1) and diffuse (beam 2) components of reflectance. The sample is mounted against a port on the side of the integrating sphere and oriented to either include the specular component of the reflection (blue dash) or exclude the speular component (red dash). The light is collected by a photomultiplier tube (PMT). The orientation of the sample is indicated by the shading of the sample. 37
4.5 Measured reflectance for a PTFE reference sample and VCSEL sample (sample V1, see Table 11.1 and section 11.3.1), relative to the initial PTFE reference calibration. 37
4.6 Schematic of the measurement area for reflectance measured at the integrating sphere sidewall (left), transmittance using the mounting plate (centre) and the mapped transmittance (right). Mapped transmittance uses the standard transmittance aperture and moves the sample along the path shown using a motorised arm. 38
4.7 Schematic of 'four-probe' and 'two-probe' measurement setup. The sample is indicated as the device under test (DUT). Equivalent circuits are shown alongside the probe configuration with lead resistance denoted as R_L. . . 39
4.8 Schematic of the optical setup used for electroluminescence and constant-irradience photoluminescence measurements. A) 1 Watt 532 nm excitation laser B) silvered mirrors C) optical periscope D) low-power green alignment laser on flip mount E) Thorlabs MLP650L partial mirror F) variable apertures G) 1" off-axis parabolic mirrors H) 3" off-axis parabolic mirrors I) motorized x-y-z-θ stage with sample holder (optional use of temperature controlled holder) J) motorised rotation mount with linear polariser on flip mount K) motorised rotation mount with linear polariser on flip mount L) collection fibre on manual x-y-z stage. The final off-axis parabolic mirror (G) focuses the light onto the collection fibre (L). The fibre leads to an Acton SpectraPro 2300i spectrometer equipped with an Andor iDus 492A InGaAs-array detector. 41
4.9 Schematic of the cryostat-compatible 'cold sticks' used for low temperature EL and PL measurements. The EL stick (left) takes a sample in a TO-46 header on a threaded insert at the base of the stick. The header socket is configured for four probe measurements with light directly coupled into a collection fibre. The PL stick (right) takes a sample mounted onto a threaded insert at the base of the stick with the excitation laser and fluorescent emission directly coupled through the same fibre. 42

4.10 A sketch indicating a selection of the signals measured during interaction of the electron beam and the sample during electron microscopy techniques. The shaded volumes indicate the depth and region within which the different interactions occur between the electrons and the sample. 43

4.11 Transmission electron microscope images showing (a) a poor quality quantum ring growth in a VCSEL (sample V2, see Table 11.1 and section 11.3.2) with defects propagating from the lower DBR through the cavity and into the upper DBR and (b) quantum rings in a VCSEL cavity (sample P3, see Table 11.1 and section 11.2). 44

4.12 Schematic of the BEXP+AFM procedure. Samples are cross sectioned at a known angle (left) using a focussed ion beam. AFM is used to measure the thickness of layers on the cross-sectioned surface (right). 45

4.13 Scanning probe microscope images of a stepped-interface DBR (presented in section 9.1) prepared for BEXP+AFM measurements (a) shown with the measured 3D height (b). 45

4.14 Schematic of a generic X-ray photoelectron spectroscopy setup. 46

4.15 (a) A schematic of the spatial dispersion of electrons through a spherical mirror analyser. The dashed versus solid lines indicate electrons with different initial lateral positions. Different colours indicate electrons with different kinetic energies. An aperture is used to select the kinetic energy of the electrons for imaging, and is indicated on the figure. (b) A schematic of the spatial dispersion of electrons with different kinetic energy through a hemispherical mirror analyser for spectroscopy measurements on a single point of the sample surface. 47

5.1 The Veeco GENxplor MBE system located at Lancaster University. Photo courtesy of Dr Peter Hodgson. 50

5.2 A schematic of the Veeco GENxplor MBE growth chamber used in this work. The system uses solid-source effusion cells for group-III materials and dopants, and valved cracker cells for the group-V sources. All of the sources are located at the base of the chamber. The chamber walls are cooled using a nitrogen jacket. Wafers are mounted on a rotating stage at the top of the chamber and covered by a shutter before and after the growth process. The MBE chamber is equipped with RHEED for in-situ analysis of the wafer surface. A heated viewport is located directly below the sample and is used for normal incidence reflectance monitoring. . . 51

5.3 Schematic of an MOCVD planetary reactor. Heated substrates process orbit the chamber with opposite rotational direction. The precursors are injected in a laminar flow from the centre of the chamber to the edge. . 53

6.1 An example of the 'focus wobble' measurement on a Picomaster 100 laser-writer used to set the appropriate height of the writing head. All of the signals are given in volts. The focus sum (red line) is indicative of the signal intensity of the reflected focus laser. The focus error (blue line) is used to determine the correct height of the module to achieve correct focus and is used in conjunction with the focus setpoint (grey dashed line). . . 57

6.2 Schematic of single layer photoresist (left) coated with gold by a physical vapour deposition process compared to a bilayer resist process with sacrificial lift-off resist (LOR) underlayer. The black arrows represent the entry point for resist remover. 58

6.3 Diagram of Moorfield Minilab thermal evaporation (top) and DC/RF sputtering (bottom) chambers. 60

6.4 (a) A scanning electron microscopy image of sputtered TiAu bondpads on a VCSEL sample. A gap in the metal is shown around the base of an etched mesa. (b) A schematic of the structure in the microscope image, the angle of the SEM image is indicated on the schematic. 61

6.5 A schematic of the chamber for an Oxford Instruments PlasmaPro 80 ICPCVD system. 62

6.6 A schematic of the chamber for an Oxford Instruments PlasmaPro 80 RIE system (top) and PlasmaPro 100 ICP-RIE system (bottom). 63

6.7 RIE etch rate calibration for Si_3N_4 etched using CHF_3 chemistry. The saturation in etch depth corresponds to a complete etch of the $\sim$200 nm Si_3N_4 layer. 64

6.8 A schematic of the Allwin21 AccuThermo AW 610 rapid thermal annealing system. The sample is loaded into a SiC-coated graphite susceptor and heated using lamps. A thermocouple is located inside the susceptor, close to the sample to monitor the temperature. A gas inlet feeds in the process gases from a mass-flow controller. 65

6.9 Diagram showing the in-house step-by-step fabrication of photolithography masks. Existing chrome layers (a) are wet-etched using chrome etchant (b+c), titanium is sputtered onto the bare quartz slide (d). S1813 is spun onto the surface and used to transfer the desired pattern (e) into the titanium using ICP dry etching (f). 66

6.10 A simplified sketch of the final QR VCSEL device geometry from a top-down view. Yellow features represent the Au/Ni/Au contacts, cyan represents the position of the Ti/Au bondpad, the red region represents the masked area for the mesa definition. Regions outside of the red area are etched. An enlarged view of the 30 µm device is shown at the bottom. . . 69

6.11 A sketch of the key steps in the fabrication flow of GaSb QR VCSEL devices including top contact deposition (a), surface passivation (b), re-access to the VCSEL surface (c), bondpad deposition (d), mesa etch (e), mesa passivation (f), re-access to bondpads and the VCSEL surface (g), back contact deposition with photoresist to protect the top-surface (h), contact annealing (i), and device mounting (j). 70

7.1 Current-voltage sweeps through adjacent top-top Ti/Au contacts on p-type GaAs show a non-linear dependence, indicative of the presence of Schottky barriers. 73

7.2 TLM-bar analysis for Au/Ni/Au contacts annealed at 450 °C for 60 s. A linear fit to resistance as a function of pad spacing allows extraction of twice the contact resistance for zero pad spacing, giving contact resistance of $(0.30 \pm 0.03)\,\Omega$ and specific contact resistance of $(6.0 \pm 0.6) \times 10^{-5}\,\Omega\,\mathrm{cm}^2$. 75

7.3 Current-voltage sweeps through adjacent top-top contacts show the presence of a Schottky-barrier in Ti/Au contacts (not annealed) on p-type GaAs. Au/Ni/Au contacts also demonstrate this non-ohmic behaviour prior to annealing. In comparison, annealed contacts of Au/Ni/Au (350 °C for 1 minute) and Au/Zn/Au (350 °C for 3 minutes) both show significantly lower resistance and an ohmic nature. 75
7.4 A comparison of differential resistance for Ti/Au and annealed Au/Ni/Au contacts in the range of −3 mV to 3 mV shows orders of magnitude difference in the contact schemes. The extended range for differential resistance of Ti/Au contacts is shown on the inset, remaining more than an order of magnitude higher resistance throughout the measured range. 76
7.5 Contact resistance for 100 µm by 200 µm contacts on p-doped GaAs at various annealing temperatures for samples spending a nominal time at the stated maximum temperature. It should be noted that the nominal duration is the time spent at the set temperature. Due to slow radiative-cooling, hotter samples will experience a longer time at elevated temperatures and may therefore undergo further annealing. For short annealing times this will be a more significant contribution to annealing time. 77
7.6 Thermal annealing can have a visible effect on the morphology of Au/Ni/Au contacts. (a) An unannealed sample as a reference. (b) A sample annealed at 300 °C for 3 minutes demonstrating little change in morphology. A subtle change in the gold tone may be visible for annealed samples. (c) A sample annealed at 450 °C for 5 minutes demonstrates visible degradation of the contacts. The gold-colour has completely disappeared, likely due to diffusion of the gold into the semiconductor material below. 77
7.7 Contact resistance for 100 µm by 200 µm Au/Ni/Au contacts annealed at 350 °C show a consistently low contact resistance of just ∼0.1 Ω irrespective of annealing duration, except for the anomalous data at 120 s. 78
7.8 X-ray photo-electron spectroscopy images of annealed (350 °C for 1 minute) Au/Ni/Au contacts on p-type GaAs showing the Au-4f peak for the unetched sample (left) and following milling to depths of (80±10) nm (centre) and (160 ± 10) nm (right). The scale represents the count rate (arbitrary units) detected by a pixel for the Au-4f peak. The images indicate removal of most of the gold by (80 ± 10) nm and residual gold from the final contact by (160 ± 10) nm. 78

8.1 a) A flowchart representing the logic behind simulations of in-situ growth monitoring. b) A section of simulated reflectance as a function of growth thickness for a stepped-interface DBR (section 9.1) in a VCSEL sample with $\lambda/2$ cavity grown by MBE and monitored by a 650 nm laser. 83
8.2 The simulated reflectance versus etch depth for a QR VCSEL sample with 21× DBR repeats in the lower DBR and 15× repeats in the upper DBR, both DBRs have step-graded interfaces (section 9.1). The blue circle indicates an example of a target endpoint for the minimum depth of a device mesa etch in the uppermost GaAs layer of the lower DBR. 84
8.3 A sketch of reflectance as a function of growth time and growth thickness. Features are separated by a time, δt, and corresponding thickness of grown material, δx. 84

8.4 The ICP chamber has a top-mounted translational stage holding a module containing the alignment camera, laser and detector. Reflectance is monitored through the top viewport at close to normal incidence. 86
8.5 The simulated and measured reflectance versus etch depth for a QR VCSEL sample with 21× DBR repeats in the lower DBR and 15× repeats in the upper DBR, both DBRs have step-graded interfaces (section 9.1). The blue circles indicate the target endpoints for the device mesa etch on the respective traces. The simulations are conducted as a function of etch depth, experimental data are collected as a function of time. 86
8.6 The Veeco GENxplor chamber is equipped with a heated viewport directly under the rotating sample stage. A laser diode and silicon photodetector are mounted below the viewport. The laser is clamped in a stand to allow for translational and rotational adjustment. The laser is driven by the reference output on an SR830 lock-in amplifier which measures the signal from the detector and provides an output which is recorded by a datalogger. 88
8.7 A simplistic representation of the path precessed by the reflected laser spot during reflectance monitoring in MBE for an angled substrate. 88
8.8 Simulated (black) and measured (red) reflectance at 650 nm for alternating AlAs/GaAs layers approximately 300 nm in thickness during MBE growth. The simulations are conducted as a function of growth thickness, experimental data are collected as a function of time. The first ∼300 nm consists of a GaAs buffer which produces no oscillations when grown on the GaAs substrate. 89
8.9 Simulated (black) and measured (red) reflectance at 650 nm versus growth thickness across a pair of AlAs and GaAs layers approximately 300 nm in thickness during MBE growth. The simulations are conducted as a function of growth thickness, experimental data are collected as a function of time. 90
8.10 A scanning electron microscope image of alternating GaAs/AlAs layers shows layer separation and uneven depths of cleaved layers. The GaAs substrate is located to the upper-right corner of the image with the sample surface lower-left. 91
8.11 Energy dispersive X-ray spectroscopy images showing the position of the gallium (a), aluminium (b), arsenic (c), and oxygen (d) along the cleaved-face of a sample with alternating GaAs/AlAs layers. Coloured pixels correspond to the presence of a given element. 92
8.12 A high-contrast scanning electron microscope image of the etch pit formed by focussed ion beam polishing normal to the sample surface for a sample consisting of alternating GaAs/AlAs layers. AlAs layers appear darker on the image. 93
8.13 Parallax-corrected SEM image of GaAs/AlAs layers polished using a focussed ion beam for layer thickness measurements (a) with boosted contrast (b). AlAs layers appear darker on the image. 93
8.14 Temperature-rate calibrations for the aluminium (a) and gallium (b) cells measured using RHEED oscillations at each of the dates given in the legend. The rates obtained using reflectance monitoring are included for comparison. 94

8.15 The percentage deviation of the calculated growth rate for GaAs layers from both reflectance monitoring and SEM, compared to the target. The black dotted line shows the mean growth rate error for the GaAs layers according to the reflectance monitoring setup. The blue dashed line is a visual aid and represents zero error. 95
8.16 The percentage deviation of the calculated growth rate for AlAs layers from both reflectance monitoring and SEM, compared to the target. The black dotted line shows the mean growth rate error for the AlAs layers according to the reflectance monitoring setup. The blue dashed line is a visual aid and represents zero error 95
8.17 The target thickness for a series of GaAs and AlAs layers, the layer thicknesses obtained using reflectance monitoring and layer thickness measured by SEM. 96

9.1 The heavy hole valence band offset relative to the hole Fermi level at a series of aluminium compositions from 30 % to 90 % for a p-doped (Be) GaAs/$Al_xGa_{1-x}As$ DBR with nominal doping density $1 \times 10^{18}\,cm^{-3}$. . . 99
9.2 The conduction band and ground state energy at the gamma point are shown as a function of position, x, along a single repeat of an $Al_{0.9}Ga_{0.1}As$-equivalent GaAs/AlAs digital alloy of length L. The electron probability density is shown on the right-hand axis, as indicated by the blue arrow. 99
9.3 The band structure is shown for a single repeat of an $Al_{0.9}Ga_{0.1}As$-equivalent GaAs/AlAs digital alloy of length L. The lowest energy dispersion curve is shown along the growth axis for the conduction band in the vicinity of the Gamma, X and L valleys. 100
9.4 Simulated reflectance for high contrast (GaAs/$Al_{0.1}Ga_{0.9}As$), low contrast (GaAs/$Al_{0.6}Ga_{0.4}As$) and stepped interface DBRs with 15, 15 and 25 repeats respectively. 100
9.5 Heavy hole valence band offset relative to the hole Fermi level for low aluminium-contrast, high aluminium-contrast and stepped-interface p-doped (Be) DBRs with nominal doping density $1 \times 10^{18}\,cm^{-3}$. 101
9.6 Simulated and measured current-voltage characteristics for high contrast, low contrast and stepped interface DBRs with 10, 17 and 11 repeats respectively. The DBRs were p-doped to a nominal density of $1 \times 10^{18}\,cm^{-3}$. Measured current density is an approximation, assuming minimal current spreading outside of the top contact. 103
9.7 Reflectivity of high contrast, low contrast, stepped interface and digital alloy DBRs relative to a PTFE reference sample. DBRs were designed for operation at 1300 nm but deviate due to inaccuracy of the grown layers. 104
9.8 An AFM image of the stepped-interface DBR cross-sectioned with BEXP for extraction of layer thickness. The narrow intermediate-composition layer is visible at the interfaces between the GaAs and $Al_{0.9}Ga_{0.1}As$. . . 104
9.9 Simulation of stepped-interface DBR reflectance as a function of wavelength based on layer thickness measurements from BEXP+AFM compared to the measured reflectance. Discrepancies between the peak reflectivity is attributed to the calibration of the measurement to an imperfect reference plate, and optical absorption in the material which has been omitted from the model. 105

9.10 The nominal doping profile (top), simulated ionised acceptor density (middle) and simulated valence band edge (bottom) for a Be-doped $Al_xGa_{1-x}As$-based DBR nominally doped at $1 \times 10^{18}\,cm^{-3}$ at 300 K. The valence band edge is included for ease of visualising the interfaces between layers. . . . 107

9.11 Measured reflectance, transmittance and the central wavelength of stopbands for DBRs unintentionally-doped (represented here as $1 \times 10^{15}\,cm^{-3}$) and with doping levels of $5 \times 10^{16}\,cm^{-3}$, $5 \times 10^{17}\,cm^{-3}$, $1 \times 10^{18}\,cm^{-3}$ and $5 \times 10^{18}\,cm^{-3}$ are shown against the effective ionised acceptor density obtained from simulation (a) and the nominal doping concentration (b). . 108

9.12 The aluminium composition for a continuously-graded $Al_xGa_{1-x}As$ DBR designed for operation around 1300 nm. 110

9.13 The simulated valence band profile of a textbook high-contrast $GaAs/Al_{0.9}Ga_{0.1}As$ DBR, graded-interface $GaAs/Al_{0.9}Ga_{0.1}As$ DBR and spiky $Al_xGa_{1-x}As$ reflector, all structures are nominally doped at $5 \times 10^{17}\,cm^{-3}$. 110

9.14 Simulated reflectance spectra for B-Std in the region of 850 nm including and excluding the effects of strong absorption. 111

9.15 The reflectance spectra of A-Std (a) and A-Spiky (b) as measured, simulated with absorption and simulated excluding absorption. 112

9.16 Measured reflectance of a spiky DBR operating at 1300 nm is compared to simulations of the structure as-designed (a), adjusted for the central wavelength as-grown (b), fitted with aluminium composition reduced to 80 % (c) and finally with reduced aluminium composition and adjusted for the central wavelength (d). 113

9.17 The normalised reflectance spectra comparing equivalent DBR designs at 850 nm and 1300 nm for samples A-Std, A-Spiky, C-Std and C-Spiky (a) and samples B-Std, B-Spiky, E-Std and E-Spiky (b) as measured using a Cary 5000 spectrophotometer with diffuse reflectance accessory. 114

9.18 Normalised reflectance spectra of sample B-Spiky (850 nm) as-measured post-growth at IQE and simulated with an overgrown GaAs capping layer. 115

9.19 Reflectance spectra of DBRs with a reflectivity in the region of 1300 nm designed with higher (a) and lower (b) reflectance targets. Higher reflectivity corresponds to samples C-Std, C-Spiky, E-Std and E-Spiky, lower reflectance corresponds to D-Std, D-Spiky, F-Std and F-Spiky. Reflectance is normalised to the peak of the most reflective DBR. 116

9.20 The simulated conduction band edge relative to the Fermi level is shown for samples B-Std and B-Spiky designed to reflect in the region of 850 nm (a) and samples E/F-Std and E/F-Spiky in the region of 1300 nm (b). The valence band offset relative to the Fermi level is shown for samples A-Std and A-Spiky designed to reflect in the region of 850 nm (c) and samples C/D-Std and C/D-Spiky in the region of 1300 nm (d). All simulations are at zero bias. 117

9.21 Current-voltage characteristics for carbon-doped (p-type) DBRs reflecting in the region of 850 nm and 1300 nm (a). Current-voltage characteristics of silicon-doped (n-type) and carbon-doped (p-type) DBRs reflecting in the region of 1300 nm (b). 118

10.1 Continuously pumped room-temperature photoluminescence measurements for three quantum ring samples grown with different Sb-flux. Samples are all pumped with the same laser power at 532 nm. 122

10.2 A cartoon band structure (right) for the schematic (left) of (a) electron capture, τ_e, (b) electron-hole recombination mechanisms, τ_{nr}, τ_{rad}, and (c) hole capture, τ_h, in the vicinity of GaSb quantum rings. 124

10.3 Photoluminescence decay of recombination for GaSb quantum rings in a VCSEL-wafer cavity off-resonance (1161nm). The decay is fitted with bi-exponential and tri-exponential decay functions. 125

10.4 Fitted lifetimes τ_1, τ_2 and corresponding average lifetimes, τ_{av}, for GaSb quantum rings in the cavity of unprocessed VCSEL material - denoted VCSEL - and bulk GaAs - denoted QR. Fitting is performed off-resonance for the cavity at 1161 nm, and on resonance at 1243 nm, with corresponding reference lifetimes collected at 1161 nm and 1250 nm. The samples were pumped by a 980 nm pulsed laser. 126

11.1 The electric field and refractive index profiles within the VCSEL are given as a function of position for the final design of a stepped-interface DBR VCSEL with $\lambda/2$ cavity length. The positions of the quantum ring layers are indicated by the vertical red lines and the outer extremes of $Al_{0.6}Ga_{0.4}As$ spacer layers in the cavity are indicated by the blue dashed lines. 129

11.2 Normalised room-temperature electroluminescence spectra of QR-VCSEL samples with low aluminium-contrast $Al_xGa_{1-x}As$ DBRs (P1 and P2) and high aluminium-contrast $Al_xGa_{1-x}As$ DBRs (P3) for VCSELs grown prior to this work. It is clear that the VCSEL incorporating high aluminium-contrast DBRs suffers from an broad and relatively intense background emission. 132

11.3 A schematic of the geometry of the fabricated VCSELs using sample P3. Top contacts are placed on an etched surface below undoped layers in the upper-DBR. Red highlighting under the contacts represents an area where much of the light may be produced. 132

11.4 Normalised room-temperature electroluminescence spectra of QR-VCSEL samples with low aluminium-contrast DBRs (P1) and high aluminium-contrast stepped-interface DBRs (V1). The spectra exhibit similar relative intensities of the background emission. 136

11.5 A model of the reflectance spectrum is shown for a VCSEL (sample V1, see Table 11.1) with stepped-interface DBRs designed for operation at 1270 nm (top). The spectrum obtained from transmittance measurements (bottom) shows a significant shift in the wavelength of the reflectance spectrum. A model that fits the shift in spectrum is shown for comparison. 137

11.6 Current-voltage characteristics of VCSEL devices. Low-contrast low-reflectivity DBRs (P1 and P2), high-contrast high-reflectivity DBRs (P3), stepped-interface high-reflectivity DBRs (V1, V2, V3 and V4). Sudden drops in the reverse IV are an artefact of the measurement and not representative of the device performance. 138

11.7 Transmission electron microscope images showing defects throughout V2. a) Defects originating in the lower DBR and propagating through a poor-quality cavity into the upper DBR. b) A poor active region showing few GaSb nano structures. c) Defects threading through the upper DBR. . . 140
11.8 Multiple transmittance sweeps of sample V2 (see Table 11.1) show a weak cavity present around 1300 nm. Scan 2 indicates that the transmittance spectrum is not consistent across the sample and that there are regions lacking a clear cavity resonance. It should be noted that the sample was visibly cloudy to the naked eye. 140
11.9 Normalised room-temperature electroluminescence spectra of QR-VCSEL sample V2. 141
11.10Normalised room-temperature electroluminescence spectra of QR-VCSEL samples V3, P1 and P2. 142
11.11Normalised electroluminescence spectra of the $\lambda/2$ stepped-DBR VCSEL structure at various drive currents. The intensity of the sidebands visibly increases relative to the cavity peak as drive current increases. 142
11.12Reflectance spectra for the $3\lambda/2$ VCSEL including the measured spectrum, and models for the original design and model based on layer thickness measured using TEM. 144
11.13Normalised electroluminescence spectra of the $\lambda/2$ (V3) and $3\lambda/2$ (V4) stepped-DBR VCSEL structures. 144
11.14a) Temperature-dependent spectra of a $3\lambda/2$ cavity VCSEL with 10 µm mesa and a temperature coefficient of (0.09 ± 0.01) nm/K. b) Room-temperature and 77K spectra of a $3\lambda/2$ cavity VCSEL with 30 µm mesa. 146
11.15a) Room-temperature (20 °C) voltage-current and intensity-current measurements for continuous operation of a $3\lambda/2$ cavity VCSEL with 10 µm mesa. b) Threshold current for continuous room-temperature (20 °C) operation of a $3\lambda/2$ cavity VCSEL with 10 µm mesa indicated at the maximum of the second derivative of the output intensity with respect to current. 148
11.16Low temperature (77 K) voltage-current and intensity-current measurements for continuous operation of a $3\lambda/2$ cavity VCSEL. 149
11.17a) Normalised emission spectra for a $3\lambda/2$ cavity VCSEL with 30 µm mesa operating at 77 K for 5 mA and 8 mA. b) The ratio of 5 mA to 8 mA drive current intensity shows a stark quenching of the cavity enhanced emission. Horizontal and vertical dashed lines have been added to guide the eye. . 150
11.18a) Area-scaled output intensity as a function of current density for a $3\lambda/2$ cavity device (V4) and $\lambda/2$ cavity (V3). b) The output intensity at the cavity resonance is given relative to the sum of the cavity resonance intensity and the maximum intensity at the first sideband on the long wavelength side of the cavity. The inset shows the ratio over a larger range for the $3\lambda/2$ structure. Intensity and current density below 5×10^{-4} mA/µm^2 should be taken with caution for the $3\lambda/2$ structure due to overall low intensity of light incident on the detector due to the small size of the device, this region is indicated by the shaded background. 152
11.19The electric field and refractive index profiles within the $3\lambda/2$ VCSEL are given as a function of position. The positions of the quantum ring layers are indicated by the vertical red lines. 153

List of Tables

2.1 Relative permeability for a selection of III-V materials. 8
2.2 Comparison of properties for material systems used in distributed Bragg reflectors. The lattice mismatch between InAs and AlAs would prevent their use in an epitaxially-grown DBR. 22

3.1 TFCalc environment parameters for simulation of VCSEL components and full VCSELs during the design and characterisation stages. 31

6.1 Resist selection and applications within this work. 59

8.1 Growth-rate calibration layers in the order that they were grown for a demonstration of growth rate monitoring capabilities and proof-of-concept for pre-growth rate determination. 89

9.1 Layer descriptions of high-contrast (alloy and digital-alloy), low-contrast and stepped-interface DBRs, as grown. All of the structures were p-doped with beryllium. 102
9.2 The target wavelength, top layer material composition and the number of DBR repeats for twelve DBR designs used to compare the performance of spiky DBRs to their traditional counterparts. Each row is designed to have equivalent peak reflectivity at the target wavelength. 111

11.1 A reference of the sample ID for each of the VCSELs discussed in this work. QR VCSELs from prior work are denoted with the letter P, samples from this work are denoted with the letter V. Samples are numbered in chronological order according to their growth date. 128
11.2 Epitaxial design of the initial QR VCSEL (P1). 131
11.3 Epitaxial design of sample P3 which utilised high-contrast abrupt interface DBRs and incorporated undoped DBR repeats at the top of the structure to minimise optical absorption which was believed to hamper performance of previous QR VCSELs. 133
11.4 Epitaxial design of the first stepped-interface QR VCSEL (V1). 135
11.5 Epitaxial design of the second-generation stepped-interface QR VCSELs (V2 and V3). 139
11.6 Epitaxial design of the third-generation stepped-interface QR VCSEL (V4). 145

A.1 The deposition recipe for SiNx used over the course of this work. 177
A.2 The etch recipe for SiNx used over the course of this work. 179

A.3 The mesa-etch recipe used to etch VCSELs and DBRs over the course of this work. 182
A.4 The mesa-etch recipe used to etch VCSELs and DBRs over the course of this work. 185

Chapter 1

Introduction

Vertical-cavity surface-emitting lasers (VCSELs) were first proposed by Professor Kenichi Iga in the late 1970s with the first publication at the end of the 1970s [1]. GaAs-based VCSELs and VCSEL arrays with quantum well active regions are ubiquitous at shorter-wavelengths (<1150 nm). They are used in a multitude of applications including datacoms transceivers, optical mice, laser printers, and perhaps most broadly and famously burst onto the scene of facial recognition systems with the release of the iPhone X [2, 3]. This thesis is comprised of the research surrounding gallium-antimonide quantum-ring (GaSb QR) VCSELs, which may be referred to in this work simply as QR VCSELs.

Lasers emitting parallel to current injection have been demonstrated as early as the 1960s [4]. The special case of the VCSEL has been the focus of numerous books and studies due to the broad scope of their applications, such devices continue to show promise in future technologies [2, 5, 6, 7, 8, 9, 10, 11].

In contrast to edge-emitting lasers (EELs), fast and non-destructive optical measurements may be performed on VCSEL wafers prior to device fabrication to obtain characteristics such as the cavity resonance which provides an indication of the emission wavelength and avoids expensive processing of sub-par material. The small footprint, combined with their vertical-emission enables the production of hundreds of thousands of devices on a single wafer and on-wafer testing which results in low manufacturing costs and high device yield in comparison to EELs [12].

VCSELs typically offer lower output powers than EELs. Hence, they may be unsuitable where a single high-power laser is required. However, in applications where laser arrays may be used, VCSELs present a strong case for high-power uses. The VCSEL devices with mesa sizes of the order of tens of micrometres have a smaller footprint on the wafer than EELs, this enables much higher packing densities of emitters in laser arrays. The small size and vertical emission of the VCSEL also enables the production of arrays with scalable output power. Such arrays could see uses in industrial 3D sensing, or consumer LiDAR (such as self-driving cars) if operated in the so-called 'eye-safe' regime [13, 14]. In cases where lower-power emission is acceptable, the VCSEL mesa offers a circular beam profile in contrast to the elliptical profile associated with many EELs.

The popularity of VCSELs is a result of their excellent electro-optical properties, low cost of production and their geometry which facilitates straightforward coupling with other technologies such as optical fibres. In the years leading up to 2028 the total market value is estimated to exceed $1 billion [3, 15].

Despite their prevalence and popularity, VCSELs have failed to break into the longer-wavelength market for datacoms at 1310 nm, 'eye-safe' LiDAR, and below-screen sensing because their emission wavelengths are currently too short. The emission wavelength of traditional GaAs-based VCSELs can be extended through increased indium fraction in the active region and are used to access up to around 1150 nm. This approach breaks down when attempting to hit wavelengths in the region of 1300 nm and beyond due to large lattice mismatch and strain accompanying the high indium content in the quantum well active region, subsequently reducing the crystal quality. The limited reach into the market of longer wavelengths is not due to a lack of interest, but due to the difficulties associated with reaching these wavelengths. As a result of this challenge, the move to longer wavelengths remains an active research area with multiple approaches to the problem, and ongoing active research from major VCSEL manufacturers. Approaches to the longer wavelengths include, but are not limited to, the development of $In_xGa_{1-x}As$

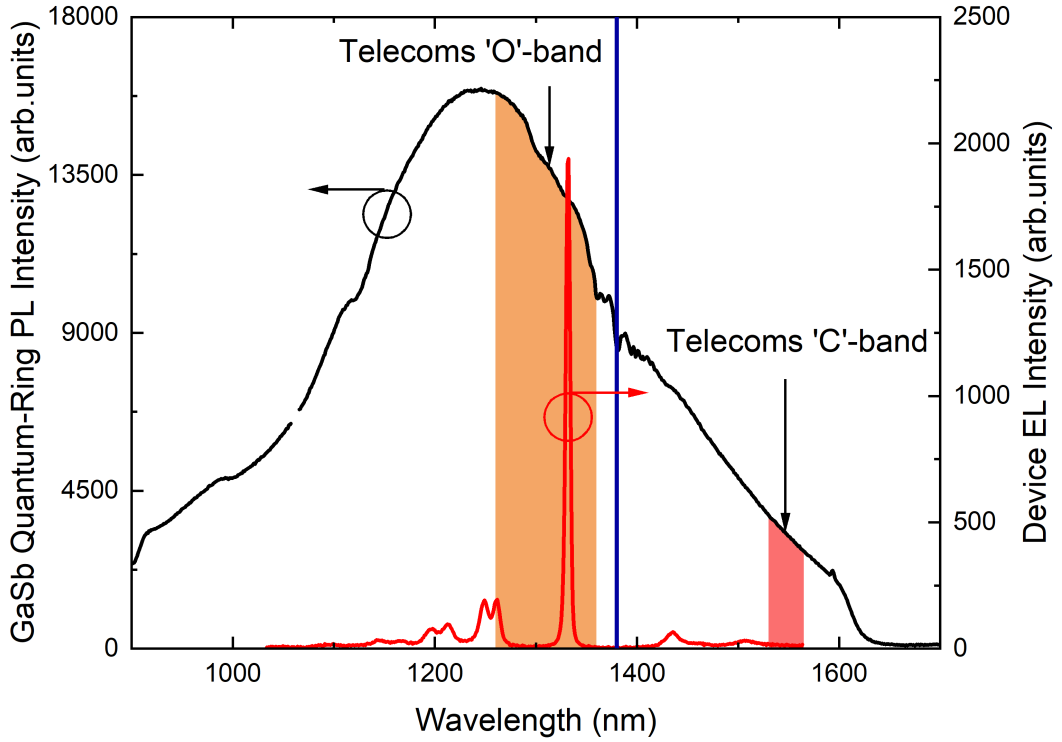

Figure 1.1: Room-temperature photoluminescence of GaSb quantum-rings (black line) with comparison to the measured electroluminescence spectrum (red line) of mesa-less GaSb QR VCSEL material (sample V1, see Table 11.1 and section 11.3.1). The telecoms 'C'-band and 'O'-band are indicated by the shaded regions whilst the lower-cutoff for below-screen applications is indicated by the vertical blue line.

and $In_xGa_{1-x}P$ quantum-dot active regions, use of alternative substrates, growth of dilute nitrides, and more complex multi-epitaxy processes [13, 16, 17, 18, 19, 20]. A summary of the telecoms and eye-safe wavelength markets and recent technologies are presented in section 2.6.

GaSb/GaAs quantum-rings are low-dimensional nanostructures with type-II band alignment. The photoluminescence emission spectrum of these structures is broad (Figure 1.1), covering the desired range of 1300 nm to 1550 nm. This longer-wavelength market is the target for GaSb QR VCSELs. The lasing wavelength supported by a VCSEL is selected by its cavity length. Consequently, the broad gain spectrum of the quantum-rings suggests that VCSELs can be made across the telecoms band, just by changing the cavity thickness and DBR stopband position.

1.1 Synopsis of Chapters

A discussion of the background theory relevant to this thesis is presented in chapter 2. The chapter first covers the mathematical methods used in the simulation of multilayer optical systems. The semiconductor and quantum physics concepts relevant to the later work are introduced, followed by the principles behind the optical and electrical properties of DBRs. Next, is an introduction to GaSb quantum rings and their properties. Finally,

the basic concept of VCSELs is presented with a discussion of the technologies used to approach telecoms-wavelengths.

Chapter 3 summarises the commercial simulation tools used in this body of work and the applications for which they are used. A variety of techniques are used to characterise the quality of epitaxial material and performance of devices, enabling the research surrounding GaSb QR-VCSELs. A summary of the techniques used in this work is provided in chapter 4.

Chapter 5 details the epitaxial techniques used to grow all of the semiconductor structures in this work. The epitaxial material is processed into devices in the Quantum Technology Centre (QTC) cleanroom at Lancaster University. Details of the fabrication techniques and the final process flow for QR VCSEL fabrication are provided in chapter 6.

The main body of results for this work is categorised by chapter. The formation of ohmic-contacts to p-type GaAs is desired for efficient electrical injection into the VCSEL semiconductor material. A study on the formation of such contacts using a nickel-based contact is presented in chapter 7.

Normal-incidence reflectance of the semiconductor is measured throughout the growth and subsequent etching of DBRs and VCSEL material to monitor the thickness of the layers during each process. The principles of operation are given in chapter 8, followed by the application in inductively-coupled plasma reactive-ion etching (ICP-RIE). Chapter 8 concludes with results demonstrating the operation of a bespoke reflectance-monitoring system that has been developed to monitor the growth of GaSb QR VCSELs by molecular beam epitaxy (MBE).

Chapter 9 details the findings of three studies into DBRs designed for devices operating at telecoms-wavelengths. The studies have an emphasis on improving the electrical characteristics of the structures without sacrificing their optical properties. The first investigation compares the performance of MBE-grown $Al_xGa_{1-x}As$-based DBRs with different compositions of materials. The DBR with the best overall performance in the first study was then regrown with a series of doping concentrations to investigate the optical-implications of beryllium dopants in $Al_xGa_{1-x}As$ DBRs at telecoms-wavelengths. The DBR chapter concludes with a comparison of novel and standard industry-grown DBR structures to examine their relative merits.

Chapter 10 contains the results of continuous-wave and time-resolved photoluminescence measurements of GaSb quantum rings. Arguments have been made for long radiative recombination lifetimes of charge carriers in GaSb quantum ring systems[21]. These measurements provide a further insight into the carrier recombination lifetimes for GaSb QRs in the presence of an optical cavity. This thesis concludes with the interpretation of electrical and optical characteristics of the QR VCSEL iterations produced throughout the course of this research (chapter 11) and a direction for further research and development of the devices (chapter 12).

Chapter 2

Background Theory

This chapter introduces the theoretical concepts used throughout the course of this work. First, the propagation of light through multilayer structures is described for the normal-incidence case. The mathematical description derived for the propagation of light forms the basis of simulations presented in chapter 8. The next subsection provides a summary of the fundamental electrical properties of semiconductors in bulk and at the interface between two different semiconductor materials, followed by a description of the metal-semiconductor interface. An introduction to the optical principles behind the operation of DBRs is given for their textbook case and followed by a discussion of their electrical properties. The use of quantum rings as the active region in VCSELs forms the cornerstone of this research. The relevant background regarding these nanostructures is provided prior to a summary of VCSELs themselves, which includes a summary of the current status of telecoms-wavelength VCSELs.

2.1 Multi-Layer Optics at Normal Incidence

In this section, a matrix-based expression for the propagation of light across a single material interface is presented at normal incidence. The single interface expression is then extended to cover transmission and reflection through a structure with an arbitrary number of interfaces. The normal-incidence multi-interface case forms the basis of the simulations in section 8.1.

For a monochromatic plane wave the amplitude of the magnetic field, $\mathbf{B}$, may be expressed using the magnitude of the electric field, $\mathbf{E}$, according to $\frac{1}{\nu}\tilde{E}$, where ν is the speed of light in the material and $\tilde{E}$ is the phase-dependent amplitude of the electric field. Considering a normal-incidence plane wave, $\tilde{\mathbf{E}}_\mathbf{I}$, moving in direction z and incident upon a single material interface in the xy plane from material 1 to material 2,

$$\tilde{\mathbf{E}}_\mathbf{I}(z,t) = \tilde{E}_{0_I} e^{i(k_1 z - \omega t)}\hat{\mathbf{x}}, \tag{2.1}$$

$$\tilde{\mathbf{B}}_\mathbf{I}(z,t) = \frac{1}{\nu_1}\tilde{E}_{0_I} e^{i(k_1 z - \omega t)}\hat{\mathbf{y}}, \tag{2.2}$$

where t represents time, k is the wavevector and ω is the angular frequency of the wave such that ωt represents a phase offset for the electric field. The boundary may give rise to a reflected wave,

$$\tilde{\mathbf{E}}_\mathbf{R}(z,t) = \tilde{E}_{0_R} e^{i(-k_1 z - \omega t)}\hat{\mathbf{x}}, \tag{2.3}$$

$$\tilde{\mathbf{B}}_\mathbf{R}(z,t) = -\frac{1}{\nu_1}\tilde{E}_{0_R} e^{i(-k_1 z - \omega t)}\hat{\mathbf{y}}. \tag{2.4}$$

and transmitted wave,

$$\tilde{\mathbf{E}}_\mathbf{T}(z,t) = \tilde{E}_{0_T} e^{i(k_2 z - \omega t)}\hat{\mathbf{x}}, \tag{2.5}$$

$$\tilde{\mathbf{B}}_\mathbf{T}(z,t) = \frac{1}{\nu_2}\tilde{E}_{0_T} e^{i(k_2 z - \omega t)}\hat{\mathbf{y}}. \tag{2.6}$$

The general boundary conditions for linear media reveal that

$$\mathbf{E}_1^{\parallel} = \mathbf{E}_2^{\parallel}, \tag{2.7}$$

$$\frac{1}{\mu_1}\mathbf{B}_1^{\parallel} = \frac{1}{\mu_2}\mathbf{B}_2^{\parallel}, \tag{2.8}$$

where $\mathbf{E}_1^{\parallel}$ and $\mathbf{E}_2^{\parallel}$ represent the parallel component of the electric field either side of an interface, $\mathbf{B}_1^{\parallel}$ and $\mathbf{B}_2^{\parallel}$ represent the parallel component of the magnetic field either side of and interface and μ is the material permeability [22]. These boundary conditions require that

$$\tilde{E}_I + \tilde{E}_R = \tilde{E}_T, \tag{2.9}$$

$$\frac{1}{\mu_1}\frac{1}{\nu_1}\left(\tilde{E}_I - \tilde{E}_R\right) = \frac{1}{\mu_2}\frac{1}{\nu_2}\tilde{E}_T. \tag{2.10}$$

From this we obtain

$$\tilde{E}_I - \tilde{E}_R = \frac{\mu_1\nu_1}{\mu_2\nu_2}\tilde{E}_T \tag{2.11}$$

and given that

$$\nu = \frac{c}{n},$$

where n is the refractive index, and the permeabilities of III-V semiconductors are effectively unity (Table 2.1), this leads to the expressions for the transmitted and reflected components relevant to this work of,

$$E_{0_R} = |\frac{n_1 - n_2}{n_1 + n_2}|E_{0_I}, \tag{2.12}$$

$$E_{0_T} = |\frac{2n_1}{n_1 + n_2}|E_{0_I}, \tag{2.13}$$

and expressions for the coefficients of reflection, r, and transmission, t,

$$r_{12} = \frac{n_1 - n_2}{n_1 + n_2}, \tag{2.14}$$

$$t_{12} = \frac{2n_1}{n_1 + n_2}. \tag{2.15}$$

The incident, reflected and transmitted power intensities of the plane wave are given by

$$I = \frac{1}{2}\epsilon\nu E_0^2, \tag{2.16}$$

$$R \equiv \frac{I_R}{I_I} = \left(\frac{E_{0_R}}{E_{0_I}}\right)^2 = \left(\frac{n_1 - n_2}{n_1 + n_2}\right)^2, \tag{2.17}$$

$$T \equiv \frac{I_T}{I_I} = \left(\frac{E_{0_T}}{E_{0_I}}\right)^2 = \frac{\epsilon_2\nu_2}{\epsilon\nu_1}\left(\frac{E_{0_T}}{E_{0_I}}\right)^2, \tag{2.18}$$

where ϵ is the material permittivity. In the case that $\mu \cong \mu_0$,

$$n \equiv \sqrt{\frac{\epsilon\mu}{\epsilon_0\mu_0}} \cong \sqrt{\epsilon_r}, \tag{2.19}$$

such that

$$T = \frac{n_2^2\frac{c}{n_2}}{n_1^2\frac{c}{n_2}}\left(\frac{E_{0_T}}{E_{0_I}}\right)^2 = \frac{4n_1n_2}{(n_1 + n_2)^2}. \tag{2.20}$$

The reflectance and transmittance are shown as a function of refractive index in Figure 2.1, indicating that high reflectivity is achieved for large refractive index contrast between materials.

Material	Relative Permeability, μ
GaAs	$9.999\,987\,8 \times 10^{-1} \approx 1$
GaSb	$9.999\,988\,9 \times 10^{-1} \approx 1$
InAs	$9.999\,983\,3 \times 10^{-1} \approx 1$

Table 2.1: Relative permeability for a selection of III-V materials [23].

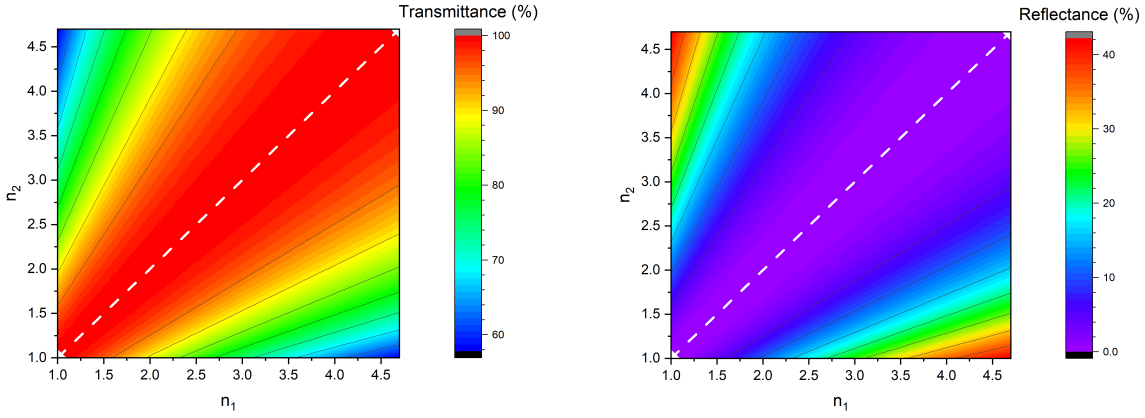

(a) (b)

Figure 2.1: Normal-incidence transmittance (a) and reflectance (b) as a function of refractive index n at the interface between two regions of material 1 and material 2.

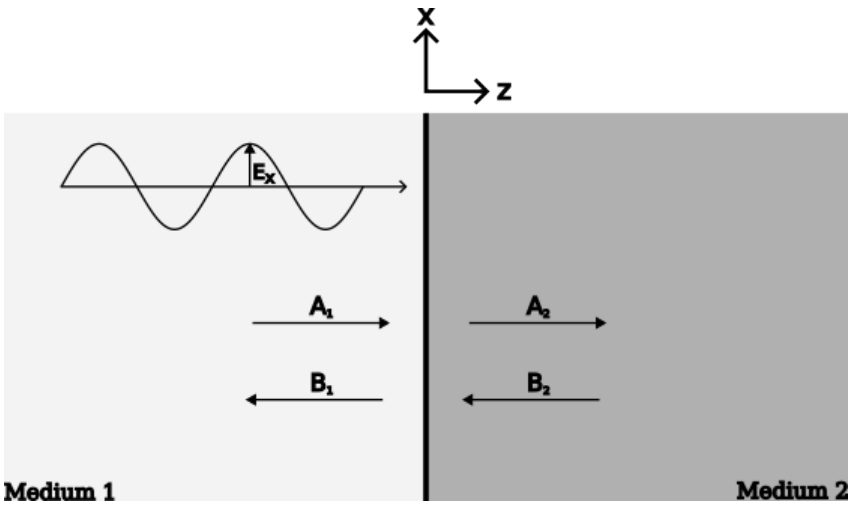

Figure 2.2: Components of plane wave of the form $\tilde{\mathbf{E}}_\mathbf{1} = A_1 e^{ik_1 z} + B_1 e^{-ik_1 z}\hat{\mathbf{x}}$ moving in the z direction towards an interface between two materials, medium 1 and medium 2, and the components of the plane wave $\tilde{\mathbf{E}}_\mathbf{2} = A_2 e^{ik_2 z} + B_2 e^{-ik_2 z}\hat{\mathbf{x}}$ after the interface.

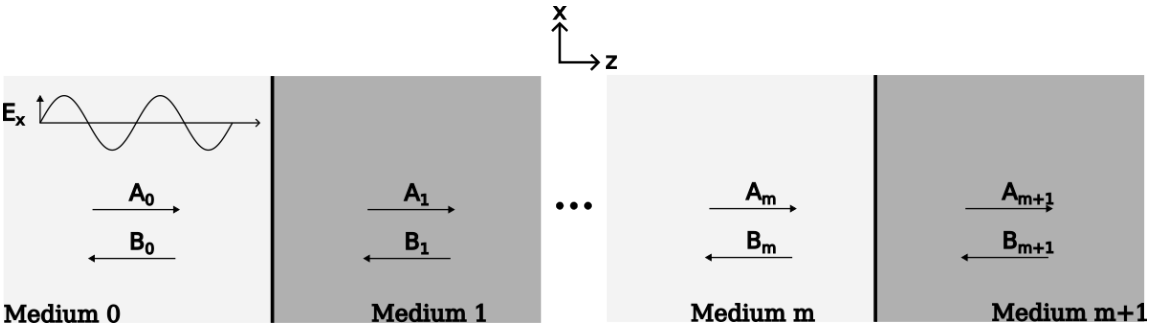

Figure 2.3: Components of plane wave of the form $\tilde{\mathbf{E}}_\mathbf{0} = A_0 e^{ik_1 z} + B_0 e^{-ik_1 z}\hat{\mathbf{x}}$ moving in the z direction towards a multi-layer material stack after the interfaces.

Interfaces in optical systems are often described in matrix form as described in the following work [24]. A plane wave with electric field in direction x, moving in the z direction, is described in medium 1 and medium 2 (Figure 2.2) in a similar fashion to equations 2.1, 2.3 and 2.5, but with the addition of a back-propagating $(-z)$ wave within medium 2,

$$\tilde{\mathbf{E}}_\mathbf{1} = A_1 e^{ik_1 z} + B_1 e^{-ik_1 z}\hat{\mathbf{x}}, \tag{2.21}$$

$$\tilde{\mathbf{E}}_\mathbf{2} = A_2 e^{ik_2 z} + B_2 e^{-ik_2 z}\hat{\mathbf{x}}. \tag{2.22}$$

Amplitudes A_1 and A_2 correspond to the forwards $(+z)$ propagating components of waves in materials 1 and 2 respectively, waves denoted B refer to backwards $(-z)$ propagating waves. As before, the boundary conditions at the interface dictate that

$$A_1 + B_1 = A_2 + B_2, \tag{2.23}$$

$$\frac{1}{\mu_1 \nu_1}(A_1 - B_1) = \frac{1}{\mu_2 \nu_2}(A_2 - B_2). \tag{2.24}$$

Rearranging equations 2.21 and 2.22 and expressing in terms of refractive index yields

$$A_1 = \frac{n_2 A_2 - n_2 B_2}{2n_1} + \frac{A_2 + B_2}{2} = \frac{1}{2}\left(\frac{n_1 + n_2}{n_1}A_2 + \frac{n_1 - n_2}{n_1}B_2\right) \tag{2.25}$$

$$B_1 = \frac{A_2 + B_2}{2} - \frac{n_2}{2n_1}(A_2 - B_2) = \frac{1}{2}\left(\frac{n_1 - n_2}{n_1}A_2 + \frac{n_1 + n_2}{n_1}B_2\right). \tag{2.26}$$

In matrix form this yields

$$\frac{1}{2}\begin{bmatrix} 1 + \frac{n_2}{n_1} & 1 - \frac{n_2}{n_1} \\ 1 - \frac{n_2}{n_1} & 1 + \frac{n_2}{n_1} \end{bmatrix}\begin{bmatrix} A_2 \\ B_2 \end{bmatrix} = \begin{bmatrix} A_1 \\ B_1 \end{bmatrix}. \tag{2.27}$$

Recalling the expressions for reflectance and transmittance from equations 2.14 and 2.15 a transmission matrix, $\mathbf{T_{12}}$, may be used to describe the transmission at the interface according to

$$\mathbf{T_{12}}\begin{bmatrix} A_2 \\ B_2 \end{bmatrix} = \begin{bmatrix} A_1 \\ B_1 \end{bmatrix}, \tag{2.28}$$

where

$$\mathbf{T_{12}} = \frac{1}{t_{12}}\begin{bmatrix} 1 & r_{12} \\ r_{12} & 1 \end{bmatrix}. \tag{2.29}$$

Following transmission through an interface, a plane wave

$$\tilde{\mathbf{E}} = Ae^{ikz} + Be^{-ikz}\hat{\mathbf{x}} \tag{2.30}$$

will propagate through the new medium over some distance, h, such that

$$\tilde{\mathbf{E}}' = A'e^{ik(z+h)} + B'e^{-ik(z+h)}\,\hat{\mathbf{x}}. \tag{2.31}$$

The propagation may be described by a propagation matrix, $\mathbf{P}$, such that

$$\mathbf{P} = \begin{bmatrix} e^{-ikh} & 0 \\ 0 & e^{ikh} \end{bmatrix} \tag{2.32}$$

$$\begin{bmatrix} A \\ B \end{bmatrix} = \begin{bmatrix} A' \\ B' \end{bmatrix}. \tag{2.33}$$

The propagation and transmission matrices can be used to describe a plane wave moving through a multilayer system of layers l and $l+1$ in the following form

$$\begin{bmatrix} A_l \\ B_l \end{bmatrix} = \mathbf{T}_{l(l+1)}\mathbf{P}_{l+1} \begin{bmatrix} A_{l+1} \\ B_{l+1} \end{bmatrix} \tag{2.34}$$

which, in the more general sense, yields an expression through an arbitrary number of layers

$$\begin{bmatrix} A_0 \\ B_0 \end{bmatrix} = \left[\prod_{l=0}^{m-1} \mathbf{T}_{l(l+1)}\mathbf{P}_{l+1}\right] \begin{bmatrix} A_m \\ B_m \end{bmatrix} \tag{2.35}$$

with resulting 2×2 matrix $\mathbf{S}$ describing transmission through the full stack,

$$\begin{bmatrix} A_0 \\ B_0 \end{bmatrix} = \mathbf{S} \begin{bmatrix} A_m \\ B_m \end{bmatrix} \tag{2.36}$$

where the coefficients of reflectance and transmittance for the full stack may be represented as

$$t = \frac{1}{S_{11}} \tag{2.37}$$

$$r = \frac{S_{21}}{S_{11}} \tag{2.38}$$

such that the reflected power, R, is given by

$$R = \left(\frac{S_{21}}{S_{11}}\right)^2. \tag{2.39}$$

This approach is known as the transfer matrix method (TMM) and forms the basis of the simulations shown in chapter 8.

2.2 Electrical Properties of Semiconductors

This work is concerned with semiconductor crystals in which individual atoms are oriented on a regular crystal lattice. When oriented on a crystal lattice, individual atoms interact and the discrete energy levels of the atoms are replaced by bands of allowed energy states,

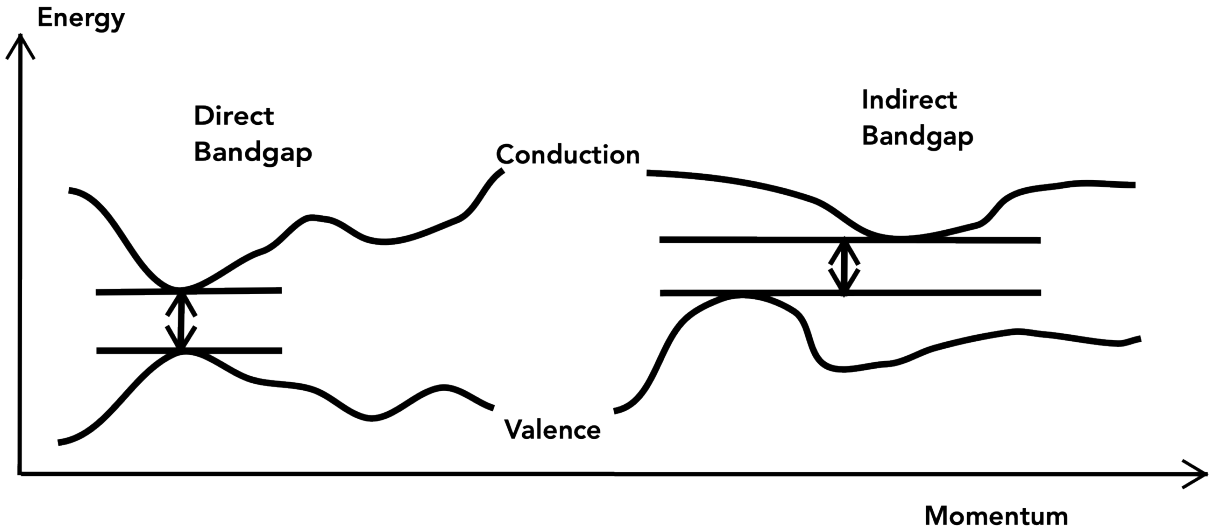

Figure 2.4: Representation of the conduction and valence band edges for a direct gap (left) and indirect gap (right) semiconductor.

as predicted by the tight binding and the nearly-free electron models [25]. In semiconductor physics, the bands of interest are referred to as the valence band in which electrons are localised, and the conduction band in which they are free to move. The bands are separated by a bandgap, E_g (Figure 2.4). In a direct band gap semiconductor the conduction band minimum coincides with the valence band maximum in momentum/k-space. For indirect band gap semiconductors, such as silicon, the conduction band minimum does not coincide with the valence band maximum in momentum/k-space. As a result of this the absorption and emission of photons at the band gap requires interaction of a phonon to account for the momentum change and results in lower emission and absorption rates than the direct-bandgap equivalent.

The crystal lattice can be represented in k-space by the Brillouin zone which depicts the points in space which are closer to $k = 0$ than any other point in the reciprocal lattice [26]. A sketch of the Brillouin zone for a face-centred cubic (FCC) lattice is shown in Figure 2.5 and is common to zinc blende crystals such as GaAs. The points Γ (Gamma), X, and L indicated on the Brillouin zone represent three points of symmetry for the FCC crystal. The centre of the Brillouin zone is referred to as the Γ point whilst the X and L points refer to the centre of the square and hexagonal faces respectively. For direct gap semiconductors the conduction band minimum is located at the Γ point. In the case that the minimum of conduction band is located at X or another point of symmetry, the semiconductor is indirect gap.

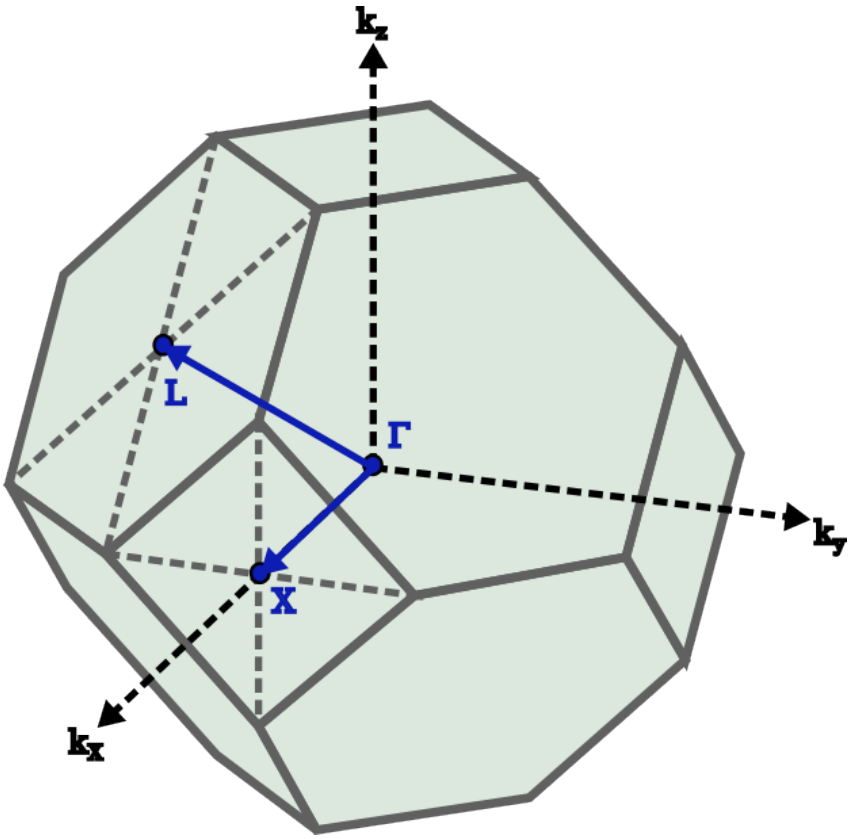

Figure 2.5: A sketch of the Brillouin zone for a face-centred cubic lattice indicating the points of symmetry referred to as X, L, and Γ.

2.2.1 Doping and Carrier Density

Electrons in a semiconductor are often described by an effective mass, m^*, that represents the curvature at the bottom of the conduction band. Considering a region in the minimum of the conduction band energy, E_0, the energy is given by a perturbation of the ground state

$$E = E_0 + \alpha \left| \mathbf{k} - \mathbf{k_0} \right|, \tag{2.40}$$

where the perturbation of the energy $\alpha > 0$, $\mathbf{k}$ is the momentum of the electron and $\mathbf{k}$ is the momentum of the electron at the bottom of the conduction band. The effective mass is given by

$$\frac{\hbar^2}{m^*} = \frac{\partial^2 E}{\partial k^2} = 2\alpha, \tag{2.41}$$

with energy

$$E = \frac{\hbar^2 \left| \mathbf{k}^2 \right|}{2m^*}, \tag{2.42}$$

which is analogous to the free-electron behaviour

$$E = \frac{\hbar^2 \left| \mathbf{k}^2 \right|}{2m}, \tag{2.43}$$

leading to a corresponding group velocity

$$\mathbf{v} = \frac{\nabla E}{\hbar} = \frac{\hbar \left(\mathbf{k} - \mathbf{k_0} \right)}{m^*}. \tag{2.44}$$

The probability that a state of energy, ϵ, is occupied at a temperature, T, is given by the Fermi-Dirac distribution [27]

$$f\left(\epsilon\right) = \frac{1}{e^{\frac{\epsilon - \mu}{k_B T}} + 1}, \tag{2.45}$$

where μ is the chemical potential (Fermi level) and k_B is the Boltzmann constant. The Fermi level is defined as the state with 50% occupancy probability at at given temperature. The density of states as a function of energy, ϵ, for electrons with effective mass m_e^* in a bulk semiconductor is given by [25]

$$g_c\left(\epsilon \geq \epsilon_c\right) = \frac{\left(2m_e^*\right)^{\frac{3}{2}}}{2\pi^2 \hbar^3} \sqrt{\epsilon - \epsilon_c}, \tag{2.46}$$

where ϵ_c is the energy of the conduction band minimum. The electron population in the conduction band of a bulk semiconductor, $n\left(T\right)$, is given by

$$n\left(T\right) = \int_{\epsilon_c}^{\infty} g_c(\epsilon) f(\epsilon)\, d\epsilon, \tag{2.47}$$

which gives rise to an expression for electron density in the conduction band

$$n = 2 \left(\frac{m_e^{*2} k_B T}{2\pi\hbar^2} \right)^{\frac{3}{2}} e^{\frac{\mu - \epsilon_c}{k_B T}}. \tag{2.48}$$

An equivalent analysis may be performed for holes with effective mass m_h^*, yielding a hole density

$$p = 2 \left(\frac{m_h^{*2} k_B T}{2\pi\hbar^2} \right)^{\frac{3}{2}} e^{\frac{\epsilon_v - \mu}{k_B T}}. \tag{2.49}$$

From this we obtain the law of mass action

$$np = 4\left(\frac{k_B T}{2\pi\hbar^2}\right)^3 (m_e m_h)^{\frac{3}{2}}\, e^{\frac{-E_g}{k_B T}}. \tag{2.50}$$

In the intrinsic (undoped) regime, the number of electrons excited into the conduction band leaves behind an equal number of holes in the valence band, such that $n = p$ and the Fermi level may be related to the carrier concentrations as follows [25, 27],

$$\mu = \frac{1}{2}E_g + \frac{3}{4}k_B T \ln\left(\frac{m_h^*}{m_e^*}\right). \tag{2.51}$$

In the intrinsic regime, this results in the Fermi level residing mid-bandgap. Impurities may be used to dope the semiconductor either by donating an electron (donor impurity), or capturing an electron (acceptor impurity). In the case of the acceptor impurity, a captured electron is equivalent to an increase in the hole concentration. From the law of mass action (equation 2.50) an increase in the electron (hole) concentration results in a corresponding decrease in the hole (electron) concentration. Consequently, doping the semiconductor either n-type or p-type results in the Fermi level moving towards the conduction or valence band respectively. It is possible to obtain expressions for doped carrier concentrations with doping level

$$D = N_D - N_A \tag{2.52}$$

and intrinsic doping

$$I_2 = np \tag{2.53}$$

such that

$$n = \frac{1}{2}\left(\sqrt{D^2 + 4I^2} + D\right), \tag{2.54}$$

$$p = \frac{1}{2}\left(\sqrt{D^2 + 4I^2} - D\right), \tag{2.55}$$

where N_D and N_A are the donor and acceptor concentrations respectively [25]. Conductivity of the semiconductor, σ, is related to carrier concentrations and mobilities, μ_e and μ_h, by the electron charge, e, according to

$$\sigma = e\left(n\mu_e + p\mu_h\right). \tag{2.56}$$

It is clear that the conductivity of the semiconductor can be increased and made majority electron or hole dominated by doping with impurities.

2.2.2 Heterojunctions

When two semiconductors are brought into contact, the band alignments of semiconductors allow for the formation of three types of heterojunction (Figure 2.6). In a type-I heterojunction the electrons and holes preferentially occupy the same spatial region which results in rapid carrier recombination. For the case of type-II semiconductor heterojunctions the electrons and holes are spatially separated, typically resulting in increased carrier lifetimes. For the type-III, the conduction band of one material overlaps with the valence band of the other such that carriers are free to flow directly across the interface.

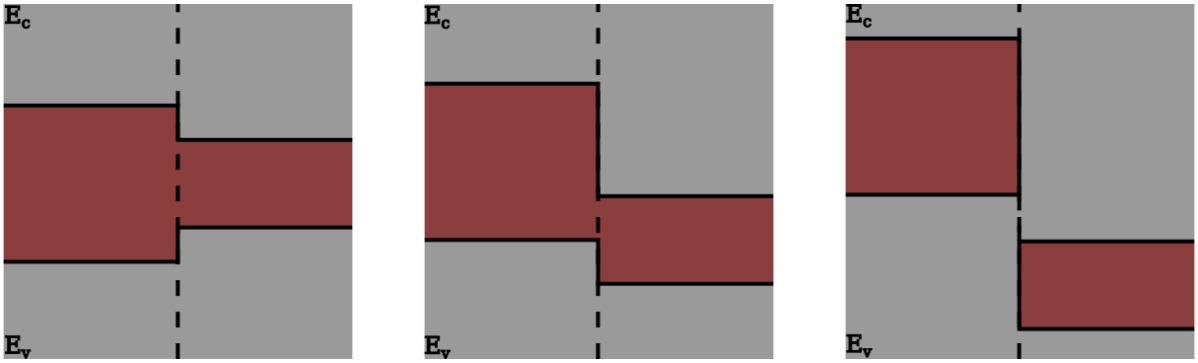

(a) (b) (c)

Figure 2.6: Representation of the conduction and valence band offsets for type-I (a), type-II (b) and type-III (c) semiconductor interfaces. The red shaded region represents the forbidden gap between the conduction (E_c) and valence (E_v) bands. The conduction and valence bands are represented by the grey shaded regions and labelled accordingly. The vertical dashed lines represent the interface between a wider bandgap semiconductor material on the left and narrower bandgap on the right.

In reality, the presence of dopants shifts the Fermi levels away from the middle of the bandgap (section 2.2.1) which results in a misalignment of the Fermi levels for neighbouring materials. A schematic of the band structure for a weakly n-doped material adjacent to a heavily N-doped material is shown in Figure 2.7a. Electrons migrate from the heavily-doped side across to the lower-doped side of the junction. The migration results in an inbuilt potential across the interface which results in a bending of the bands. The band bending forms a well for electrons on the lower-doped side, followed by a step in the conduction band. The equivalent case for a p-type junction is shown in Figure 2.7b.

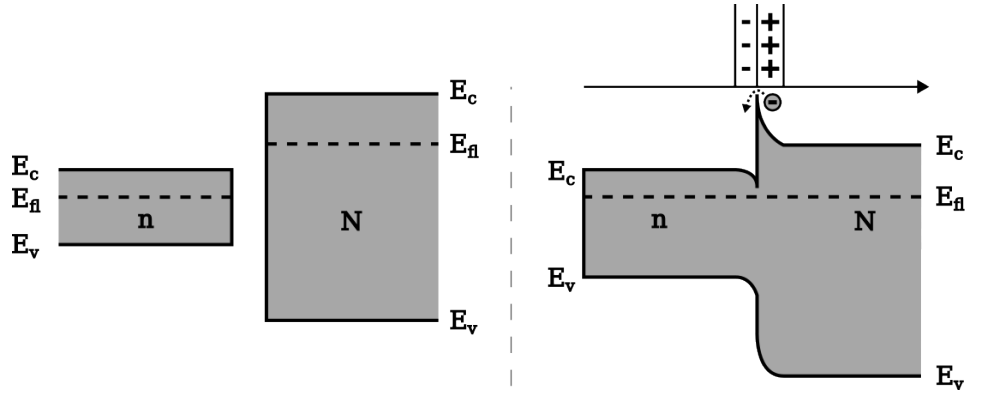

(a) Reproduced from Kittel[27]

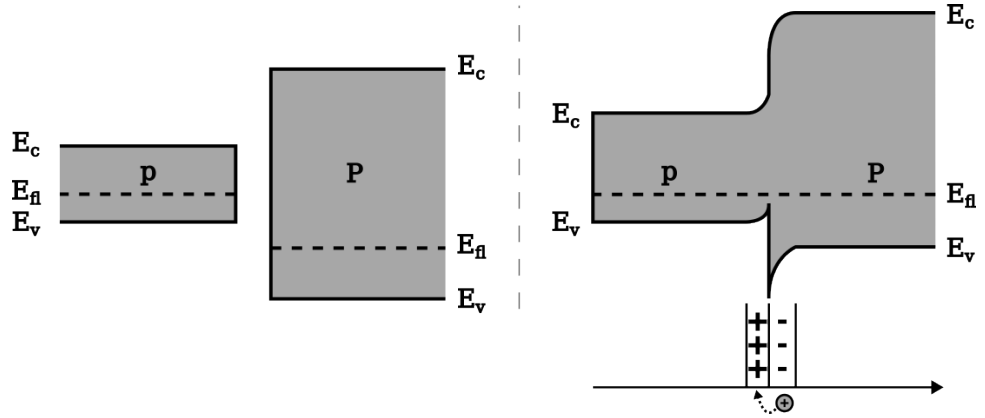

(b)

Figure 2.7: Schematic of the heterojunction between separate (left) and contacted (right) lightly n-doped (a) / p-doped (b) and heavily N-doped (a) / P-doped (b) materials in a type-I heterojunction. The positions of the conduction band, E_c, valence band, E_v, and Fermi level, E_{fl}, are indicated and the depletion region with net charge is indicated across the interface. The arrow indicates the charge carrier migration across the interface that gives rise to the net charge.

2.2.3 Metal-Semiconductor Interfaces

A metal-semiconductor interface can be presented in a similar fashion to the heterojunctions shown in section 2.2.2. Upon contact between the metal and the semiconductor charges migrate across the interface such that the Fermi level of the metal and the semiconductor are coincident. The migration of charges results in an inbuilt potential adjacent to the interface and results in the bending of the bands within the semiconductor [27]. A example schematic of a metal-semiconductor interface is given in Figure 2.8 for an n-doped semiconductor and a metal with a work function greater than the electron affinity of the semiconductor.

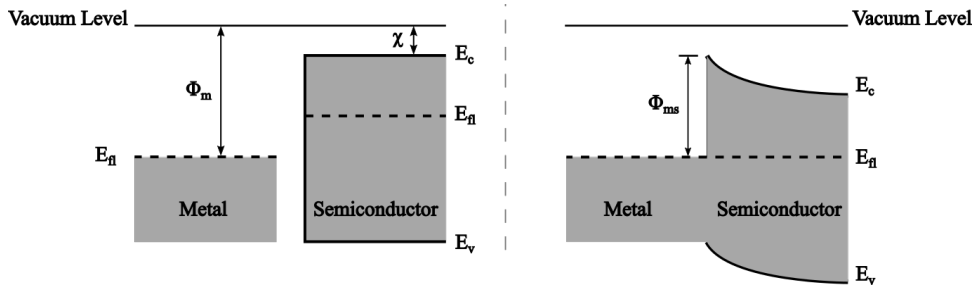

Figure 2.8: Schematic of the band structure of a separate (left) and a contacted (right) metal-semiconductor interface. The Fermi level, E_{fl}, is indicated and the positions of the conduction band, E_c, and valence band, E_v, are indicated for the semiconductor. The work function of the metal, Φ_m, and the electron affinity of the semiconductor, χ, are indicated on the left hand side of the diagram and the barrier at the metal semiconductor interface, Φ_{ms}, is shown for the contacted case.

The band bending can lead to the formation of a Schottky-barrier which in the ideal case has a barrier height, Φ_{ms}, given by

$$\Phi_{ms} = \Phi_m - \chi, \tag{2.57}$$

where Φ_m is the work function of the metal and χ is the electron affinity of the semiconductor [24]. In reality, the barrier height at the interface and properties of the contacts are affected by other factors such as defect levels, diffusion of metals across the interface and the method used to deposit the contact; therefore, effort is still directed towards the experimental characterisation of contacts [28].

2.3 Quantum Tunnelling Through a Triangular Barrier

The realisation of an approximately-triangular barrier is seen at the interface between doped semiconductors in Figure 2.7. This section presents the tunnelling probability for the triangular barrier which can provide insight into the electrical characteristics of barriers at semiconductor interfaces. In particular, this is relevant to transport in DBRs which is considered in chapter 9.

For a particle in free space moving in one direction (x) the wavefunction may be expressed in the form

$$\psi(x) = Ae^{ikx}, \tag{2.58}$$

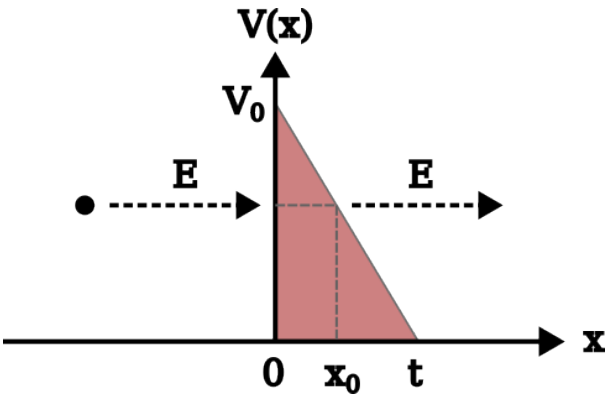

Figure 2.9: Representation of an electron with energy, E, tunnelling through a triangular potential-energy barrier, $V(x)$, of height, V_0, and width, t.

with amplitude, A, and wave vector, k. For a particle moving in varying potential energy, $V(x)$, the wavevector is not constant. According to the Wentzel, Kramers, and Brillouin (WKB) approximation, for a slowly-varying potential it is possible to express the wavevector in the form [29]

$$|k(x)| = \sqrt{\frac{2m\left(E - V(x)\right)}{\hbar^2}}, \tag{2.59}$$

for a particle of energy, E, such that the wavefunction takes the form

$$\psi(x) = \frac{a}{\sqrt{k(x)}} e^{i\int_{x_1}^{x_2} k(x')\mathrm{d}x'}, \tag{2.60}$$

with amplitude, a, and where

$$k(x) = \sqrt{\frac{2m\left(E - V(x)\right)}{\hbar^2}}, \qquad \text{for } E > V, \tag{2.61}$$

$$k(x) = i\sqrt{\frac{2m\left(V(x) - E\right)}{\hbar^2}}, \qquad \text{for } E < V. \tag{2.62}$$

Using the WKB approximation, the tunnelling probability through an arbitrary smoothly-varying potential may be written as

$$T = e^{-2\int_{x_1}^{x_2} |k(x)|\mathrm{d}x}, \tag{2.63}$$

$$k(x) = i\sqrt{\frac{2m\left(V(x) - E\right)}{\hbar^2}}. \tag{2.64}$$

For the case of a triangular barrier shown in Figure 2.9 with height, V_0, and width, t, the potential may be expressed as

$$V(x) = V_0 - V_0\frac{x}{t}. \tag{2.65}$$

The tunnelling probability, from $x = 0$ to x_0, is given as

$$T = e^{-2\int_0^{x_0} \sqrt{\frac{2m}{\hbar^2}\left(V_0 - \frac{x}{t}V_0 - E\right)}\mathrm{d}x}. \tag{2.66}$$

To solve the integral in the exponential, let $u = V_0 - \frac{V_0}{t}x - E$,

$$\frac{\mathrm{d}u}{\mathrm{d}x} = \frac{V_0}{t} \tag{2.67}$$

$$\sqrt{\frac{2m}{\hbar^2}}\int_0^{\frac{V_0-E}{V_0}t}\sqrt{\left(V_0 - \frac{x}{t}V_0 - E\right)}\mathrm{d}x = \sqrt{\frac{2m}{\hbar^2}}\int_{V_0-E}^{V_0-\frac{V_0}{t}\left(\frac{V_0-E}{V_0}\right)t-E} -\frac{t}{V_0}u^{\frac{1}{2}}\mathrm{d}u \tag{2.68}$$

$$= -\frac{2t}{3V_0}\sqrt{\frac{2m}{\hbar^2}}\left[u^{\frac{3}{2}}\right]_{V_0-E}^{0} \tag{2.69}$$

$$= \frac{2t}{3V_0}\sqrt{\frac{2m}{\hbar^2}}\left(V_0 - E\right)^{\frac{3}{2}}. \tag{2.70}$$

The tunnelling probability for the triangular barrier is therefore given by

$$T = e^{-\frac{4t}{3V_0}\sqrt{\frac{2m}{\hbar^2}}(V_0-E)^{\frac{3}{2}}}. \tag{2.71}$$

This result demonstrates that the transmission probability through a triangular barrier decreases exponentially with the thickness of the barrier and with the square root of the barrier height.

2.4 Distributed Bragg Reflectors

Distributed Bragg reflectors (DBRs) are widely used as mirrors in VCSELs, resonant-cavity light-emitting diodes (RCLEDs), resonant-cavity photo-detectors and other opto-electronic devices [24, 30, 31]. DBRs utilise constructive interference of reflections occurring at interfaces between multiple layers of contrasting refractive index. This generates a range of high reflectance wavelengths around a specific target wavelength. The highly reflective band of wavelengths is known as the stopband (Figure 2.10). The reflectance outside of the stopband oscillates, with each of the local maxima known as a side-band. For the textbook case, a DBR consists of pairs of quarter Bragg-wavelength layers with refractive indices n_1 and n_2 respectively [24]. In this case the layers will have thickness

$$t_{1,2} = \frac{\lambda_0}{4n_{1,2}}, \tag{2.72}$$

where λ_0 is the wavelength of light in vacuum for the peak reflectance of the DBR. The reflectance, R, for this special case may be expressed as a function of the coefficient of reflection, r_N, for N DBR periods according to [24]

$$R = |r_N|^2 = \left|\frac{(n_2/n_1)^{2N} - 1}{(n_2/n_1)^{2N} + 1}\right|^2. \tag{2.73}$$

The magnitude of the reflectivity is related to the reflectivity of a single interface. From Figure 2.1 it is clear that a large refractive index contrast is required for high reflectivity at a single interface. From equation 2.73 we can see that a large refractive index contrast results in higher reflectivity and reduces the number of repeats required for a DBR to achieve high reflectance.

In addition to the optical function, DBRs traditionally fulfil a second role in VCSELs as a route for current injection into the active region (section 2.6). Poor electrical

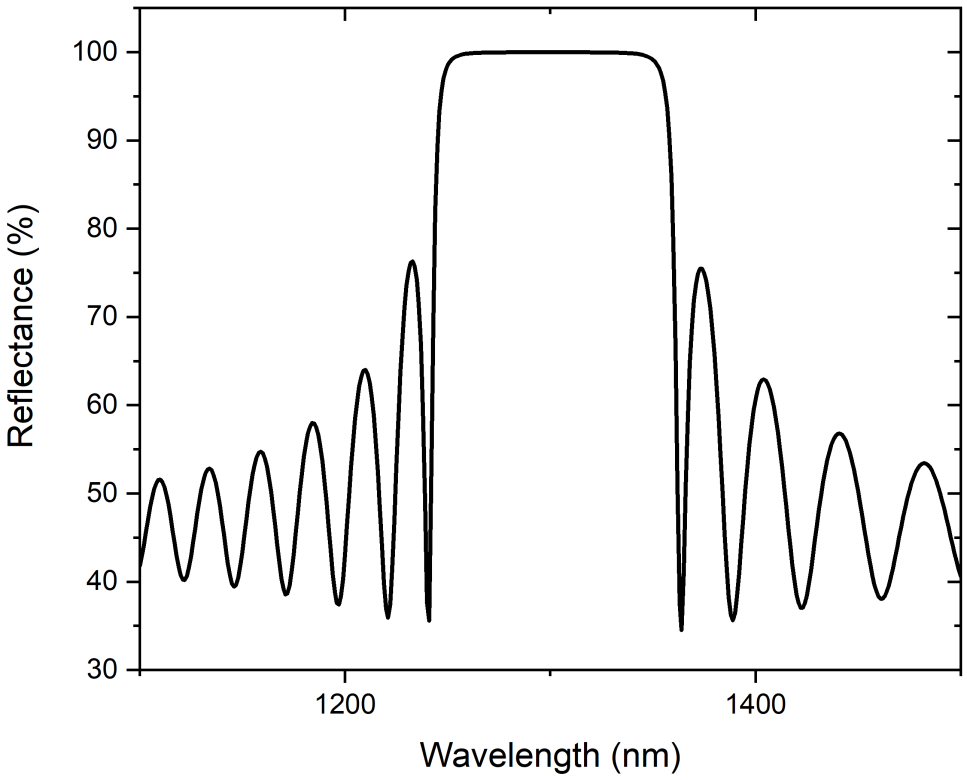

Figure 2.10: The reflectance spectrum for an undoped GaAs/$Al_{0.9}Ga_{0.1}As$ first-order DBR consisting of 35 pairs on a thick GaAs substrate with a target wavelength of 1300 nm.

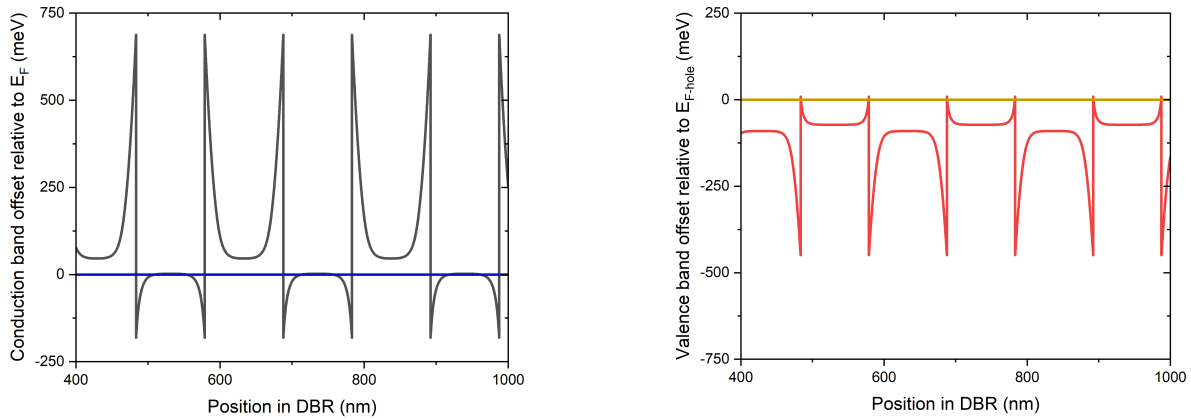

(a) (b)

Figure 2.11: The conduction (a) and valence (b) band edges for n-type and p-type GaAs/$Al_{0.9}Ga_{0.1}$As DBRs doped to 1×10^{18}cm^{-3} have large barriers to their respective charge carriers at the material interfaces, as seen by the offset of the bands with respect to the Fermi level. In both cases the Fermi level (indicated by the horizontal lines) sits further from the band edge within the $Al_{0.9}Ga_{0.1}$As layer.

characteristics of the DBR leads to high series resistance and heating, which are both detrimental to VCSEL performance. Undoped DBRs display poor electrical characteristics so n-type and p-type dopants are routinely added to semiconductor DBRs to reduce the resistance of the stack. There are two clear sources of series resistance when comparing the position of the conduction band relative to the Fermi level for an n-doped Al_xGa_{1-x}As-based DBR (Figure 2.11a). As discussed in section 2.2.1, the proximity of the Fermi level to the conduction band edge relates to the carrier density in the conduction band and subsequently the conductivity of the material. The conduction band in the Al_xGa_{1-x}As layer of the GaAs/Al_xGa_{1-x}As DBR is visibly further from the Fermi level, contributing to resistance in the bulk material (Figure 2.11). In addition, tall potential barriers at GaAs/Al_xGa_{1-x}As heterojunctions in the mirror (see section 2.2.2) act as barriers to transport for electrons and dominate the resistance in the DBR [5]. The complimentary example for a p-doped DBR is shown in Figure 2.11b. In both cases the barrier to transport for textbook GaAs/Al_xGa_{1-x}As interfaces and gap from the Fermi level to conduction/valence bands are considerably more than the thermal energy

$$E_t = k_B T, \tag{2.74}$$

which is approximately 26 meV at room temperature. Comparing the probability of an electron occupying a state with energy equal to the barrier (equation 2.45) and the probability of tunnelling through an approximately triangular barrier (equation 2.71), it is understood that the transmission through the barriers is largely dominated by tunnelling. The majority carrier concentration and tunnelling probability are both a function of the effective mass, explaining why p-type DBRs exhibit higher resistance than n-type for the same doping concentration.

Table 2.2 presents a number of material systems for use in telecoms-wavelength VCSELs. The table demonstrates the larger refractive index constant and thermal conductivities of Al_xGa_{1-x}As based DBRs compared to their indium-containing alternatives, note that InAs/AlAs is listed in the table but cannot be grown with sufficient material

Material System	n_{high}	n_{low}	Δn	Thermal Conductivity at 300 K [W/mK]
GaAs/AlAs (1300 nm)	3.4	2.9	0.5	46/80
GaAs/$Al_{0.9}Ga_{0.1}As$ (1300 nm)	3.4	3.0	0.4	46/65
GaAs/$Al_{0.6}Ga_{0.4}As$ (1300 nm)	3.4	3.1	0.3	46/17
$Al_{0.12}Ga_{0.88}As$/$Al_{0.9}Ga_{0.1}As$ (1300 nm)	3.4	3.0	0.4	33/65
InAs/AlAs (1300 nm)	3.45	2.9	0.55	27.3/80
InP/GaInAs (1550 nm)	3.45	3.17	0.28	68/16

Table 2.2: Comparison of properties for material systems used in distributed Bragg reflectors. The lattice mismatch between InAs and AlAs would prevent their use in an epitaxially-grown DBR. [32, 33, 34, 35, 36]

quality at the thicknesses required for a DBR because of the large lattice mismatch. The $Al_xGa_{1-x}As$ material system is already favoured in the VCSEL industry due to its high refractive index contrast, low strain throughout the composition range and lack of thermal issues associated with InP-based systems. $Al_xGa_{1-x}As$-based DBRs also benefit from a lack of optical absorption at telecoms-wavelengths, reducing optical losses in VCSEL structures.

Nextnano++ software is used to simulate barriers in the band structure and electrical characteristics of the DBR structures in this work [37, 38]. Measurements of the optical properties are carried out on a Cary 5000 spectrophotometer, as discussed in section 4.1. Electrical characteristics are measured directly on a probestation (section 4.2).

2.5 GaSb Quantum Rings Background

GaSb quantum rings on GaAs are zero-dimensional semiconductor nanostructures with type-II band offset (Figure 2.6b). A transmission electron microscope (TEM) image showing a set of cross-sectioned GaSb quantum-rings within the GaAs cavity of a VCSEL can be seen in Figure 2.12. The rings are initially grown as GaSb quantum dots on a wetting layer using the Stranski-Krastanov method. The dots have an areal density in the region of $1 \times 10^{10}\,\mathrm{cm}^{-2}$ to $5 \times 10^{10}\,\mathrm{cm}^{-2}$ inferred from cross-sectional scanning tunnelling microscopy measurements and measurement of surface dot densities using atomic force microscopy [39, 40]. Upon capping with a GaAs 'cold' cap arsenic and antimony exchange takes place, forming the rings and reducing strain in the crystal [41, 42]. The growth parameters of the capping layer must be carefully controlled to prevent complete consumption of the rings. A schematic of the growth process is shown in Figure 2.13. At the time of writing, GaSb quantum-dots have been grown by MOCVD and MBE droplet epitaxy, but all of the known GaSb quantum-ring growths have utilised molecular beam epitaxy (MBE) [43, 44].

The type-II band offset of the quantum rings forms a potential well in the valence band which provides strong hole-confinement and localisation of holes within the quantum rings. Electrons are attracted to the rings by the Coulomb potential but remain spatially separated from the holes as a result of the type-II offset and demonstrate no quantised confinement [21]. Capacitive charging effects blue-shift the emission of the quantum rings as more holes are added to the ring [45]. It is believed that recombination always occurs with the blue-shifted ground-state heavy-hole, due to selection rules,

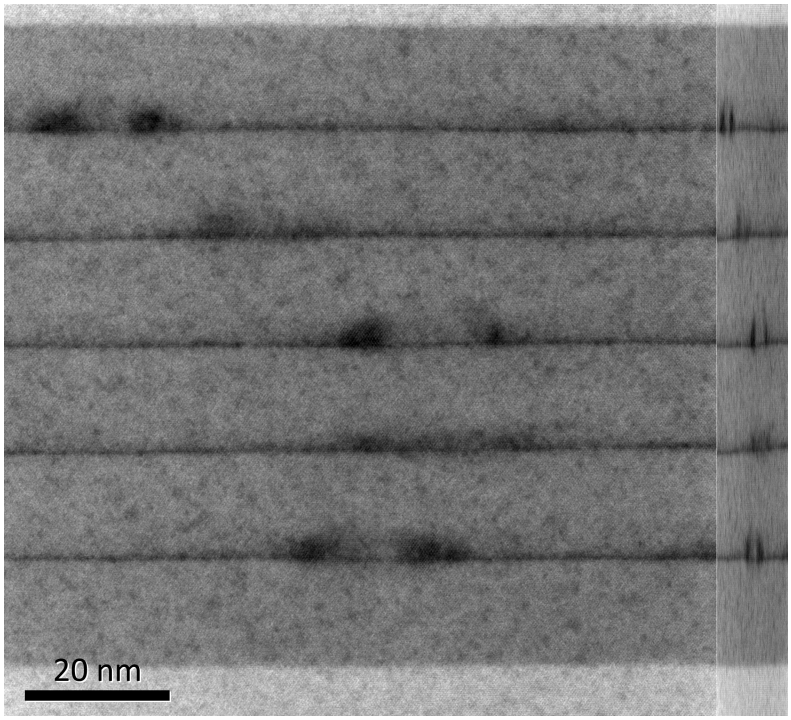

Figure 2.12: Transmission electron microscope image of cross-sectioned GaSb quantum-rings within the GaAs cavity of a VCSEL (sample P3, see Table 11.1 and section 11.2).

rather than excited states being the origin of the blue-shift. Experimental evidence for this comes from the linear increase in emission energy with increasing hole occupation, consistent with capacitive charging only, and no contribution from higher energy quantised states [42]. The capacitive charging and lack of electron energy quantisation results in a broad luminescence spectrum for the rings (Figure 2.14) that covers the telecoms O-band, C-band and the transparency window utilised for below-screen sensing in mobile devices. Spatial separation (delocalisation) of electrons and holes leads to increased spontaneous recombination lifetimes believed to be on the order of microseconds [21]. A further study of the quantum ring carrier lifetime is presented in chapter 10, including the effect of cavity enhanced recombination lifetimes.

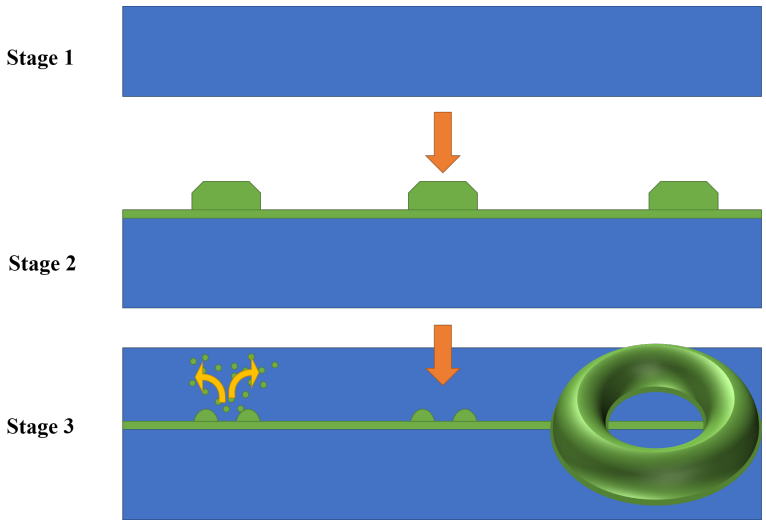

Figure 2.13: An artistic interpretation of the cross-section for growth of GaSb quantum dots on GaAs by the Stranski-Krastanow (SK) method before capping with a carefully controlled GaAs layer results in the formation of rings through As-Sb exchange. Stage 1 represents a GaAs surface, upon which the wetting layer and SK GaSb QDs are grown (stage 2). The final stage involves the growth of a cold-cap GaAs layer (upper blue layer in stage 3) and As-Sb exchange which results in the ring geometry. The final cross-section indicates the lobes of a cross-sectioned ring.

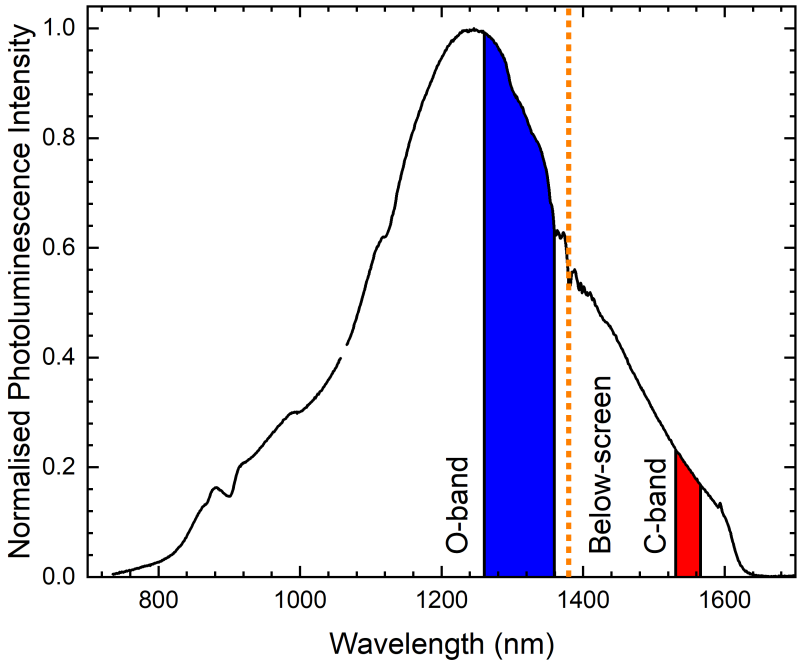

Figure 2.14: The broad room-temperature photoluminescence spectrum of GaSb quantum rings. The blue section represents the telecoms O-band, the red shaded region shows the telecoms C-band, and the orange dotted line represents the transparent region for below-screen applications.

2.6 VCSELs

In its basic form a VCSEL consists of a pair of highly-reflective mirrors, typically in excess of 99.9 %, separated by a Fabry-Perot cavity with optical thickness of the order of λ, where λ is the emission wavelength. Various designs are used but common cavity lengths include $\lambda/2$, λ and $3\lambda/2$ [9, 46]. The short cavity length only supports a single longitudinal mode at the cavity resonance, therefore defining the supported lasing wavelength and rejecting other emission wavelengths. The active region is centred around the maximum field intensity within the cavity and has a gain spectrum coincident with the cavity-supported wavelength. An oxidation ring is typically implemented in the region of the cavity and its surrounding layers for both optical and electrical confinement (Figure 2.15).

In contrast to EELs where the active region may be millimetres long, active regions in a VCSEL are usually just the thickness of a small number of quantum well or quantum dot layers (nanometres thick). VCSELs have inherently low gain per round trip of the cavity because of the extremely short active region. The relative confinement factor,

$$\Gamma_r = \frac{L}{d_a} \frac{\int_{d_a} |E(z)|^2 \, \mathrm{d}z}{\int_{d_L} |E(z)|^2 \, \mathrm{d}z}, \tag{2.75}$$

describes the average intensity of the electric field, E, confined to the total thickness of the active region, d_a, within the cavity length, L [7]. The threshold gain g_{th} of a VCSEL is described by

$$g_{th} = \alpha_a + \frac{1}{\Gamma_r d_a} \left[\alpha_i \left(L_{eff} - d_a \right) + \ln \frac{1}{\sqrt{R_t R_b}} \right], \tag{2.76}$$

where α_a is the loss in the active sections of the cavity, α_i is the loss in the passive sections of the cavity, L_{eff} is the effective cavity length and R_t and R_b are the top and bottom mirror reflectivity respectively [24]. High-reflectivity top and bottom mirrors are required to minimise mirror losses and lower the threshold gain of a VCSEL to the gain achievable in the thin active layers.

There is renewed industrial interest in VCSELs operating between 1300 nm and 1550 nm for applications in the telecoms O-band and C-band, short-wavelength infrared (SWIR) medical imaging [47, 48], datacoms, below-screen mobile sensing (1380 nm) and so-called 'eye-safe' lasers (>1400 nm) for LiDAR in mobile devices and autonomous vehicles [49]. Typically, the $Al_xGa_{1-x}As$ material system is used for shorter-wavelength VCSELs, but the GaAs bandgap places a fundamental limitation on the maximum emission wavelength for GaAs-based active regions (∼870 nm at room temperature) [50] which is too short for the desired wavelength range. Narrower-bandgap indium-based material systems are widely used to increase the emission wavelength [13, 17]. Incorporation of indium into traditional $GaAs/Al_xGa_{1-x}As$ quantum wells extends the emission wavelength but is prevented from reaching 1550 nm emission using conventional $GaAs/Al_xGa_{1-x}As$ DBRs because the increased lattice mismatch and strain accompanying the high indium content in the quantum well active region reduces the crystal quality. This leaves a gap in the VCSEL market.

Systems such as strained InAs QDs are capable of emission in the telecoms range; however, the InAs/Al(In)As system does not lend itself to fabrication of DBRs because of the low thermal conductivity and low refractive index contrast between layers when compared to the $Al_xGa_{1-x}As$ system. InAs quantum dot systems can be incorporated onto GaAs/AlGaAs distributed Bragg reflectors (DBRs) but this typically requires complicated regrowth or wafer bonding techniques which are undesirable for commercial

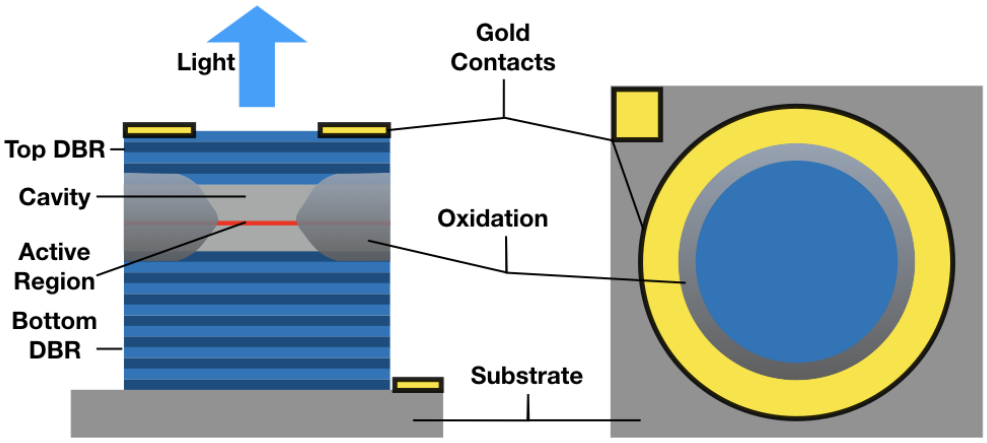

Figure 2.15: Schematic of a generic top-emitting VCSEL. The active region is contained within a short optical cavity defined by a pair of semiconductor-based DBRs. An oxidation ring is used in the vicinity of the cavity for both optical and electrical confinement.

applications[16, 17, 18]. Another material system that may be considered for longer-wavelength emission is InAlGaAsP/InP, but it has been reported to suffer from strong free-carrier absorption, particularly in the p-type layers [17]. It is believed that absorption in the materials will result in losses within the DBR, increasing the threshold gain and reducing the output efficiency. VCSELs emitting in the region of 1.55 µm have been realised using AlGaInAs quantum well active regions paired with dielectric or GaAs/$Al_xGa_{1-x}As$ DBRs [19]. Growth of AlGaInAs structures on $Al_xGa_{1-x}As$ is made more complicated by the lattice mismatch between the materials. To avoid the lattice mismatch, wafer bonding is often utilised to allow strain-free growth of DBRs and the active region on separate substrates. Recent work has demonstrated emission at 1.55 µm using wafer fusion and regrowth techniques [16]. Although this realises functional devices the process flow is complicated and the use of multiple substrates increases production cost. Traditionally, growth of nitrogen-containing Ga(In)NAs systems by MOCVD has suffered from difficulties maintaining high-quality optical films. Recent developments demonstrated growth of GaInNAsSb quantum well VCSELs using a commercial MBE, realising high-speed telecoms-wavelength VCSELs operating around 1300 nm semiconductors [13, 20]. Other devices face their own processing challenges, inspiring the search for a new system allowing for the production of long-wavelength VCSELs monolithically-grown on GaAs substrates.

The room temperature emission spectrum of GaSb QRs extends beyond the limitations of purely GaAs/$Al_xGa_{1-x}As$ devices towards 1600 nm (section 2.5). Conventionally, a zero-dimensional active region with a broad gain spectrum is indicative of inhomogeneous growth [51]. Such inhomogeneity reduces the maximum gain at a nominal wavelength and would be detrimental to laser performance. In the case of quantum rings, it is believed that the broad emission spectrum of the rings is dominated by capacitive charging effects rather than inhomogeneous growth. Since the emission wavelength for a VCSEL is defined by the cavity length, this should result in a narrow emission line and rejection of other wavelengths, including those contained within the gain spectrum of the active region. Work in the InP material system has utilised broad gain spectra for the demonstration of wavelength-tunable lasers [52], in a similar sense the broad spectrum

may enable the production of VCSELs across the telecoms bands using a single active region. In addition to the suitable optical performance of the rings, they can be grown directly on GaAs by MBE making them ideal for incorporation into industry-standard GaAs/Al_xGa_{1-x}As-based DBRs. The GaAs/Al_xGa_{1-x}As material system is of particular interest for the DBRs due to its transparent nature in the telecoms wavelength range.

GaSb quantum rings may present a number of potential advantages over alternative approaches to telecoms VCSELs. The advantages are primarily associated with the ease of growth and fabrication of GaSb QR VCSEL devices. Recent improvements in material quality for dilute nitride films have utilised MBE growth techniques [13, 20]. In contrast to the challenges associated with dilute nitride growth, GaSb nanostructures may be grown by MOCVD [53] and are compatible with existing commercial GaAs/Al_xGa_{1-x}As DBR technology which is promising from the perspective of mass-production. As discussed previously, indium-based approaches to date have been required to choose between inferior indium-containing DBRs, more expensive InP substrates and more complex methods of fabrication involving multi-stage epitaxy or wafer-bonding fabrication flows which both incur additional expense. These challenges may be avoided by the monolithic growth of GaSb QR VCSELs on GaAs substrates which eliminates a number of the material and strain challenges associated with indium-based telecoms-wavelength VCSELs.

Chapter 3

Simulations

3.1 Nextnano++

Nextnano++ is a technology computer-aided design (TCAD) program, dedicated to the simulation of semiconductor devices and structures. The *nextnano++* package provides the tools for 1D, 2D and 3D modelling of devices; in this work only the 1D case is explored. Material parameters are obtained from the inbuilt material database. *Nextnano++* calculates the electronic properties of semiconductor structures and the optical spectra. Simulations include the effect of strain but do not account for optical effects such as enhancement of the emission into optical cavity modes. The details of the computation are hidden from the user but a discussion of the methods can be found elsewhere [37, 38]. The user of the software merely provides an input file detailing the materials and geometry of the device, including position and type of doping and electrical contacts, the parameters of interest and preferred mathematical technique used by the software. Simulations in this work use the *nextnano++* self-consistent Poisson and current-Poisson (with drift-diffusion model) solvers to calculate the conduction and valence bands of semiconductors, and the current-voltage (IV) characteristics of DBRs.

3.2 TFCalc

One-dimensional optical reflectance and transmittance simulations of devices are performed using the commercial software TFCalc by Spectra Inc. Environments (Figure 3.1) are defined with light from an incident medium onto user-defined 'front' layers at angle θ with $0° \leq \theta < 90°$. TFCalc simulates the propagation of light into and through the front layers, substrate, back layers and into the exit medium. The simulations assume a thick substrate in which light loses coherence. Absorption is calculated within the substrate but reflections from the back interface of the substrate do not interfere with the material layers. The software outputs include the total transmittance, reflectance, absorption, phase and electric field intensity (EFI) within the simulated environment.

The user provides a wavelength-dependent material database of real refractive index, n, and extinction coefficient, k for each material of interest. Optical constants for the GaAs/$Al_xGa_{1-x}As$ system in this work are taken from Adachi et al. and all simulations assume a temperature of 300 K [33]. The effect of dopants is not simulated by TFCalc and there is limited published data on free carrier absorption of light caused by dopants in the $Al_xGa_{1-x}As$ system at the wavelengths of interest for this work. It is also believed that much of the knowledge surrounding the measured refractive index and absorption coefficients of doped-$Al_xGa_{1-x}As$ is kept as an industry secret. However, the predicted contributions of free carrier absorption and refractive index change are small for $Al_xGa_{1-x}As$ in the wavelength range of interest [54, 55, 56, 57, 58]. In addition, it is demonstrated later in this work (section 9.2) that doping does not have a measurable effect on the optical characteristics of DBRs grown back to back by MBE at Lancaster. This suggests that any effect of doping on the resonant wavelength of devices is negligible compared to the variations in layer thickness during epitaxial growth. As a result of this, VCSEL and DBR simulations in this work assume zero absorption in the $Al_xGa_{1-x}As$ materials at wavelengths above the material band gap.

TFCalc allows the definition of models with up to 5000 bulk-material layers, each with a finite thickness. The restriction of bulk-material layers requires that graded-concentration layers are approximated as a stack of thin intermediate composition layers. Structures with repeating units may be designed in TFCalc using the 'Stack Formula'

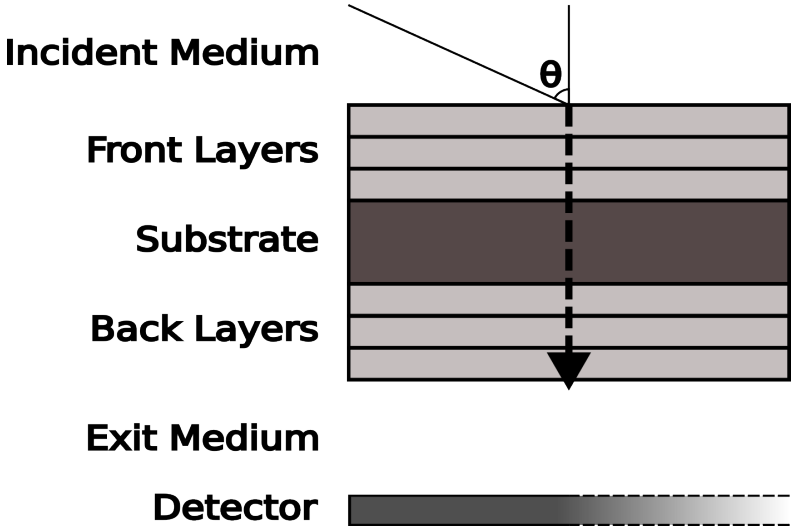

Figure 3.1: Schematic of the TFCalc simulation environment. Light is incident on the front layers and detected in the exit medium. Simulations are treated in one dimension so the detector collects all light in the exit medium.

option but this is limited to 26 materials per simulation, which imposes a realistic upper limit of 26 material compositions for any graded structure generated in the software.

Table 3.1 describes the environment used to simulate DBRs and VCSELs, corresponding to the schematic in Figure 3.1. Semiconductor layers are described within the front layers of the simulation, with the back layers remaining empty. In all cases optical measurements are carried out with a beam incident from air onto the top surface of the epitaxially-grown material (section 4.1). In contrast, the VCSEL DBRs should be designed to reflect back into the cavity; therefore, the reflectivity should be tuned for light incident from the $Al_{0.6}Ga_{0.4}As$ layer at the edge of the cavity.

Component	Incident Medium	Substrate	Exit Medium	Stage
Lower DBR	$Al_{0.6}Ga_{0.4}As$	GaAs	Air	Design
Lower DBR	Air	GaAs	Air	Measurement
Upper DBR	$Al_{0.6}Ga_{0.4}As$	GaAs	Air	Design
Upper DBR	Air	GaAs	Air	Measurement
Full VCSEL	Air	GaAs	Air	Design & Measurement

Table 3.1: TFCalc environment parameters for simulation of VCSEL components and full VCSELs during the design and characterisation stages.

Chapter 4

Characterisation Techniques

In order to correlate results of experiment and theory it is necessary to characterise the properties of epitaxially-grown material such as layer thicknesses, composition and crystal quality. The evaluation of device performance requires measurements of their optical and electrical properties. A variety of techniques were used to measure the optical, electrical and material properties of the samples produced over the course of this project. The following section provides a summary of the characterisation methods used throughout this work.

4.1 Spectrophotometer Transmittance and Reflectance Measurements

Transmittance and reflectance measurements provide insight into the accuracy of VCSEL and DBR growths through comparison of the measured and modelled spectra[59]. The position and width of the stopband indicate whether DBR layers have been grown to the correct thickness, a decrease in central wavelength corresponds to layers that have been grown too thin and an increase corresponds to layers grown too thick. The cavity resonance of VCSELs can be observed directly in the transmittance and reflectance spectra prior to any fabrication or device processing, making it ideal for rapid characterisation of the grown material. An example of the reflectance measurement is shown in Figure 4.1. In this instance the DBR repeats were grown thinner than required for the design wavelength, shifting the spectrum to the left. The cavity layers were grown thicker relative to the DBRs, shifting the resonance to the longer wavelength side of the spectrum. When simulated using layer thicknesses measured using TEM, the model matches up well with the measured reflectance. This non-destructive measurement indicates the final emission wavelength of the VCSEL and can be used to verify that the cavity measurement is close to the centre of the stopband before device fabrication commences.

Optical transmittance and reflectance measurements are performed using a Cary 5000 spectrophotometer. The spectrophotometer uses a halogen light source, coupled into a monochromator and split into two beams before being passed through the sample compartment. A solid sample stage was used for double beam transmission measurements (Figure 4.2). One beam serves as a reference beam, whilst the other measures the relative transmittance of the sample. The double beam configuration reduces the impact of machine emission intensity fluctuations in real time by taking the ratio of the sample and reference beams. Absolute transmittance measurements can be obtained with accurate calibration of zero and 100% transmittance. The sample beam is left unobstructed to perform the 100% transmittance calibration; 0% transmittance is obtained by blocking the sample beam with an aluminium plate which is opaque in the wavelength ranges of interest. Transmission measurements are favoured in the Cary system due to the ease of setup and accuracy of calibration. However, highly absorbing samples can result in low levels of transmitted light and poor resolution of the cavity resonance without extended measurement time (Figure 4.3).

In contrast to the small signal around the cavity resonance for transmittance measurements, reflectance measurements result in a large signal in the vicinity of the stopband allowing for quick identification of the cavity resonance position. Reflectance measurements are carried out using a diffuse-reflectance accessory (DRA) with integrating sphere. This is not a purely normal-incidence measurement and so results in an apparent broadening of the reflectance spectrum (Figure 4.3), and less accurate determination of the

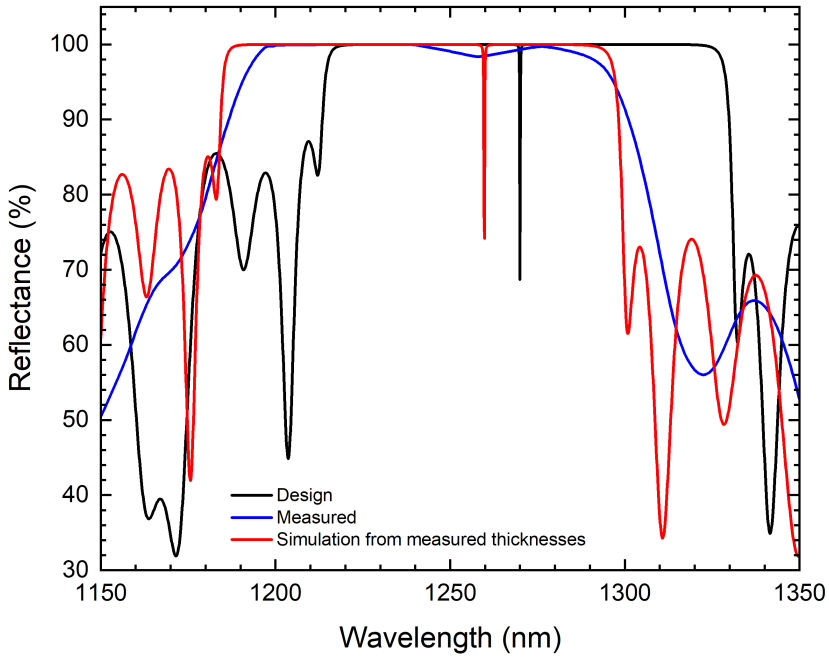

Figure 4.1: Measured and modelled reflectance for a VCSEL with a $3\lambda/2$ cavity length designed for operation at 1270 nm (sample V4, see Table 11.1 and section 11.3.3). The mismatch between the reflectance of the designed and grown structures indicates a deviation from the design. The DBR is shifted to shorter wavelengths and the cavity resonance shifted to the longer-wavelength side of centre in the stopband.

cavity length. As shown in Figure 4.4 the sample may be mounted to include both the specular and diffuse components (blue dash), or to exclude the specular component (red dash) by reflecting the specular component beam through the exit port.

A standard Polytetrafluoroethylene (PTFE) reference sample (Cary reference part number: 410143900) is used to calibrate the nominal 100% reflectance. For the 0% reflectance calibration, the beam is allowed to terminate in the sample compartment with the sample port left unobstructed. The reflectance of the reference sample in the short-wave infrared (SWIR) is notably less than 100%. This results in apparent reflectance measurements of greater than 100% for some samples (example in Figure 4.5). For cases with reflectance >100 % the reflectivity is normalised to 100 %. The reference sample calibration allows direct comparison of DBR samples in this work; however, the unknown reflectance of the reference prevents measurement of absolute reflectance and direct comparison with absolute reflectance in simulations. The position of the cavity resonance, stopband and sidebands give insight into the growth accuracy without the requirement for knowledge of the absolute reflectivity.

The reflectance and transmittance measurement techniques discussed so far perform a measurement on a single small area of a sample, as shown in Figure 4.6. An indication of the VCSEL growth uniformity in this work can be built up from repeated transmittance measurements located across the wafer. A home-built wafer mapper is used to move the sample in discrete steps in front of the standard transmittance aperture (Figure 4.6) [60].

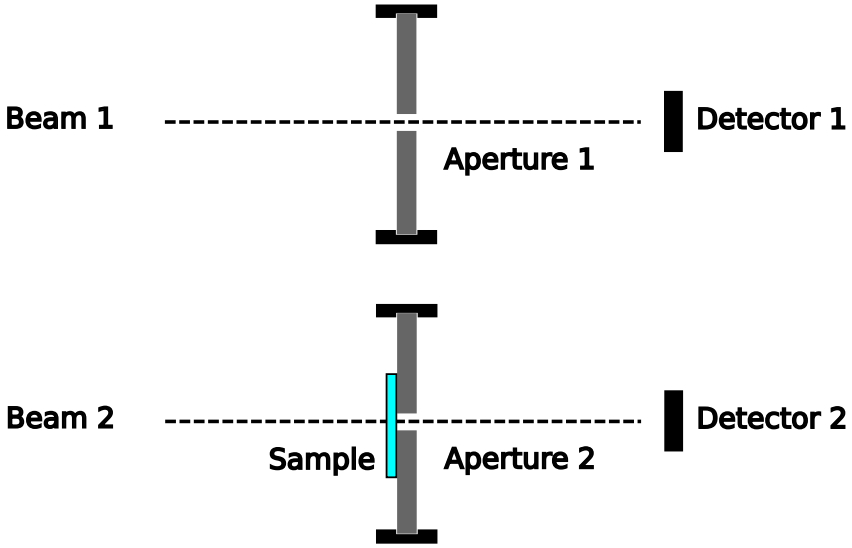

Figure 4.2: The Cary 5000 solid sample stage transmission measurement uses two beams passing through a pair of apertures. Beam 1 is used as a reference to minimise the impact of instrument fluctuations. The sample is placed flush against the aperture in the path of the measurement beam.

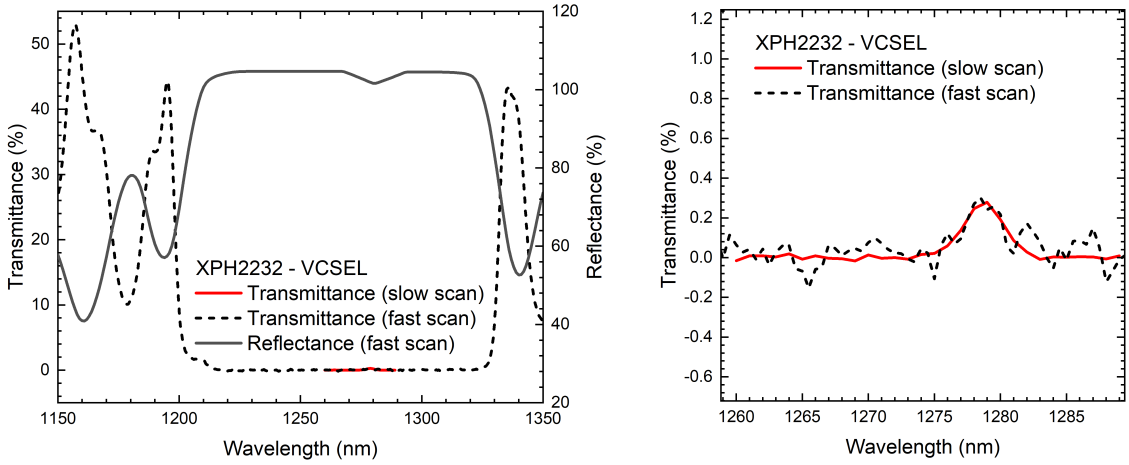

Figure 4.3: Reflectance and transmittance measurements for a VCSEL (sample V3, see Table 11.1 and section 11.3.2), indicating a resonance in the region of 1280 nm. A magnified view of the transmittance (right) demonstrates better wavelength-resolution of the cavity but much weaker response compared to the reflectance measurement. Fast scans correspond to an integration time of 0.5 seconds per point, and 10 seconds per point for a slow scan.

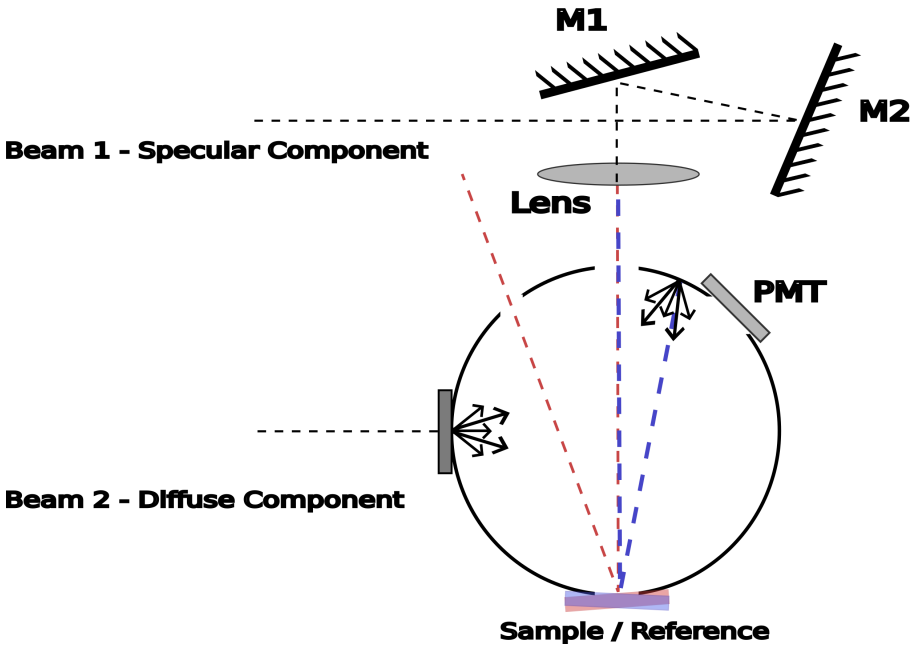

Figure 4.4: The Cary 5000 diffuse reflectance accessory measures the combined specular (beam 1) and diffuse (beam 2) components of reflectance. The sample is mounted against a port on the side of the integrating sphere and oriented to either include the specular component of the reflection (blue dash) or exclude the speular component (red dash). The light is collected by a photomultiplier tube (PMT). The orientation of the sample is indicated by the shading of the sample.

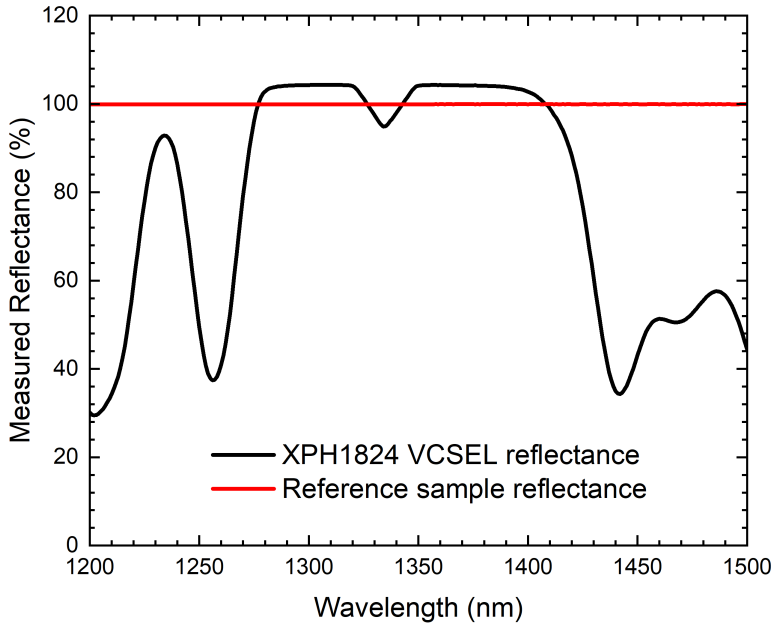

Figure 4.5: Measured reflectance for a PTFE reference sample and VCSEL sample (sample V1, see Table 11.1 and section 11.3.1), relative to the initial PTFE reference calibration.

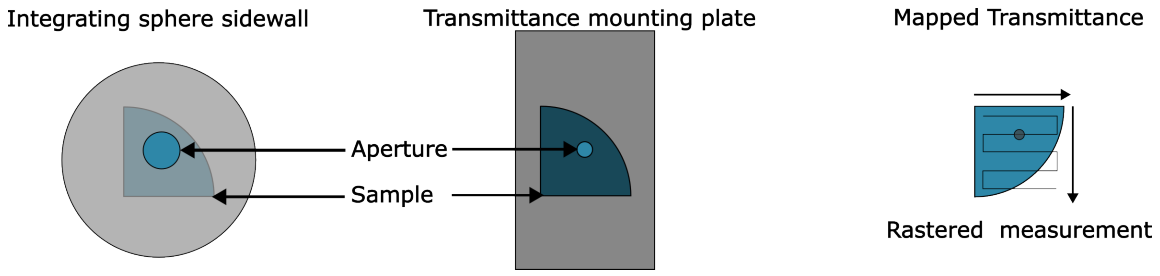

Figure 4.6: Schematic of the measurement area for reflectance measured at the integrating sphere sidewall (left), transmittance using the mounting plate (centre) and the mapped transmittance (right). Mapped transmittance uses the standard transmittance aperture and moves the sample along the path shown using a motorised arm.

4.2 Electrical Characterisation

Electrical characterisation of contacts, DBRs and VCSELs in this work is performed using Keithley source measurement units (SMUs). Contacts on unpackaged samples are directly probed using a room-temperature probestation and current-voltage characteristics measured using a Keithley 2634b SMU. Electrical characterisation of header-mounted devices is performed in the setup for photoluminescence measurements discussed in section 4.3. Devices are mounted on TO-46 headers using silver electrodag or conductive silver epoxy to form a back contact to the header and gold wire bonds are used to connect to bondpads to the measurement pins. The TO-46 headers are placed into a temperature controlled mount, configured for four-wire measurements.

For a two-probe configuration (Figure 4.7) the potential difference measured by the test equipment may be represented as follows,

$$V = I \times (R_{DUT} + 2R_L)\,, \tag{4.1}$$

where V is the potential difference, I is the current through the circuit, R_{DUT} is the resistance of the sample, and R_L is represents the combined resistance of the test leads, probes and probe-contact connection. In the case that $R_{DUT} \gg R_L$ this may be reduced to

$$V = IR_{DUT}. \tag{4.2}$$

In many cases, the resistance of the test leads is not negligible compared to the sample resistance and the two-probe measurement is not appropriate. This is particularly relevant for the electroluminescence (EL) measurements discussed in section 4.4 where long leads are required to reach the sample mount from the measurement rack. Four-probe measurements are used to eliminate the contributions of measurement leads. In four-probe measurements (Figure 4.7) no current flows through the voltage-measurement loop; therefore, no voltage is dropped across the measurement leads, eliminating the resistance contribution of measurement leads. The potential difference measured by the test equipment in a four-probe configuration is therefore equivalent to the expression given in equation 4.2.

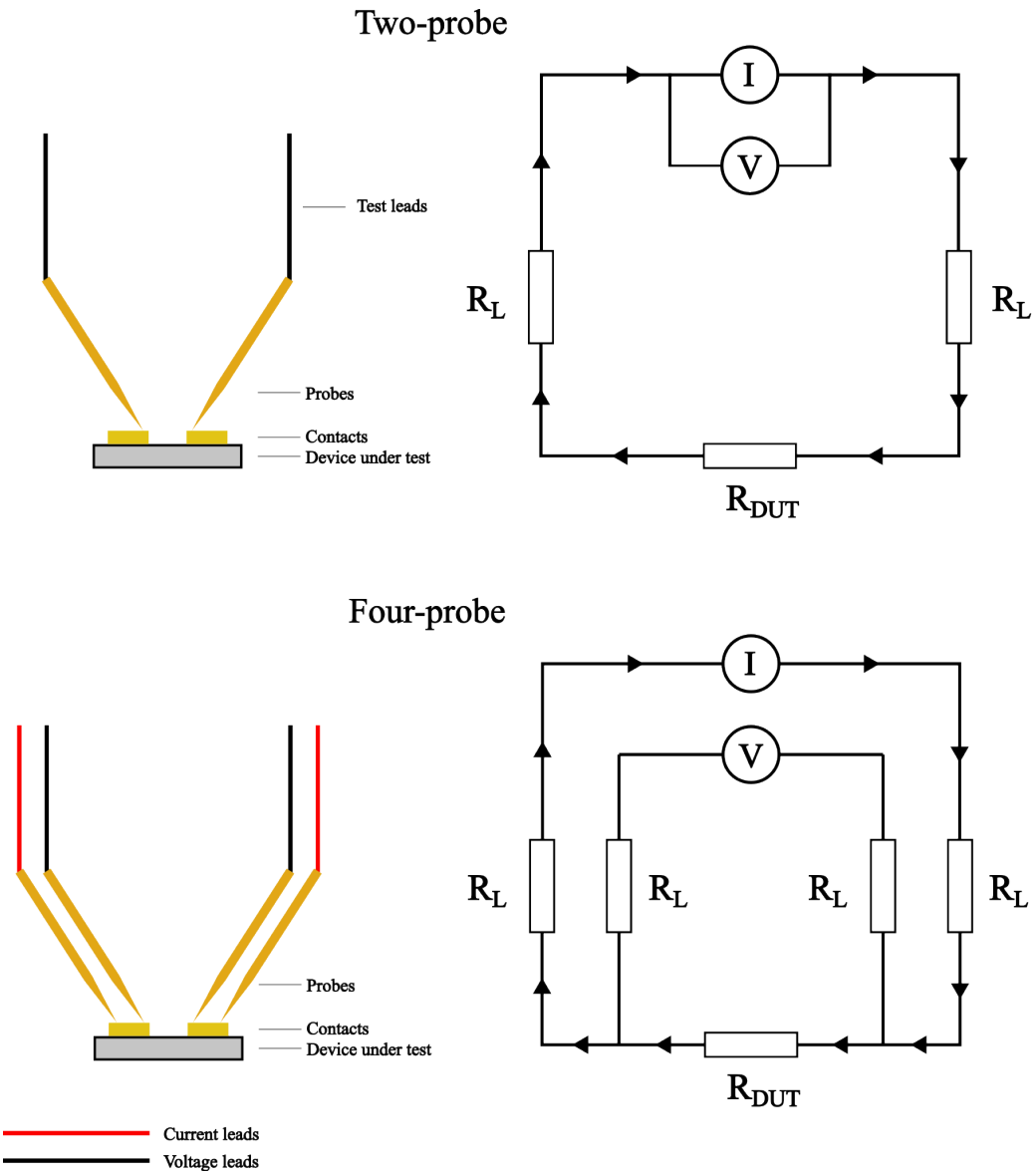

Figure 4.7: Schematic of 'four-probe' and 'two-probe' measurement setup. The sample is indicated as the device under test (DUT). Equivalent circuits are shown alongside the probe configuration with lead resistance denoted as R_L.

4.3 Photoluminescence and Time-Resolved Photoluminescence

Photoluminescence (PL) and time-resolved photoluminescence (TRPL) measurements are used to provide insight into carrier recombination within the GaSb quantum rings for VCSEL and QR-only samples. During the PL measurement, light is incident on the semiconductor material with energy of at least the bandgap of the material of interest. This excites carriers into higher energy states. The carriers may then relax to lower energy states, typically through phonon emission, and recombine either radiatively or non-radiatively. The spectrum of light emitted by the sample is collected and interpreted to draw conclusions about the sample material. This work considers two forms of photoluminescence. Measurements taken under continuous illumination of the sample will be referred to simply as photoluminescence (PL) measurements. A second technique, TRPL, excites the material with a series of short laser pulses and measures how the light intensity decays over time. TRPL provides information regarding the recombination lifetime of carriers in the semiconductor within the measured wavelength range.

PL measurements taken under continuous illumination use the experimental setup shown in Figure 4.8. A 532 nm excitation laser is coupled into the beamline using a series of silver mirrors, an optical periscope and a partial mirror (Thorlabs DMLP650L dichroic mirror) before being focused onto the sample. Emission from the sample is collected by a large 3" off-axis parabolic mirror with short focal length to maximise the collection angle. The collected light is transferred from the 3" beam line to the 1" upper beam line through a beam reducer constructed from a pair of off-axis parabolic mirrors with coincident focal points. The upper beam line consists of linear and quarter-waveplate polarising optics to enable polarisation measurements. Polarising optics are mounted on flip mounts to enable measurements without polarisation. A final off-axis parabolic mirror focuses the light onto the collection fibre which leads to an Acton SpectraPro 2300i diffraction grating spectrometer and 1-D Andor iDus DU492A InGaAs-array CCD detector. The partial mirror in the upper beamline stops reflections of the excitation laser from entering the spectrometer. This avoids detector blinding and any signal detected at 1064 nm from the second-order diffraction of the 523 nm laser. Initial alignment of samples for PL measurements is conducted with a low-power flip-in flip-out alignment laser. The temperature-controlled sample holder may be exchanged for a fibre coupling to allow for low temperature measurements at 77 K. In this configuration the sample is held in a cryostat compatible 'cold stick' with a fibre positioned directly over the device (Figure 4.9). The sample is carefully lowered into a liquid nitrogen bath for measurements at 77 K.

TRPL measurements are performed on a PicoQuant FluoTime 300 Spectrometer. A pulsed 980 nm laser was used to excite carriers within the active region of two QR-containing samples. 980 nm is below the bandgap energy of $Al_xGa_{1-x}As$, so can penetrate to the active region without being absorbed in $Al_xGa_{1-x}As$ DBRs or GaAs capping layers. Analysis of the TRPL measurements was performed using *EasyTau* software, discussion of the fitting will be provided in chapter 10.

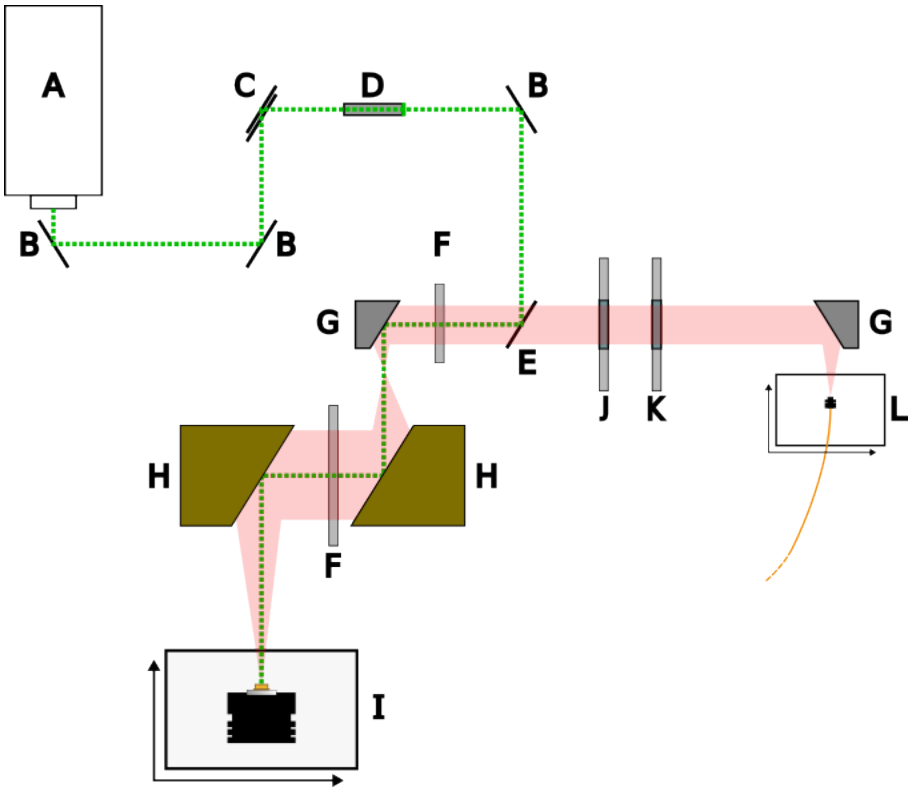

Figure 4.8: Schematic of the optical setup used for electroluminescence and constant-irradience photoluminescence measurements. A) 1 Watt 532 nm excitation laser B) silvered mirrors C) optical periscope D) low-power green alignment laser on flip mount E) Thorlabs MLP650L partial mirror F) variable apertures G) 1" off-axis parabolic mirrors H) 3" off-axis parabolic mirrors I) motorized x-y-z-θ stage with sample holder (optional use of temperature controlled holder) J) motorised rotation mount with linear polariser on flip mount K) motorised rotation mount with linear polariser on flip mount L) collection fibre on manual x-y-z stage. The final off-axis parabolic mirror (G) focuses the light onto the collection fibre (L). The fibre leads to an Acton SpectraPro 2300i spectrometer equipped with an Andor iDus 492A InGaAs-array detector.

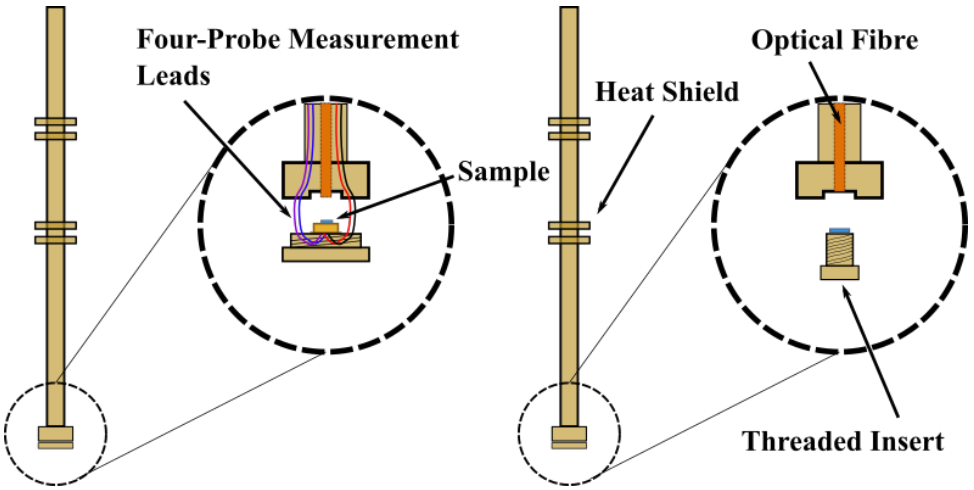

Figure 4.9: Schematic of the cryostat-compatible 'cold sticks' used for low temperature EL and PL measurements. The EL stick (left) takes a sample in a TO-46 header on a threaded insert at the base of the stick. The header socket is configured for four probe measurements with light directly coupled into a collection fibre. The PL stick (right) takes a sample mounted onto a threaded insert at the base of the stick with the excitation laser and fluorescent emission directly coupled through the same fibre.

4.4 Electroluminescence

Electroluminescence (EL) measurements are performed using the optical setup depicted in Figure 4.8. Devices are mounted onto TO-46 headers using either conductive silver electrodag or conductive silver epoxy. The headers are mounted in a thermoelectric mount with active temperature control in the range 15 °C to 85 °C. A Keithley 2400 SMU performs simultaneous current and voltage measurements whilst EL spectra are measured by the linear-array detector in conjunction with the spectrometer. The beamline remains as described for the PL measurements in section 4.3, with the device located at the focus of the 3" off-axis parabolic mirror. The sample stage has three axes of translational movement and rotational control in the azimuthal axis for fine positioning of the device at the focus of the collection mirror. A grid search of x-y-z positions is performed to move the device around the focus point of the collection mirror. The device is driven with a constant drive current and the maximum count rate recorded by the detector is used to determine the optimal focus position. The VCSEL devices may be mounted on a cold-stick for low temperature measurements (Figure 4.9). Four probe measurements are used to eliminate resistance contributions of the electrical leads, as discussed in section 4.2.

4.5 Electron Microscopy

A number of electron microscopy techniques are utilised in this work. The basic principles of the techniques and their applications are presented here. In all of these cases an electron beam is incident upon the sample surface, the electrons then interact with the sample within a characteristic volume below the surface and produce a signal (Figure 4.10) that is measured by a detector.

Transmission electron microscopy (TEM) is an advanced microscopy technique capable of atomic-resolution imaging [61]. This technique produces images using the trans-

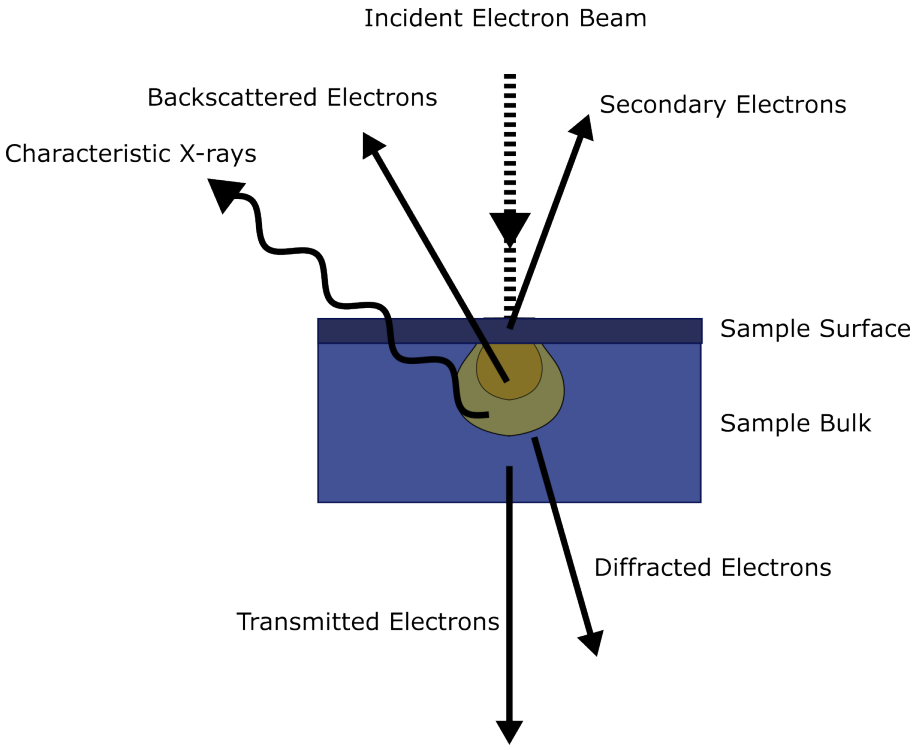

Figure 4.10: A sketch indicating a selection of the signals measured during interaction of the electron beam and the sample during electron microscopy techniques. The shaded volumes indicate the depth and region within which the different interactions occur between the electrons and the sample.

mitted and diffracted electrons shown in Figure 4.10. TEM imaging for this work was performed by Francisco Alvarado-Cesar at Warwick University using a JEOL 2100 system. As shown in Figure 4.11a, the images may be used to identify defects and failure modes in epitaxially-grown materials. TEM may also be used to exclude growth as a cause of poor device performance in instances where material quality is good and quantum rings are well formed (Figure 4.11b). Direct measurement of DBR and VCSEL layer thickness over a small region of the wafer may be performed using TEM. Transmission electron measurements require ultra-thin samples, this necessitates the thinning of epitaxial material and destruction of the sample material.

Additional imaging and analysis is carried out using scanning electron microscopy (SEM) on a TESCAN SEM. During SEM, an electron beam is accelerated and deflected by a series of coils in order to scan across the surface of a sample. The electrons may interact close to the surface, exciting a secondary electron which is then detected. For the secondary electron to be detected it must have sufficient energy to reach the surface of the sample and escape into the vacuum of the SEM. Therefore, this technique is limited to providing information about the surface of the sample and its topography. Alternatively, the incident electron can recoil elastically within the sample. Such backscattered electrons typically originate from deeper within the sample and can provide good contrast between different materials.

The SEM used in this work is equipped with an Oxford Instruments Ultim Max 40 energy-dispersive X-ray spectroscopy (EDS) detector. During EDS measurements, the incident electron beam excites electrons within the atoms of the sample. De-excitation of more energetic electrons to inner-electron vacancies of the atom results in the emission

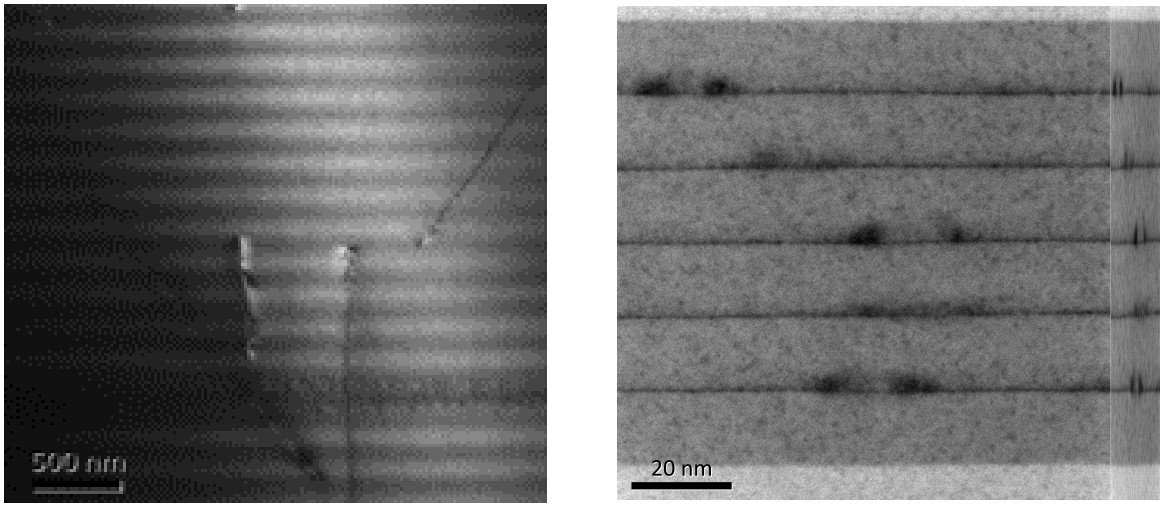

(a) (b)

Figure 4.11: Transmission electron microscope images showing (a) a poor quality quantum ring growth in a VCSEL (sample V2, see Table 11.1 and section 11.3.2) with defects propagating from the lower DBR through the cavity and into the upper DBR and (b) quantum rings in a VCSEL cavity (sample P3, see Table 11.1 and section 11.2).

of X-rays with characteristic energies for each element. It is possible to build up an elemental map of the sample by scanning the electron beam across the surface of the sample and measuring the spectrum of emitted X-rays at each location.

4.6 BEXP+AFM

Beam-exit cross-sectional polishing and atomic force microscopy (BEXP+AFM) is a destructive measurement technique developed at Lancaster University that allows for direct measurement of layer thickness on a cross-sectioned device post-growth [62]. Measurements were performed by *Lancaster Materials Analysis*. A small sample approximately 5 mm x 5 mm is cross-sectioned at an angle using a focussed argon ion beam with a resulting surface roughness on the order of nanometres (Figure 4.12). Angled cross-sectioning increases the apparent thickness of the layers, reducing the error in subsequent thickness measurements. Selective etching of $Al_xGa_{1-x}As$ samples using citric acid increases the contrast between layers for atomic force microscopy measurements. A series of 3D maps are carried out across the sample (figures 4.12 and 4.13), from which the thickness of VCSEL and DBR layers can be obtained. BEXP+AFM measurements have been shown to agree with TEM to within a few percent for thin layers (10 nm to 15 nm) and the accuracy improves with layer thickness.

Figure 4.12: Schematic of the BEXP+AFM procedure. Samples are cross sectioned at a known angle (left) using a focussed ion beam. AFM is used to measure the thickness of layers on the cross-sectioned surface (right).

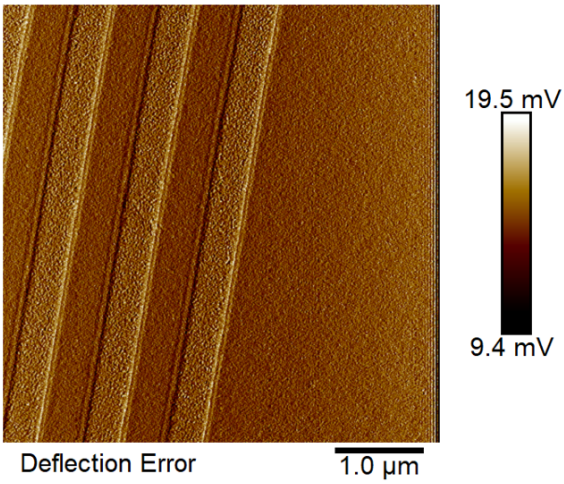

(a)

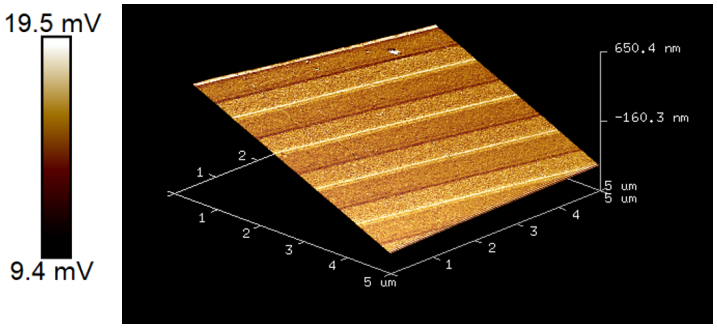

(b)

Figure 4.13: Scanning probe microscope images of a stepped-interface DBR (presented in section 9.1) prepared for BEXP+AFM measurements (a) shown with the measured 3D height (b).

4.7 X-ray Photoelectron Spectroscopy

X-ray photoelectron spectroscopy (XPS) is a surface analysis tool capable of measuring the elemental and electronic states of the sample surface. XPS measurements are carried out at Lancaster University by Elizabeth Bancroft and Dr Sam Jarvis on a Kratos Analytical AXIS Supra fitted with a monochromatic Al K_α 1486.7 eV X-ray source. XPS measurements are conducted under ultra-high vacuum (UHV) conditions, at vacuum pressures better than 5×10^{-10} mbar. The system consists of a monochromatic X-ray source to eject electrons from the sample surface with an electron gun for charge neutralisation of the sample. The photo-liberated electrons are collected and passed through an analyser to distinguish the residual kinetic energies of the electrons. After passing through the analyser the electrons are incident on an electron-counting detector which builds up the XPS spectrum of the elemental and electronic structure of the surface. A diagram of a generic XPS setup is shown in Figure 4.14.

A variation of the XPS technique - XPS imaging - creates an elemental map of the sample surface. The Kratos system is equipped with a hemispherical analyser for spectroscopy, consisting of a pair of charged plates which separate the electrons according to their kinetic energy (Figure 4.15). XPS imaging uses a spherical mirror analyser to maintain the lateral distribution of the electrons between the sample and the detector [63, 64]. Apertures inside the spherical mirror analyser are used to select the kinetic energy of the electrons to be imaged.

The addition of an in situ Kratos Minibeam 6 Gas Cluster Ion Source (GCIS) enables depth-profiled XPS measurements. The ion beam is raster-scanned over the surface to mill a 4 mm by 4 mm area; uniform milling is obtained by rotating the sample [65]. XPS measurements can be performed at the centre of the raster scanned region to gain depth-dependent characterisation of the sample surface, whilst XPS imaging provides position resolution of the elemental make-up.

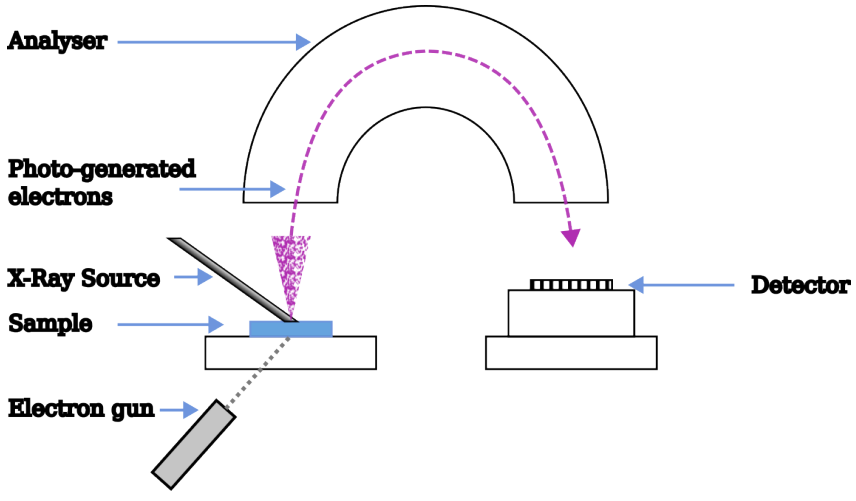

Figure 4.14: Schematic of a generic X-ray photoelectron spectroscopy setup.

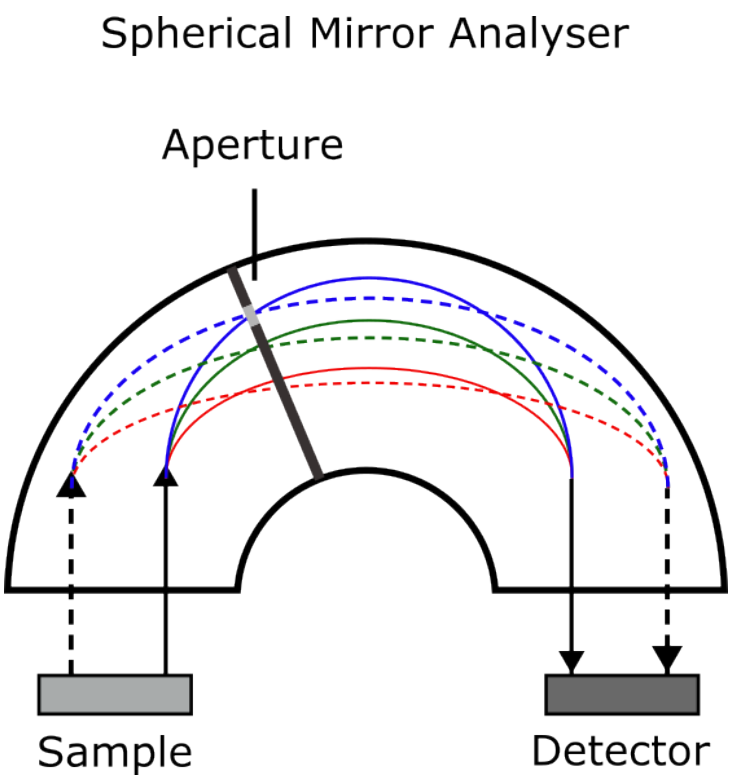

(a)

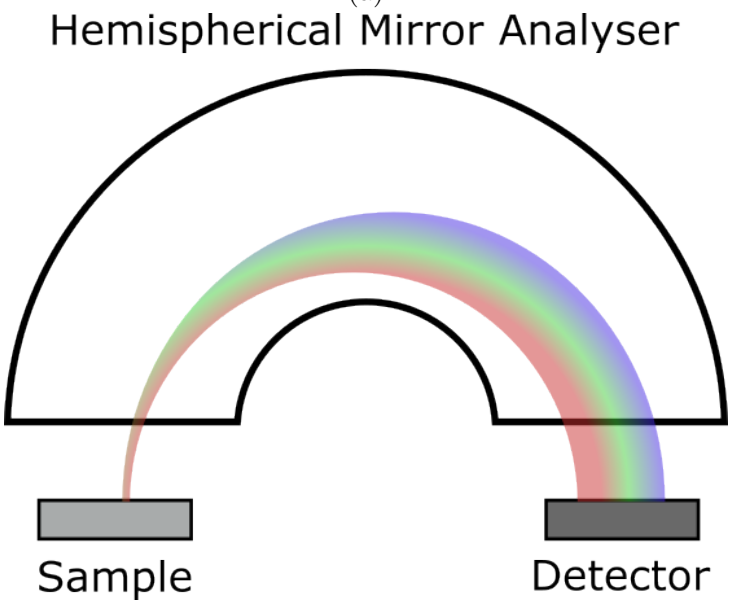

(b)

Figure 4.15: (a) A schematic of the spatial dispersion of electrons through a spherical mirror analyser. The dashed versus solid lines indicate electrons with different initial lateral positions. Different colours indicate electrons with different kinetic energies. An aperture is used to select the kinetic energy of the electrons for imaging, and is indicated on the figure. (b) A schematic of the spatial dispersion of electrons with different kinetic energy through a hemispherical mirror analyser for spectroscopy measurements on a single point of the sample surface.

Chapter 5

Epitaxial Growth

5.1 Molecular Beam Epitaxy

Molecular beam epitaxy (MBE) is used for the growth of high-quality semiconductor films on single crystalline wafers and was developed in the late 1960s [66]. Surface contaminants and impurities in growth chambers result in defects in epitaxially-grown layers [67], so a great deal of effort is directed towards maintaining a clean, low pressure environment for growth [68]. Over the years chamber pressures have been reduced from 1×10^{-9} mbar in the late 1970s to pressures on the order of 1×10^{-11} mbar in modern systems [69]. MBE technology saw rapid development in the 1970s and 1980s due to the complementary nature of MBE and optoelectronics research [70] and, since its invention, has been the topic of numerous studies, book chapters and reviews [69].

The MBE technique offers high-quality material and can achieve atomically-sharp interfaces with fine control over the layer thickness making it a popular tool in research environments. Growth of the semiconductor crystals is performed monolayer-by-monolayer on heated substrates under ultra-high vacuum (UHV) conditions. The substrates are heated to several hundred degrees Celsius to provide the necessary temperatures for high-quality growth [71]. A detailed review of growth mechanisms is beyond the scope of this work but is readily available in the wider literature [72].

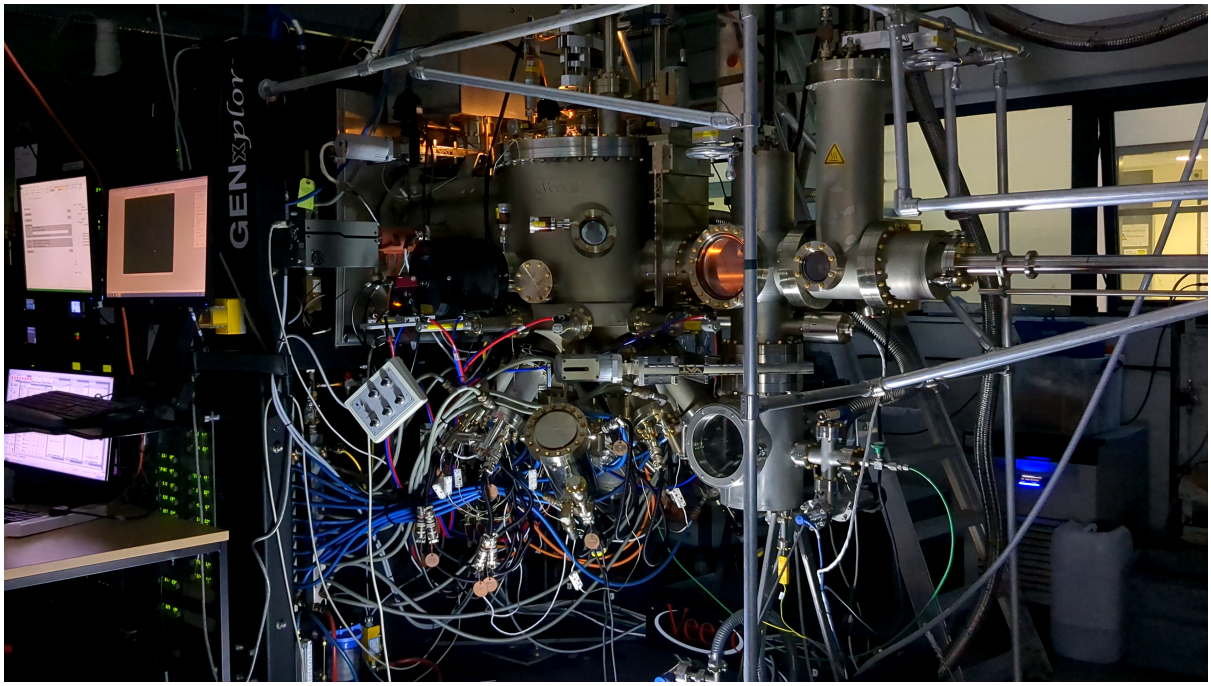

Figure 5.1: The Veeco GENxplor MBE system located at Lancaster University. Photo courtesy of Dr Peter Hodgson.

A basic schematic of the Veeco GENxplor (Figure 5.1) chamber used in this work is shown in Figure 5.2. The reactor walls are cooled by a liquid nitrogen cryopanel to freeze out impurities in the chamber and help to achieve UHV conditions. The growth chamber is equipped with a helium cryopump, an ion pump and a titanium sublimation pump. The system is also equipped with an ion pump on the substrate preparation chamber and has a turbomolecular pump on the load lock backed by a scroll pump. A series of effusion cells are arranged around the base of the chamber and act as sources for the group-III material and dopants, each with its own independent shutter. The cells are typically

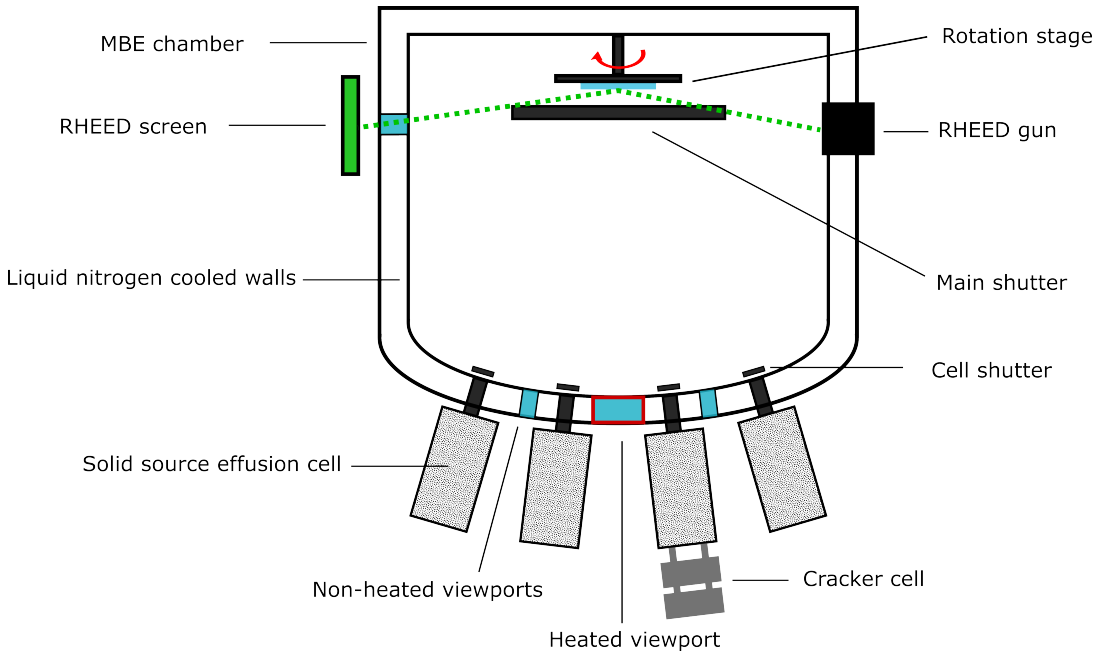

Figure 5.2: A schematic of the Veeco GENxplor MBE growth chamber used in this work. The system uses solid-source effusion cells for group-III materials and dopants, and valved cracker cells for the group-V sources. All of the sources are located at the base of the chamber. The chamber walls are cooled using a nitrogen jacket. Wafers are mounted on a rotating stage at the top of the chamber and covered by a shutter before and after the growth process. The MBE chamber is equipped with RHEED for in-situ analysis of the wafer surface. A heated viewport is located directly below the sample and is used for normal incidence reflectance monitoring.

made of pyrolytic boron nitride as other materials are known to emit contaminants when heated [70]. In this case the MBE is equipped with one indium cell, one aluminium cell, two gallium cells, one beryllium cell and one silicon cell. Cracker cells are used for the group-V arsenic and antimony sources, with valves to regulate the beam flux. Samples are loaded into the chamber on molybdenum substrate holders and placed in a rotating mount at the top of the chamber. A heating element and virtual substrate are located in close proximity for substrate heating and reference of the substrate temperature. A heated-viewport is located directly underneath the sample allowing for normal-incidence in-situ growth monitoring. A reflection high energy electron diffraction (RHEED) screen is fitted to the side of the machine for real-time structural analysis of the surface. A separate load-lock and substrate preparation chamber maintain the UHV conditions in the growth chamber during sample loading and allow for substrate outgassing independent of the main growth chamber. The growth of GaSb QR VCSELs by MBE is not ideal as growths take in the region of 24 hours, with limited maximum doping concentration and less-than ideal layer thickness control. However; at this point in time MBE is needed for GaSb QR growth and is available in Lancaster so is used for growth of VCSELs in this project. All of the GaSb QR, VCSEL and DBRs grown by MBE as a part of this work were grown by Dr Peter Hodgson at Lancaster University.

5.1.1 Growth Rates in MBE

MBE growth rates are typically on the order of $1\,\mu m\,h^{-1}$. Under normal operation of the machine, growth rates are limited by the group-III beam flux at the wafer surface. The flux is determined by the temperature of the effusion cell along with geometrical factors such as the distance between the source and wafer surface [72]. Molecular beam sources are angled with respect to the substrate which results in non-uniform flux across the wafer surface, so substrate rotation is introduced to improve uniformity of the growth rate across the wafer.

A popular method for growth rate calibration relies on oscillations of the RHEED spot intensity. During growth of unstrained-semiconductor layers the incident atoms begin to form small islands on the surface. It is energetically favourable for additional atoms to migrate to the edge of the islands as the growth proceeds and eventually form a complete layer [73, 74]. The intensity of the RHEED spots are at a minimum when the surface is dominated by islands of growth. This is due to scattering of the electrons by atomic steps in the surface. The RHEED intensity is at its highest for smooth layers with a completely constructed surface [75]. The RHEED intensity oscillations follow the growth of the surface, with one oscillation corresponding to the growth of one monolayer [76] so are used for the calibration of growth rates.

Growth rate calibrations based on RHEED oscillations provide a good starting point for the recipes used in MBE growth of VCSELs and DBRs. Unfortunately, errors in the growth rate obtained from RHEED can be several percent or more [77]. In addition, the growth rates may drift by a few percent over time as a result of a number of factors including, but not limited to, instability in cell temperatures [77], transient temperatures of the cell when shutters are operated [78] and redistribution of source material in the cells when temperatures are changed. Due to the sensitivity of VCSELs and DBRs to exact layer thickness it is preferable to monitor the growth in real-time to feed back into control of the growth process [77, 79]. Continued use of RHEED oscillations is unsuitable for monitoring a full VCSEL or DBR growth. Primarily, the RHEED oscillations are performed on a stationary substrate which is incompatible with uniform growth across the wafer. It is possible to lock in to the rotation frequency of the substrate but this is an added level of complexity [80, 81]. In addition, RHEED oscillations are damped as growth proceeds due to an increase in the long range disorder and roughness on the wafer surface [73]. Techniques have been developed to reduce the the wafer roughness [82], but these add further complications to the growth process.

Many MBE systems are equipped with tools for in-situ monitoring of the growth progress and conditions which assists in the reliable and reproducible growth of structures. Pyrometric interferometry (PI) is a non-contact method that has demonstrated real-time monitoring of layer thicknesses using interference techniques and simltaneously measured substrate temperature [83]. PI has demonstrated excellent repeatability of VCSEL growths, with resonant wavelength variations on the order of 0.2 % [84]. An alternative home-built laser-interferometry technique is introduced in chapter 8.

5.2 Metal Organic Chemical Vapour Deposition

Metal organic chemical vapour deposition (MOCVD), also known as organo-metallic vapour-phase epitaxy (OMVPE) or metal organic vapour phase epitaxy (MOVPE) is another method used to grow high-quality epitaxial material. MOCVD is widely used in

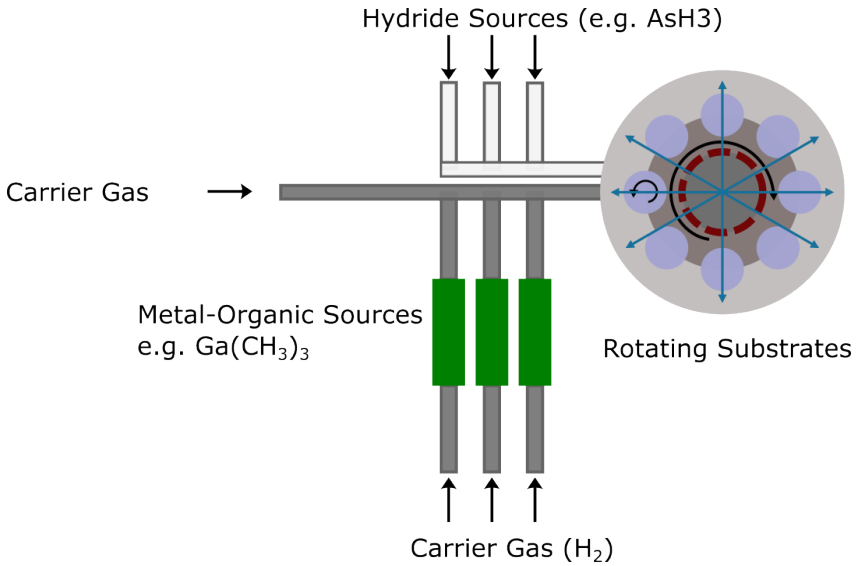

Figure 5.3: Schematic of an MOCVD planetary reactor. Heated substrates process orbit the chamber with opposite rotational direction. The precursors are injected in a laminar flow from the centre of the chamber to the edge.

industry for the growth of optoelectronic devices and is particularly relevant for volume-growth of VCSELs [85]. The MOCVD process is better suited to commercial applications due to the higher growth rates, and reduced cost when compared to MBE. The DBRs in section 9.3 were grown using a commercial Aixtron G3 planetary reactor by IQE.

Planetary reactors such as the Aixtron G3 are designed for simultaneous multi-wafer epitaxy. Gas-phase organometallic and hydride precursors are injected into the chamber with their carrier gas (H_2) in a laminar flow from the centre of the chamber at pressures around 10 mbar to 100 mbar. Mass flow controllers (MFCs) provide precise control over the composition of precursors entering the chamber. Each organometallic precursor bubbler has an individual mass flow controller. The wafers orbit the chamber whilst rotating counter to their procession direction to maximise the growth uniformity. A diagram of an MOCVD planetary reactor is shown in Figure 5.3. As for MBE, the growth mechanisms and details of MOCVD are beyond the scope of this work but can be found elsewhere [86, 87, 88].

Chapter 6

Device Fabrication Techniques

6.1 Lithography

This chapter covers the processing techniques used to produce the devices associated with QR VCSEL research. The processes described in the sections that follow act on the entire sample surface and have little control over the spatial profile of the process. Without patterning, the processed samples would be entirely planar devices with no lateral control over the manufacturing of devices. Masking techniques are required to introduce spatial control over deposition and etching processes. One such masking technique makes use of physical shadow masks for evaporation processes which, as the name suggests, are suspended between the sample and evaporation source. Shadow masking has also been demonstrated for sputtering processes [89]. The practicality of such masks is limited and they are unsuitable for many of the plasma coating and etching processes used in this work. Alternatively, photoresist masking is the most commonly used form of lithography in high-volume semiconductor manufacturing [90]. The use of photoresists, often simply referred to as resists, is widespread in both academic environments and research environments. Lithography techniques are used to transfer patterns to a polymer coating (resist) on the surface of a sample. The resist masks areas of the sample and provides windows through which deposition and etching can be performed. A wide range of resists and lithography techniques have been developed over the years, each with individual advantages and disadvantages. This section focuses on photolithography performed using a 4Pico (now Raith) Picomaster 100 direct laser writer, and single-shot exposures through a chrome-plated photomask on a Süss MJB4 mask aligner. In addition to photoresists, electron-beam-sensitive resists are popular for achieving small features in research environments [91], the principles are similar for both cases but the focus in this work is on photolithography.

For direct laser writing, samples are coated with a desired thickness of resist using the corresponding manufacturer-defined spin-coating and pre-exposure bake conditions. The spin speed is used to control the resist thickness, before baking to evaporate excess solvent in the resist. After coating, the sample is loaded into the laser-writer. For correct dosing of the resist and accurate feature sizes, the exposure laser must be focussed within the resist. A red laser (635 nm) is used measure the distance between the objective focussing lens for the exposure laser and the sample surface. The red laser is reflected from the surface of the sample and collected on a four-quadrant sensor. The position of the objective lens is wobbled within a set range and a so-called error signal describing the position of the focus is shown on the screen of the computer controlling the machine. The height of the write-module is adjusted until the signal matches the manufacturer-stated ideal trace. An example trace is shown in Figure 6.1. The focus sum (red line) is indicative of the signal intensity of the reflected focus laser and should nominally sit between 1.5 V and 7.5 V. The focus error (blue line) should cross the 0 V axis in two positions which should be coincident with the focus setpoint (grey dashed line) crossing the same axis. After setting the focus, the sample is aligned optically using a camera located within the write-module of the machine. The exposure laser (405 nm) is then rastered across the sample area exposing a pattern defined by a virtual (software) mask. The exposure time depends on a number of factors including the exposure resolution and written-area. Direct laser writing allows changes to mask designs to be implemented immediately in the fabrication process, without the additional cost or time delay associated with production of chrome masks.

Standard mask-based photolithography follows equivalent sample preparation steps.

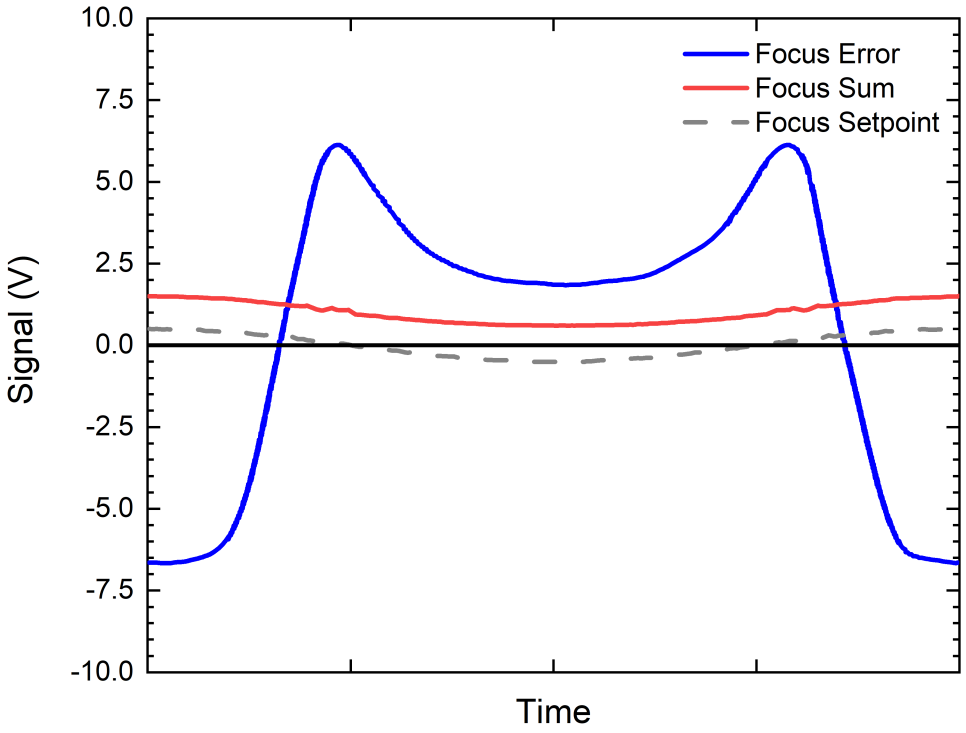

Figure 6.1: An example of the 'focus wobble' measurement on a Picomaster 100 laser-writer used to set the appropriate height of the writing head. All of the signals are given in volts. The focus sum (red line) is indicative of the signal intensity of the reflected focus laser. The focus error (blue line) is used to determine the correct height of the module to achieve correct focus and is used in conjunction with the focus setpoint (grey dashed line).

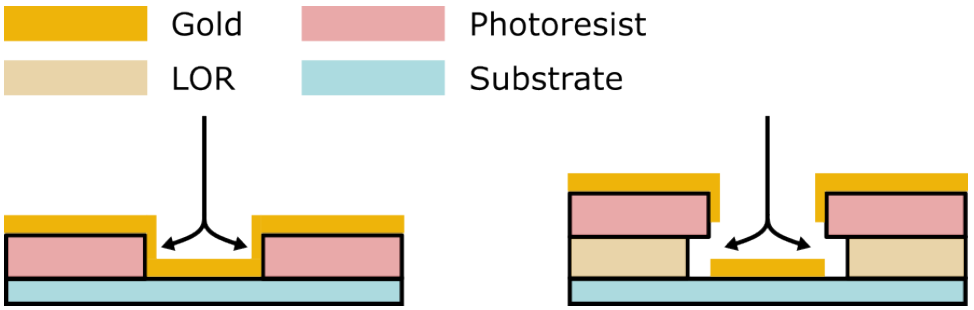

Figure 6.2: Schematic of single layer photoresist (left) coated with gold by a physical vapour deposition process compared to a bilayer resist process with sacrificial lift-off resist (LOR) underlayer. The black arrows represent the entry point for resist remover.

Typically, a chrome-plated quartz mask is produced with transparent windows in the chrome through which the sample is exposed. A microscope on the mask aligner is used to view markers common to the mask and sample. Micrometers on the sample stage are used to align the sample under the desired area of the mask. Once aligned, the sample and mask are brought into soft contact. The ultra-violet (UV) source is positioned over the sample and a shutter is opened for a fixed duration to expose the photoresist with a specific dose through the photomask. A post-exposure bake may be required by certain resists prior to development in the corresponding developer.

The appropriate photoresist selection is dependent on the desired application. Single-layer resists are often appropriate for pattern transfer via etching processes, both wet and dry. For long etches or etches that are aggressive to resist-masks, the pattern may be transferred into a hard mask via an alternative etch or through use of alternative lithography processes such as electron beam lithography using hydrogen silsesquioxane (HSQ) resists [92]. In this work, a simple approach of coating the sample with two layers of resist is sufficient to mask deeper etches. For lift-off processes of metals and dielectrics deposited by physical vapour deposition (PVD) it is often favourable to use a bi-layer resist. In the PVD process, deposition on the resist sidewall can inhibit the subsequent removal of the resist and lift-off of the PVD coated layer. Lift-off resist, such as LOR3A, serves as a sacrificial layer which may be undercut beneath the imaging resist and provide an entry path for subsequent lift-off chemicals (Figure 6.2).

Tall extruding features with high aspect ratios prevent conformal coating of the sample surface when the thickness of the spin-coated resist is thinner than the features. An example of this is the patterning of deep-etched DBR mesas in section 9.3, some of which exceed 10 µm in height. In these cases, thick AZ 40XT-11D is used without a lift-off resist to pattern the top and bottom contacts surrounding deep-etched mesas in DBR material. AZ 40XT-11D resist is designed for electrochemical plating applications and is spun to thicknesses of tens of micrometres. The thickness of AZ 40XT-11D allows for conformal coating of the tall mesas, with successful lift-off of approximately 200 nm of sputtered metal. Manufacturers suggest that the baking temperature of thick resists such as AZ 40XT-11D is ramped slowly when the samples are baked in hard contact with the hotplate. This is hard to reproduce in a repeatable fashion on a basic hotplate, such as those present in the QTC cleanroom, and may have contributed to the device-to-device variation of measurements in cases where AZ 40XT-11D was used. Details for the resists used in this work are provided in Table 6.1.

Resist	Exposure Technique	Use Case
S1813	Mask aligner & Direct Laser Writing	Shallow etches
Bilayer S1813	Mask aligner & Direct Laser Writing	Deep mesa etches
LOR3A + S1813	Mask aligner & Direct Laser Writing	Lift-off of PVD metal
AZ 40XT-11D	Mask aligner	Deep mesa etching and lithography on samples with high aspect-ratio mesas

Table 6.1: Resist selection and applications within this work.

6.2 Metal Deposition Techniques

GaSb QR VCSELs in this work are electrically pumped. Consequently, metal contacts are deposited on the semiconductor surface for current injection and bonding to external packages, details of the contacts are provided in chapter 7. In this work, metal films are deposited by thermal evaporation and sputtering PVD processes.

The Moorfield Minilab 60 thermal evaporator used in this work consists of a single chamber pumped by a rear-mounted turbo molecular (turbo) pump with dry scroll backing pump. Samples are attached to a roof-mounted rotating sample plate using Kapton tape. A quartz crystal monitor (QCM) is located adjacent to the sample to allow for monitoring of the deposition rate and thickness. Four resistively-heated baskets are located at the base of the chamber for evaporation of the source material. The baskets are sensitive to rapid changes in temperature so the source voltage must be ramped up and down slowly. These baskets can only be operated independently. A moveable shutter prevents deposition on the sample before the desired deposition conditions have been reached; the shutter is also used to terminate the deposition before the source current is ramped down. A schematic of the chamber is shown in Figure 6.3.

The chamber is evacuated to pressures below 3×10^{-6} mbar. A current is passed through a basket constructed of tungsten, or alumina-coated tungsten, dependent on the evaporation material. The current resistively heats the basket, which heats the source material. Once the temperature of the source material is high enough it evaporates. The evaporation rate is determined by the vapour pressure of the source material and controlled by changing the temperature of the source basket [93]. Sample rotation is used to improve the uniformity of the film deposited on the substrate. Thermal evaporation is appropriate for Au, Ni, Ti, Zn and the AuGe alloys used in this work, but is unsuitable for metals with higher melting and evaporation temperatures such as Pt and Pd [94].

Direct current (DC) and radio frequency (RF) sputtering is performed in a similar chamber. The Moorfield Minilab 60 sputterer used in this work consists of a single chamber pumped by a rear-mounted turbo pump with dry scroll backing pump. A variable angle valve between the chamber and turbo pump is used to control the pumping rate and provide control over the pressure within the chamber. A mass-flow controller supplies argon gas into the chamber. Samples are attached to a roof-mounted rotating sample plate using Kapton tape. An independent QCM is located adjacent to the sample to allow for monitoring of the deposition rate and thickness for each sputtering target. The chamber has independent DC and RF controllers compatible with $3-$inch diameter

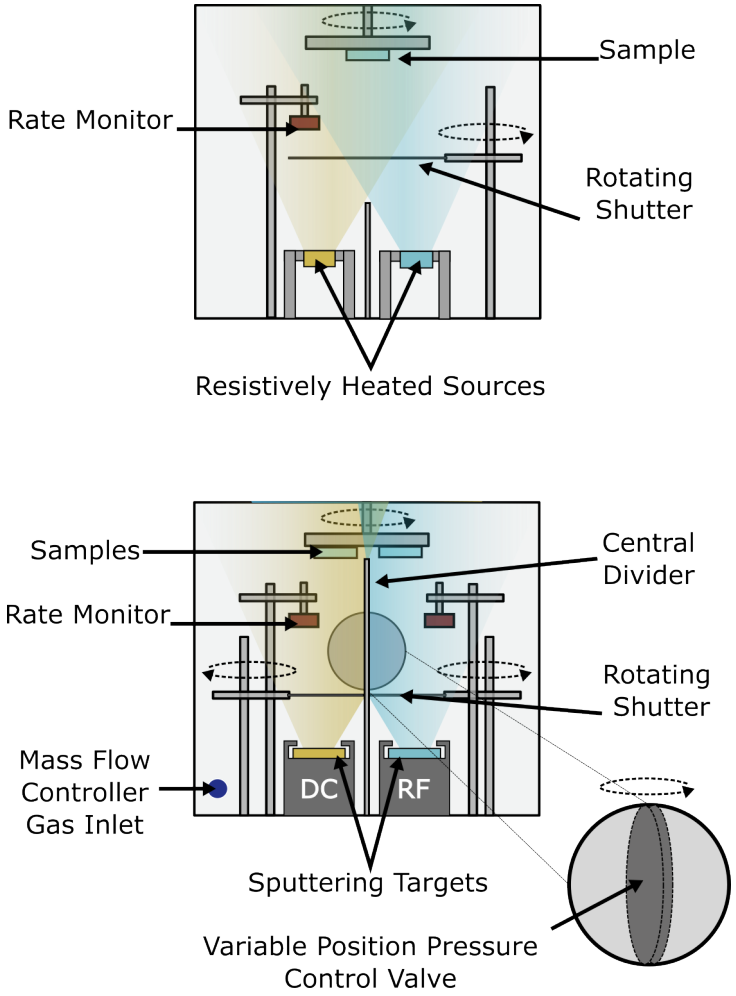

Figure 6.3: Diagram of Moorfield Minilab thermal evaporation (top) and DC/RF sputtering (bottom) chambers.

sputtering targets. Each target has independent shutters to prevent unwanted deposition on the substrate. The sputtering chamber is pumped down to pressures better than 3×10^{-6} mbar prior to deposition. A schematic of the chamber is shown in Figure 6.3.

There is anecdotal evidence for better adhesion of TiAu films deposited by sputtering at Lancaster when compared to thermal evaporation, so RF sputtering of Ti and DC sputtering of Au are used to deposit bondpads in this work. To sputter Ti, an argon plasma is struck above the target using the RF source at approximately 20 mbar before being reduced to the final sputtering pressure. Argon ions collide with the target surface, ejecting atoms that travel towards and deposit on the sample surface and chamber walls [95]. An initial pre-sputter is performed to remove surface oxides from the target prior to deposition on the sample. Once the oxide has been removed from the target the plasma undergoes a characteristic colour change from purple to a vibrant cobalt blue. A further titanium pre-sputter is used to coat the walls of the chamber in titanium, the titanium acts as a getter pump also known as a sputter ion pump and adsorbs impurities present in the chamber. The RF plasma and argon flow are stopped and the chamber is pumped down further to base pressures in the region of 10^{-7} mbar. The argon flow is resumed and the plasma struck at approximately 20 mbar before being reduced to the final sputtering pressure, the shutter is then opened to expose the sample.

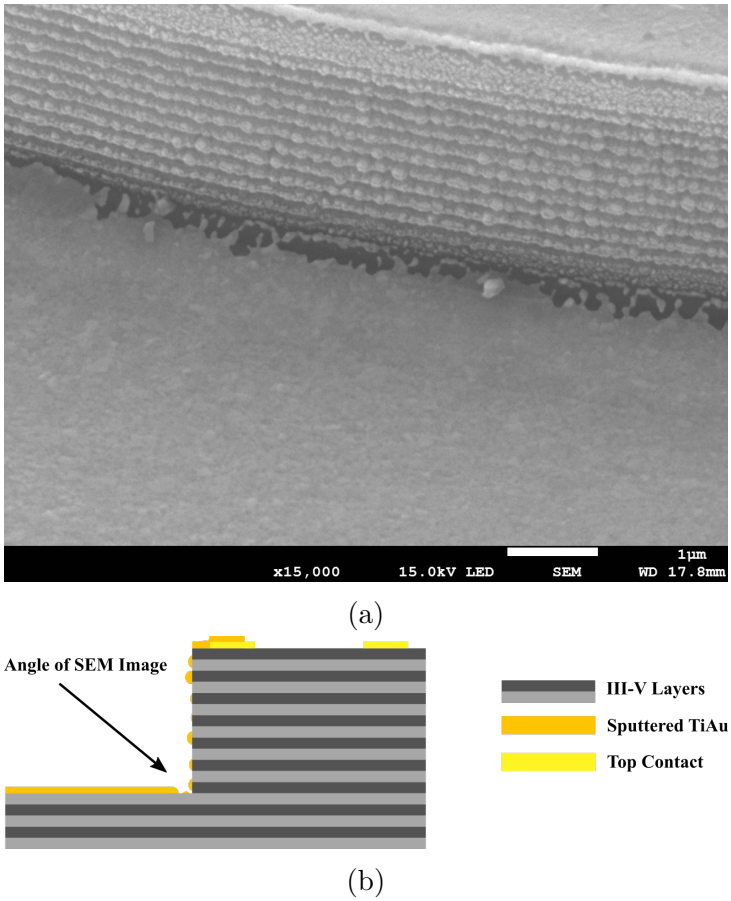

Figure 6.4: (a) A scanning electron microscopy image of sputtered TiAu bondpads on a VCSEL sample. A gap in the metal is shown around the base of an etched mesa. (b) A schematic of the structure in the microscope image, the angle of the SEM image is indicated on the schematic.

DC sputtering follows a similar procedure and is used in this work for the deposition of Au. An optional pre-sputter of titanium onto the chamber walls may be used to reduce the chamber pressure, alternatively the chamber is pumped until the pressure is 3×10^{-6} mbar or lower. To sputter Au, an argon plasma is struck above the target using the DC source. A short pre-sputter is used to remove adsorbates from the surface of the target before the shutter is opened to expose the sample.

The relatively high pressure in the sputtering chamber compared to evaporation chambers results in a shorter mean free path for the source material than thermal evaporation and greater isotropy of the deposition [96]. Intentional deposition of metal on mesa sidewalls remains a challenge in the Moorfield system despite the greater isotropy of sputter deposition. High aspect-ratio structures with an abrupt step may shadow the surrounding material and result in a break in the track between the upper and lower deposited films. Typically, the sidewall coverage may be improved by increasing the chamber pressure, utilising sample rotation and by angling the sample. Due to the central divider present in the Moorfield sputtering system it is not beneficial to introduce rotation. A particularly strong example of the challenges with sidewall coating in this system is shown in Figure 6.4.

6.3 Plasma Enhanced Chemical Vapour Deposition of Dielectric Materials

Dielectric materials are used for electrical isolation of semiconductor surfaces to avoid unwanted short circuits and may also be used to passivate surfaces and protect devices from environmental impurities such as dust, water and oxygen. Plasma enhanced chemical vapour deposition (PECVD) is a subcategory of chemical vapour deposition (CVD) which is commonly used for the deposition of dielectric layers. Parallels may be drawn with the MOCVD technique discussed in section 5.2. For PECVD the precursors are stored in pressurised gas cylinders with the flow into the chamber and ratio of precursors controlled by mass flow controllers. Pressures in the deposition chamber range between a few millibar and few hundred millibar. An Oxford Instruments PlasmaPro 80 inductively coupled plasma chemical vapour deposition (ICPCVD) system is used in this work. An RF electric field is formed between an electrode and grounded sample plate. The system has an additional RF coil located around the chamber to provide separate control over the ion density and ion energy at the sample surface. A schematic of the chamber can be seen in Figure 6.5.

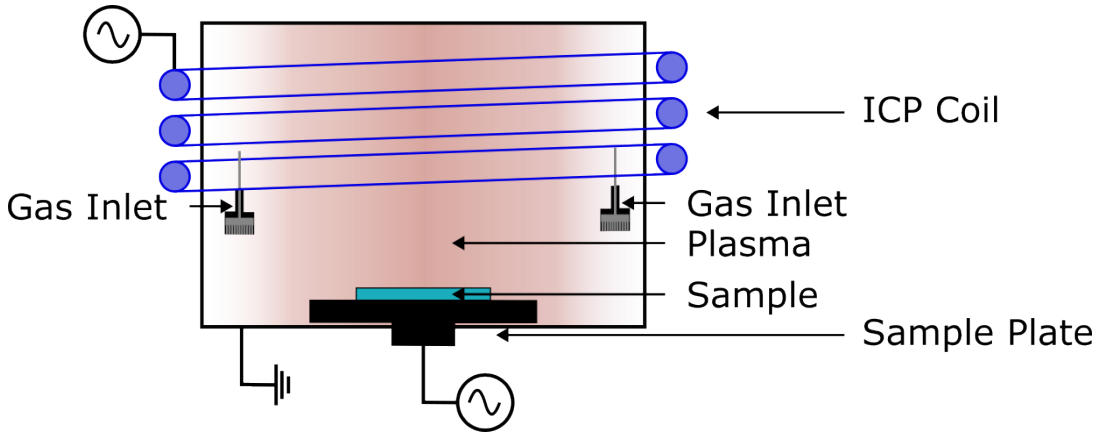

Figure 6.5: A schematic of the chamber for an Oxford Instruments PlasmaPro 80 ICPCVD system.

The oscillating fields form a plasma of the precursors. It is the ionisation of the precursors that enables deposition on a heated substrate at significantly lower temperatures than traditional CVD and MOCVD growth. The process results in isotropic deposition of the target material with high deposition rates (approximately 70 nm/min in this work). More in-depth discussion of PECVD can be found elsewhere [97, 98]. The recipe for silicon nitride used in this work can be found in the appendix.

6.4 Plasma Etching Systems

The fabrication of QR VCSELs requires etching of semiconductor material to form device mesas, and the etching of dielectric layers to regain access to the bare semiconductor surface.

Inductively-coupled plasma reactive ion etching (ICP-RIE), which may be referred to simply as ICP, enables isotropic etching of semiconductor material. The ICP-RIE process

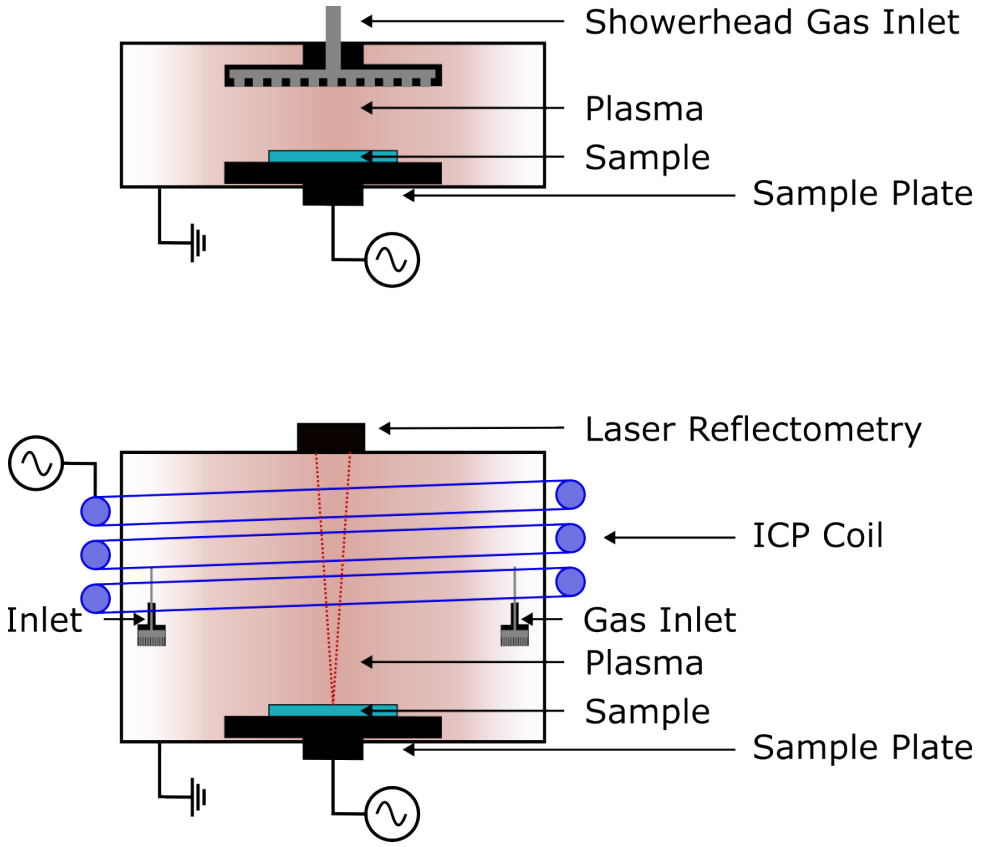

Figure 6.6: A schematic of the chamber for an Oxford Instruments PlasmaPro 80 RIE system (top) and PlasmaPro 100 ICP-RIE system (bottom).

is virtually indistinguishable from ICPCVD with almost identical chamber configurations. The primary difference between the techniques is the choice of precursor injected into the chamber. The plasma process is known as a 'dry' process due to the absence of wet chemistry and leaves little residue after etching. Depending on the blend of precursors and chamber conditions, the etch can be varied from a largely isotropic chemical etch, to a physical-etching dominated anisotropic etch. A typical process uses a combination of chemical and physical etching to achieve fast etch rates and anisotropic etch profiles. In the reactive ion etching (RIE) process, the ionised precursors react with the sample surface which, depending on the etch chemistry, will either remove surface material or reduce the resistance of the surface to physical sputtering. Bombardment from ions of the reactants and any inert precursors (often argon) contributes to an anisotropic physical sputtering component to the etch which accelerates the etch process.

ICP-RIE is an advancement on standard RIE etching. The Oxford Instruments PlasmaPro 80 RIE tool used in this work utilises a grounded chamber and RF-driven sample plate, a single RF plasma source determines both ion density and energy. A diagram of the two chamber designs is shown in Figure 6.6. The addition of the ICP coil provides independent control over the plasma density and ion bombardment energy at the substrate. Higher plasma densities enable higher etch rates. Independent control over the ion energy can be used to control selectivity and reduce damage through the use of lower energy ion bombardment.

The ICP system used in this work is equipped with in-situ laser reflectometry (section 8.2) for real-time monitoring of the etch depth. In contrast, the RIE system relies on

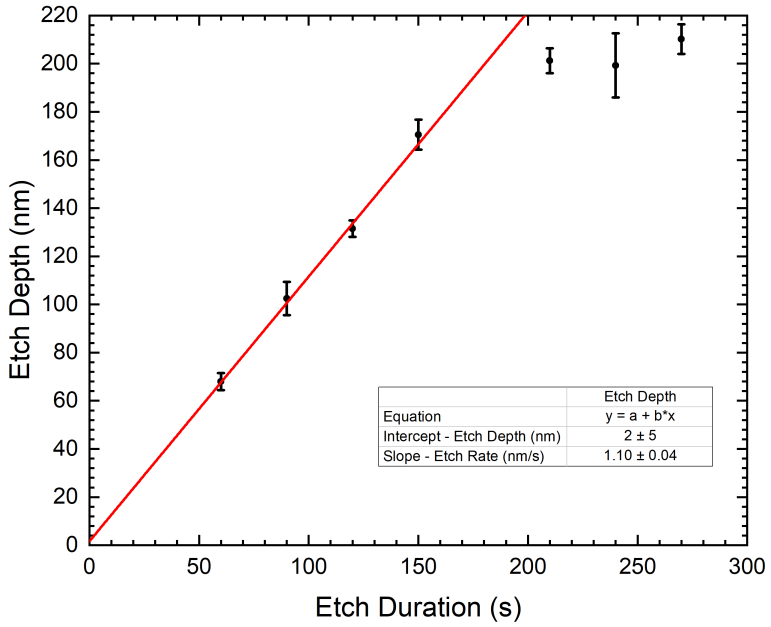

Figure 6.7: RIE etch rate calibration for Si_3N_4 etched using CHF_3 chemistry. The saturation in etch depth corresponds to a complete etch of the ~200 nm Si_3N_4 layer.

pre-calibrated etch rates and etch times to ensure that the correct etch depth is achieved.

Each machine also has a different set of precursors which determines the selectivity of the etch to the desired material over the material underneath. The RIE system is equipped with a CHF_3 gas line which is suitable for selective etching of Si_3N_4 passivation layers over underlying GaAs. An example etch rate calibration in shown in Figure 6.7. The intercept of the etch depth at zero seconds is indicative of the etch characteristics during the plasma striking stage. A positive value indicates a high initial etch rate as the plasma strikes, a negative value corresponds to a period of slow or no etching as the plasma strikes and stabilises. In this instance, the intercept is zero within error indicating that there is no significant offset to the etch depth.

Halogen-based (Cl_2 and BCl_3) plasmas are widely used for etching in III-V processing [99]. The III-V semiconductor layers in this work exhibit variations in composition and inconsistent layer thickness from sample to sample. The variation in material composition affects the etch rate of each process. Coupled with inconsistent layer thickness, this means that a time-based termination of the etch is no longer applicable. The halogen-based precursors and in-situ etch-monitoring equipment are only available on the ICP in the Lancaster QTC cleanroom. For these reasons the ICP is preferentially used for etching of QR VCSEL semiconductor layers. The etching recipes used in this work are given in the appendix.

6.5 Rapid Thermal Annealing

This work is concerned with electrically-injected GaSb QR VCSELs. The metal contacts deposited on the semiconductor surface in this work do not form a good electrical contact

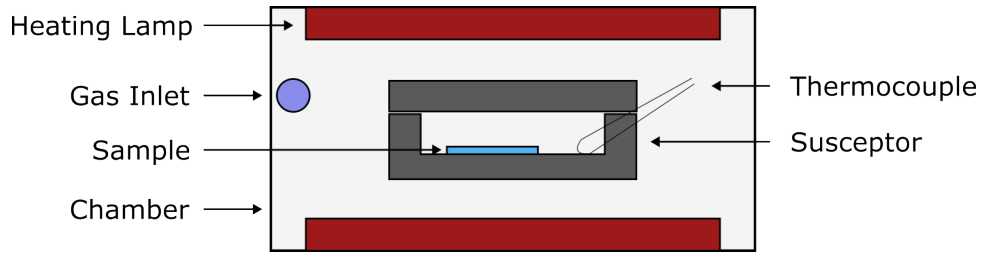

Figure 6.8: A schematic of the Allwin21 AccuThermo AW 610 rapid thermal annealing system. The sample is loaded into a SiC-coated graphite susceptor and heated using lamps. A thermocouple is located inside the susceptor, close to the sample to monitor the temperature. A gas inlet feeds in the process gases from a mass-flow controller.

without further processing. Details of the annealing conditions used to form good contacts in this work are discussed in chapter 7.

An Allwin21 AccuThermo AW 610 rapid thermal processing unit is used for all annealing processes in this work. Samples are loaded inside a SiC-coated graphite susceptor. The Allwin21 system uses a series of infrared lamps to heat the susceptor and continuously monitors the temperature using a thermocouple. Samples are enclosed within the susceptor and are assumed to be in thermal equilibrium with the susceptor. A mass-flow controller provides control over the flow rate and composition of process gases. A diagram of the system is shown in Figure 6.8. The annealing system has no active cooling so relies on radiative cooling and cooling from process gases flowing over the surface of the susceptor.

Run-to-run variability of the annealing process and non-uniform temperature across the sample can affect the annealed properties of contacts from device to device. To improve run-to-run reproducibility the system is preheated to the final annealing temperature and allowed to cool to 50 °C before loading the samples, this is to minimise variation in the start-temperature for each process. An additional pre-heating step is used to stabilise the susceptor at around 60 °C before ramping to the final annealing temperature to further increase the reproducibility. Despite the pre-heating steps, the annealing conditions are known to be inconsistent across the sample and from run to run. Inconsistencies are attributed to non-uniform thermal contact between the sample and susceptor and variations in thermocouple position relative to the sample.

6.6 In-House Mask Fabrication

This section covers the process flow for in-house mask fabrication. The Picomaster direct laserwriting system in the Lancaster QTC is fitted with a 405 nm laser which is incompatible with the exposure of AZ 40XT-11D photoresist. In addition, direct laser writing is significantly slower than mask aligning for large-area samples. In these cases, mask alignment is used for lithography processes. An in-house mask fabrication flow has been developed to reduce the time and expense associated with purchasing externally-made photomasks.

Existing chrome-plated quartz masks are stripped using Sigma Aldrich chrome-etchant. 100 nm of titanium is sputtered onto the quartz plate. S1813 photoresist is then spin-coated onto the surface and the desired pattern transferred into photoresist using direct laser writing. The titanium is etched by ICP until the reflectance monitored by laser

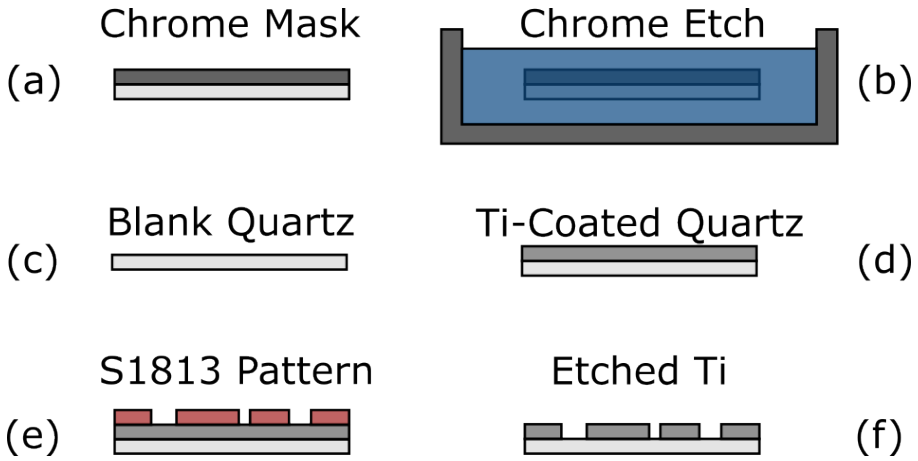

Figure 6.9: Diagram showing the in-house step-by-step fabrication of photolithography masks. Existing chrome layers (a) are wet-etched using chrome etchant (b+c), titanium is sputtered onto the bare quartz slide (d). S1813 is spun onto the surface and used to transfer the desired pattern (e) into the titanium using ICP dry etching (f).

reflectometry plateaus, indicating complete etching of the Ti layer. A step-by-step flow of the process is shown in Figure 6.9.

6.7 GaSb QR VCSEL Fabrication Flow

This section covers the fabrication of GaSb QR VCSELs at Lancaster University. The top-contact metals are deposited before any other processing to allow for deposition on a planar surface with minimal contaminant levels. Au/Ni/Au contacts are used to form a good ohmic-contact without the need for high doping levels which are not achieved during the growth of the QR VCSEL material in MBE. A discussion of contacts to p-type GaAs is given in chapter 7. During the fabrication of VCSELs, the contact annealing step is delayed until the end of the process to enable simultaneous annealing of the back-contact. Poor adhesion of Au/Ni/Au contacts to the semiconductor surface makes it difficult to form gold wirebonds when mounting devices. To aid bonding a separate bondpad that overlaps the contact is formed using sputtered Ti/Au.

The combined thickness of spin-coated S1813 and LOR3A is significantly less than the depth of etched mesas in the fabrication of QR VCSELs. This prevents adequate coverage of un-etched features during the spin-coating process so it is necessary to minimise the number of lithography steps after the mesa etch. For this reason, surface isolation using silicon nitride and the subsequent bondpad deposition is performed prior to the mesa etch. A narrow un-etched bridge connects the bondpad to the device mesa, as shown in Figure 6.10. The bridged-mesa design also maintains a planar bondpad track to the top of the device, avoiding complications with step coverage. A small cut-out opposite the bridge is incorporated to improve the lift-off yield for annular contacts. It is important to note that the bridged-mesa design results in a path for current to flow from the top contact to the area beneath the bondpad. This leakage path will enable electrical pumping of the active region outside of the cylindrical device mesa and may contribute to lower output powers, increased threshold currents and spontaneous-emission contributions from the region beneath the bondpad. Alternative process flows are discussed in section 11.3.5.

Controlled etching of the passivating layer is required to avoid etching of the VCSEL

semiconductor surface. In addition, the passivating layer should be electrically isolating and stable under atmospheric conditions. Reactive ion etching of silicon nitride using CHF_3 can be used to obtain a stable etch rate with an etch selectivity over GaAs of approximately 10:1 in this work. Hence, silicon nitride is selected for passivation of the GaSb QR VCSEL devices.

The Si_3N_4 in this work is deposited using PECVD. Dielectrics may also be deposited using RF sputtering. However, the control over layer thickness and conformity is inferior when compared to PECVD processes so is not considered for the passivation of QR VCSELs. The formation of bubbles and subsequent de-lamination of silicon nitride is sometimes observed following rapid thermal annealing processes at Lancaster. It is believed that the bubbles are caused by the rapid expansion of moisture adsorbed by the sample surface which escape through the silicon nitride. Typically, the stabilisation of the flow of gas precursors and the deposition process of silicon nitride begins shortly after the chamber is pumped down to its base pressure. To avoid issues with de-lamination, a dehydration step is incorporated into the silicon nitride deposition recipe. The sample stage is held at 110 °C with the chamber pumped to base pressure for in excess of one hour prior to introduction of precursors into the deposition chamber. Figure 6.11 shows a schematic of the key stages of fabrication in the VCSEL process flow.

The final process flow for QR VCSEL fabrication in this work is summarised as follows:

a) **Au/Ni/Au top contact** Au/Ni/Au (15 nm/30 nm/50 nm) is thermally-evaporated onto the sample surface, as discussed in chapter 7.

b) **Surface isolation** The GaAs surface is isolated using 200 nm of Si_3N_4 deposited by PECVD.

c) **Regain access to the VCSEL emission surface** A window is etched in Si_3N_4 over the top-surface of the VCSEL to regain access to the top contact and emission surface. The Si_3N_4 is etched using a CHF_3-based RIE process. The etch is masked using a single layer of S1813 photoresist.

d) **Bondpad deposition** Ti/Au (20 nm/180 nm) bondpads are deposited by RF and DC sputtering respectively. The pattern is defined by LOR3A+S1813 lift-off process.

e) **Mesa etching** Devices are defined by a mesa etch. The mesa etch begins with a CHF_3-based RIE etch to remove the Si_3N_4. A continuation of the mesa etch in DBR layers is then performed using $BCl_3/Cl_2/Ar$ plasma in ICP. Endpoint reflectance monitoring (section 8.2) is used to stop the etch in the uppermost GaAs layer in the lower DBR. The pattern is defined using an S1813 mask. Two layers of S1813 are used to ensure that there is sufficient resist thickness to protect the surface for the full duration of the etch processes.

f) **Device passivation** Si_3N_4 is deposited by PECVD to protect against environmental conditions and unintended short-circuits between bond wires and etched surfaces during device mounting.

g) **Regain access to bondpads and emission surface** A CHF_3-based RIE etch is used to etch through the Si_3N_4 over the bondpads and over the top-surface of the VCSEL to regain access for wirebonding and to reveal the emission surface. Here, the residual resist mask is left on the sample until after the next

step. This prevents contact between the top surface and mounting plate in the thermal evaporator, protecting against damage.

h) **Back contact deposition** A global AuGe/Ni/Au (100 nm/35 nm/100 nm) back-side contact is deposited using thermal evaporation.

i) **Annealing of contacts** Rapid thermal annealing is performed at 300 °C for 3 minutes under nitrogen atmosphere to form ohmic contacts (see chapter 7).

j) **Device mounting** Individual devices are cleaved from the sample and mounted onto TO-46 headers using conductive silver epoxy and bonded using a gold-ball wire-bonder.

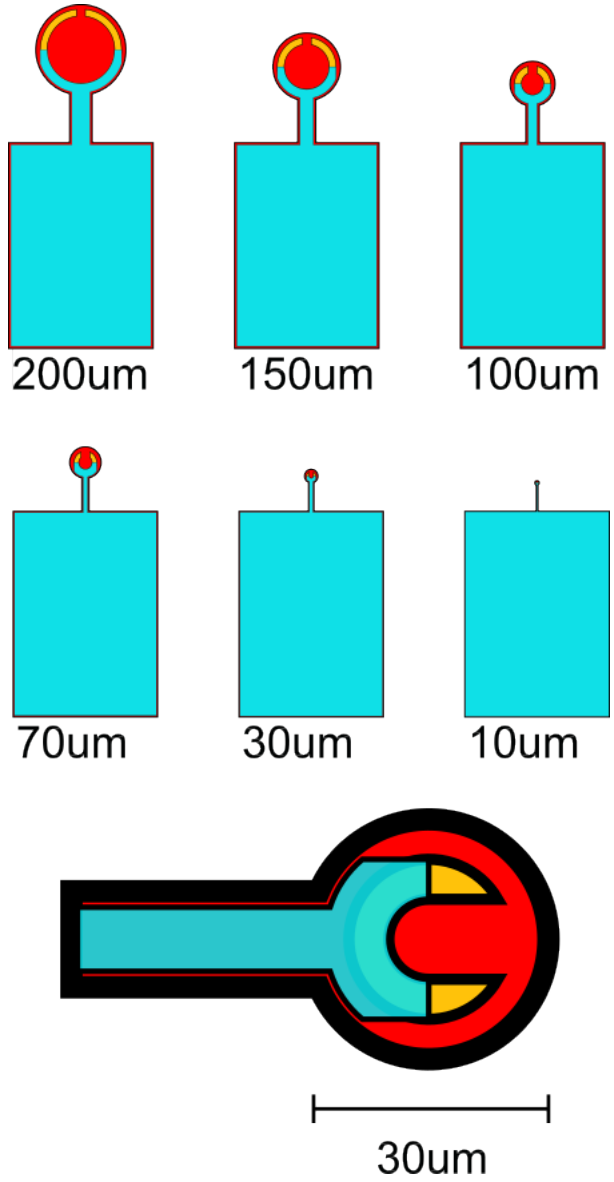

Figure 6.10: A simplified sketch of the final QR VCSEL device geometry from a top-down view. Yellow features represent the Au/Ni/Au contacts, cyan represents the position of the Ti/Au bondpad, the red region represents the masked area for the mesa definition. Regions outside of the red area are etched. An enlarged view of the 30 µm device is shown at the bottom.

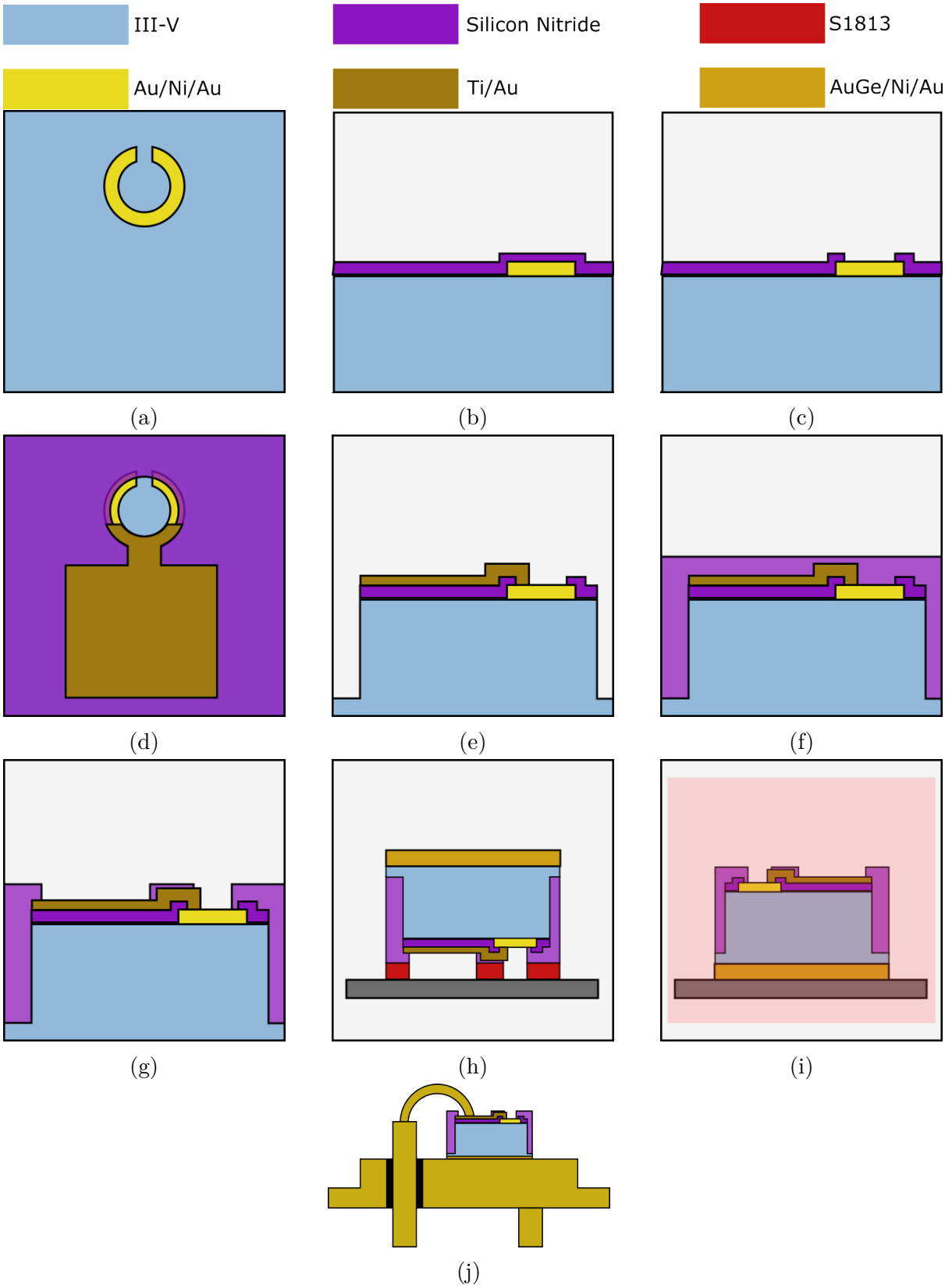

Figure 6.11: A sketch of the key steps in the fabrication flow of GaSb QR VCSEL devices including top contact deposition (a), surface passivation (b), re-access to the VCSEL surface (c), bondpad deposition (d), mesa etch (e), mesa passivation (f), re-access to bondpads and the VCSEL surface (g), back contact deposition with photoresist to protect the top-surface (h), contact annealing (i), and device mounting (j).

Chapter 7

Ohmic-Contacts to p-Type GaAs

7.1 Declaration

This chapter is an adaptation of a paper submitted to the Institute of Physics Journal of Semiconductor Science and Technology which was accepted for publication [100]. The investigation was carried out in line with the interests of GaSb QR VCSEL research and co-authored by Professor Manus Hayne, Dr Samuel Jarvis and Elizabeth Bancroft.

7.2 Au/Ni/Au as a Contact for p-Type GaAs

GaAs has a multitude of applications including high-speed field-effect transistors [101, 102], solar cells [103] light-emitting diodes [104, 105, 106, 107, 108] and diode lasers [12], to name but a few. Device specifics aside, in any application it is desirable to minimise parasitic resistance at the semiconductor-contact interface, improving power efficiency and increasing switching speed. As a result, well-performing ohmic contacts will find an extensive range of applications ranging from fundamental materials research through to finalised device production. Variations of Ti/Au metallisation are a common choice for current injection contacts in III-V semiconductor technology. However, in the case of p-type GaAs this results in an undesirable Schottky barrier at the metal-semiconductor interface [109], as seen in Figure 7.1.

There have been numerous studies of contacts to n-type GaAs, a historical review of which was provided by Baca et al. [110]. In contrast, and despite the fact that semiconductor devices invariably require both n-type and p-type contacts, there are relatively few studies of the formation of ohmic contacts to p-GaAs. These have been thoroughly reviewed by Lin et al. [111], and the interested reader is referred to their work for detailed information. Existing schemes used to form ohmic contacts to p-type GaAs include Pt-based contacts deposited on extremely highly doped GaAs ($10 \times 10^{20}\,\mathrm{cm}^{-3}$), and alloyed Zn-based contacts [111, 112, 113, 114]. Various approaches have been taken, including the addition of an epitaxially-grown doped-InAs contact layer [115]. In a study of Ti/Pt/Au contacts to p-type GaAs [111], a low specific contact resistance was obtained using ultra-highly-carbon-doped contact layers and multi-layer Si/Ni(Mg) depositions with thermal annealing steps for extended durations [116, 117], but such complex fabrication flows may not be practical, applicable or desirable in many cases. As a result, Ti/Pt/Au remains a popular choice for many p-GaAs contacts [111]. However, platinum is expensive and requires evaporation temperatures that may exceed those reasonable in resistive heating systems [94], so is commonly deposited using e-beam evaporation. Zn-based contacts have exhibited low specific contact resistance [114, 118], but suppliers warn that thermal evaporation of Zn can lead to contamination in the deposition chamber which may affect subsequent films [119]. A few works have also explored Ni-based contacts to p-GaAs [120]. In particular, Filippov, Luzyanin and Bogonosov recently investigated Ni films on p-GaAs produced using electrochemistry [121]. However, these studies fall short of providing a Ni-based p-type GaAs contact scheme that is suitable for general use. Here, we present an alternative metallisation consisting of Au and Ni for ohmic-contacts to p-type GaAs doped between $5 \times 10^{18}\,\mathrm{cm}^{-3}$ and $1 \times 10^{19}\,\mathrm{cm}^{-3}$, which are typical for growth by molecular beam epitaxy (MBE). The contacts may also work at lower doping concentrations and are presumed to work at higher doping concentrations, such as those available in growth by metal organic chemical vapour deposition. The Au/Ni/Au contacts [122] are formed without the need for Zn or Pt, making them suitable for use in research environments, in applications wishing to avoid Zn-contamination and for avoiding the need for e-beam

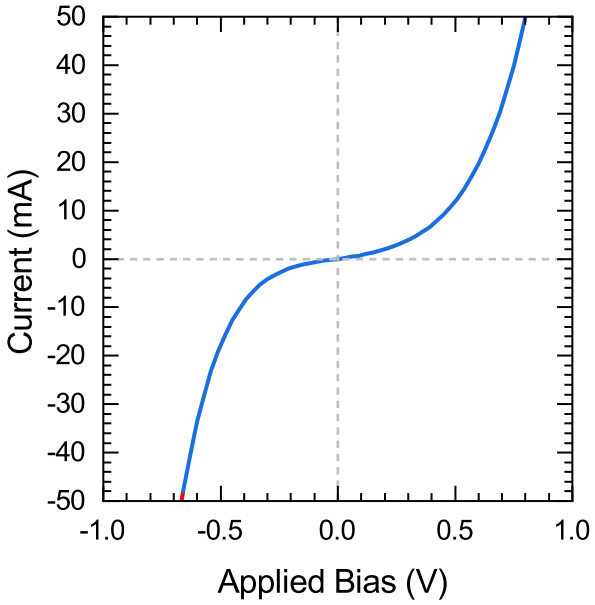

Figure 7.1: Current-voltage sweeps through adjacent top-top Ti/Au contacts on p-type GaAs show a non-linear dependence, indicative of the presence of Schottky barriers.

evaporation of Pt, which can cost 1,000 times more per kg than Ni [123]. It is worth noting that the Schottky barrier heights of contacts to semiconductors can be affected by the deposition technique used. In particular, it has been shown that sputtering may result in bombardment-induced hydrogen injection into the material and subsequent passivation of defects and dopant centres which, in turn, affect the nature of contacts [124]. The contacts in this work are deposited using thermal evaporation, a further study of sputtered Au/Ni/Au contacts is beyond the scope of this work. A WaferTech Zn-doped GaAs wafer with nominal doping range $5 \times 10^{18}\,\mathrm{cm}^{-3}$ - $5 \times 10^{19}\,\mathrm{cm}^{-3}$ was submerged in HCl:H2O (1:5) to remove surface oxides before being cleaned in acetone and isopropyl alcohol under ultrasonic agitation. A dehydration bake was performed at 170 °C before the wafer was patterned with bilayer LOR3A/S1813 photoresist to define rectangular contacts 100 µm by 200 µm in a transmission line measurement (TLM) bar arrangement with pads separated by 5 µm, 10 µm, 20 µm, 30 µm and 50 µm. A gentle O_2 plasma was used to remove residual resist from the contact-region of the wafer surface. Au/Ni/Au (15 nm/30 nm/50 nm) metallisation was performed in a Moorfield MiniLab thermal evaporator at a chamber pressure of $\sim 3 \times 10^{-6}$ mbar, followed by lift-off in Shipley Microposit Remover 1165 at 80 °C. The sample was then scribed and cleaved into individual pieces ready for annealing, such that each sample consisted of approximately 30 TLM bars. All samples were annealed in an Allwin21 AW610M rapid thermal processing (RTP) unit under nitrogen gas flow at atmospheric pressure. The authors see no reason why the process gas should be limited to nitrogen, and have seen promising results with the use of argon in work outside of the scope of this paper. Peak temperatures ranged from 250 °C up to 450 °C, with the duration of the hold at the peak temperature ranging from 30 seconds to 300 seconds. All samples had the same 60 s ramp time; however, hotter samples took longer to cool due to the lack of any active cooling mechanism. Shorter annealing times were found to be more susceptible to the inconsistent run-to-run performance of the annealing process during use of this system. Furthermore, it was observed that the initial heating ramp often overshot the target, whilst in other cases it undershot

taking up to 30 s longer than programmed to reach the target temperature. In addition to run-to-run variations, there were variations across samples in the same annealing run, which we attribute to non-uniform temperature distribution across the susceptor. Nevertheless, despite these difficulties ohmic contacts were achieved with orders of magnitude reduction in contact resistance compared to Ti/Au metallisation. Indeed, to enable comparison with existing contact schemes the same lithographic steps and lift-off procedure were performed on a fresh WaferTech Zn-doped GaAs wafer with Ti/Au and Au/Zn/Au metallisations, as described in the literature [118]. The two zinc-containing samples were independently annealed at 450 °C for 5 minutes and 350 °C for 3 minutes in the same RTP unit. A Keithley 2634b source measurement unit was used to perform current-voltage (IV) sweeps across adjacent top-top contacts for each sample, with a four-probe technique to eliminate effects of stray resistance in the probes and probe leads. Two methods were used to investigate the contact resistance of each sample. Initially, standard TLM-bar analysis was performed for a single TLM-bar arrangement on each sample, with the contact resistance extracted from a plot of resistance against pad spacing, as shown in Figure 7.2. In a number of cases this TLM-bar style analysis does not provide an accurate representation of the contact resistance due to large pad-to-pad variation in resistance which dominates the spacing-dependant resistance change. Thus, a second approach was employed in which an IV sweep was performed across the pad pair with a spacing corresponding to 50 µm on each of the thirty TLM bars. These measurements were used to give an indication of the pad-to-pad variation in resistance for a given sample. Due to the low resistance of the highly-doped wafer the assumptions were made that the resistance between pads with 50 µm spacing is a result of the contact resistance, and that the current penetrates the full length of the contact. The assumption of a large contribution to TLM resistance from the contact resistance is supported by the data in Figure 7.2, which shows that the pad-to-pad TLM resistance at 50 µm is fractionally more than the resistance for zero separation obtained from a linear fit to the data. Following these assumptions, the contact resistance for a pair of pads may also be represented by this so-called "two-pad" measurement.

Prior to annealing, the Au/Ni/Au contact scheme displays a Schottky characteristic. During the annealing process the contacts evolve from a Schottky contact to an ohmic contact and show greatly improved electrical performance, as seen in Figure 7.3. The marked improvement of these contacts over traditional Ti/Au contacts can be seen in comparisons of the differential resistance (Figure 7.4). Orders of magnitude improvement in contact resistance is visible across the range of applied biases, corresponding to the range required to drive approximately 40 mA through the Au/Ni/Au contact (Figure 7.4). Annealing of the Ti/Au contact scheme was not considered in this work as previous attempts at annealing the contact in-house did not show ohmic behaviour.

A clear trend in contact resistance was not evident within the range of annealing parameters investigated (Figure 7.5), but it was observed that annealing for too long, or with a temperature that is too high, can result in breakdown of the contacts, visible under an optical microscope (Figure 7.6). However, except for one anomalous two-minute anneal, the lowest contact resistances of $(0.09 \pm 0.02)\,\Omega$ were obtained for a temperature of 350 °C at every time interval (Figure 7.7), corresponding to specific contact resistances ρ_c, of just $(1.8 \pm 0.4) \times 10^{-5}\,\Omega\,\mathrm{cm}^2$. The lowest resistance obtained for the series of times and temperatures explored in this work was measured for annealing conditions of 350 °C for 60 seconds giving ρ_c of $(2.0 \pm 0.2) \times 10^{-5}\,\Omega\,\mathrm{cm}^2$ for the two-pad method and $(1.6 \pm 0.2) \times 10^{-5}\,\Omega\,\mathrm{cm}^2$ for the TLM analysis. The standard Au/Zn/Au process annealed

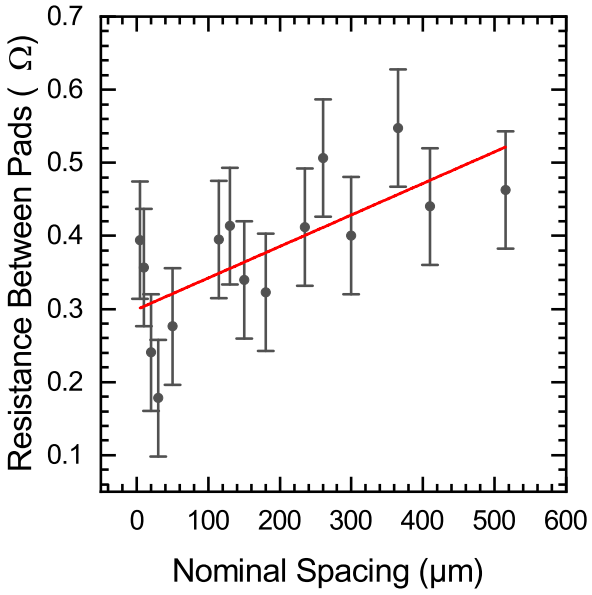

Figure 7.2: TLM-bar analysis for Au/Ni/Au contacts annealed at 450 °C for 60 s. A linear fit to resistance as a function of pad spacing allows extraction of twice the contact resistance for zero pad spacing, giving contact resistance of $(0.30 \pm 0.03)\,\Omega$ and specific contact resistance of $(6.0 \pm 0.6) \times 10^{-5}\,\Omega\,\mathrm{cm}^2$.

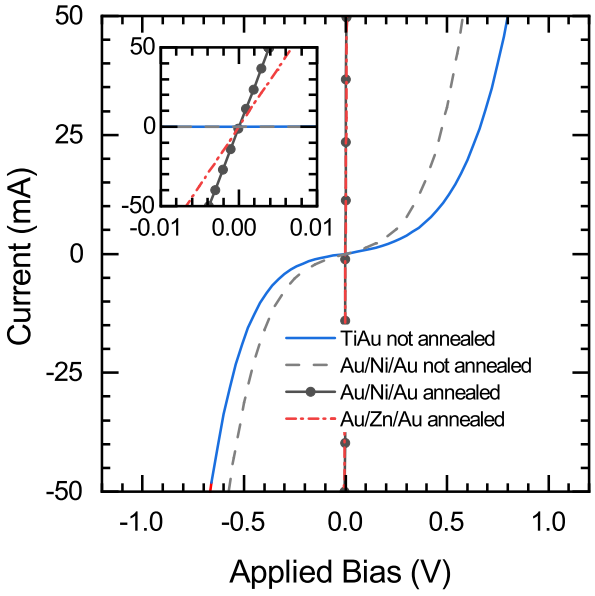

Figure 7.3: Current-voltage sweeps through adjacent top-top contacts show the presence of a Schottky-barrier in Ti/Au contacts (not annealed) on p-type GaAs. Au/Ni/Au contacts also demonstrate this non-ohmic behaviour prior to annealing. In comparison, annealed contacts of Au/Ni/Au (350 °C for 1 minute) and Au/Zn/Au (350 °C for 3 minutes) both show significantly lower resistance and an ohmic nature.

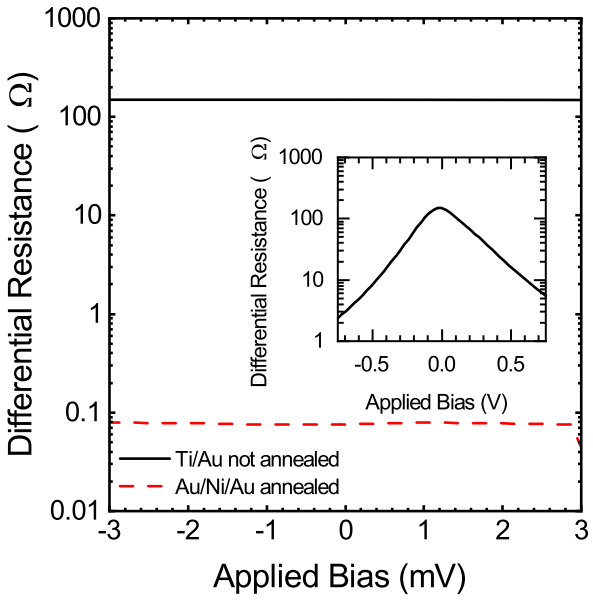

Figure 7.4: A comparison of differential resistance for Ti/Au and annealed Au/Ni/Au contacts in the range of −3 mV to 3 mV shows orders of magnitude difference in the contact schemes. The extended range for differential resistance of Ti/Au contacts is shown on the inset, remaining more than an order of magnitude higher resistance throughout the measured range.

at 350 °C for 3 minutes yields a ρ_c of $(1.4 \pm 0.1) \times 10^{-5}\,\Omega\,\mathrm{cm}^2$ using the two-pad method, indicating that the Ni-based contact is of the same quality as the Zn contact for a similar process and equivalent substrate material in the same fabrication environment.

To investigate the origin of pad-to-pad contact variation, X-ray photoelectron spectroscopy (XPS) imaging (section 4.7) was performed in conjunction with ion-beam milling, enabling examination of the depth-profile composition and morphology of the contacts. XPS was performed using a Kratos Analytical AXIS Supra spectrometer with monochromatic Al K_α 1486.7 eV X-ray source, operating at 15 kV, 15 mA, and equipped with an electron gun for charge neutralization [125]. XPS images were acquired using a spherical mirror analyser, which maintains the photoelectron's lateral distribution as it propagates through the analyser [126, 63]. Sample milling was carried out using an in-situ Kratos Minibeam 6 Gas Cluster Ion Source (GCIS) in 5 kV monotonic mode raster scanned across 4 mm × 4 mm regions. A spot size of 110 µm located in the centre of the raster scanned region was used for XPS measurements between milling steps, and a rotating sample stage used to ensure even milling across the sample [127]. Measurements were carried out at vacuum pressures better than 5×10^{-10} mbar. A pass energy of 80 eV was used for all spectra to maximize the count rate whilst ensuring good energy resolution. All spectra were analysed using CASAXPS (Casa Software Ltd, UK). In these experiments, images were collected in the Au-4f region and are shown in Figure 7.8. The sample with the lowest contact resistance (annealed at 350 °C for 1 minute) was milled in 20 nm increments between images. XPS imaging indicates that the gold diffuses into the semiconductor to a depth of (80 ± 10) nm. The Au-4f signal of the far-left contact in Figure 7.8 persists longer in the milling sequence, to a depth of (160 ± 10) nm. This is evidence of non-uniformity in the fabrication of neighbouring contacts, as discussed earlier.

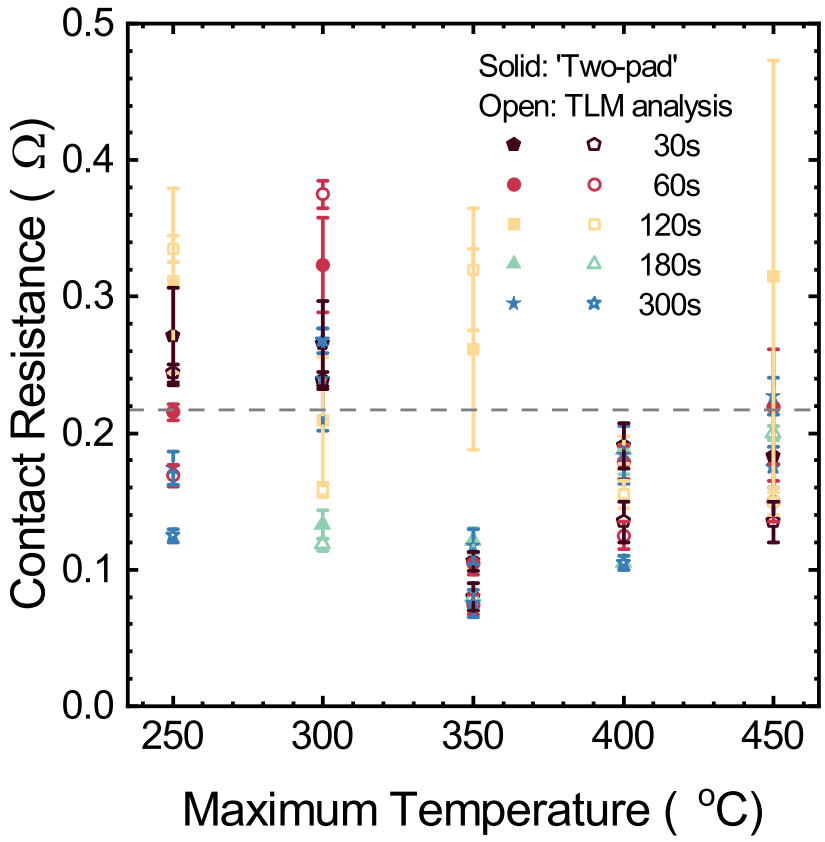

Figure 7.5: Contact resistance for 100 µm by 200 µm contacts on p-doped GaAs at various annealing temperatures for samples spending a nominal time at the stated maximum temperature. It should be noted that the nominal duration is the time spent at the set temperature. Due to slow radiative-cooling, hotter samples will experience a longer time at elevated temperatures and may therefore undergo further annealing. For short annealing times this will be a more significant contribution to annealing time.

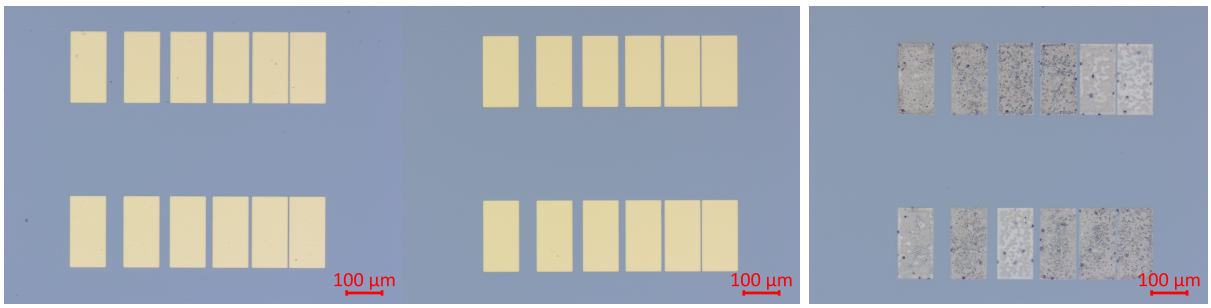

(a) (b) (c)

Figure 7.6: Thermal annealing can have a visible effect on the morphology of Au/Ni/Au contacts. (a) An unannealed sample as a reference. (b) A sample annealed at 300 °C for 3 minutes demonstrating little change in morphology. A subtle change in the gold tone may be visible for annealed samples. (c) A sample annealed at 450 °C for 5 minutes demonstrates visible degradation of the contacts. The gold-colour has completely disappeared, likely due to diffusion of the gold into the semiconductor material below.

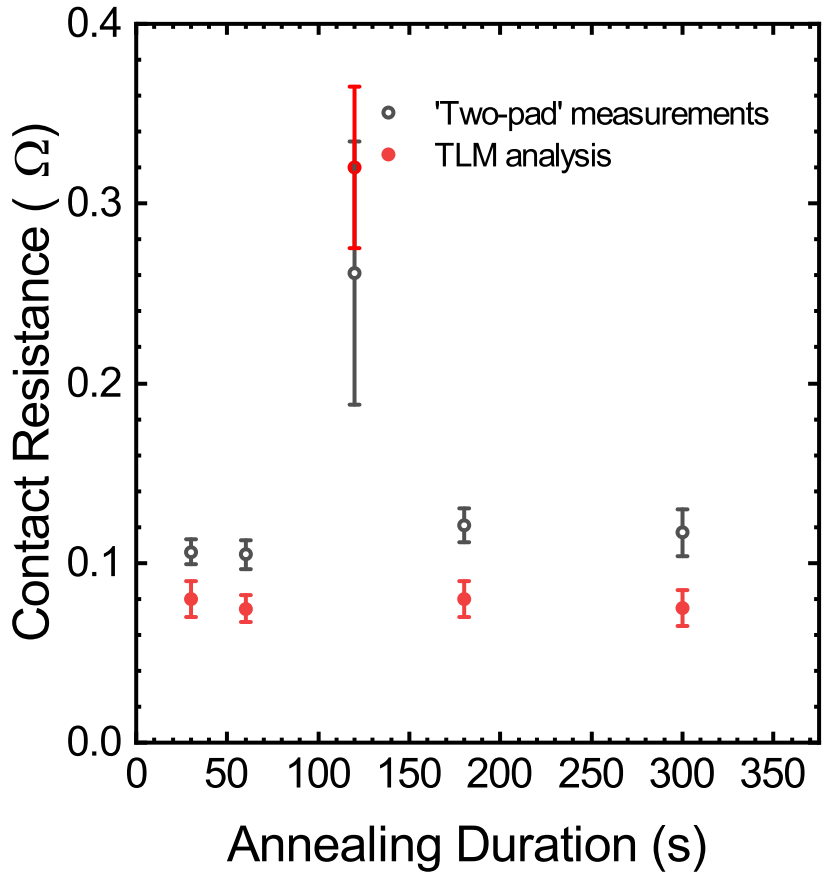

Figure 7.7: Contact resistance for 100 µm by 200 µm Au/Ni/Au contacts annealed at 350 °C show a consistently low contact resistance of just ∼0.1 Ω irrespective of annealing duration, except for the anomalous data at 120 s.

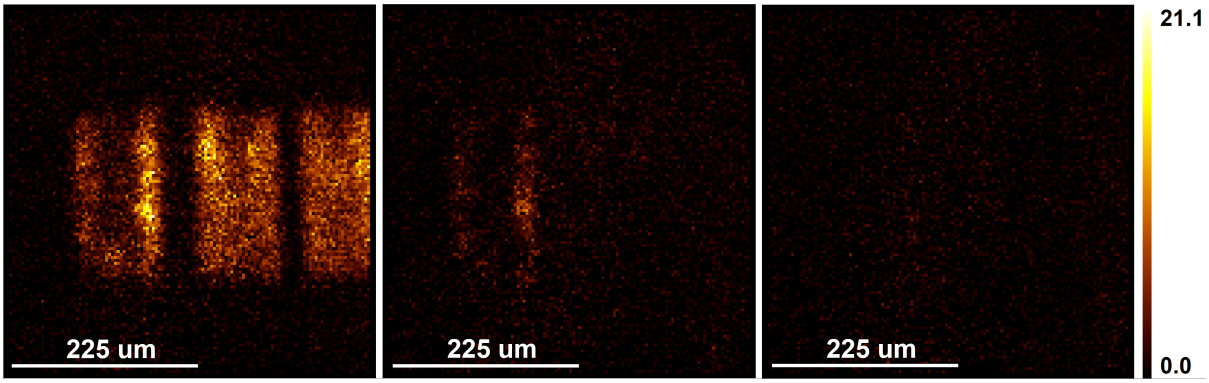

Figure 7.8: X-ray photo-electron spectroscopy images of annealed (350 °C for 1 minute) Au/Ni/Au contacts on p-type GaAs showing the Au-4f peak for the unetched sample (left) and following milling to depths of (80 ± 10) nm (centre) and (160 ± 10) nm (right). The scale represents the count rate (arbitrary units) detected by a pixel for the Au-4f peak. The images indicate removal of most of the gold by (80 ± 10) nm and residual gold from the final contact by (160 ± 10) nm.

In conclusion, we have introduced an alternative contact scheme for p-type GaAs, which is known for its prevalence to form Schottky barriers. Rapid thermal annealing of evaporated Au/Ni/Au (15 nm/30 nm/50 nm) was shown to produce ohmic contacts to p-type GaAs with specific contact resistance of $(1.6 \pm 0.2) \times 10^{-5}\,\Omega\,\mathrm{cm}^2$. A slightly higher specific contact resistance of $(2.0 \pm 0.2) \times 10^{-5}\,\Omega\,\mathrm{cm}^2$ was obtained for a simpler measurement using pairs of closely spaced pads. There was no clear trend in contact resistance with annealing duration and temperature within the precision and accuracy of the annealing equipment used, but the lowest contact resistances were achieved for an annealing temperature of 350 °C, with four out of five yielding a specific contact resistance of $(1.8 \pm 0.4) \times 10^{-5}\,\Omega\,\mathrm{cm}^2$. These values are all orders of magnitude lower than for Ti/Au contacts, and comparable to those obtained for Au/Zn/Au contacts when deposited on equivalent material in the same fabrication environment. The contacts presented in this work are compatible with doping concentrations achievable in MBE-grown material and therefore provide an excellent alternative to Pt and Zn-based contacts for many GaAs-based applications at all stages from fundamental materials research to device production. The mechanical stability was not studied for any of the contacts in this work; however, poor adhesion during attempts at wire-bonding samples with Au/Ni/Au contacts suggests that a separate bondpad consisting of Ti/Au or similar may be desirable where mechanical stability is required.

Chapter 8

Reflectance Monitoring for Growth and Etching

This chapter discusses the requirement for monitoring of growth and etching processes in the fabrication of VCSELs. As mentioned in section 5.1, VCSEL performance is sensitive to variations in the thickness of layers. In addition, layers grown systematically too thick or too thin result in a shift of the DBR stopband position, reduced quality of the stopband profile and a shift of the cavity wavelength. VCSEL wafers grown at Lancaster up to this point frequently show discrepancies up to 50 nm between the design and realised emission wavelengths due to variations in growth rates of GaAs and $Al_xGa_{1-x}As$ layers over time. A solution for in-situ growth monitoring and rate calibration has been developed, the results of which are presented in section 8.3 and may be used to produce VCSELs closer to the design in future growth runs.

Post-growth and during device fabrication, VCSEL mesa etches routinely target layers less than 100 nm thick that are buried several microns deep. The layers either side of the target often contain high concentrations of aluminium and oxidise upon contact with air. Therefore, accurate etching is required to hit the target layer and prevent oxidation of the etched surface. Typically, calibrated etch times are impractical in the research stage. The etching systems in the Lancaster QTC cleanroom are used to etch a variety of materials with a wide range of etching chemistries. Despite cleaning and conditioning processes being performed prior-to and post-etching, some variation in etch rates in this environment is unavoidable. In addition, wafer-to-wafer structure changes result in compositional and thickness changes for layers which would require re-calibration of etch rates each time a new structure is grown. To avoid the need for etch rate calibrations this work makes use of etch monitoring which is presented in section 8.2

The principles behind reflectance monitoring of growth processes are discussed in section 8.1. Since the principles are equivalent for growth and etching, one effectively being the reverse of the other, the discussion of etch monitoring is omitted for clarity.

8.1 Principles of In-Situ Reflectance Monitoring for Molecular Beam Epitaxy and Inductively-Coupled Plasma Etching

The growth of multi-layer semiconductor structures produces distinct, characteristic reflectance traces as a function of the growth thickness. These traces can be monitored using in-situ reflectance techniques and improve the accuracy of growths through the use of real-time tracking of the growth-thickness.

Since the wavelengths used by reflectance monitoring lasers currently in use at Lancaster (650 nm and 670 nm) are above the band gap energy of the GaAs substrates used in this work, light reaching the substrate is heavily absorbed. As a result, the back-surface of the substrate does not produce coherent reflections and the substrate can be treated as infinite, which simplifies the simulation problem dramatically. A suitable approximation for the TMM model may be made for normal-incidence reflectance of samples with an infinitely thick substrate as the final layer in the simulation. From this the characteristic models of reflectance as a function of growth thickness can be simulated as material is added.

Software implementing the TMM method to model the reflectance traces was written in-house at Lancaster University using the C programming language by Dr Tom Wilson [60]. The TMM method (section 2.1) is used recursively to simulate the re-

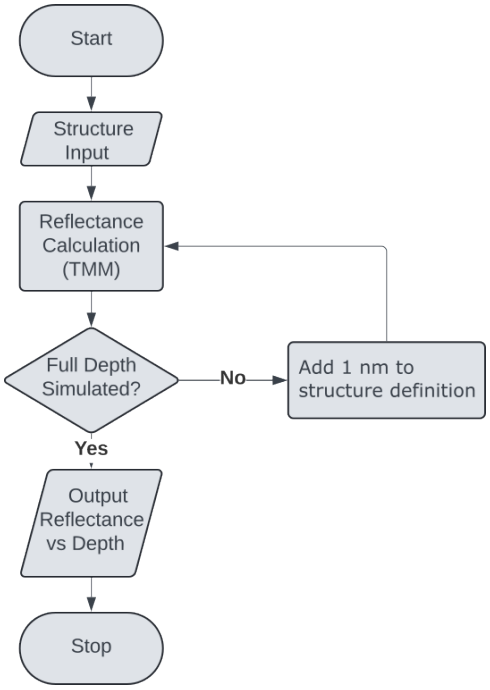

(a)

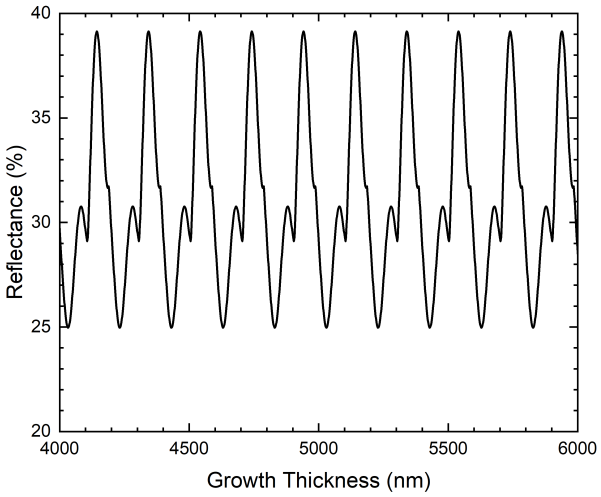

(b)

Figure 8.1: a) A flowchart representing the logic behind simulations of in-situ growth monitoring. b) A section of simulated reflectance as a function of growth thickness for a stepped-interface DBR (section 9.1) in a VCSEL sample with $\lambda/2$ cavity grown by MBE and monitored by a 650 nm laser.

flectance of the full device structure with incremental growth of 1 nm between simulations, a flow diagram describing the simulation is shown in Figure 8.1a. It is important to consider the temperature of the material under growth conditions, as this has a considerable impact on refractive index and consequently on the reflectance-depth trace. Existing work has investigated the influence of temperature on refractive index at growth temperatures in MOCVD [128]. Numerous studies have been conducted with the intention of determining accurate optical constants for the $Al_xGa_{1-x}As$ material system [128, 129, 130, 131, 132, 133]. This work uses optical constants calculated according to the work from Gonzalez et al. [134] that includes the temperature-dependence.

The reflectance spectra can be used either for endpoint detection, or calculation of growth rates. Endpoint detection is the simplest case. In this instance, the ideal point at which the growth should be terminated is identified on the trace. Section 8.3 provides a more detailed explanation of why endpoint monitoring is not used during growth in this work. In this instance the examples are given for etch monitoring as it is more applicable. An example endpoint for an etch process is shown by the blue circle in Figure 8.2. The reflectance trace would be monitored during the etch process and the etch terminated at the position indicated by the blue circle.

For the alternative method relying on rates it is necessary to observe the positions of distinctive features in the reflectance traces. These features typically take the form of turning points in the trace at reflectance maxima and minima. The features are separated by a known thickness, δ_x, and a time, δ_t, which is unique to each growth. Figure 8.3 provides a visual representation of features in a reflectance trace representative of epitaxial growth. Corresponding separations of features are shown for two examples

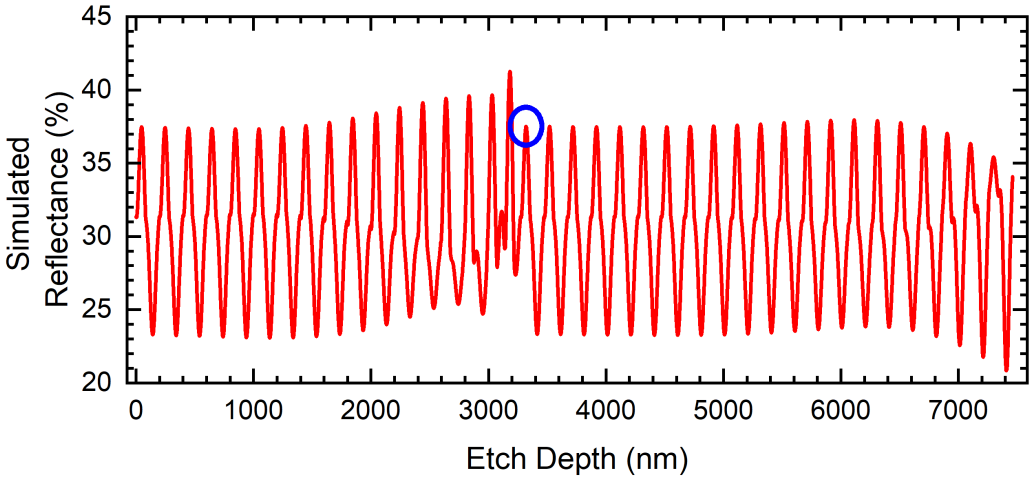

Figure 8.2: The simulated reflectance versus etch depth for a QR VCSEL sample with 21× DBR repeats in the lower DBR and 15× repeats in the upper DBR, both DBRs have step-graded interfaces (section 9.1). The blue circle indicates an example of a target endpoint for the minimum depth of a device mesa etch in the uppermost GaAs layer of the lower DBR.

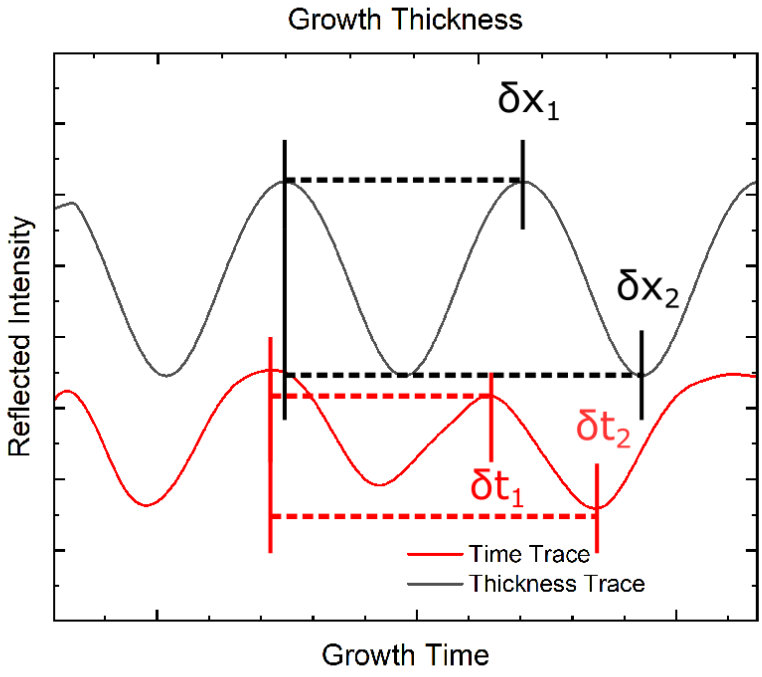

Figure 8.3: A sketch of reflectance as a function of growth time and growth thickness. Features are separated by a time, δt, and corresponding thickness of grown material, δx.

in thickness and in time.

For the case of a consistent growth rate. The growth rate, R, of a material may be calculated according to

$$R = \frac{\delta x_i}{\delta t_i}, \tag{8.1}$$

where δx_i is the thickness of material that is grown between features and δt_i is the time taken to grow that material. The total thickness of the layer, x_L, is then obtained according to

$$x_L = R \times t_L, \tag{8.2}$$

where t_L is the time spent growing the corresponding layer. The thickness of each layer can be obtained for a full structure by repeating the analysis for every layer.

8.2 In-Situ Monitoring for ICP

The ICP reflectance monitoring in this work uses a Horiba LEM laser interferometry system equipped with a 670 nm laser and is operated in the geometry shown in Figure 8.4.

The laser is visually aligned over the sample using a camera and once aligned does not change throughout the duration of the etch. The absence of sample rotation means that the reflectance can be monitored continuously and is limited by the maximum sampling rate of the monitoring system that can be achieved with sufficiently low measurement noise. Reflected intensity was typically reported at 1 Hz for etches in this work.

The mesa isolation etches in this work are tolerant to etch depth variation. The etch must reach into the lower DBR to appropriately isolate the active region of the devices. A specified GaAs layer within the lower DBR is chosen as an indicator, after which the etch may be terminated. In this work the etch targeted GaAs layers to avoid exposing large areas of Al-containing layers to the atmosphere, giving a window of approximately 100 nm within which the etch may be stopped. It may not be practical to stop in a precise layer for the processing of full wafers; however, there was no evidence that this was an issue for the etch uniformity of the approximately 10 mm by 10 mm chips used in this work. An example of the simulated and measured reflectance for the etch through a full GaSb QR VCSEL structure is shown in Figure 8.5. Measured at 670 nm, the peaks in reflectance coincide with the GaAs in the upper DBR layers, two large peaks within the cavity layers, then the GaAs in the lower DBR layers. A sampling frequency of 1 Hz corresponds to an increment of approximately 15 nm between samples for the etches performed in this work. Therefore, the acquisition rate for etch monitoring and tolerance to variations in etch depth means that an endpoint based approach is suitable for controlling the etch of VCSEL DBRs.

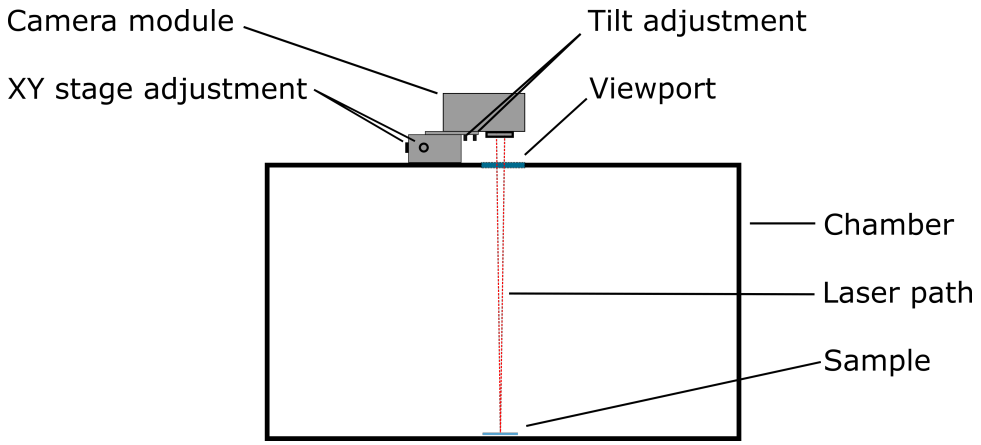

Figure 8.4: The ICP chamber has a top-mounted translational stage holding a module containing the alignment camera, laser and detector. Reflectance is monitored through the top viewport at close to normal incidence.

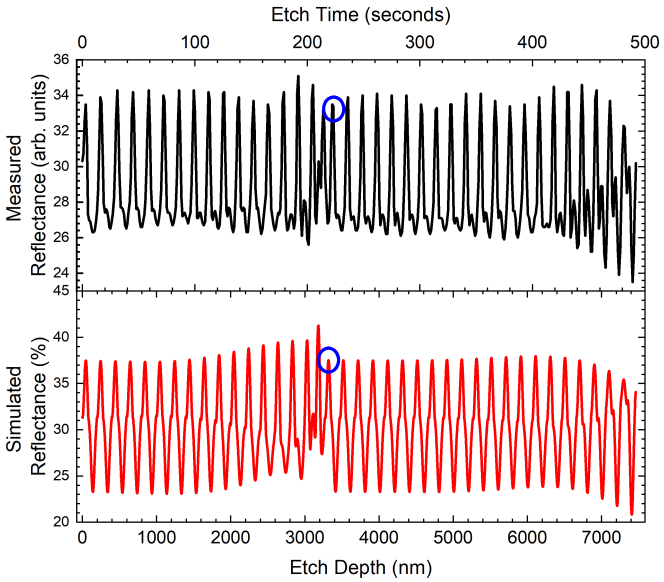

Figure 8.5: The simulated and measured reflectance versus etch depth for a QR VCSEL sample with 21× DBR repeats in the lower DBR and 15× repeats in the upper DBR, both DBRs have step-graded interfaces (section 9.1). The blue circles indicate the target endpoints for the device mesa etch on the respective traces. The simulations are conducted as a function of etch depth, experimental data are collected as a function of time.

8.3 In-Situ Monitoring for MBE

Monitoring of sample reflectance during MBE growth is considerably more complex than during ICP etch processes. MBE growth chambers pose a number of geometrical challenges. The growth chamber is typically large in the dimension which is normal to the plane of the wafer. Typically, the wafers in a research machine such as the Veeco system used in this work are mounted in a wafer holder and suspended in a claw. The heated viewport on the Veeco system prevents the buildup of material on the window during growth and allows for continuous monitoring which may be approximated as normal-incidence. A schematic of the growth-monitoring setup is shown in Figure 8.6. The reference output of an SR830 lock-in amplifier is used to drive a laser diode which is mounted below the heated viewport. The reflected light is incident upon a silicon photodetector with the signal measured by the lock-in amplifier and recorded by a data-logger.

The loading and mounting mechanisms of the chamber prevent the wafer from sitting perfectly flat and normal to the axis of rotation, this is exacerbated by material build-up on the claw over time. The long beam path and variations in substrate angle make alignment of the reflected spot and detector challenging. Samples are rotated during growth to improve uniformity across the wafer. This causes the position of the reflected spot to precess around a closed path when the sample rotation begins. It is typical for the reflected spot to precess along a circular path, traversing the detector once per rotation of the substrate (Figure 8.7). For reliable growth monitoring, the reflectance should be measured at a consistent point on each rotation. Consequently, the rotation speed of the sample dictates the maximum sampling rate of the reflectance. All samples grown in this work had a rotation speed of 10 rpm yielding an acquisition rate of one reflectance point per six seconds. The low acquisition rate of datapoints for MBE growth makes endpoint detection challenging so a rate-based approach is favoured.

A sample was designed to explore the applicability of the home-built reflectance-monitoring to calibration of growth rates in MBE. The growth rates of III-V materials in MBE are dictated by the group-III flux when grown with a V/III ratio greater than one. The composition of mixed group-III materials is simply determined by the relative flux of each group-III element. The total rate is the sum of the rates of the group-III materials. A sample consisting of a series of alternating GaAs and AlAs layers was designed for calibration of group-III growth-rates, the structure is shown in Table 8.1. The target thickness of each layer is determined by the target growth rate and the duration of the step during growth. For simplicity, the growth duration attributed to each step was set to an integer numbers of minutes and designed such that each layer had a thickness in the region of 300 nm.

A comparison of the simulated and measured reflectance during growth of the calibration sample is shown in Figure 8.8. The first ∼300 nm consist of a GaAs buffer grown on a GaAs substrate, the lack of refractive index contrast prevents any visible oscillations in reflected intensity. During the first ∼2000 seconds of the reflectance measurement the substrate temperature is ramped up and down to remove any oxide from the wafer and prepare the surface for growth. The oscillations in the corresponding region of Figure 8.8 are a result of reflected intensity changing during these periods of temperature change before ∼1000 seconds of GaAs buffer growth. The measured intensity of the reflected light differs from the simulation due to changes in substrate temperature, differing growth rates providing a relative stretching and compression of the oscillations, growth interrupts, and noise in the measurement due to instability in the laser power. The growth interrupts

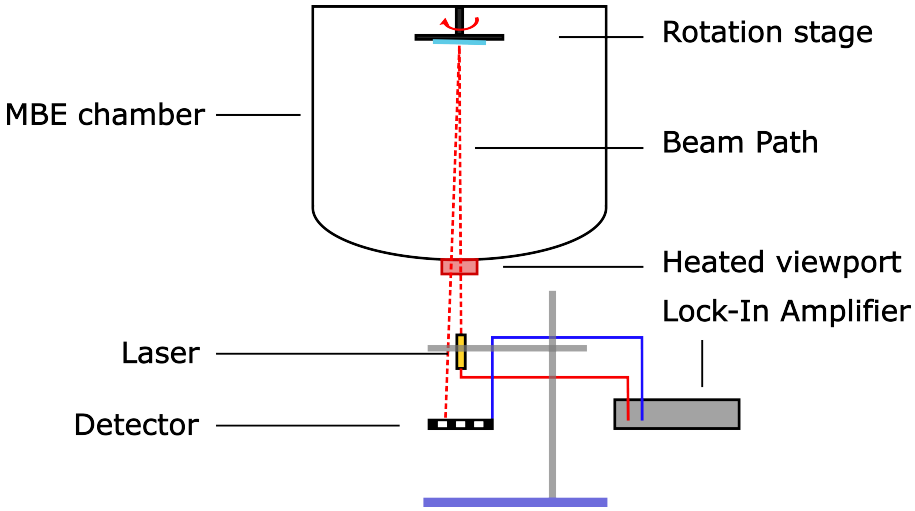

Figure 8.6: The Veeco GENxplor chamber is equipped with a heated viewport directly under the rotating sample stage. A laser diode and silicon photodetector are mounted below the viewport. The laser is clamped in a stand to allow for translational and rotational adjustment. The laser is driven by the reference output on an SR830 lock-in amplifier which measures the signal from the detector and provides an output which is recorded by a data-logger.

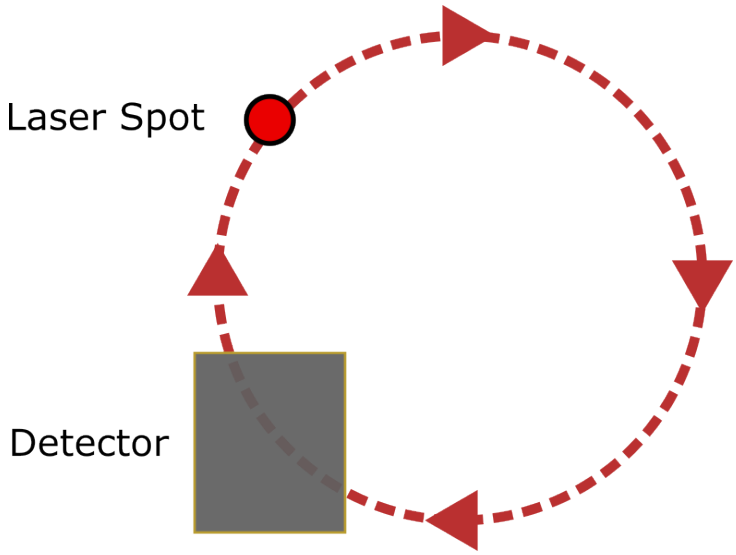

Figure 8.7: A simplistic representation of the path precessed by the reflected laser spot during reflectance monitoring in MBE for an angled substrate.

	Layer	Thickness (nm)		Target	Monitored
		Target	Achieved	Rate (ML/s)	Rate (ML/s)
1	AlAs - Lower	305	332	0.45	0.49±0.01
2	GaAs - Lower	306	386	0.30	0.38±0.01
3	AlAs - Middle	305	308	0.90	0.91±0.02
4	GaAs - Middle	321	407	0.60	0.76±0.01
5	AlAs - Upper	305	326	0.45	0.48±0.01
6	GaAs - Upper	305	393	1.00	1.29±0.01

Table 8.1: Growth-rate calibration layers in the order that they were grown for a demonstration of growth rate monitoring capabilities and proof-of-concept for pre-growth rate determination.

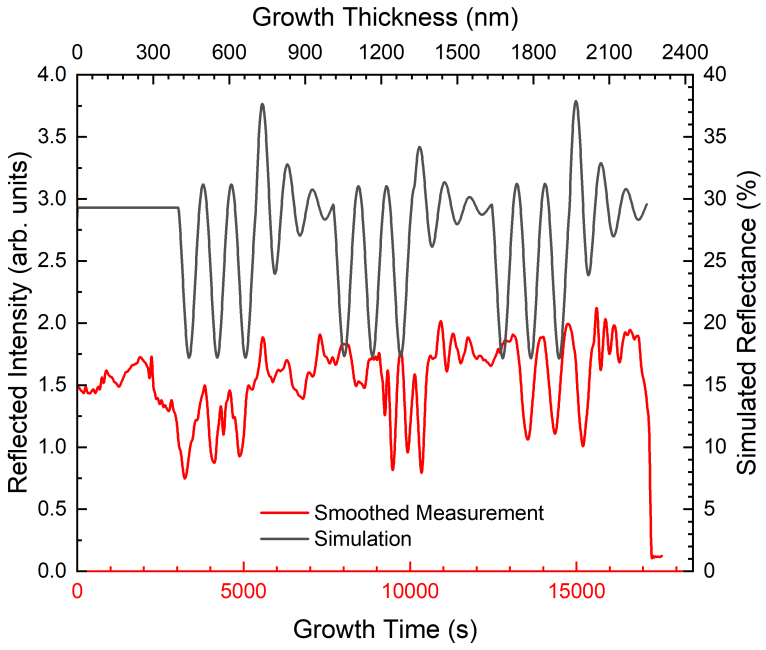

Figure 8.8: Simulated (black) and measured (red) reflectance at 650 nm for alternating AlAs/GaAs layers approximately 300 nm in thickness during MBE growth. The simulations are conducted as a function of growth thickness, experimental data are collected as a function of time. The first ∼300 nm consists of a GaAs buffer which produces no oscillations when grown on the GaAs substrate.

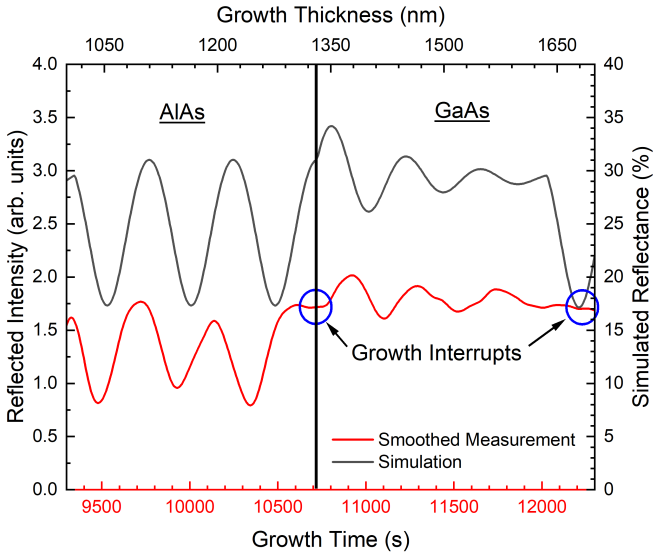

Figure 8.9: Simulated (black) and measured (red) reflectance at 650 nm versus growth thickness across a pair of AlAs and GaAs layers approximately 300 nm in thickness during MBE growth. The simulations are conducted as a function of growth thickness, experimental data are collected as a function of time.

after each of two consecutively-grown AlAs and GaAs layers are shown in Figure 8.9. The growth-rates obtained from the in-situ growth monitoring using equation 8.1 are shown in Table 8.1. The thickness for each layer was calculated by multiplying the growth rate by the length of time for which the corresponding MBE shutters were open, in accordance with equation 8.2 and will be presented later in this section.

To assess the accuracy of the reflectance monitoring setup the thickness of each layer must be verified using another technique. A TESCAN scanning electron microscope was used to measure the as-grown layer thickness. Initially, the sample was cleaved in atmospheric conditions. This resulted in a rough, non-uniform cleave and de-lamination (Figure 8.10) of the semiconductor layers which is likely due to oxidation of the aluminium-containing layers. Energy-dispersive X-ray spectroscopy (EDS) shows a clear reduction in arsenic in the aluminium-containing layers and a strong oxygen signal corresponding to oxidation of the aluminium layers 8.11. Oxidation of AlAs-containing layers and the uneven cleave prevents accurate measurement of semiconductor layer thickness.

The sample was polished using a gallium focussed-ion-beam to remove the influence of oxidation, and to provide a smooth surface for layer-thickness measurements. The resulting etch-pit is shown in Figure 8.12. The TESCAN microscope software corrects for the angle of the sample to provide an accurate scale along the polished cross-section of the material. Images of the polished layers are shown in Figure 8.13. The thickness of each layer is obtained by measuring the thickness of the corresponding region on the SEM images, the results of which will be presented later in this section.

It is interesting to investigate the extent to which the reflectance monitoring and SEM measurements are in agreement. It is known that group-III growth rates change each time the cells are heat cycled between growth campaigns (see Figure 8.14). Heat cycling introduces an offset in the growth rates which is approximately uniform across the calibrated temperature range, this is particularly apparent in Figure 8.14b. In com-

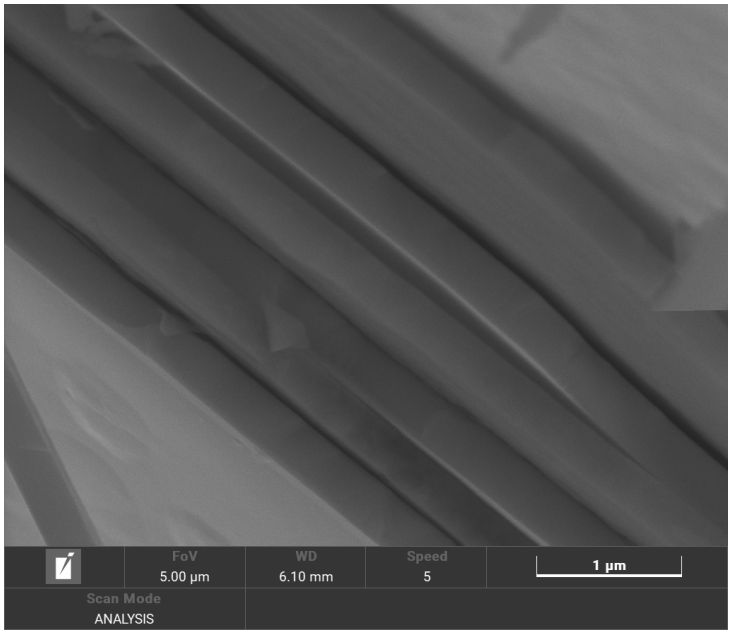

Figure 8.10: A scanning electron microscope image of alternating GaAs/AlAs layers shows layer separation and uneven depths of cleaved layers. The GaAs substrate is located to the upper-right corner of the image with the sample surface lower-left.

parison, the random deviation in growth rate caused by small temperature cycling during a single growth run causes relatively small changes in rate. From this, it is expected that the error in the growth rate should be broadly similar for each GaAs layer within the sample despite the different target growth rates. The error in the growth rate may be described by a growth rate error according to

$$\text{growth rate error} = \frac{\text{monitored rate - target rate}}{\text{target rate}} \times 100. \tag{8.3}$$

As shown in Figure 8.15 the reflectance monitoring indicates a consistent error in growth rate. In contrast, the SEM measurements show a clear change in growth rate error with depth in the sample but remains consistent within error. It seems coincidental that the growth rate error measured by SEM drops consistently with depth in the structure and may in fact be indicative of a geometric error in the FIB polishing and angle-corrected cross-section images.

Similarly, for the upper and lower AlAs layers (Figure 8.16) with nominally-identical growth rates, the reflectance monitoring shows identical growth rate deviation within error. In contrast, the values obtained using SEM are not in agreement. Since the growth rate is expected to be consistent for these layers and the reflectance monitoring supports this, it seems likely that the SEM imaging has resulted in an inaccurate thickness for this layer with the upper layer appearing thicker. The origin of this may be a combination of the uncertainty in finding the edge of layers due to lack of sharp-contrast in the SEM images, inaccuracies in the correction of angle for the polished surface, and distortion of the layer thickness by the SEM picture drifting during image capture. Further measurements using techniques such as TEM or BEXP+AFM would be required to gain a better understanding of the discrepancy between reflectance monitoring and SEM measured values for the upper AlAs layer.

A comparison of the growth thickness obtained from reflectance monitoring and SEM

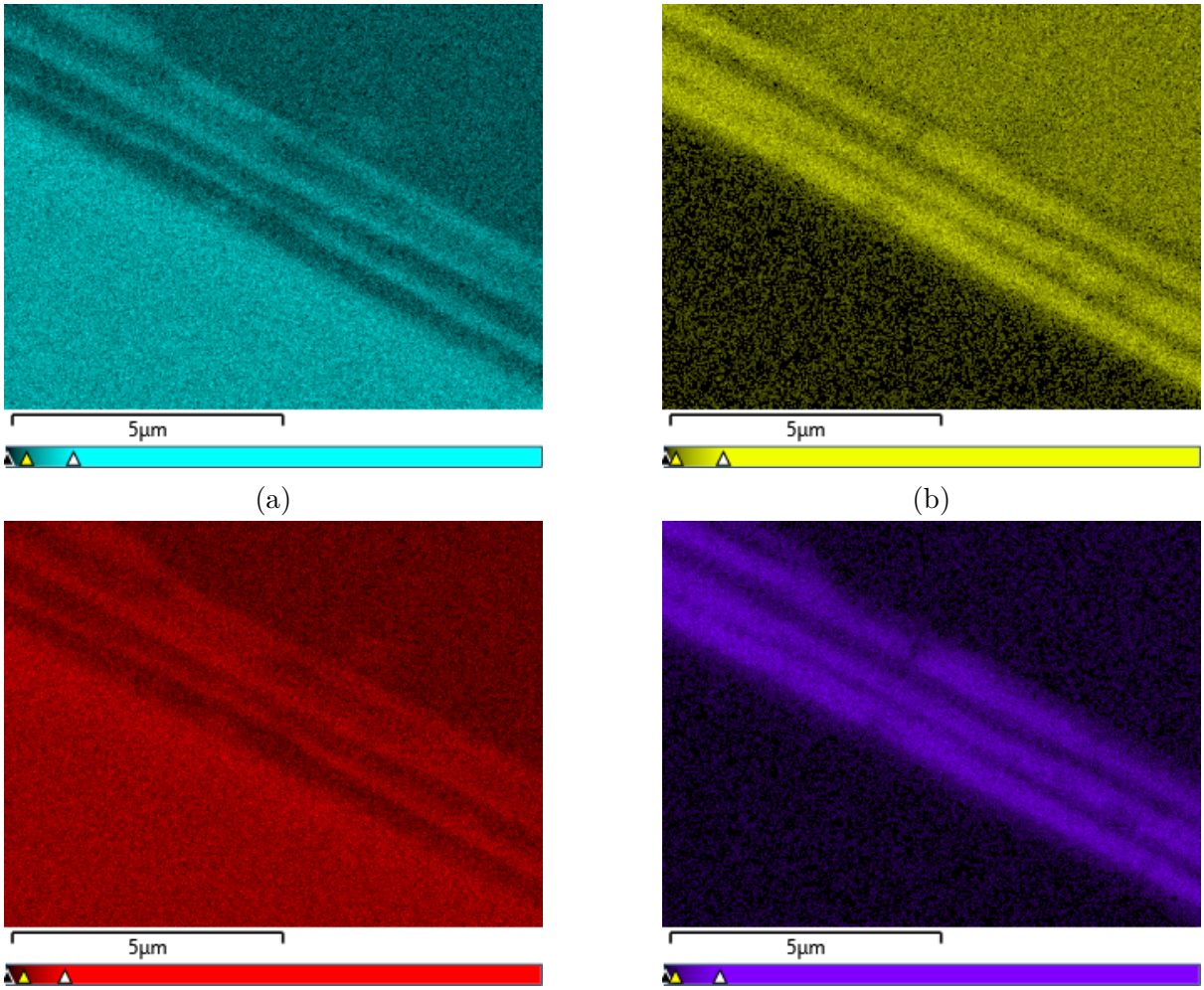

(a) (b)

(c) (d)

Figure 8.11: Energy dispersive X-ray spectroscopy images showing the position of the gallium (a), aluminium (b), arsenic (c), and oxygen (d) along the cleaved-face of a sample with alternating GaAs/AlAs layers. Coloured pixels correspond to the presence of a given element.

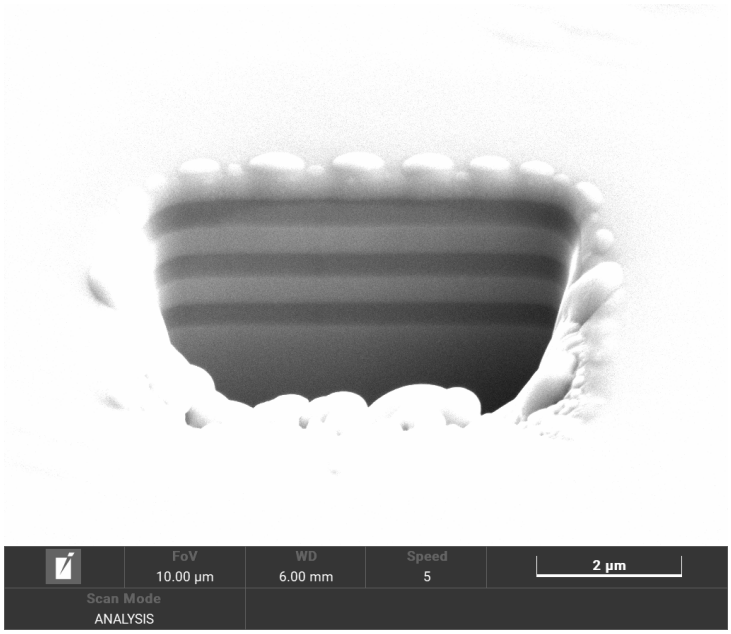

Figure 8.12: A high-contrast scanning electron microscope image of the etch pit formed by focussed ion beam polishing normal to the sample surface for a sample consisting of alternating GaAs/AlAs layers. AlAs layers appear darker on the image.

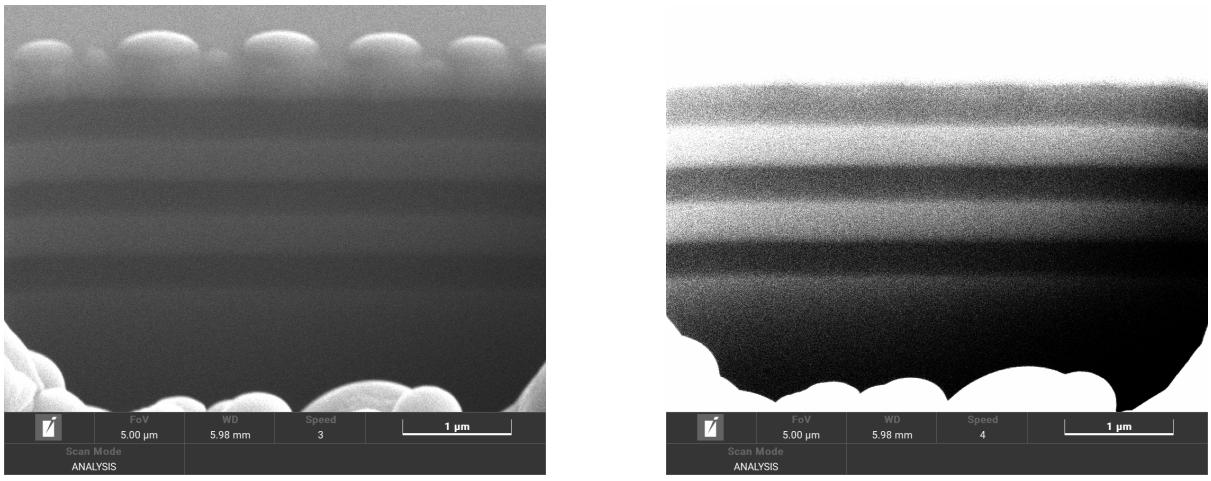

(a) (b)

Figure 8.13: Parallax-corrected SEM image of GaAs/AlAs layers polished using a focussed ion beam for layer thickness measurements (a) with boosted contrast (b). AlAs layers appear darker on the image.

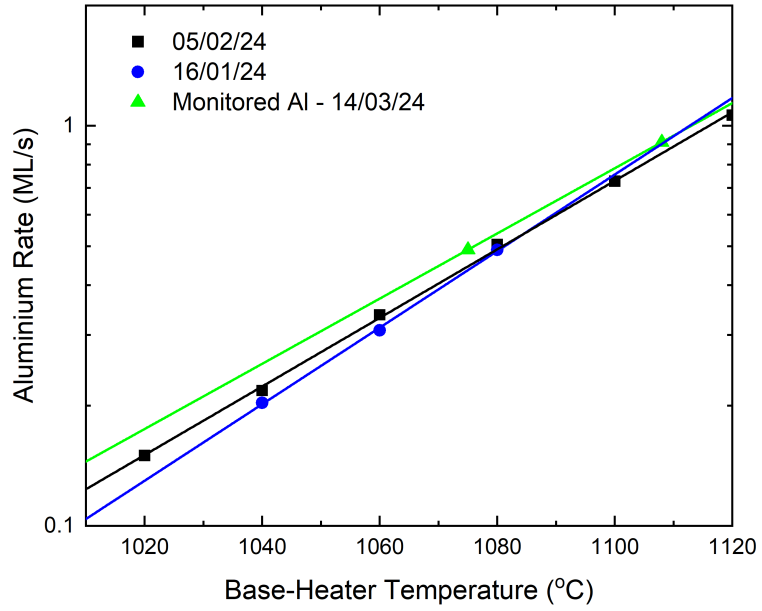

(a)

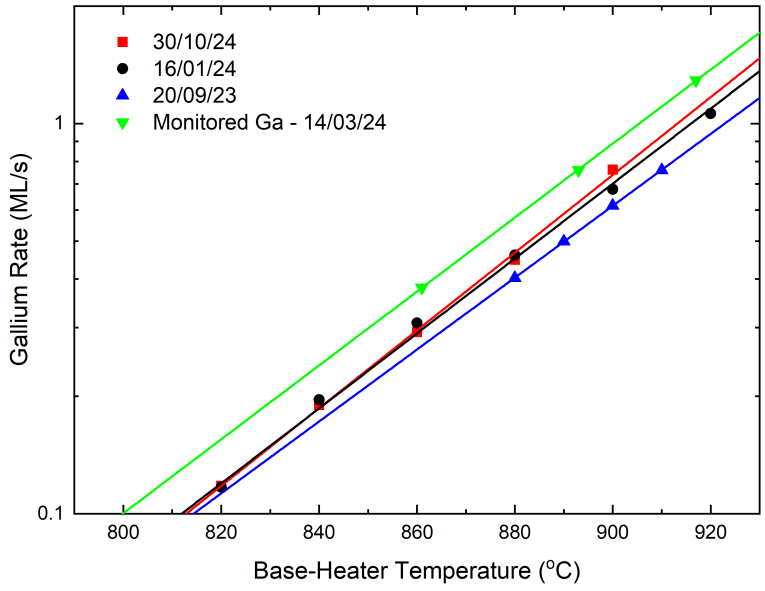

(b)

Figure 8.14: Temperature-rate calibrations for the aluminium (a) and gallium (b) cells measured using RHEED oscillations at each of the dates given in the legend. The rates obtained using reflectance monitoring are included for comparison.

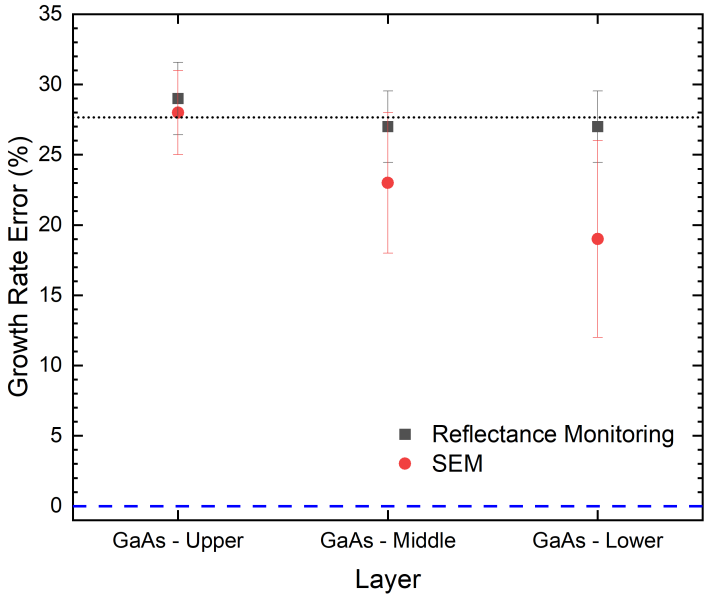

Figure 8.15: The percentage deviation of the calculated growth rate for GaAs layers from both reflectance monitoring and SEM, compared to the target. The black dotted line shows the mean growth rate error for the GaAs layers according to the reflectance monitoring setup. The blue dashed line is a visual aid and represents zero error.

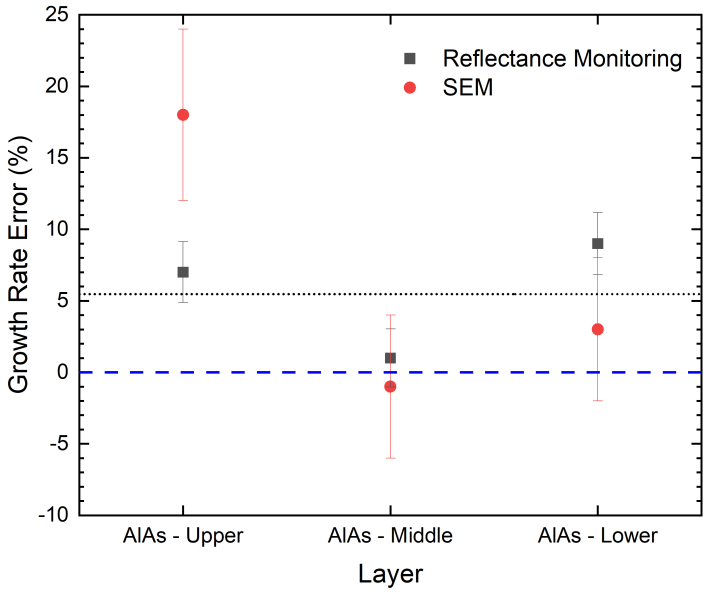

Figure 8.16: The percentage deviation of the calculated growth rate for AlAs layers from both reflectance monitoring and SEM, compared to the target. The black dotted line shows the mean growth rate error for the AlAs layers according to the reflectance monitoring setup. The blue dashed line is a visual aid and represents zero error

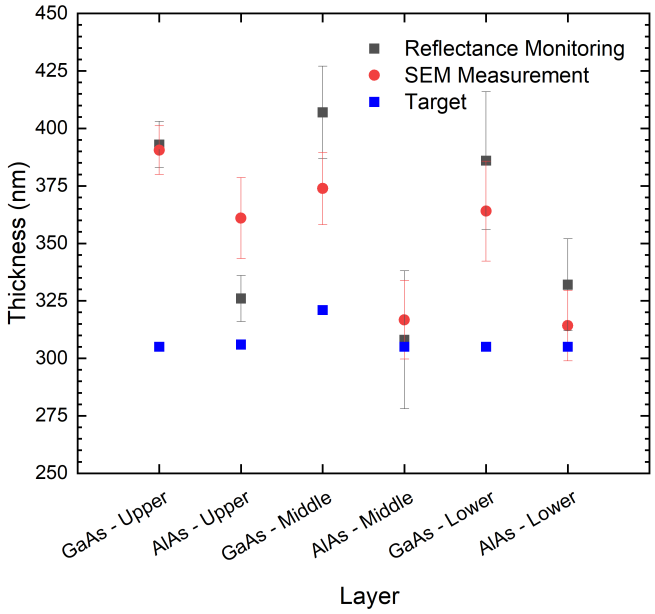

Figure 8.17: The target thickness for a series of GaAs and AlAs layers, the layer thicknesses obtained using reflectance monitoring and layer thickness measured by SEM.

imaging is shown in Figure 8.17. It is clear that the GaAs layers exhibit a larger offset from their target thickness than the AlAs layers, which is consistent with the deviation between the monitored growth rate and growth rate obtained by calibrations (Figure 8.14). With the exception of the upper AlAs layer the reflectance monitoring and SEM measurements agree within error. This result supports the accuracy of the growth monitoring system. It is evident that the thickness of each layer is noticeably larger than the target, and that the use of reflectance monitoring provides a better indication of growth rates than the latest group-III growth rate calibrations.

8.4 Summary of Reflectance Monitoring

This chapter was concerned with the tracking of semiconductor growth and etching using the measured-intensity of light reflected at normal-incidence to the wafer surface. The principles behind reflectance monitoring techniques were presented and the use of endpoint-detection for control over the depth of plasma etches was demonstrated. Next, a sample was designed and subsequently grown to explore the use of a home-built reflectance monitoring setup to determine the growth-rate of group-III elements in MBE. Focussed ion beam polishing and scanning electron microscopy were used to measure the thickness of each layer post-growth, and used to verify the findings of the results of reflectance monitoring. The results of layer thickness measurement and calculated thickness from the reflectance monitoring agreed within error, demonstrating the applicability of the home-built reflectance monitoring setup to group-III growth-rate determination.

Chapter 9

Distributed Bragg Reflectors

This section includes studies on the optical and electrical properties of DBRs. GaSb QR VCSELs are grown by molecular beam epitaxy so investigations into the interface design were conducted in an attempt to reduce their series resistance (section 9.1). In addition, the DBRs are designed to operate at telecoms-wavelengths and must be doped to achieve good electrical performance. A study into the optical effects of doping is presented in section 9.2. Finally, MOCVD grown DBRs provide insight into the performance of a new continuously-graded structure in section 9.3.

9.1 Reduced DBR Resistance using Tailored Interfaces

GaSb QR-VCSELs fabricated at Lancaster University are grown on a Veeco GENxplor MBE reactor and require longer-wavelength DBRs than typical GaAs/$Al_xGa_{1-x}As$ VCSELs, here they operate out to ∼1300 nm. As explained in section 2.4, the resistance of DBRs is largely influenced by the interfaces between neighbouring semiconductor layers. A large contrast in refractive index is preferable for good optical performance of the DBR but this is typically accompanied by inferior electrical performance due to larger barriers to electrical transport at the semiconductor interfaces. Figure 9.1 demonstrates how the barrier to transport in the valence band of a GaAs/$Al_xGa_{1-x}As$ DBR changes with increasing aluminium fraction from 30 % to 90 %. Industry standard DBRs at shorter wavelengths, 1100 nm and below, typically use a graded composition at the interface to reduce the series resistance of the DBRs. However, this is more complicated to realise in a reliable and reproducible manner on a research MBE system such as the Veeco GENxplor than on an industrial MOCVD reactor. An alternative is to perform discrete steps in composition at the semiconductor interface [135]. In this section four designs of DBRs compatible with MBE growth and operating at telecoms wavelengths will be investigated, all of the DBRs were p-doped with beryllium to a nominal doping concentration of $1 \times 10^{18}\,cm^{-3}$. The first consists of the textbook high-contrast DBR with alternating layers of GaAs/$Al_{0.9}Ga_{0.1}As$. The second consists of alternating layers of $Al_{0.6}Ga_{0.4}As$/GaAs, where the lower aluminium fraction in the $Al_xGa_{1-x}As$ material is used to reduce the barrier height at the interfaces. The third structure consists of a stepped-interface design, whereby high-contrast GaAs/$Al_{0.9}Ga_{0.1}As$ layers are separated by a thin, 15 nm $Al_{0.6}Ga_{0.4}As$ layer which should maintain much of the optical performance for the high-contrast structure, whilst reducing the interface barriers. The final design resembles the high contrast DBR, with a 40 period GaAs/AlAs digital alloy in place of the $Al_{0.9}Ga_{0.1}As$ layers. Figure 9.2 shows a *nextnano++* simulation of the energy level and probability distribution for the ground state in the gamma band of the digital-alloy within a single digital repeat. The simulation indicates the presence of energy states below the band edge that are accessible to electrons. Figure 9.3 shows the electron and hole dispersion curves for the digital alloy along the growth direction of the digital alloy and in the vicinity of the Gamma, X and L valleys (section 2.2). The simulation shows equivalence to the $Al_{0.9}Ga_{0.1}As$ bandgap at the same temperature, with the band gap associated with the X valley. Each structure was simulated in TFCalc and the number of DBR repeats adjusted to ensure a reflectance of 98% at 1300 nm (Figure 9.4). The number of repeats was reduced by one third of the designed mirror to reduce growth times, the resulting target structures for growth are represented in Table 9.1. The reduced number of repeats is expected to scale the resistance by an equal factor for each

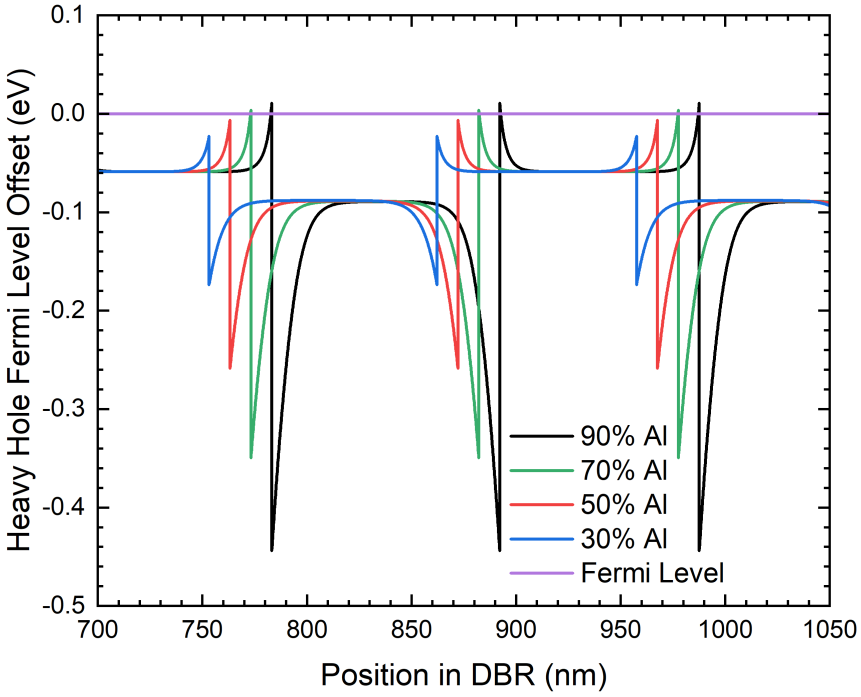

Figure 9.1: The heavy hole valence band offset relative to the hole Fermi level at a series of aluminium compositions from 30 % to 90 % for a p-doped (Be) GaAs/$Al_xGa_{1-x}As$ DBR with nominal doping density $1 \times 10^{18}\,\mathrm{cm}^{-3}$.

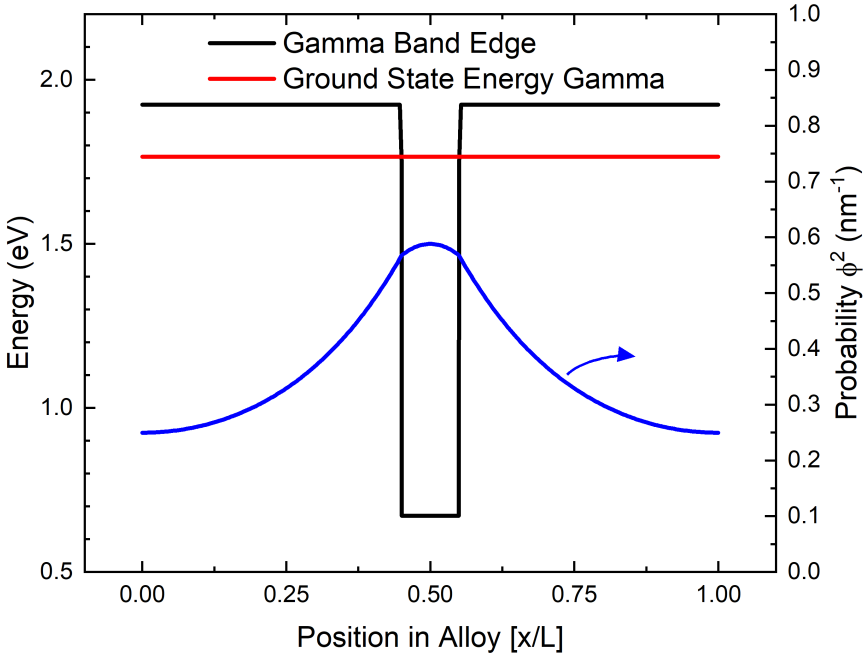

Figure 9.2: The conduction band and ground state energy at the gamma point are shown as a function of position, x, along a single repeat of an $Al_{0.9}Ga_{0.1}As$-equivalent GaAs/AlAs digital alloy of length L. The electron probability density is shown on the right-hand axis, as indicated by the blue arrow.

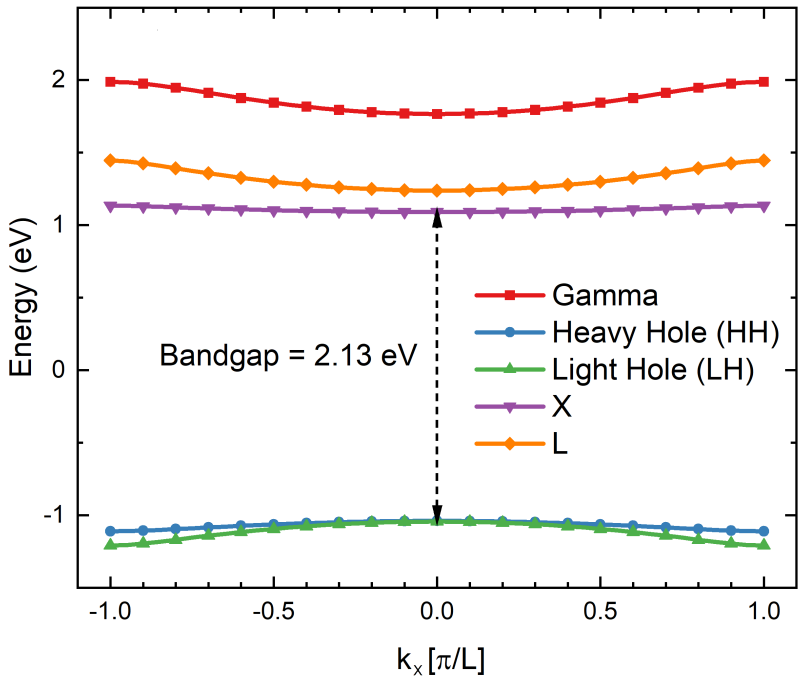

Figure 9.3: The band structure is shown for a single repeat of an $Al_{0.9}Ga_{0.1}As$-equivalent GaAs/AlAs digital alloy of length L. The lowest energy dispersion curve is shown along the growth axis for the conduction band in the vicinity of the Gamma, X and L valleys.

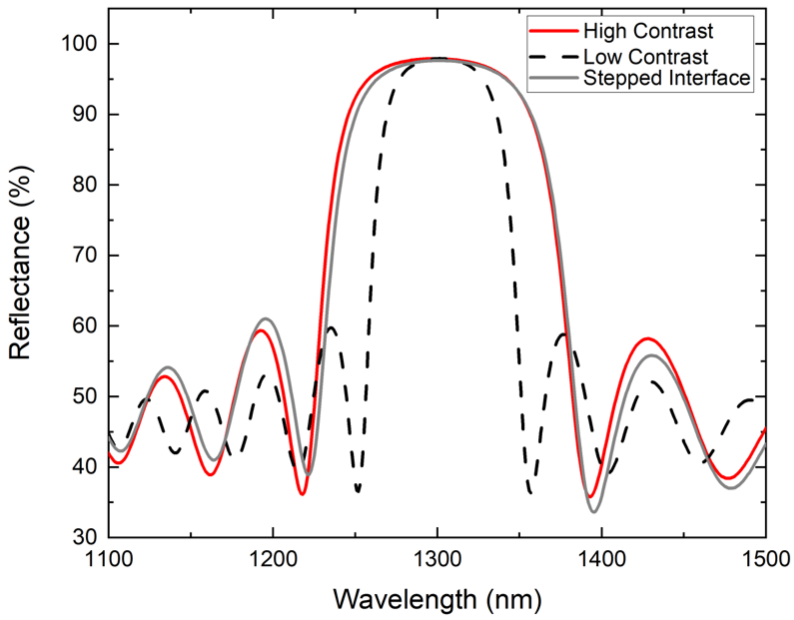

Figure 9.4: Simulated reflectance for high contrast ($GaAs/Al_{0.1}Ga_{0.9}As$), low contrast ($GaAs/Al_{0.6}Ga_{0.4}As$) and stepped interface DBRs with 15, 15 and 25 repeats respectively.

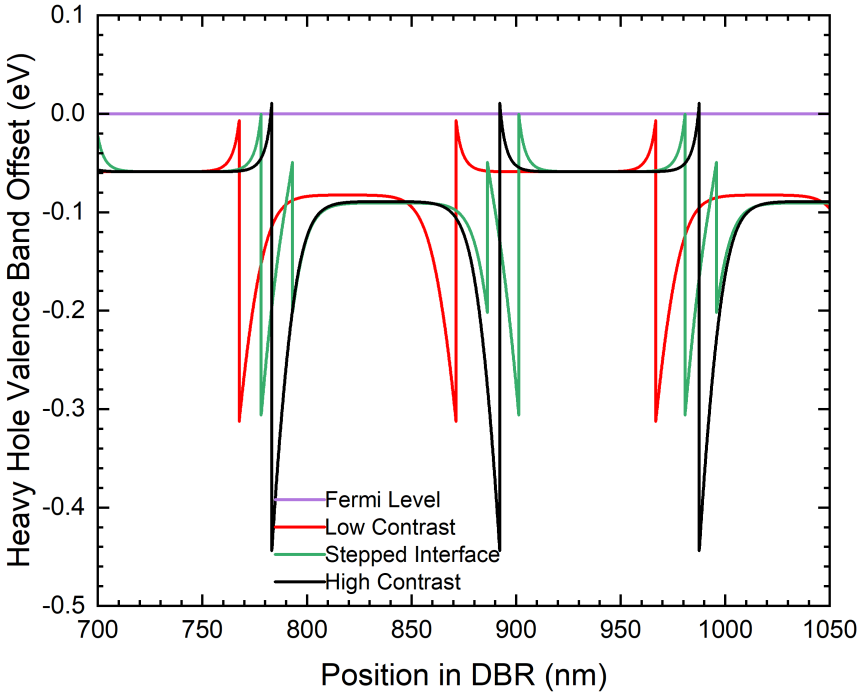

Figure 9.5: Heavy hole valence band offset relative to the hole Fermi level for low aluminium-contrast, high aluminium-contrast and stepped-interface p-doped (Be) DBRs with nominal doping density $1 \times 10^{18}\,\mathrm{cm}^{-3}$.

of the structures.

Figure 9.5 shows the simulated band structure at semiconductor heterointerfaces for three designs of DBR, excluding the digital alloy. Simulations are performed assuming activation energies from Watanabe et al. and Chand et al. [136, 137]. It is apparent that the high contrast structure has a significantly larger barrier to transport than either the low contrast or stepped interface structure. The low contrast design exhibits the smallest energy barrier per DBR repeat out of the three designs which would suggest a series resistance improvement; however, significantly more repeats are required to regain the desired reflectivity. For the case of a 98% reflectance DBR the number of repeats is increased by two-thirds with respect to the high contrast DBR. Intuitively, we can see that the stepped-interface structure should show a significant improvement in resistance compared to the high contrast case due to the smaller barrier at each interface, and comparable number of repeats to form a high-reflectivity DBR. The simulations in Figure 9.6 indicate that the high contrast DBR is the most resistive of the three designs, exhibiting a significantly lower current density than the other designs across the entire voltage range shown.

In reality dopant levels and the dopant profile are affected by diffusion of dopants through the semiconductor during growth, particularly at GaAs/$Al_xGa_{1-x}As$ interfaces [138]. During the growth of these DBRs, the temperature of the doping cell (Be) remains constant to ensure a stable flux. When coupled with different growth rates of the III-V layers and varying incorporation rate of dopants into $Al_xGa_{1-x}As$ layers with differing aluminium compositions, this contributes to a complex non-idealised doping profile in the grown-DBRs. In addition to this, the activation energy of Beryllium dopants may differ

	Material	Doping (cm^{-3})	Thickness (nm)
High Contrast			
(Final Layer Doping)	-	4×10^{18}	-
High Contrast DBR ×10	GaAs $Al_{0.9}Ga_{0.1}As$	1×10^{18}	95.4 109
Buffer	GaAs	1×10^{18}	170
Substrate	GaAs	1×10^{18} to 5×10^{18}	0.35 mm
High Contrast - Digital			
(Final Layer Doping)	-	4×10^{18}	-
High Contrast DBR - Digital x10	GaAs GaAs AlAs } × 40	1×10^{18}	95.4 0.27 2.45
Buffer	GaAs	1×10^{18}	170
Substrate	GaAs	1×10^{18} to 5×10^{18}	0.35 mm
Low Contrast			
(Final Layer Doping)	-	4×10^{18}	-
Low Contrast DBR ×17	GaAs $Al_{0.6}Ga_{0.4}As$	1×10^{18}	95.5 103.7
Buffer	GaAs	1×10^{18}	170
Substrate	GaAs	1×10^{18} to 5×10^{18}	0.35 mm
Stepped-Interface			
(Final Layer Doping)	-	4×10^{18}	-
Stepped-Interface DBR ×11	GaAs $Al_{0.6}Ga_{0.4}As$ $Al_{0.9}Ga_{0.1}As$ $Al_{0.6}Ga_{0.4}As$	1×10^{18}	79.5 15 93.2 15
Buffer	GaAs	1×10^{18}	170
Substrate	GaAs	1×10^{18} to 5×10^{18}	0.35 mm

Table 9.1: Layer descriptions of high-contrast (alloy and digital-alloy), low-contrast and stepped-interface DBRs, as grown. All of the structures were p-doped with beryllium.

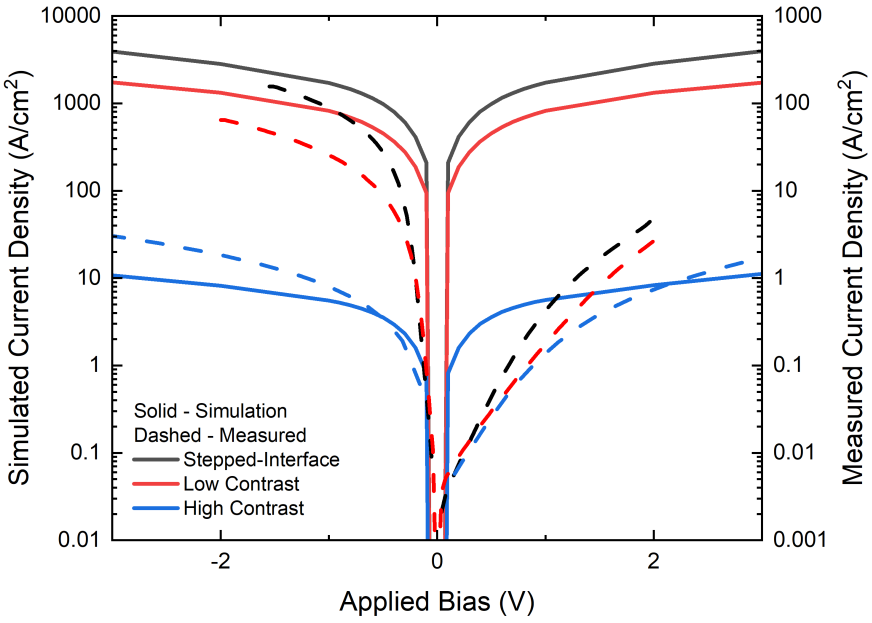

Figure 9.6: Simulated and measured current-voltage characteristics for high contrast, low contrast and stepped interface DBRs with 10, 17 and 11 repeats respectively. The DBRs were p-doped to a nominal density of $1 \times 10^{18}\,\mathrm{cm}^{-3}$. Measured current density is an approximation, assuming minimal current spreading outside of the top contact.

from those presented by Chand et al. [137] that were used in the simulation. Furthermore, non-ideal growth of the DBRs inevitably results in non-uniform dopant distribution and profiles due to varying growth rates, non-uniform doping incorporation, inaccurate mean doping concentration and variation in aluminium composition. In addition to non-ideal growth, the dopant activation energies are approximations from the literature [136, 137]. A digital alloy allows for more straightforward control of the growth conditions during the growth process. Individual growth rates of the GaAs and AlAs layers may be matched to ensure a more uniform distribution of dopants throughout the DBRs. To test the simulation results the structures shown in Table 9.1 were grown. All samples were grown as single-sample runs with minimal calibration so slight deviation from the designed wavelength is to be expected, as seen in Figure 9.7. The stopband for the low contrast device is significantly narrower than the other designs which would make the final VCSEL growths more sensitive to growth variations as the high-reflectivity region of the DBRs is narrower and therefore less tolerant to variations in cavity length and DBR stopband centre mismatch. The stopband for the stepped-interface DBR is at a significantly longer wavelength than the other samples. BEXP+AFM (section 4.6) of the stepped-interface DBR (Figure 9.8) confirmed that this was due to inaccurate growth of the designed layers due to calibration of the MBE growth rates; $Al_{0.9}Ga_{0.1}As$ layers were approximately 5% thicker than designed, with all other layers overgrown by approximately 20%. Simulation of the measured layer thickness shows reasonable agreement with the measured reflectivity (Figure 9.9).

Electrical contacts were formed by thermal evaporation of Ti/Au onto the topside and backside of a cleaved area of wafer approximately 1 cm by 1 cm, no mesa-isolation was performed. The topside contacts were square contacts 360 µm by 360 µm. Electrical

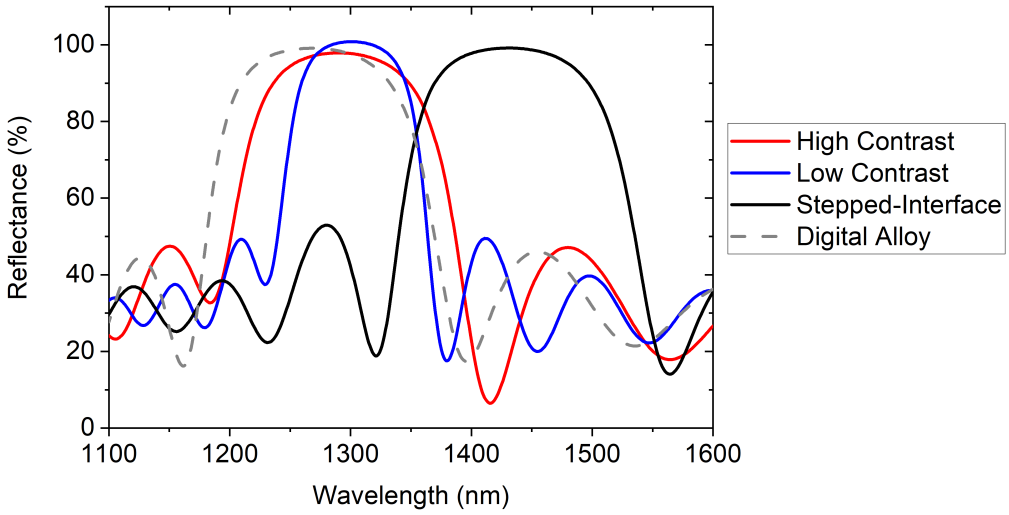

Figure 9.7: Reflectivity of high contrast, low contrast, stepped interface and digital alloy DBRs relative to a PTFE reference sample. DBRs were designed for operation at 1300 nm but deviate due to inaccuracy of the grown layers.

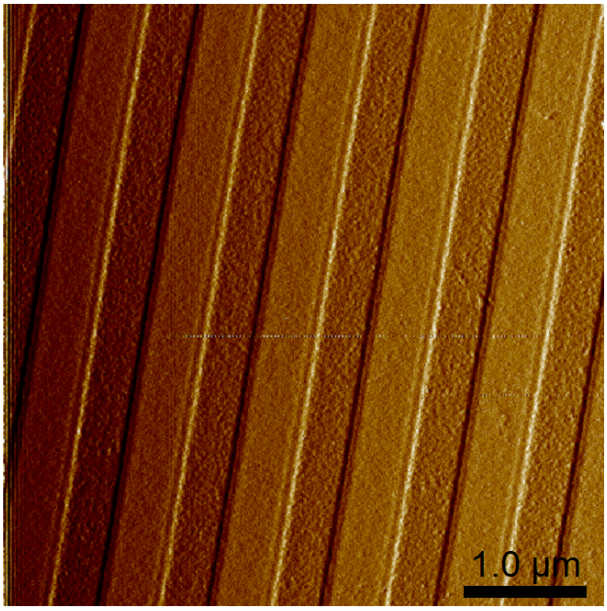

Figure 9.8: An AFM image of the stepped-interface DBR cross-sectioned with BEXP for extraction of layer thickness. The narrow intermediate-composition layer is visible at the interfaces between the GaAs and $Al_{0.9}Ga_{0.1}As$.

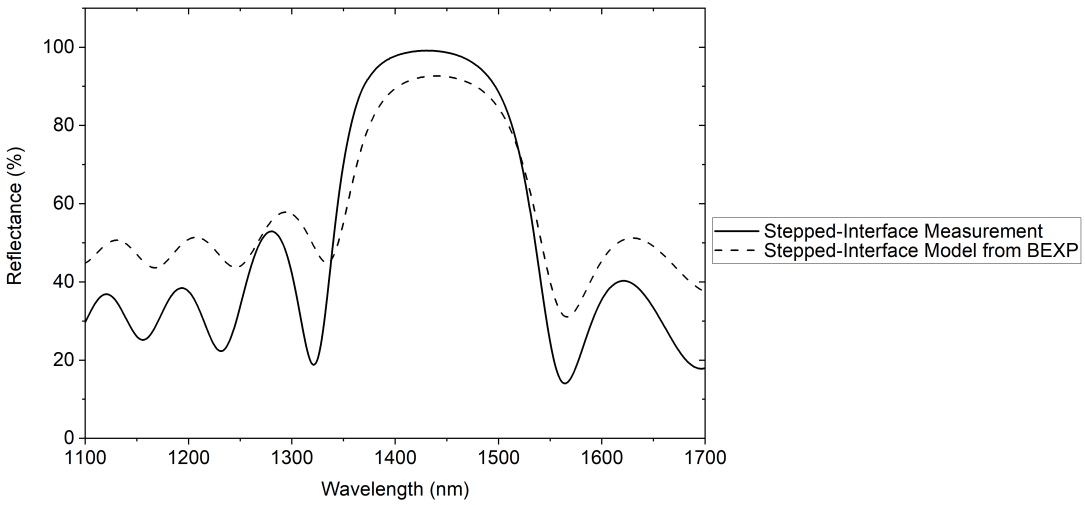

Figure 9.9: Simulation of stepped-interface DBR reflectance as a function of wavelength based on layer thickness measurements from BEXP+AFM compared to the measured reflectance. Discrepancies between the peak reflectivity is attributed to the calibration of the measurement to an imperfect reference plate, and optical absorption in the material which has been omitted from the model.

characterisation of the structures consisted of a two-probe current-voltage sweep. Current density of the measured sample is an approximation and overestimation as it assumes no current spreading outside of the top contact area. The order of magnitude discrepancy in current density and relative differences between the DBRs are attributed to a number of factors. It is known that increased doping concentrations reduce electron and hole mobility due to charge carriers scattering from ionised impurities [139]. The models used in these simulations assume a constant mobility at all doping concentrations which will be reflected in the simulations by a higher current density. At doping concentrations $>10^{18}\,\mathrm{cm}^{-3}$ this corresponds to approximately an order of magnitude drop in mobility and subsequently current density which is not represented in simulation. In addition to the challenges with growth rates and dopant incorporation discussed above, the *nextnano++* simulations also assume perfect ohmic contacts with zero contact resistance, whilst Ti/Au contacts are known to form a Schottky barrier with p-type GaAs. These effects directly affect the results shown in Figure 9.6.

The measurement results show qualitative agreement with the simulations, indicating that the stepped-interface DBR is a viable option for reduced series resistance in VCSELs operating at 1300 nm (Figure 9.6).

9.2 Optical Absorption at Telecoms Wavelengths

Section 9.1 explored the effect of material composition on the resistivity of DBRs, another consideration in the resistivity of VCSEL DBRs is the magnitude of the dopant concentration. The barrier height and conduction band edge can be moved closer to the Fermi level by increasing the doping concentration of the material. Conventionally, high doping levels have been avoided for fear of increased free-carrier absorption which is often cited as a drawback of higher doped DBRs [55, 56, 57, 140, 141]. The effect of doping DBRs in

the telecoms wavelength range is not widely studied in the literature. To directly measure the effect of doping on DBRs at telecoms wavelengths a series of ten-repeat p-doped (Be) stepped-interface DBRs were grown unintentionally doped and with nominal doping levels of $5 \times 10^{16}\,\mathrm{cm}^{-3}$, $5 \times 10^{17}\,\mathrm{cm}^{-3}$, $1 \times 10^{18}\,\mathrm{cm}^{-3}$ and $5 \times 10^{18}\,\mathrm{cm}^{-3}$. All structures incorporated a highly-doped ($4 \times 10^{18}\,\mathrm{cm}^{-3}$) contact layer to be consistent with a final VCSEL and to allow for contact formation. The DBRs were grown on undoped GaAs wafers to minimise absorption in the substrate, so a doped buffer-layer was also included to allow for bottom contact. The ionised acceptor density was calculated throughout the structure (Figure 9.10 middle) using *nextnano++* under the assumption that the incorporated dopant density is equal to the design (Figure 9.10 top). The nominally undoped sample is represented by a doping concentration on the order of $1 \times 10^{15}\,\mathrm{cm}^{-3}$ to ensure it is visible on the scale in Figure 9.11, this concentration is a few orders of magnitude higher than unintentional background doping shown in the literature [142] but is more consistent with background doping for samples grown using the MBE system used in this work [21], which is believed to be carbon-based. As in section 9.1, the experimentally-realised doping levels will be affected by growth conditions and dopant diffusion. Beryllium doping activation energies were taken from Chand et al.[137]. An effective ionised acceptor density, P_{eff}, was obtained by integrating the ionised acceptor concentration over the depth of the structure as follows,

$$P_{eff} = \int_{x=0}^{end} \rho_p \cdot \mathrm{d}x, \tag{9.1}$$

where x is the depth in the structure and ρ_p is the depth-dependent ionised acceptor density. The effective ionised acceptor density is representative of the acceptor density assuming the DBR to be a bulk structure and takes into account the increased doping in the contact layers.

Figures 9.11a and 9.11b indicate that the reflectance of each DBR is within error of the mean reflectance for all structures. As a result, there is no clear dependence of optical absorption on doping concentration in the ∼1300 nm wavelength region. Changes in wavelengths are attributed to growth rate variation between growths. This is consistent with more recent work by Charles et al. [129], in which Si-doped and Be-doped GaAs samples were grown by MBE on a Veeco GENXplor MBE system and measured using ellipsometry to determine the complex reflectivity of doped GaAs across a range of wavelengths. The study demonstrated a negligible extinction coefficient for both p-doped and n-doped GaAs in the telecoms 'O' and 'C' bands, whereas absorption was present below ∼1 µm and in the mid-infrared and longer. In conclusion, Be-doping in the $Al_xGa_{1-x}As$ mirrors has no discernible impact on the optical properties of the DBR up to doping levels on the order of $5 \times 10^{18}\,\mathrm{cm}^{-3}$ so there is no need to reduce doping levels for the risk of free-carrier absorption at this wavelength.

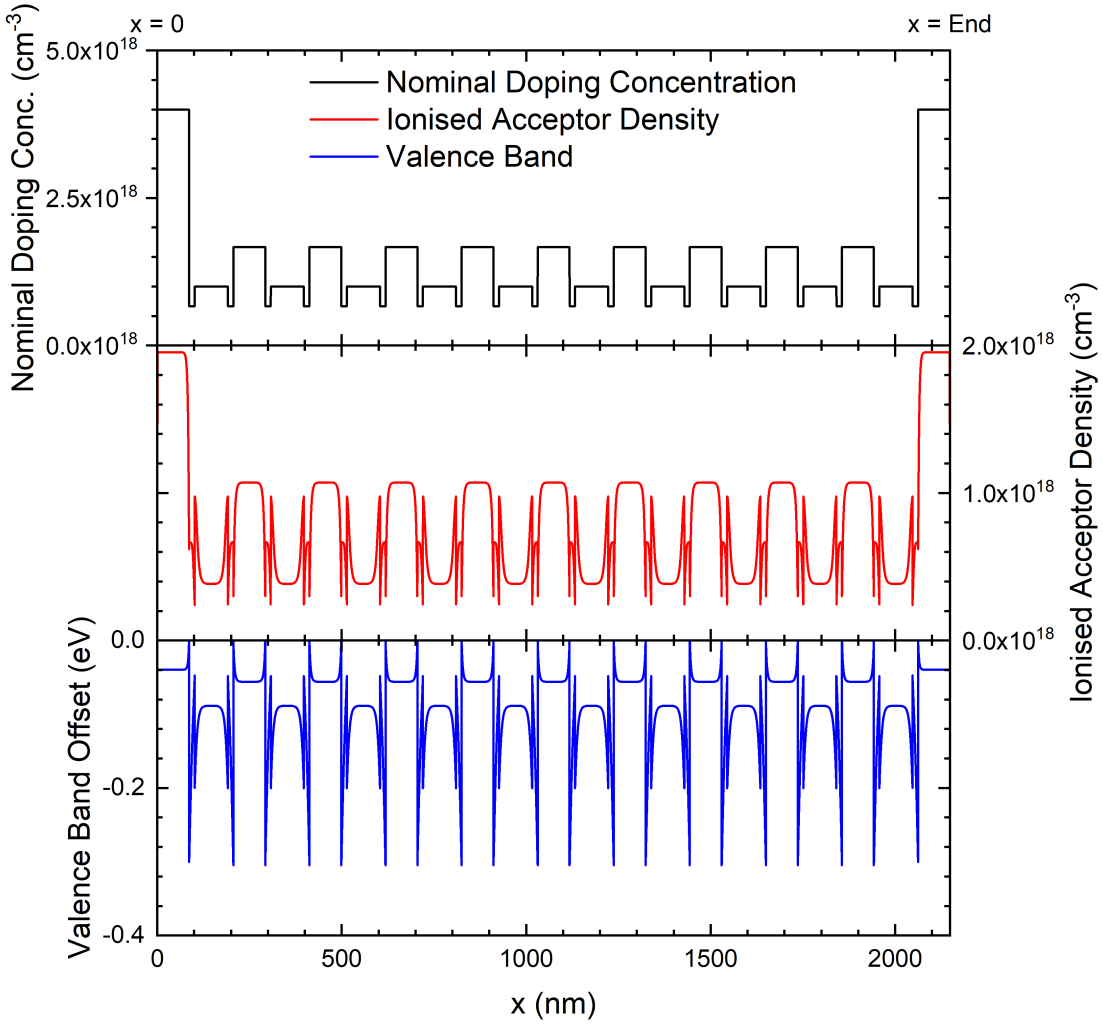

Figure 9.10: The nominal doping profile (top), simulated ionised acceptor density (middle) and simulated valence band edge (bottom) for a Be-doped $Al_xGa_{1-x}As$-based DBR nominally doped at $1 \times 10^{18}\,cm^{-3}$ at 300 K. The valence band edge is included for ease of visualising the interfaces between layers.

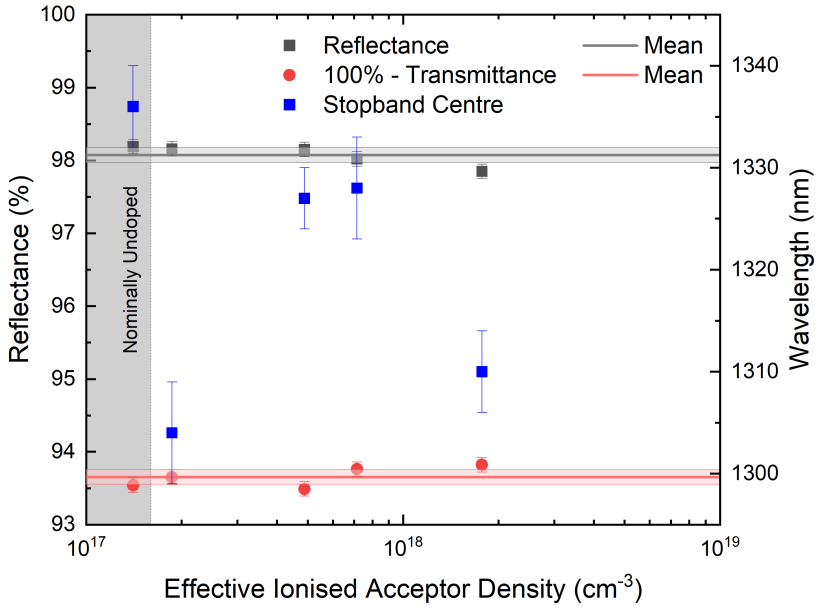

(a)

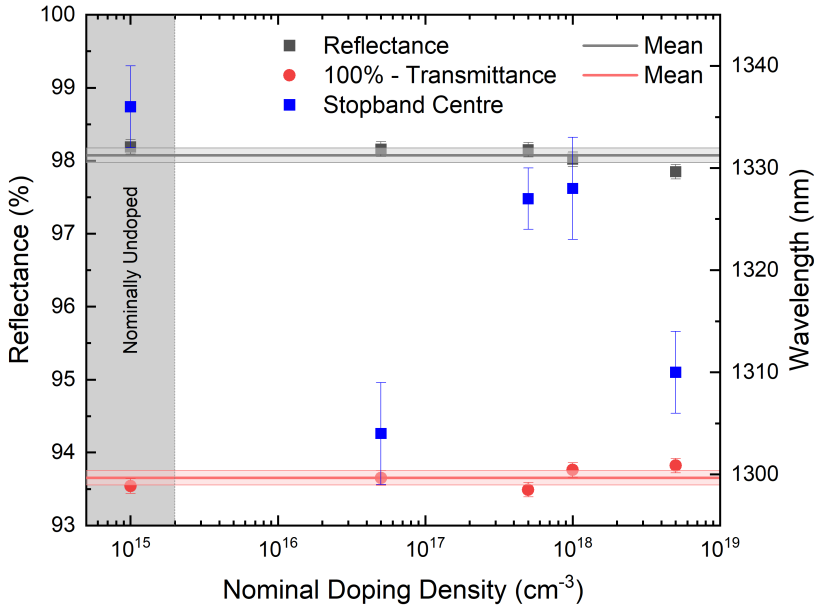

(b)

Figure 9.11: Measured reflectance, transmittance and the central wavelength of stopbands for DBRs unintentionally-doped (represented here as $1\times10^{15}\,\mathrm{cm}^{-3}$) and with doping levels of $5 \times 10^{16}\,\mathrm{cm}^{-3}$, $5 \times 10^{17}\,\mathrm{cm}^{-3}$, $1 \times 10^{18}\,\mathrm{cm}^{-3}$ and $5 \times 10^{18}\,\mathrm{cm}^{-3}$ are shown against the effective ionised acceptor density obtained from simulation (a) and the nominal doping concentration (b).

9.3 Spiky DBRs

Section 9.1 demonstrated the electrical benefits of a thin intermediate-composition layer at the interface between high and low aluminium-concentration layers. This section expands on the idea of reducing barriers at the interfaces by considering the extreme case of a continuously-graded structure in which the composition is linearly graded between maxima and minima in the aluminium concentration of an $Al_xGa_{1-x}As$ reflector (Figure 9.12). The continuously-graded structures may be referred to as 'spiky' due to the nature of their aluminium-composition profile. A comparison of the barriers to hole transport in the valence band of p-doped ($5 \times 10^{17}\,cm^{-3}$) spiky, conventional graded-interface (20 nm grading) and textbook high-contrast DBRs is shown in Figure 9.13. The spiky structure is graded between $Al_{0.12}Ga_{0.88}As$ and $Al_{0.9}Ga_{0.1}As$, the other structures switch between GaAs and $Al_{0.9}Ga_{0.1}As$ layers. In the first instance, the spiky DBRs exhibit reduced barriers to hole transport compared to the other structures. Therefore, it is expected that this will result in improved electrical performance across an individual interface. The graded-nature of the spiky DBRs will, inevitably, reduce the optical performance of such a mirror compared to the traditional case and necessitate more repeats of the structure to recover the lost performance. A compromise is formed between reduced barrier heights within the structure, and an increase in the number of barriers formed by the increase in number of repeats.

To allow for experimental comparison of the spiky and traditional graded-interface DBRs, twelve structures were designed and subsequently grown by MOCVD. The growth was performed on an industrial Aixtron planetary reactor at IQE. A 25 nm doped-GaAs layer was used to cap the DBRs after growth to prevent oxidation of the aluminium-containing top layers and enable the formation of metal contacts to the surface. Six standard graded-interface DBRs and six continuously-graded reflectors were designed with maximum and minimum group-III aluminium concentrations of 90 % and 12 % respectively. The graded-interface structures were based on two standard industry designs consisting of highly-reflective 850 nm DBRs with 34× and 41× repeats, terminated by low ($Al_{0.12}Ga_{0.88}As$) and high ($Al_{0.9}Ga_{0.1}As$) aluminium-content layers respectively. A further four standard DBRs were designed for operation at 1310 nm. 1310 nm was chosen as it is the wavelength target for upstream gigabit passive optical network (GPON) [143] connections and datacentre use. From now on these graded-interface structures may be referred to as 'standard' DBRs. The first pair of standard 1310 nm DBRs were designed to match the total reflectivity of the standard 850 nm DBRs, the second pair were designed with an equivalent number of DBR repeats. Six continuously-graded (spiky) reflectors were designed as a counterpart to the standard designs, each with a target wavelength and reflectance equivalent to their standard-DBR partner. A summary of the twelve structures is shown in Table 9.2 and given a unique sample name for ease of reference throughout this chapter.

The optical properties of the DBRs will be presented first, followed by a discussion of the electrical properties. Simulations of B-Std demonstrating the effects of absorption are shown in Figure 9.14. A comparison of the measured and simulated reflectance spectra for A-Std (850 nm) is shown on a normalised scale in Figure 9.15a. Equivalent normalised spectra for the corresponding spiky DBR are shown in Figure 9.15b and demonstrate a noticeably narrower stopband. It is worth noting that the accuracy of optical constants for $Al_xGa_{1-x}As$ in the material database used for these simulations is limited and exhibits an over-estimation of the absorption coefficients. The increased absorption results in

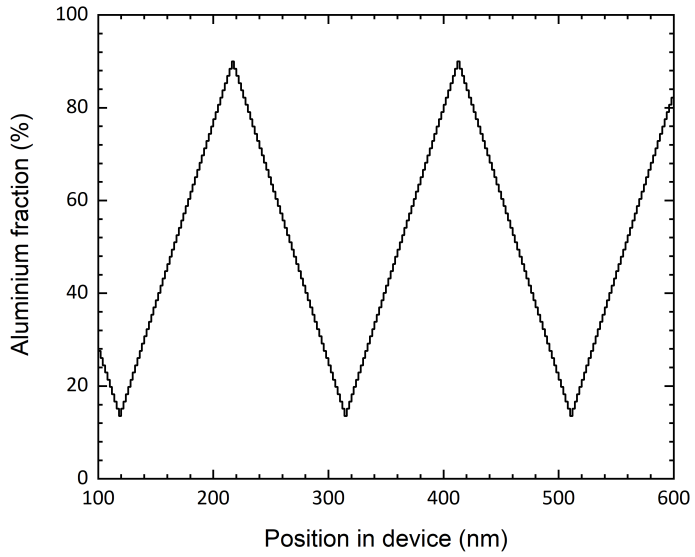

Figure 9.12: The aluminium composition for a continuously-graded $Al_xGa_{1-x}As$ DBR designed for operation around 1300 nm.

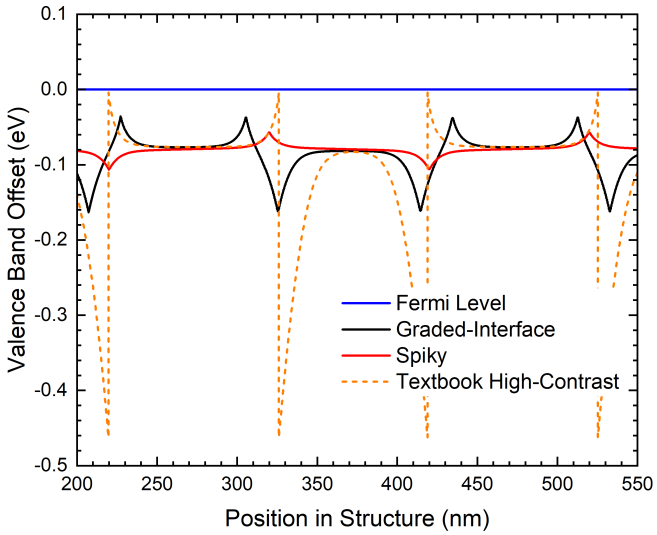

Figure 9.13: The simulated valence band profile of a textbook high-contrast $GaAs/Al_{0.9}Ga_{0.1}As$ DBR, graded-interface $GaAs/Al_{0.9}Ga_{0.1}As$ DBR and spiky $Al_xGa_{1-x}As$ reflector, all structures are nominally doped at $5 \times 10^{17}\,cm^{-3}$.

Wavelength	Dopant	Top Layer	Repeats	Sample Name
850 nm	Carbon (p)	$Al_{0.12}Ga_{0.88}As$	20 32	A-Std A-Spiky
850 nm	Silicon (n)	$Al_{0.9}Ga_{0.1}As$	34 42	B-Std B-Spiky
1310 nm	Carbon (p)	$Al_{0.12}Ga_{0.88}As$	23 37	C-Std C-Spiky
1310 nm	Carbon (p)	$Al_{0.12}Ga_{0.88}As$	20 33	D-Std D-Spiky
1310 nm	Silicon (n)	$Al_{0.9}Ga_{0.1}As$	38 49	E-Std E-Spiky
1310 nm	Silicon (n)	$Al_{0.9}Ga_{0.1}As$	34 43	F-Std F-Spiky

Table 9.2: The target wavelength, top layer material composition and the number of DBR repeats for twelve DBR designs used to compare the performance of spiky DBRs to their traditional counterparts. Each row is designed to have equivalent peak reflectivity at the target wavelength.

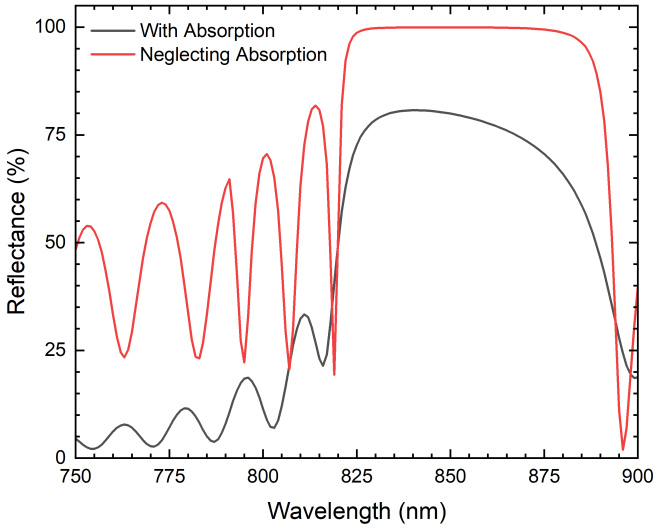

Figure 9.14: Simulated reflectance spectra for B-Std in the region of 850 nm including and excluding the effects of strong absorption.

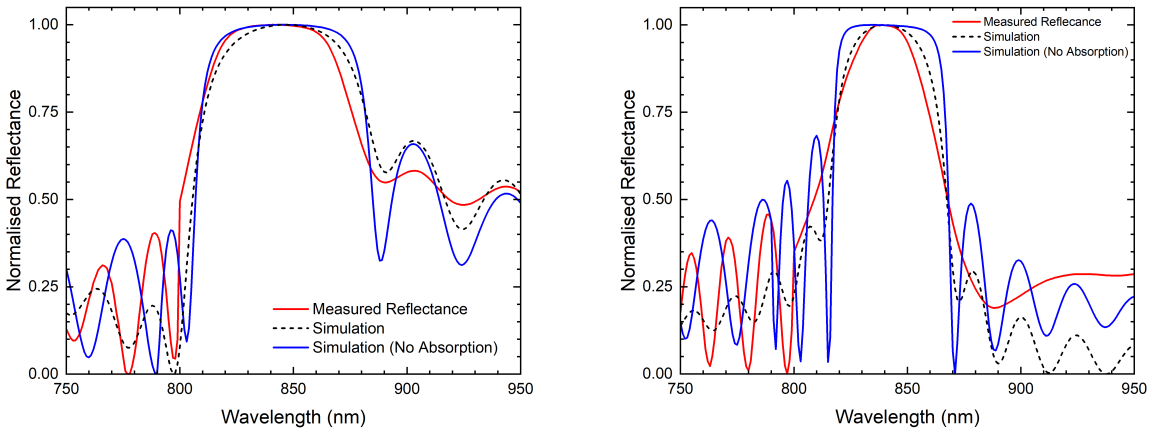

(a) (b)

Figure 9.15: The reflectance spectra of A-Std (a) and A-Spiky (b) as measured, simulated with absorption and simulated excluding absorption.

a low total-reflectivity of the DBR which is not physical. The decision was taken to neglect absorption when designing each structure. Whilst this is not physical, particularly for energies greater than the GaAs band gap, it is consistent for each structure and is appropriate for the longer-wavelength DBRs reflecting at 1300 nm where absorption is negligible. It is clear that excluding the effects of absorption produces a stopband that is broader than the measured case and exhibits stronger modulation of reflectance in the sidebands of the DBR (Figure 9.15).

The designed and measured reflectance for F-Spiky is shown in Figure 9.16a. Two aspects of the curves are immediately apparent; the measured wavelength is shorter than designed and the measured stopband is narrower than the simulations predict. During the growth campaign, the recipes were tuned to maximise the reflectance at 1300 nm, this resulted in each layer being reduced in thickness. After accounting for the new target wavelength the measured stopband remains narrower than the design (Figure 9.16b). Instead, by modifying the simulation such that the aluminium composition is graded between $Al_{0.12}Ga_{0.88}As$ and $Al_{0.8}Ga_{0.2}As$ rather than $Al_{0.9}Ga_{0.1}As$ the width of the stopband becomes consistent with the design (Figure 9.16c) but the wavelength difference remains. Incorporating both the reduced layer thickness and maximum aluminium composition of the structure into the simulation results in a reasonable agreement between the experiment and simulation (Figure 9.16d). It is unclear as to whether the small but necessary changes in aluminium composition and layer thickness are representative of the real growth, indicate small inaccuracies in the optical constants used in the simulations, or are a feature of approximating the grading as a finite number of discrete steps. In summary, the final structures differ slightly from the original designs; however, this is not significant enough to impact the findings of the study that follow.

The normalised reflectance spectra of the four $Al_{0.12}Ga_{0.88}As$-terminated DBRs designed to have equivalent maximum reflectance (A-Std, A-Spiky, C-Std and C-Spiky) are shown in Figure 9.17a. The corresponding $Al_{0.9}Ga_{0.1}As$-terminated DBRs (B-Std, B-Spiky, E-Std and E-Spiky) are shown in Figure 9.17b. In all cases, the spiky DBR exhibits a narrower stopband than its standard counterpart. For A-Spiky and C-Spiky the reflectance of the spiky DBRs peak at over 99 % of their standard counterpart. For

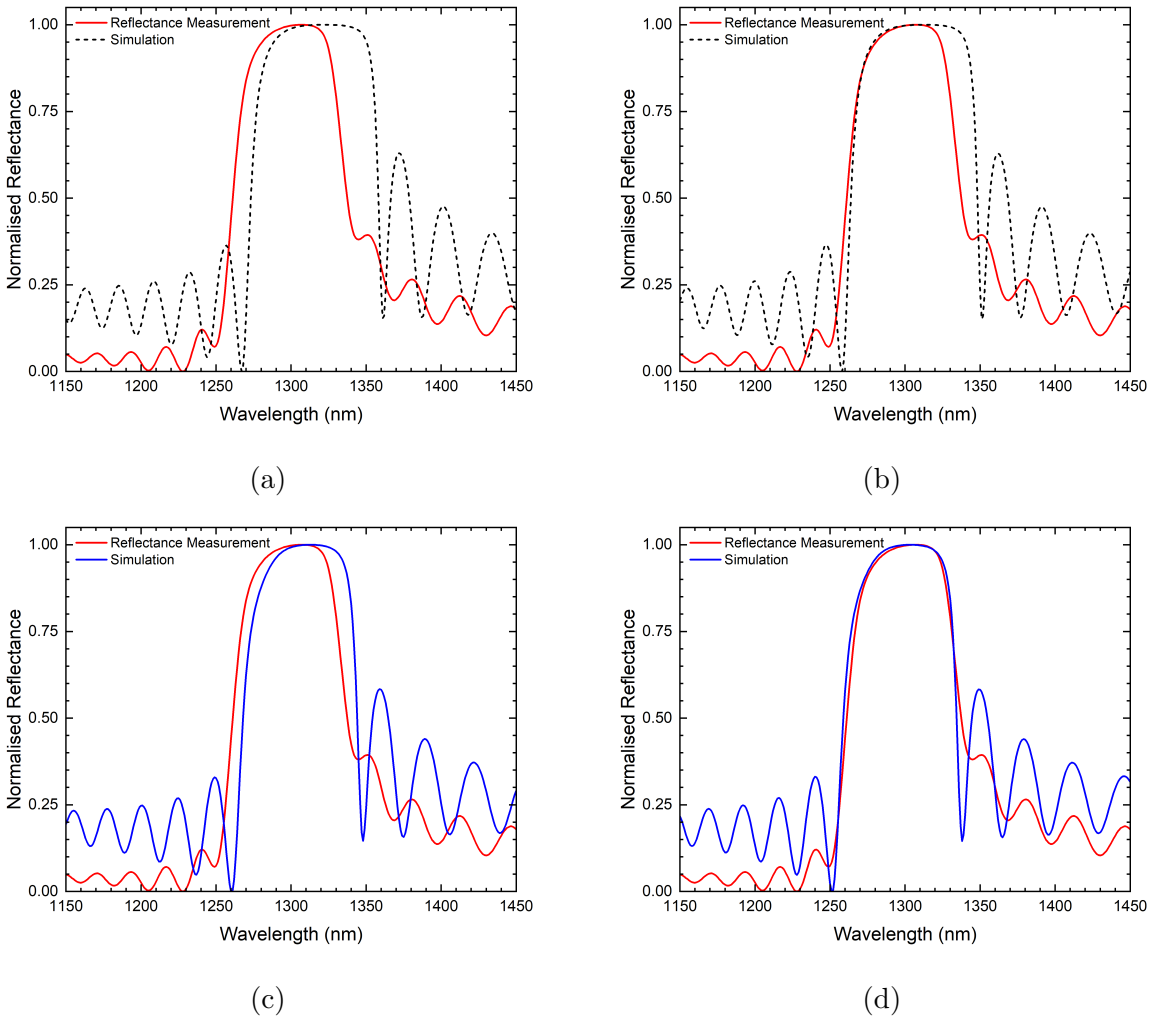

Figure 9.16: Measured reflectance of a spiky DBR operating at 1300 nm is compared to simulations of the structure as-designed (a), adjusted for the central wavelength as-grown (b), fitted with aluminium composition reduced to 80 % (c) and finally with reduced aluminium composition and adjusted for the central wavelength (d).

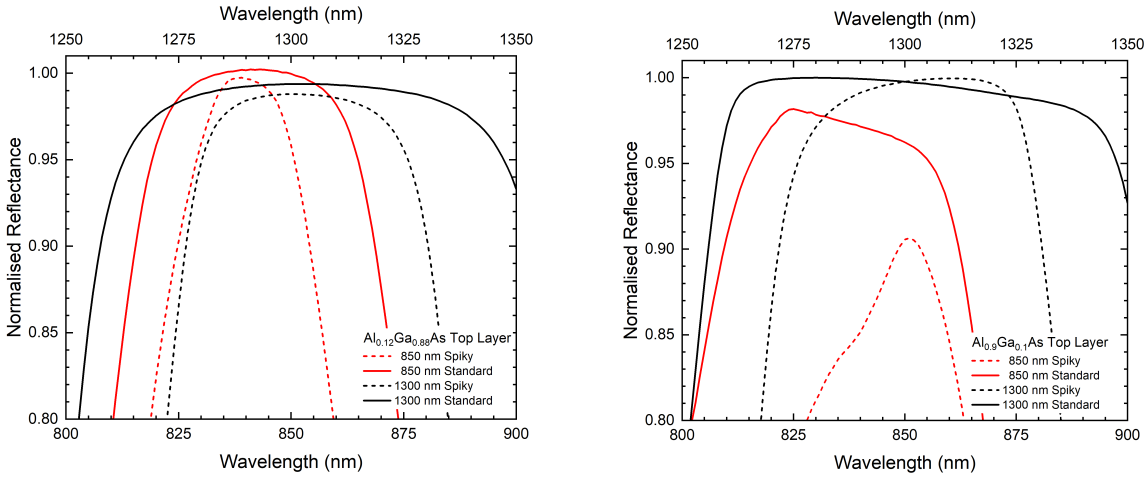

(a) (b)

Figure 9.17: The normalised reflectance spectra comparing equivalent DBR designs at 850 nm and 1300 nm for samples A-Std, A-Spiky, C-Std and C-Spiky (a) and samples B-Std, B-Spiky, E-Std and E-Spiky (b) as measured using a Cary 5000 spectrophotometer with diffuse reflectance accessory.

the case of E-Spiky the reflectance at 1300 nm appears equivalent; whereas for B-Spiky a significantly lower reflectance is achieved than for B-Std. This apparent reduction in reflectance is likely due to interference effects in the GaAs capping layer on B-Spiky. The reflectance spectra for B-Spiky as-measured by IQE following the growth campaign is shown in Figure 9.18. A distinct dip is present in the stopband of the DBR. A simulation of the designed structure with the GaAs capping layer overgrown to 87.5 nm shows the same characteristic dip in reflectance (Figure 9.18). Whilst no direct measurements have been performed on the GaAs cap, it is likely that such interference effects are responsible for the lower reflectivity of the anomalous sample. It is unexpected that the cap thickness would deviate from the target value by such a large amount. However, as for the longer wavelength structures, the thickness of layers was tuned during the growth runs to achieve the target wavelength. This may result in significant deviation from the design. In addition, it is likely that inaccuracies in the material parameters used for simulations lead to further discrepancies between the real layer thickness and thickness indicated by the model both pre-growth and post-growth.

Figure 9.19 presents the optical measurements for each of the 1300 nm DBRs grown for this study. Again, in all cases the spiky DBR stopband is narrower than the standard structure which is consistent with simulations. For large numbers of DBR repeats the reflectivity of the spiky structures begins to regain the peak reflectivity of the standard structures, as evidenced by the 49× repeat structure in Figure 9.19a. These initial measurements demonstrate the potential for good optical performance of the spiky DBR design, supporting the high-reflectance quoted by the simulations. With sufficient repeats, the spiky DBRs are able to recover the peak reflectance of the traditional graded-interface designs but maintain a relatively narrow stopband.

Simulations and experiment will now be used to provide insight into the electrical characteristics of these DBRs. Band-edge simulations for each variation of the final DBR designs were performed using *nextnano++*. The conduction and valence band edges are

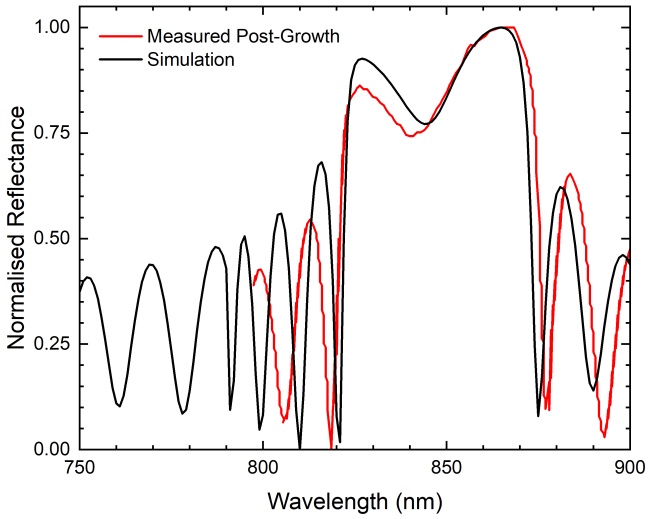

Figure 9.18: Normalised reflectance spectra of sample B-Spiky (850 nm) as-measured post-growth at IQE and simulated with an overgrown GaAs capping layer.

shown in Figure 9.20 and consistently demonstrate reduced barriers to transport in the spiky structures. The implications of the reduced barrier heights over the full DBR stack with multiple repeats is investigated experimentally. Each DBR was grown on top of a doped GaAs contact layer and consisted of a doped GaAs cap. Contacts were placed on the upper and lower contact layers using the follow process:

a) Define mesas using bilayer S1813 photoresist.

b) Etch mesas to the contact layer using ICP and $Cl_2/BCl_3/Ar$ plasma.

c) Define contacts on mesas and the etch-floor using AZ40XT-11D photoresist.

d) Sputter Ti/Au contacts.

The top contact consisted of a 150 µm by 150 µm square pad on top of a 250 µm by 250 µm square mesa. All of the samples were processed in parallel to minimise variation in processing conditions between samples. Contact lift-off failed on samples B-Spiky and D-Std. Subsequently samples A, C and F were selected for provisional electrical characterisation. Four-probe current-voltage sweeps were performed to characterise the electrical properties of the DBRs.

A comparison of the current-voltage characteristics and differential resistance for each of the p-doped DBRs (Figure 9.21a) does not show a clear and significant benefit to any of the DBR candidates. In all cases, the DBRs exhibit similar currents for a given applied bias and any variation is masked by variation in the processed devices. In contrast, the n-doped DBRs exhibit significantly lower resistance under forward bias compared to the p-doped DBRs (Figure 9.21b). In this instance the difference between the spiky and standard DBRs is insignificant when compared to the variation caused by n-type versus p-type doping. The origin of the asymmetric current-voltage characteristics in Figure 9.21b may be asymmetric doping within the structure, in particular asymmetric doping of the contact layers. Such doping may produce asymmetric current-voltage characteristics within the semiconductor layers and of the performance of contacts deposited

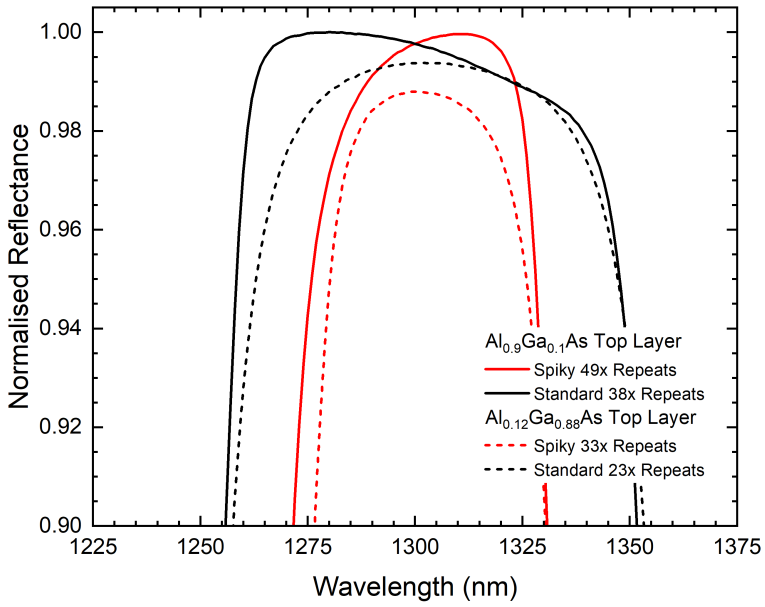

(a)

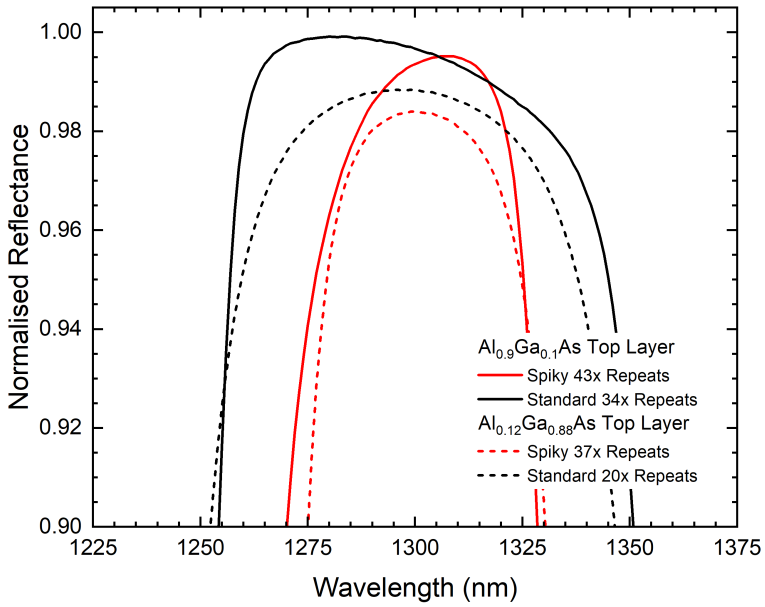

(b)

Figure 9.19: Reflectance spectra of DBRs with a reflectivity in the region of 1300 nm designed with higher (a) and lower (b) reflectance targets. Higher reflectivity corresponds to samples C-Std, C-Spiky, E-Std and E-Spiky, lower reflectance corresponds to D-Std, D-Spiky, F-Std and F-Spiky. Reflectance is normalised to the peak of the most reflective DBR.

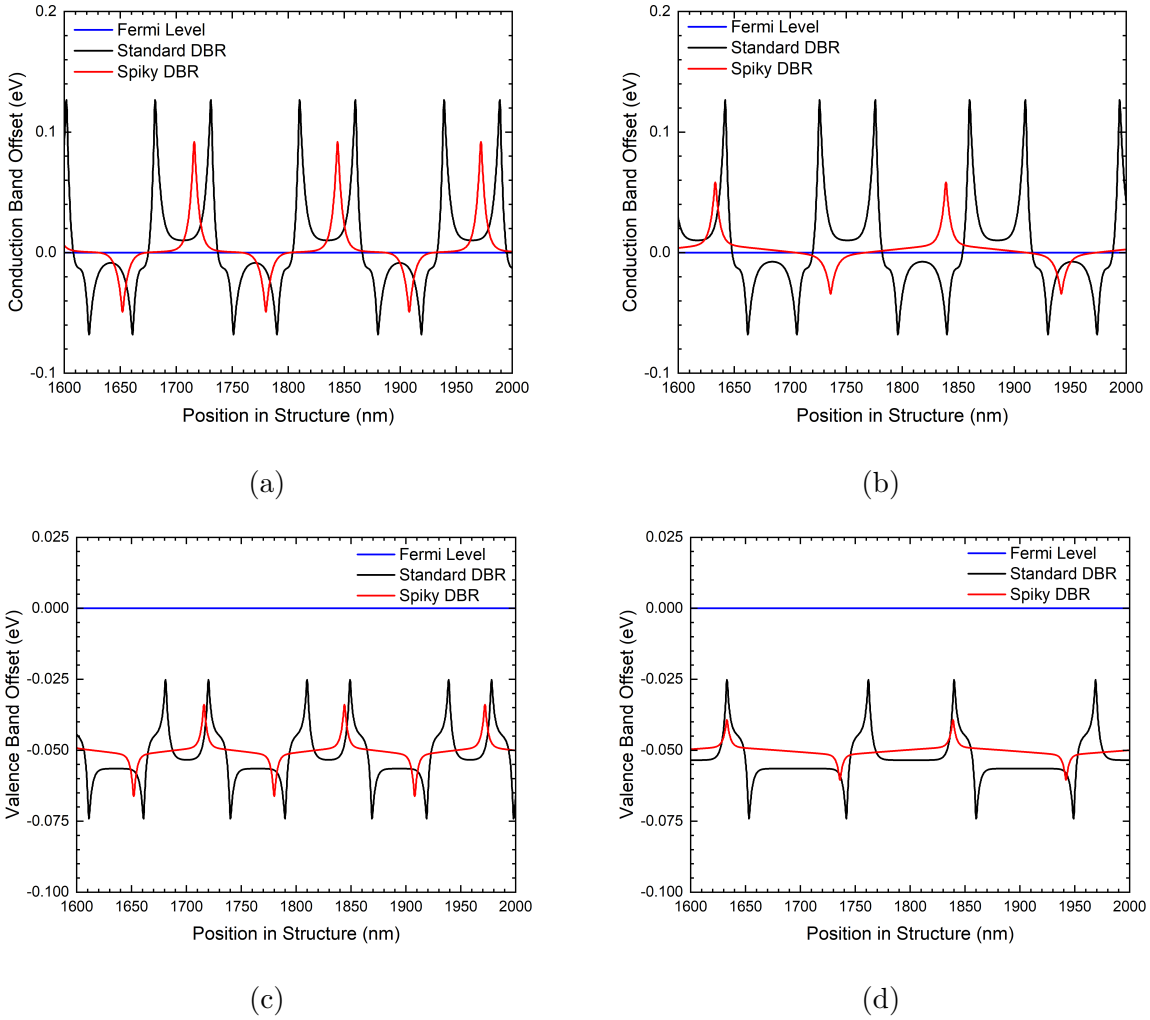

Figure 9.20: The simulated conduction band edge relative to the Fermi level is shown for samples B-Std and B-Spiky designed to reflect in the region of 850 nm (a) and samples E/F-Std and E/F-Spiky in the region of 1300 nm (b). The valence band offset relative to the Fermi level is shown for samples A-Std and A-Spiky designed to reflect in the region of 850 nm (c) and samples C/D-Std and C/D-Spiky in the region of 1300 nm (d). All simulations are at zero bias.

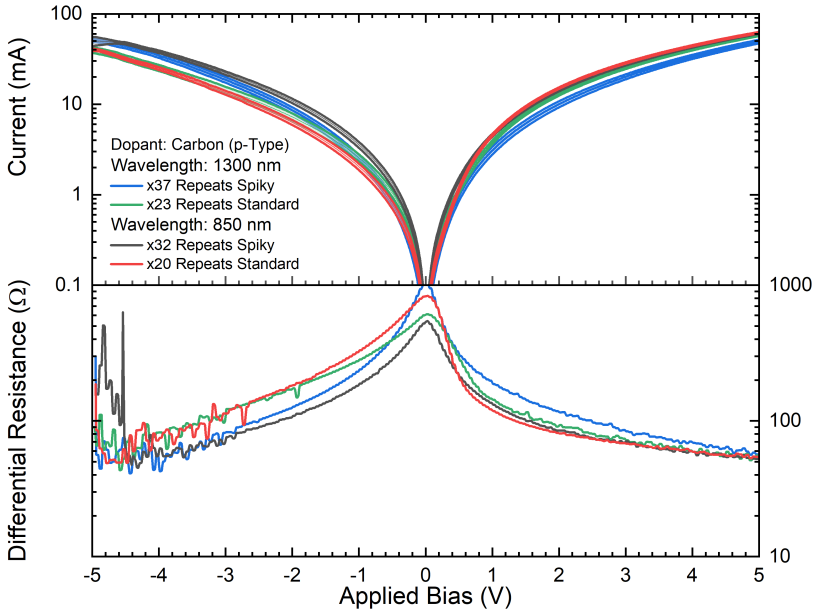

(a)

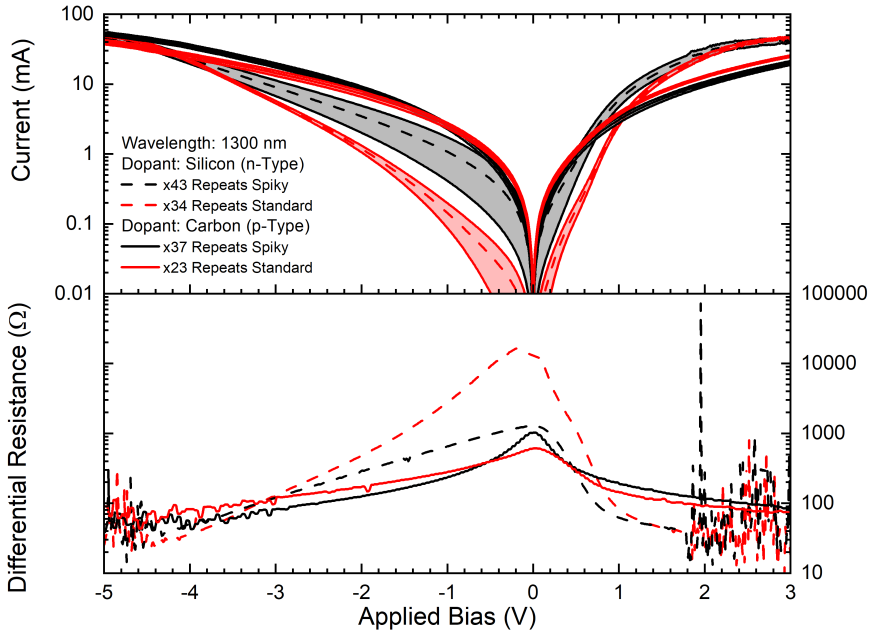

(b)

Figure 9.21: Current-voltage characteristics for carbon-doped (p-type) DBRs reflecting in the region of 850 nm and 1300 nm (a). Current-voltage characteristics of silicon-doped (n-type) and carbon-doped (p-type) DBRs reflecting in the region of 1300 nm (b).

on the sample surface. Current-voltage simulations were attempted using *nextnano++* software and the number of DBR repeats reduced by one-third in an attempt to reduce the computational intensity. Despite this, the simulations did not fully converge and exhibited current densities that appeared orders of magnitude too high. On this basis, the results of the simulations were omitted but it is interesting to note that the simulations showed some aspects of qualitative agreement with the experiment.

In summary, the electrical characteristics of the structures grown for this study indicate no significant difference between the standard and spiky DBRs. It is likely that the barrier heights between adjacent materials have been reduced to the extent that they are no longer a significant consideration for the design of DBRs. High reflectivity of the spiky DBR designs can approach their standard graded-interface counterparts with sufficient repeats of the graded structure; however, the resulting DBR stopband is narrow which may be detrimental to the sensitivity of epitaxial growth if such mirrors were to be incorporated into a VCSEL or similar structure. In addition, whilst thermal properties of the DBRs were not studied, the performance of the spiky DBR design is expected to be worse. The spiky DBR is likely to experience similar levels of Joule heating to the standard design due to approximately equal electrical performance; however, the drastic increase in overall reflector stack thickness will contribute to an inferior thermal conductivity.

9.4 Summary of DBR Studies

This chapter was concerned with the opto-electric study of DBRs. The intention of the studies was to develop a DBR for use in GaSb QR VCSELs operating at telecoms-wavelengths with improved electrical properties compared to previous designs used in these structures. Initially, a series of DBRs were grown by MBE at Lancaster to investigate the electrical implications of interfaces between $Al_xGa_{1-x}As$ layers of different compositions within the DBR. It was determined that a stepped-interface design provided the best electrical performance whilst maintaining the optical performance of the DBR. Secondly, the absorption of the DBR material as a function of doping concentration was studied at telecoms-wavelengths. No significant absorption was measured in doping concentrations up to $5 \times 10^{18}\,\mathrm{cm}^{-3}$. Given the findings of the MBE-grown DBR studies it was decided that future GaSb QR VCSELs should utilise highly-doped stepped-interface DBRs when grown by MBE at Lancaster. A separate study on novel spiky DBRs was performed. In conclusion, the structures demonstrated high reflectivity at the designed wavelength and electrical properties comparable to industry-standard DBRs. Unfortunately, the narrow stopband and overall increase in DBR thickness indicate that the spiky DBR is unlikely to be appropriate for use in VCSELs.

Chapter 10

Photoluminescence and Time-Resolved Photoluminescence of GaSb Quantum Rings

This section explores the electron-hole recombination mechanisms for GaSb rings in bulk GaAs and rings contained within a VCSEL cavity. The recombination of electron-hole pairs in QR-containing samples may occur through multiple processes, both radiative and non-radiative, each playing a role in the emission characteristics of the rings.

Three QR calibration samples (Q1, Q2 and Q3) were grown back-to-back by MBE with subtly different Sb-valve positions during the growth resulting in Sb-flux variations between the growths. Samples Q1, Q2 and Q3 had valve positions of 110 mil, 130 mil and 90 mil respectively. The precise details of valve position are not important as the flux is also dependent on the specific MBE conditions at the time of growth; however, they provide insight into the relative Sb-flux for each sample. Continuously-pumped photoluminescence measurements (discussed in section 4.3) for the three QR samples in bulk-GaAs are shown in Figure 10.1, all samples were excited with the same laser power. The spectra reveal a broad photoluminescence response spanning approximately 1.1 µm to 1.4 µm. The peak on the left hand side of the spectrum is attributed to GaAs emission. In all cases the emission spectrum resides in the same wavelength range but with varying emission intensity relative to the GaAs peak. The emission spectrum is dominated by the capacitive charging of quantum rings [144]. In addition, Hodgson et al. found that the occupancy of GaSb QRs at a given excitation power is self-limited [21], resulting in an emission spectrum which depends on excitation power and recombination dynamics, rather than local doping and carrier concentration. It is therefore unsurprising that rather subtle changes in Sb flux do not significantly impact the emission spectrum. Sample Q3 produced the most luminous quantum rings and was used for the TRPL measurements used later in this chapter. The final VCSEL in this work with a cavity length of $3\lambda/2$ (chapter 11) was grown immediately after the Q3 calibration sample with the same calibrated growth parameters.

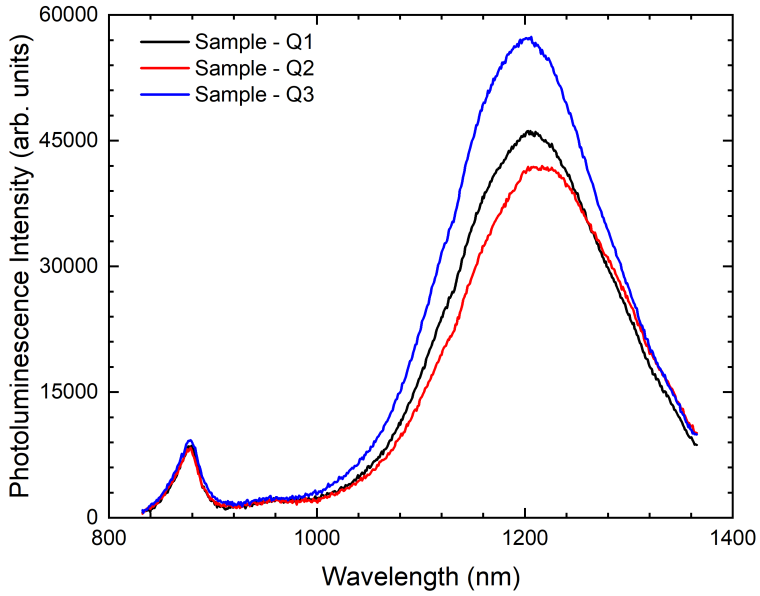

Figure 10.1: Continuously pumped room-temperature photoluminescence measurements for three quantum ring samples grown with different Sb-flux. Samples are all pumped with the same laser power at 532 nm.

Time-correlated single-photon counting (TCSPC) time-resolved photoluminescence (TRPL) measurements were performed on sample Q3 and on GaSb quantum rings within a VCSEL cavity to investigate the dynamics of the recombination. It has been reported that GaSb quantum rings exhibit very long recombination lifetimes, with radiative lifetimes on the order of microseconds [21]. The recombination lifetimes are also believed to be dependent on the emission energy of the rings, with higher charge states corresponding to a stronger coulomb binding energy and faster recombination lifetimes [145]. The long lifetimes of the quantum rings are promising for VCSELs due to a reduction in the pumping rate required to achieve population inversion of carriers in the active region. The spontaneous emission coupling factor, β, is defined as the spontaneous emission power coupled into a single mode as a proportion of the power coupled into all modes [24]. A marked reduction in carrier lifetime at the resonant wavelength of the cavity would correspond to an increase in β for the cavity, a reduction in threshold current for a laser and allow for higher-frequency modulation. It is of interest to determine whether the carrier lifetime is significantly enhanced by the introduction of a cavity, or whether there are other limiting factors on the recombination rate.

It is important to note that a series of studies have published TRPL measurements on GaSb quantum dot systems. The previous work at Lancaster studied the recombination lifetimes of MBE-grown GaSb quantum rings contained within $Al_xGa_{1-x}As$ quantum wells. In the experiment, the recombination lifetimes were unaffected by all but the narrowest 5 nm quantum well. The long microsecond timescale obtained by the work is in contrast to other work on MBE-grown GaSb quantum dots which suggests lifetimes on the nanosecond scale [146, 147]. The coexistence of short nanosecond lifetimes and a much slower microsecond decay rate has been observed in MOCVD-grown quantum dots [148].

It is believed that the recombination rate of GaSb quantum dots is heavily linked to the localised carrier density around the quantum dots/rings [148]. In addition, the electron-hole interaction which influences the recombination time of GaSb nanostructures has been shown to vary depending on subtle morphological differences at the nanoscale [149].

Initially, this raises two possibilities for the contrasting nanosecond and microsecond lifetimes in the literature. Primarily, it is likely that the lifetimes quoted in the literature are a reflection of the carrier density achieved during the experiments. The nanosecond lifetimes would accompany high carrier densities in samples pumped with higher laser powers and the microsecond lifetimes appearing in samples pumped with less power, or once the initial high carrier density has decreased. It would be of interest to observe the decay of samples quoted to exhibit nanosecond recombination lifetimes over a longer time scale to explore whether this is purely a measurement associated with high carrier densities and if the microsecond lifetime also becomes apparent in these samples as the carrier density decreases.

Secondly, each of the samples are prepared and capped under different growth conditions. Capping of GaSb quantum dots using $In_xGa_{1-x}As$ not only changes the band structure of system being studied, but is also likely to affect the morphology of the dots. In addition, MOCVD growth will lead to inherently different morphology of quantum dots when compared to MBE-grown quantum rings. It would not be surprising that different growth conditions yield significant differences in the recombination lifetimes.

In hindsight, it is likely that some of the studies of MBE-grown dots were in fact be performed on GaSb quantum rings as no microscopy was published confirming the dot-like nature of the GaSb nanostructures which are known to decompose under As-flux

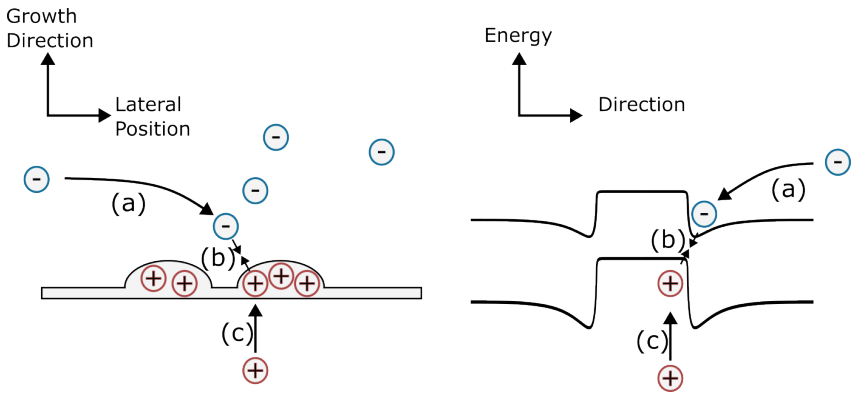

Figure 10.2: A cartoon band structure (right) for the schematic (left) of (a) electron capture, τ_e, (b) electron-hole recombination mechanisms, τ_{nr}, τ_{rad}, and (c) hole capture, τ_h, in the vicinity of GaSb quantum rings.

in MBE. For the case of MOCVD grown dots it is likely that As-Sb intermixing occurred and that such dots are in fact composed of $GaSb_xAs_{1-x}$ [53].

In light of the variation in lifetimes presented in the literature and the clear differences in morphology of the nanostructures when compared to MBE-grown quantum rings capped with GaAs, it is of interest to study the recombination mechanisms of the quantum rings further and in the presence of the VCSEL cavity.

The previous works have used lasers emitting above the bandgap energy of GaAs and InGaAs, therefore pumping the materials cladding the quantum dots and rings. In this work a 980 nm pump laser is used for the TRPL measurements, ensuring that only the quantum rings and wetting layer may be excited.

The recombination mechanisms in quantum rings are complex and dependent on multiple processes each with a characteristic lifetime and dependence on local charge density. Electrons away from the quantum rings are delocalised and free to move, these electrons may be captured by a ring with an electron capture lifetime, τ_e. It is important to note that the type-II nature of the rings means that electrons are not trapped by a potential well in the conduction band, but by Coulomb interaction with confined holes. Electrons and holes within a quantum ring may then recombine either radiatively or non-radiatively with characteristic lifetimes τ_{rad} and τ_{nr}. Quantum ring recharging occurs via a further hole-recapture mechanism with lifetime, τ_h. The hole-recapture is expected to be very fast due to the deep hole-confining potential. The three categories of process that contribute to the recombination in quantum rings are depicted in Figure 10.2. This simplistic view of the recombination mechanisms reveals already-complex dynamics for the quantum ring system. In reality, there are additional processes to account for such as electrons escaping before recombination can occur and multiple forms of each radiative/non-radiative process. In addition, the carrier-density dependent rate of each process may introduce non-linear behaviour of the decay rate in time.

The intensity of the photoluminescence emission is fit using exponential decay models to determine the lifetime of the various processes involved with carrier recombination. It is not appropriate to fit the TRPL decay using a multi-exponential decay model with separate lifetime for each process as the fit may be over-parametrised and un-physical. The photoluminescence decay for QRs in a VCSEL off-resonance was fitted using bi-exponential and tri-exponential decay models (Figure 10.3) to obtain an average lifetime, τ_{av}, for carriers based on the dominant τ_{rad} and τ_{nr} rate-limiting mechanisms. Both fits

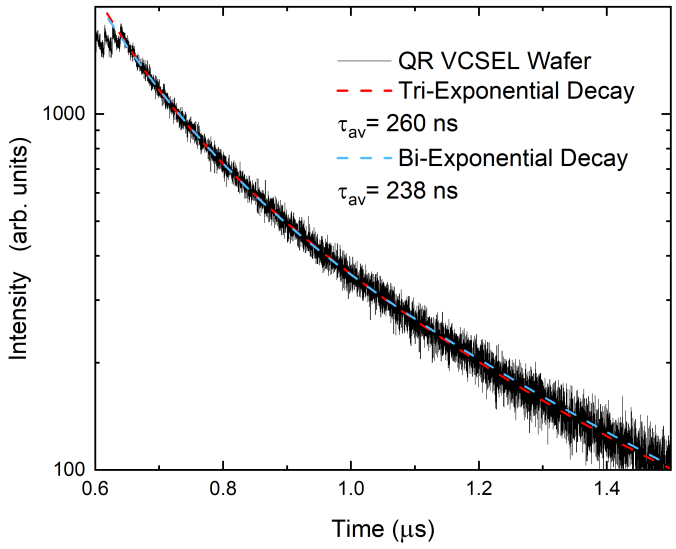

Figure 10.3: Photoluminescence decay of recombination for GaSb quantum rings in a VCSEL-wafer cavity off-resonance (1161nm). The decay is fitted with bi-exponential and tri-exponential decay functions.

yield an average decay time between 200 ns and 300 ns which is consistent with previous measurements by Hodgson et al. [21]. The type-II rings exhibit comparatively long lifetimes to type-I quantum dot systems which have radiative recombination lifetimes on the order of nanoseconds [150, 151, 152] and may have faster non-radiative recombination mechanisms. It has been suggested that the radiative and non-radiative lifetimes are in competition, with radiative lifetimes believed to be on the order of microseconds and dominated by order of magnitude faster non-radiative recombination [21].

The optical cavity formed between a pair of DBRs is expected to reduce the radiative lifetime, τ_{rad}, and enhance emission at the resonant wavelength of the cavity [153] whilst leaving non-radiative lifetimes τ_{nr}, τ_e, and τ_h unaffected. A bi-exponential decay model with characteristic lifetimes τ_1 and τ_2 was used to investigate the reduced carrier lifetime. An unmistakable drop in lifetime τ_1 is seen at the cavity emission wavelength (Figure 10.4). This corresponds to a factor of three lifetime reduction compared to off-resonance emission in the VCSEL and reduction compared to the rings-in-GaAs control sample. In contrast, τ_2 does not show a significant reduction in lifetime so the reduction in average lifetime, τ_{av}, is a result of τ_1. The reduction in τ_1 is consistent with a cavity enhanced emission and therefore corresponds to a recombination mechanism with an optical component. This result has stark implications regarding the recombination mechanisms. At first, one might suspect a much shorter radiative lifetime for quantum rings in the range of 100 ns which is in contrast to the microsecond recombination suggested previously. In reality, the lifetime τ_1 is representative of multiple capture and recombination pathways and distinction between radiative and non-radiative lifetimes requires further investigation which is beyond the scope of this work. It is possible that fast non-radiative recombination is limited by a slower capture mechanism; simultaneously, the radiative recombination can contribute more strongly to the overall emission whilst having a slower recombination rate. This strong recombination would simultaneously allow a

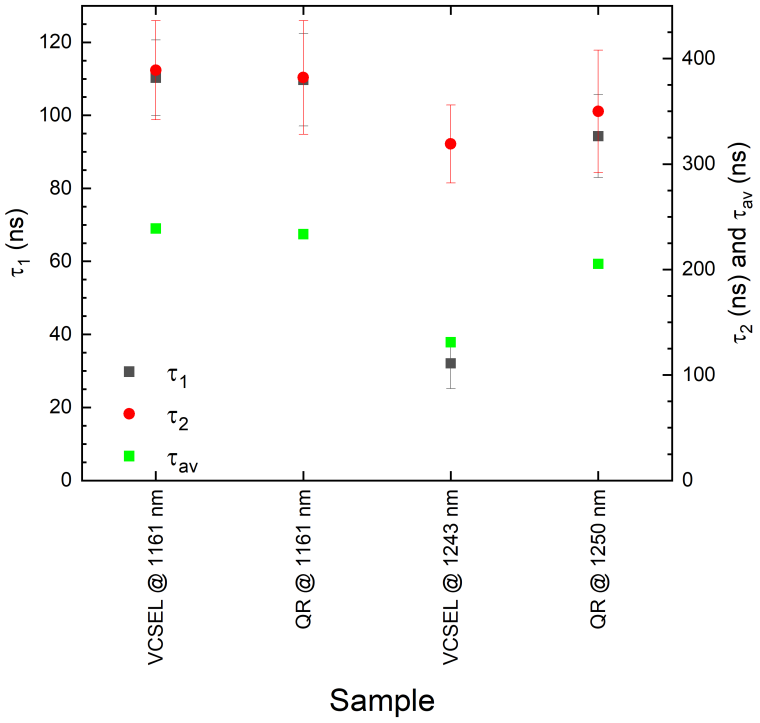

Figure 10.4: Fitted lifetimes τ_1, τ_2 and corresponding average lifetimes, τ_{av}, for GaSb quantum rings in the cavity of unprocessed VCSEL material - denoted VCSEL - and bulk GaAs - denoted QR. Fitting is performed off-resonance for the cavity at 1161 nm, and on resonance at 1243 nm, with corresponding reference lifetimes collected at 1161 nm and 1250 nm. The samples were pumped by a 980 nm pulsed laser.

fast non-radiative recombination mechanism which is inhibited by a slower process, and a reduction in radiative recombination lifetime, which together contribute to a reduced average lifetime. Primarily, it is clear that the cavity enhances the recombination of the rings at the cavity resonance which will reduce the threshold current and increase the maximum modulation frequency.

Chapter 11

GaSb Quantum Ring VCSELs

As far as can be seen in the literature, GaSb QR VCSEL research is exclusive to Lancaster University. GaSb quantum dots and rings have been utilised in optically-pumped photonic crystal cavities and microdisk lasers [154, 155, 156], whilst electrically-pumped lasers have been realised by the inclusion of GaSb quantum dots within $In_xGa_{1-x}As$ quantum wells [157]. Room-temperature lasing of the electrically-pumped devices was reported for a device of 2 mm in length. The emission wavelengths of the existing lasers are in the region of approximately 950 nm to 1050 nm. It is the intention for future GaSb QR VCSELs to demonstrate electrically-pumped lasing at longer wavelengths than existing GaSb QD/QR devices.

This chapter provides a summary of GaSb quantum ring VCSEL design and modelling, followed by experimental results demonstrating the performance of such devices. First, the simulation of VCSELs is introduced with comments on the applicability of widely-available models to GaSb QR-based VCSELs. The status of GaSb QR VCSEL device performance prior to the work of this thesis is presented in section 11.2, and acts as the base from which this work is built (section 11.3). Next, the characteristics and performance of devices produced as a part of this work are presented with a discussion of the implications of the device performance on the physics of these devices. Finally, a direction for future work and the outlook for QR VCSELs is given.

A summary of the VCSEL samples discussed in this work is given in Table 11.1 for reference. The specific details of each structure are contained in sections 11.2 and 11.3.

Sample ID (Alternative name)	**Summary/Defining Features**
	Prior Work
P1	Low-contrast GaAs/$Al_{0.6}Ga_{0.4}As$ DBRs.
P2	Similar to P1, targeting longer wavelengths.
P3	High-contrast GaAs/$Al_{0.9}Ga_{0.1}As$ DBRs.
	This Work
V1	Stepped-interface DBRs with low doping.
V2	A failed growth for a VCSEL consisting of stepped-interface DBRs with higher doping and more DBR repeats than V1.
V3	A successful regrowth of V2.
V4	The QR VCSEL cavity length was extended to $3\lambda/2$ and an $Al_{0.98}Ga_{0.02}As$ layer was incorporated for the option of oxide aperture formation.

Table 11.1: A reference of the sample ID for each of the VCSELs discussed in this work. QR VCSELs from prior work are denoted with the letter P, samples from this work are denoted with the letter V. Samples are numbered in chronological order according to their growth date.

11.1 VCSEL Design and Modelling

VCSEL simulations are often performed using finite-difference time-domain (FDTD) software packages, such as Harold VCSEL by *PhotonDesign*. These models are capable of

solving for optical cavity modes in three-dimensions, taking into account geometry of fabricated devices. Such models include effects of scattering from oxide apertures and reflection from contacts. Electrical characteristics of the VCSELs are simulated including aspects such as current confinement due to oxide apertures, contact resistances and the calculation of leakage currents. Full VCSEL simulations claim to track the time-evolution of such characteristics including effects of Joule heating in the bulk and contacts, carrier recombination mechanisms, free carrier absorption, and intervalence band absorption. Advanced models are readily available for commonplace quantum-well devices, with quantum dot models under active development. At the time of this work, parameters such as the gain spectrum of GaSb quantum rings are unknown and as such, complex FDTD models are not available for GaSb quantum rings, nor are they practical to produce within the scope of this work. However, FDTD models would be a beneficial tool in the latter stages of GaSb QR VCSEL device design and remains an important area for further study. In light of the simulation challenges of these devices, the decision is taken to perform an experimentally-aligned investigation of QR VCSEL device properties.

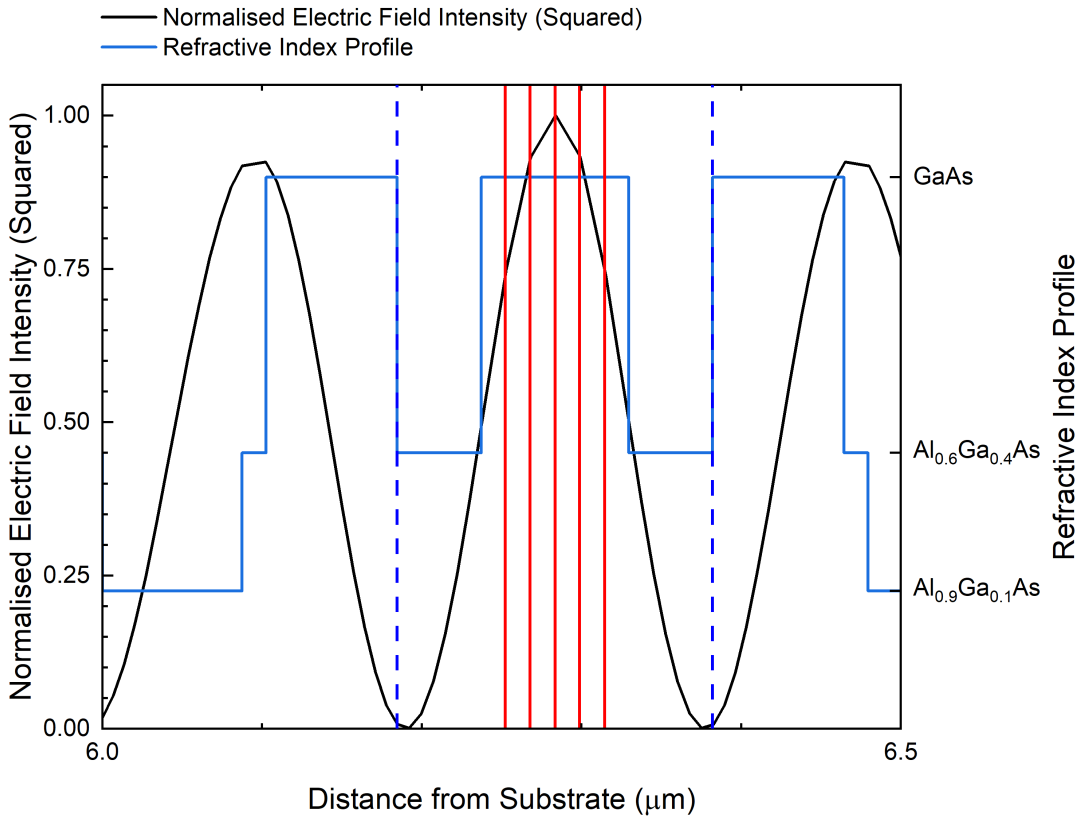

Figure 11.1: The electric field and refractive index profiles within the VCSEL are given as a function of position for the final design of a stepped-interface DBR VCSEL with $\lambda/2$ cavity length. The positions of the quantum ring layers are indicated by the vertical red lines and the outer extremes of $Al_{0.6}Ga_{0.4}As$ spacer layers in the cavity are indicated by the blue dashed lines.

The initial design of QR VCSEL devices is aided by commercial TFCalc modelling software (chapter 3) using the following design flow. Top and bottom DBRs are designed

with the maximum reflectance at the VCSEL target wavelength according to chapter 9. The number of repeats in each DBR is tuned such that the reflectance of light incident from the $Al_{0.6}Ga_{0.4}As$ spacer layers is equal to that of the desired reflectance. A full VCSEL stack is then described in TFCalc and consists of the GaAs substrate, lower DBR, $Al_{0.6}Ga_{0.4}As$ spacer layers, GaAs and GaSb cavity and QR layers, an optional $Al_{0.98}Ga_{0.02}As$ oxidation layer, and the upper DBR. Normal-incidence reflectance of the VCSEL stack is simulated from the top-surface and the spacer layer thicknesses are tuned to ensure coincidence of the Fabry-Perot cavity resonance with the target emission wavelength. One-dimensional models of the optical mode profile are represented by the electric field intensity (EFI) profile calculated within the VCSEL stack (Figure 11.1). Thicknesses of GaAs layers in the cavity are tuned to ensure that the quantum ring layers are aligned centrally over the maxima of the EFI profile. The resulting designs provide reasonable agreement with the desired wavelength using the material parameters available. It is worth noting that these models do not account for variations in refractive index that may occur under high carrier densities, nor the effects of three-dimensional device geometry or metal contacts.

11.2 Prior Work

Prior to this work numerous QR VCSEL design variations were investigated, a key subset of the devices is summarised here. In the first instance, low-contrast $GaAs/Al_{0.6}Ga_{0.4}As$ DBRs were used, with a single high aluminium composition layer at the cavity edge (structure in Table 11.2), this structure (P1) was grown on an older VG80 MBE reactor at Lancaster University. A similar structure was regrown on the newly commissioned VEECO GENXplor at a later date (P2) incorporating thicker DBR and spacer layers, with the target of reaching longer wavelengths. Both devices exhibited background emission across the QR spectrum (Figure 11.2) and immeasurably low output powers. One possible cause of the low power output, poor efficiency and background emission profile was the low contrast of the DBR layers which resulted in relatively low reflectivity DBRs of 94.2% (upper) and 98.6% (lower) [60]. A series of VCSELs were then produced using $GaAs/Al_{0.9}Ga_{0.1}As$ high-contrast DBRs with the aim of producing a stronger cavity resonance [60]. The success of these devices was limited, with devices exhibiting either extraordinarily high series resistance, requiring tens of volts to achieve milliamp currents, or reasonable electrical characteristics but poor emission profiles (Figure 11.2). In an attempt to reduce the resistance contributions of the upper DBR, the p-side contacts were placed close to the cavity (Figure 11.3) and culminated in the design and growth of sample P3 (see Table 11.3). The uppermost five DBR-repeats of the VCSEL structure were left undoped, as it was believed that optical absorption was hampering the performance of previous QR VCSELs. Placing the contacts closer to the active region meant that there was no reason to continue to dope the uppermost layers. Reasonable electrical characteristics were obtained in the final iteration of the high-contrast VCSELs (P3). It is believed that the contact placement, coupled with the lack of a current-guiding aperture, resulted in the poor emission profile (Figure 11.2) and low output efficiency. It is possible that much of the emission at the resonant wavelength was generated directly below the top contact which subsequently blocked the output emission.

	Material	Dopant	Concentration (cm^{-3})	Thickness (nm)
		P1		
Contact Layer	GaAs	p-type (Be)	1.7×10^{19}	92.5
Upper DBR x24	$Al_{0.6}Ga_{0.4}As$	p-type (Be)	2×10^{18}	104.5
	GaAs	p-type (Be)	5×10^{18}	92.5
High-Al Repeat	$Al_{0.9}Ga_{0.1}As$	p-type (Be)	2×10^{18}	108.3
Spacer	$Al_{0.6}Ga_{0.4}As$	i	-	156.1
GaSb QR x5	GaAs	i	-	10
	GaAs (cold)	i	-	5
	GaSb	i	-	2.1 ML
Cavity	GaAs	i	-	15
Spacer	$Al_{0.6}Ga_{0.4}As$	i	-	156.1
High-Al Repeat	$Al_{0.9}Ga_{0.1}As$	n-type (Si)	5×10^{17}	108.3
Lower DBR x34	GaAs	n-type (Si)	1.3×10^{18}	92.5
	$Al_{0.6}Ga_{0.4}As$	n-type (Si)	5×10^{17}	104.5
Buffer	GaAs	n-type (Si)	5×10^{18}	190
Substrate	GaAs	n-type (Si)	1×10^{18} to 5×10^{18}	0.35 mm

Table 11.2: Epitaxial design of the initial QR VCSEL (P1).

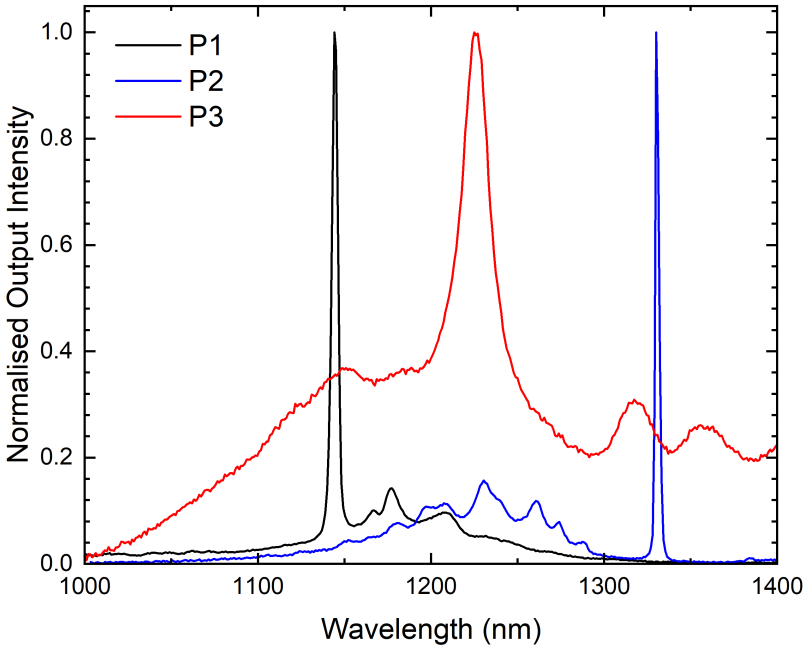

Figure 11.2: Normalised room-temperature electroluminescence spectra of QR-VCSEL samples with low aluminium-contrast $Al_xGa_{1-x}As$ DBRs (P1 and P2) and high aluminium-contrast $Al_xGa_{1-x}As$ DBRs (P3) for VCSELs grown prior to this work. It is clear that the VCSEL incorporating high aluminium-contrast DBRs suffers from an broad and relatively intense background emission.

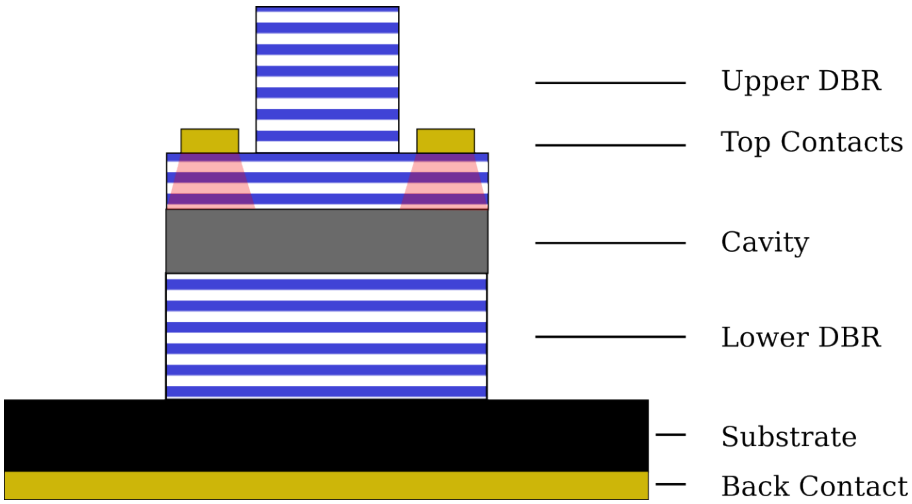

Figure 11.3: A schematic of the geometry of the fabricated VCSELs using sample P3. Top contacts are placed on an etched surface below undoped layers in the upper-DBR. Red highlighting under the contacts represents an area where much of the light may be produced.

	Material	Dopant	Concentration (cm^{-3})	Thickness (nm)
		P3		
Contact Layer	GaAs	i	-	92.1
Upper DBR x5	$Al_{0.9}Ga_{0.1}As$	i	-	106.4
	GaAs	i	-	93.1
Upper DBR x10	$Al_{0.9}Ga_{0.1}As$	p-type (Be)	2×10^{18}	106.4
	GaAs	p-type (Be)	2×10^{18}	93.1
Spacer	$Al_{0.6}Ga_{0.4}As$	i	-	44.9
GaSb QR x5	GaAs	i	-	10
	GaAs (cold)	i	-	5
	GaSb	i	-	2.1 ML
Cavity	GaAs	i	-	15
Spacer	$Al_{0.6}Ga_{0.4}As$	i	-	44.9
Lower DBR x30	GaAs	n-type (Si)	2×10^{18}	93.1
	$Al_{0.6}Ga_{0.4}As$	n-type (Si)	2×10^{18}	106.4
Buffer	GaAs	n-type (Si)	2×10^{18}	-
Substrate	GaAs	n-type (Si)	1×10^{18} to 5×10^{18}	0.35 mm

Table 11.3: Epitaxial design of sample P3 which utilised high-contrast abrupt interface DBRs and incorporated undoped DBR repeats at the top of the structure to minimise optical absorption which was believed to hamper performance of previous QR VCSELs.

11.3 This Work

The high-resistance but high-reflectivity DBRs in the previous generation of VCSELs inspired the studies in chapter 9 that lead to the design of lower-resistance DBRs with high reflectivity. The VCSELs in this work are based on the stepped-interface DBR, with high doping levels used to improve the electrical performance. The low-resistance high-reflectivity mirrors enable the design of a high-quality cavity whilst keeping the contacts further from the active region of the device to allow for current spreading in the absence of a current-guiding aperture. QR-VCSEL devices in this work consist of a cavity containing the active region defined by a pair of semiconductor DBRs. A high aluminium content $Al_{0.98}Ga_{0.02}As$ layer may be included above the cavity with the intention to form an oxide aperture. At present, the devices exhibit a large background emission and discrepancies between the designed and epitaxially-grown VCSEL-material. Because of the large background and growth discrepancies, the additional processing associated with the oxide aperture has not been justified.

11.3.1 First-Generation Stepped-Interface VCSEL - V1

Table 11.4 describes the structure of the first VCSEL produced as part of this work, with a target emission wavelength of 1270 nm. 1270 nm was chosen as it is the wavelength used for upstream transmission on the XGS-PON standard [158]. The upper and lower DBRs were designed with a reflectivity of 97.9 % and 98.5 % respectively. As seen in Figure 11.4, the emission wavelength is longer than intended. The longer wavelength is attributed to layers that were grown too thick due to inaccurate calibration of growth rates in the MBE. The exact layer thicknesses for this sample were never measured but an illustrative model for alternative layer thicknesses is shown in Figure 11.5. In addition to the inaccurate growth rate calibration, it was later discovered that the beryllium doping cell was obstructed during this growth campaign. The obstruction led to lower than anticipated doping and is likely responsible for the poor electrical characteristics of this structure that are seen in Figure 11.6. Nevertheless, despite the poor electrical characteristics, this sample exhibited a more prominent cavity peak than the previous high-reflectivity sample and a measurable spectrum at lower drive currents. Without the ability to measure both P1 and V1 in the same optical set-up, it is neither possible nor appropriate to compare the output intensity on an absolute scale.

	Material	Dopant	Concentration (cm^{-3})	Thickness (nm)
		V1		
Contact Layer	GaAs	p-type (Be)	5×10^{18} to 1×10^{19}	82.2
Upper DBR x15	$Al_{0.6}Ga_{0.4}As$	p-type (Be)	5×10^{18}	15
	$Al_{0.9}Ga_{0.1}As$	p-type (Be)	5×10^{18}	87.3
	$Al_{0.1}Ga_{0.9}As$	p-type (Be)	5×10^{18}	15
	GaAs	p-type (Be)	5×10^{18}	82.2
Spacer	$Al_{0.6}Ga_{0.4}As$	i	-	52.7
GaSb QR x5	GaAs	i	-	10
	GaAs (cold)	i	-	5
	GaSb	i	-	2.1 ML
Cavity	GaAs	i	-	15
Spacer	$Al_{0.6}Ga_{0.4}As$	i	-	52.7
Lower DBR x21	GaAs	n-type (Si)	1×10^{18}	82.2
	$Al_{0.6}Ga_{0.4}As$	n-type (Si)	5×10^{18}	15
	$Al_{0.9}Ga_{0.1}As$	n-type (Si)	5×10^{18}	87.3
	$Al_{0.6}Ga_{0.4}As$	n-type (Si)	5×10^{18}	15
Buffer	GaAs	n-type (Si)	5×10^{18}	170
Substrate	GaAs	n-type (Si)	1×10^{18} to 5×10^{18}	0.35 mm

Table 11.4: Epitaxial design of the first stepped-interface QR VCSEL (V1).

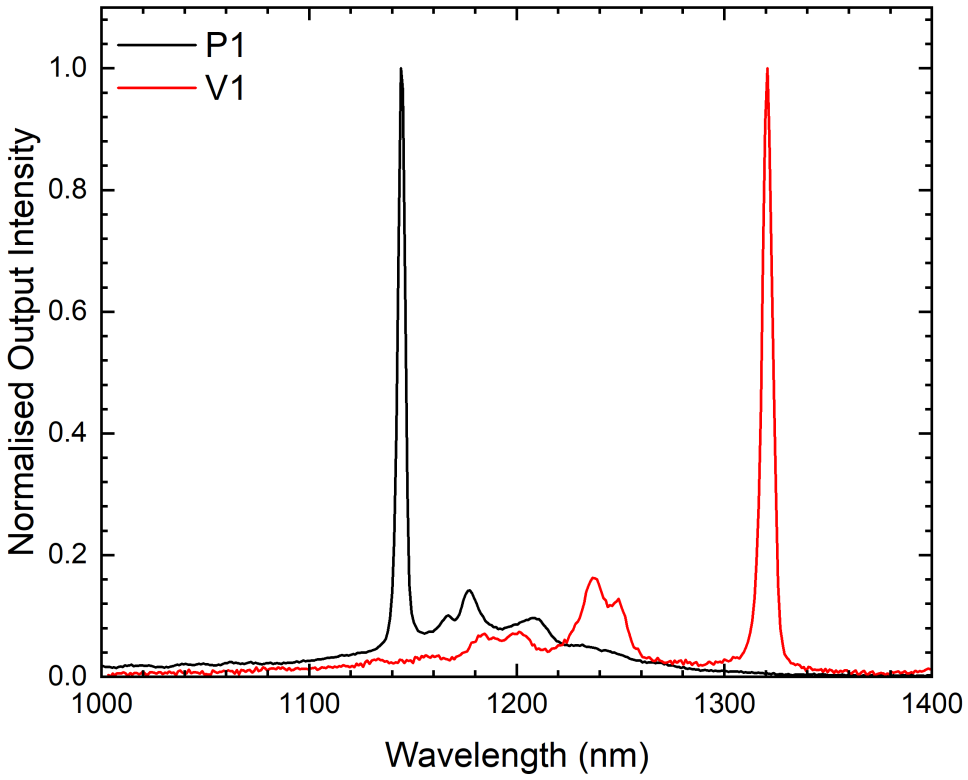

Figure 11.4: Normalised room-temperature electroluminescence spectra of QR-VCSEL samples with low aluminium-contrast DBRs (P1) and high aluminium-contrast stepped-interface DBRs (V1). The spectra exhibit similar relative intensities of the background emission.

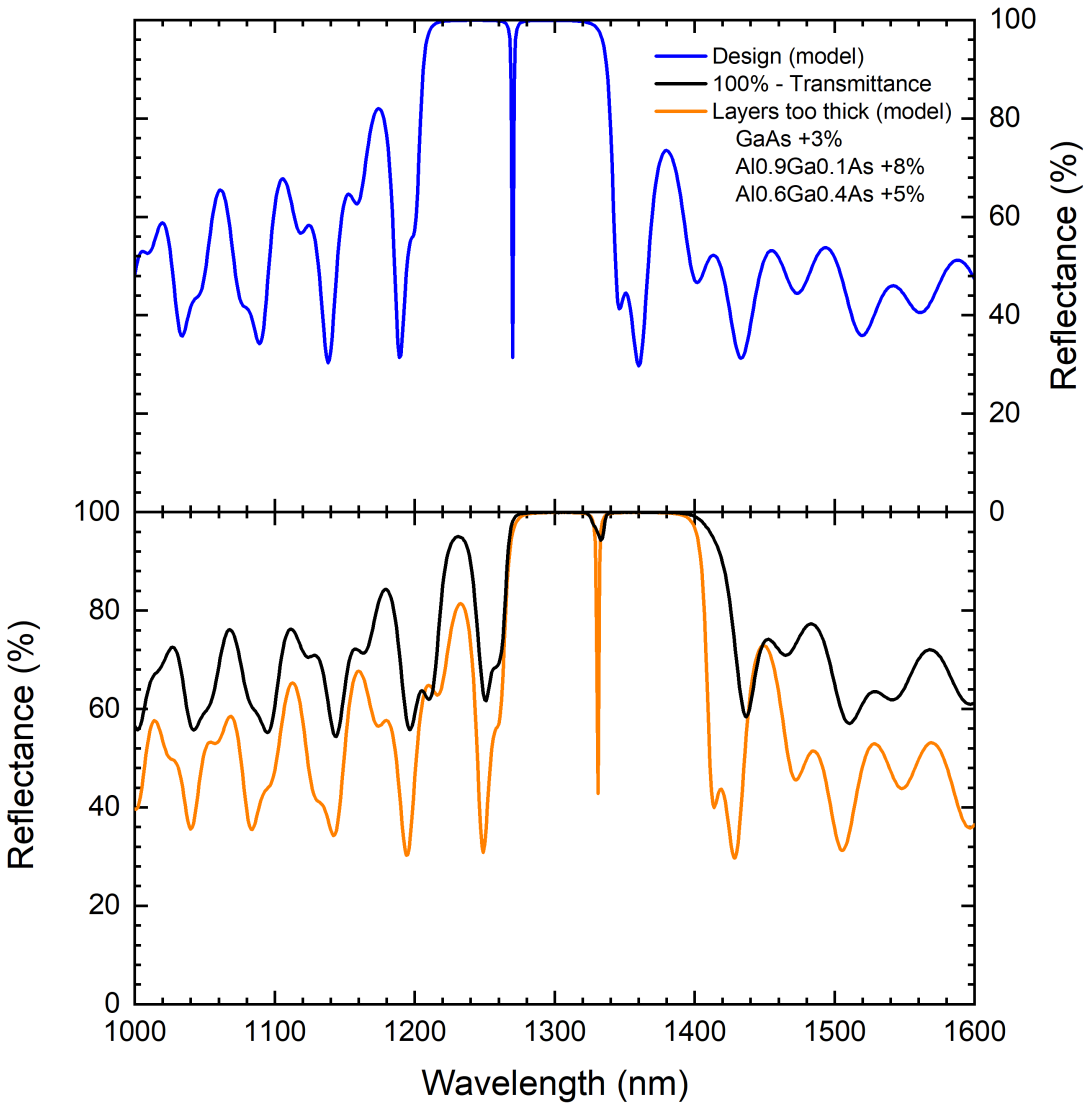

Figure 11.5: A model of the reflectance spectrum is shown for a VCSEL (sample V1, see Table 11.1) with stepped-interface DBRs designed for operation at 1270 nm (top). The spectrum obtained from transmittance measurements (bottom) shows a significant shift in the wavelength of the reflectance spectrum. A model that fits the shift in spectrum is shown for comparison.

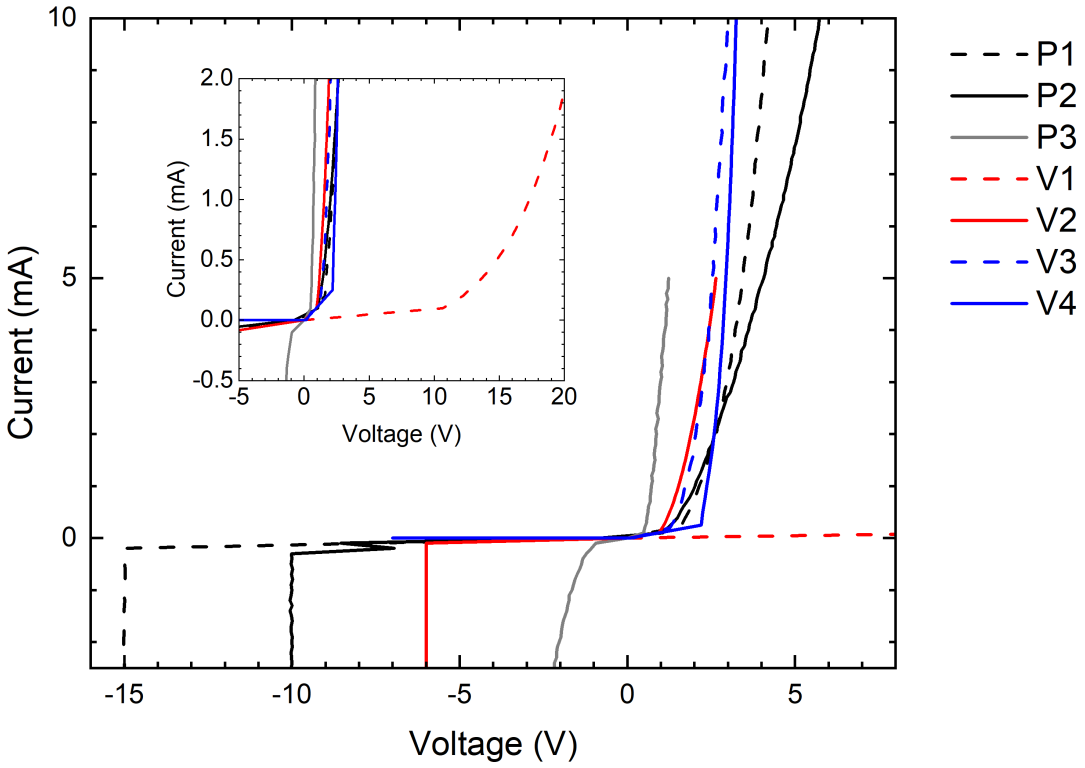

Figure 11.6: Current-voltage characteristics of VCSEL devices. Low-contrast low-reflectivity DBRs (P1 and P2), high-contrast high-reflectivity DBRs (P3), stepped-interface high-reflectivity DBRs (V1, V2, V3 and V4). Sudden drops in the reverse IV are an artefact of the measurement and not representative of the device performance.

	Material	Dopant	Concentration (cm^{-3})	Thickness (nm)
V2 and V3				
Contact Layer	GaAs	p-type (Be)	5×10^{18} to 1×10^{19}	82.2
Upper DBR x21	$Al_{0.6}Ga_{0.4}As$	p-type (Be)	5×10^{18}	15
	$Al_{0.9}Ga_{0.1}As$	p-type (Be)	5×10^{18}	87.3
	$Al_{0.1}Ga_{0.9}As$	p-type (Be)	5×10^{18}	15
	GaAs	p-type (Be)	5×10^{18}	82.2
Spacer	$Al_{0.6}Ga_{0.4}As$	i	-	52.6
GaSb QR x5	GaAs	i	-	10
	GaAs (cold)	i	-	5
	GaSb	i	-	2.1 ML
Cavity	GaAs	i	-	15
Spacer	$Al_{0.6}Ga_{0.4}As$	i	-	52.6
Lower DBR x34	GaAs	n-type (Si)	1×10^{18}	82.2
	$Al_{0.6}Ga_{0.4}As$	n-type (Si)	5×10^{18}	15
	$Al_{0.9}Ga_{0.1}As$	n-type (Si)	5×10^{18}	87.3
	$Al_{0.6}Ga_{0.4}As$	n-type (Si)	5×10^{18}	15
Buffer	GaAs	n-type (Si)	5×10^{18}	170
Substrate	GaAs	n-type (Si)	1×10^{18} to 5×10^{18}	0.35 mm

Table 11.5: Epitaxial design of the second-generation stepped-interface QR VCSELs (V2 and V3).

11.3.2 Second-Generation Stepped-Interface VCSELs - V2 and V3

The first iteration of the stepped-interface VCSEL showed no significant difference in the intensity of the background emission profile of the QR VCSEL when compared to the original low-contrast DBR VCSELs (Figure 11.4). A second design (Table 11.5) was produced with further increased mirror reflectivity with the intention of reducing the background in the emission profile. According to simulations, the upper and lower DBRs had reflectivity of 99.5 % and 99.9 % respectively. Unfortunately, the first growth to this design (V2) was visibly cloudy upon removal from the MBE chamber. TEM images (Figure 11.7) indicated numerous defects within the DBRs and a lack of distinct GaSb nano structures in the cavity. Figure 11.8 shows the transmittance spectra for a series of measurements across the wafer. In some cases a cavity resonance is visible in the region of 1300 nm, in others (scan 2) there is no apparent resonance. Despite the defects, the devices exhibited good electrical performance which cannot be explained by leakage currents due to the low levels of leakage under reverse bias. This indicates a recovery of the electrical properties of the stepped-interface DBRs when sufficient doping is present. The electroluminescence spectrum (Figure 11.9) shows a poor emission profile, in this

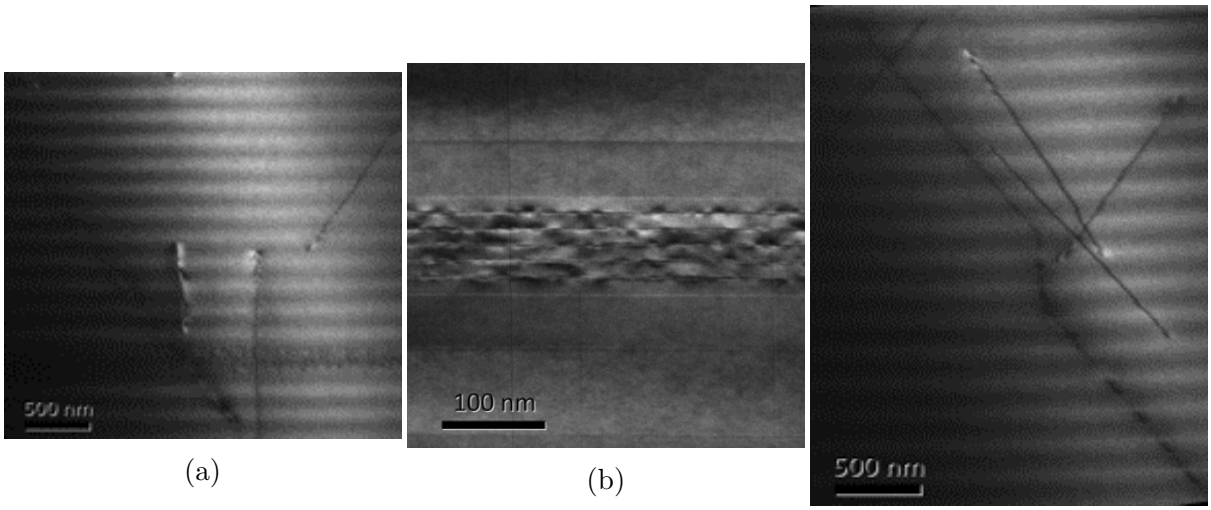

(a) (b) (c)

Figure 11.7: Transmission electron microscope images showing defects throughout V2. a) Defects originating in the lower DBR and propagating through a poor-quality cavity into the upper DBR. b) A poor active region showing few GaSb nano structures. c) Defects threading through the upper DBR.

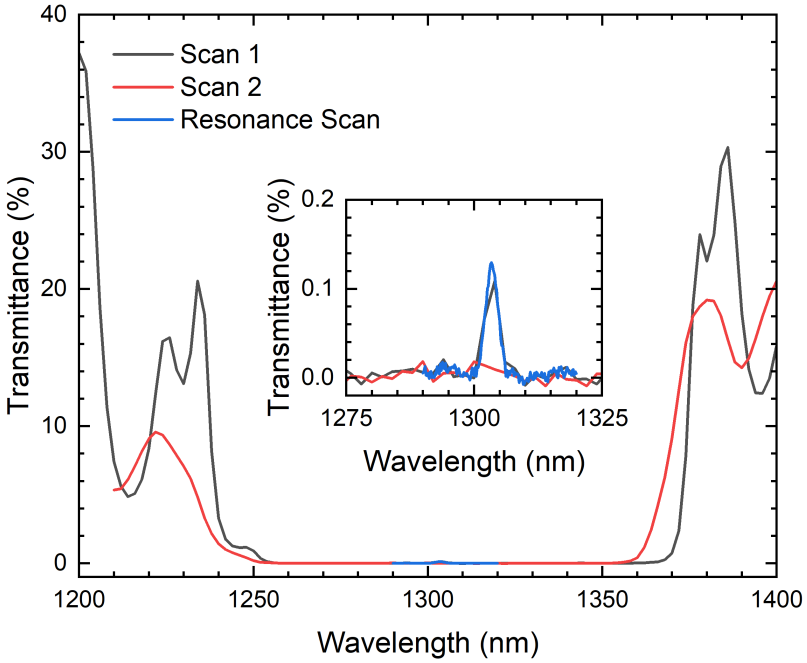

Figure 11.8: Multiple transmittance sweeps of sample V2 (see Table 11.1) show a weak cavity present around 1300 nm. Scan 2 indicates that the transmittance spectrum is not consistent across the sample and that there are regions lacking a clear cavity resonance. It should be noted that the sample was visibly cloudy to the naked eye.

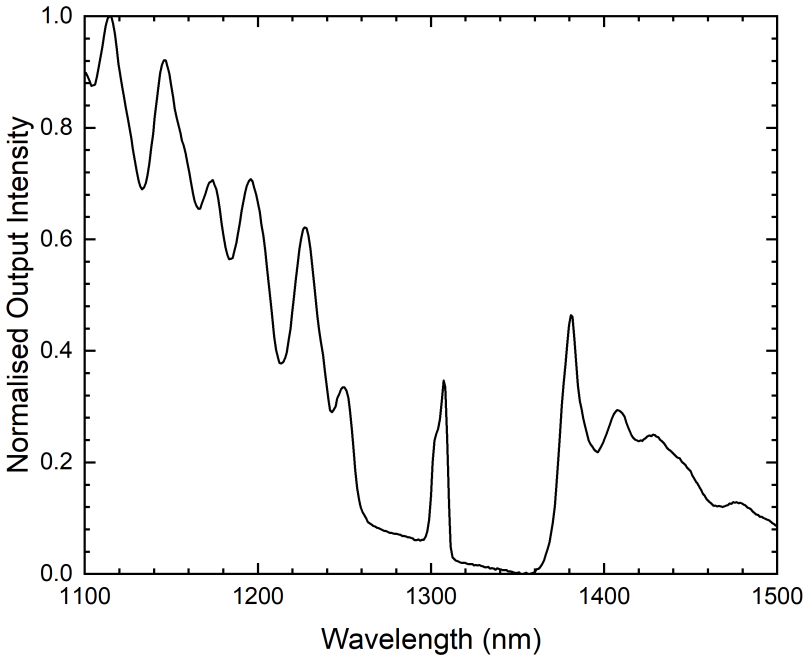

Figure 11.9: Normalised room-temperature electroluminescence spectra of QR-VCSEL sample V2.

case the emission intensity at the cavity resonance is lower than the emission at the sidebands. The poor emission profile may be attributed to a number of factors including a lack of stimulated emission due to a poor quality cavity at the resonant wavelength, weak emission from poorly-grown rings and optical losses through defects. This result demonstrates the need for a good optical cavity and high-quality growth. In addition, it also boosts confidence in the stimulated nature of emission at the cavity resonance for other devices in this work, both past and present.

Sample V3 is a successful regrowth of the cloudy sample, and hereafter may be referred to interchangeably as the $\lambda/2$ structure or as V3. V3 demonstrated some of the best electrical properties exhibited in this work (Figure 11.6), with a clear emission in the region of 1280 nm (Figure 11.10). The output intensity across the QR spectrum remains of the same relative amplitude as for the original low-contrast DBR VCSELs. This suggests that the emission profile is not solely linked to the quality of the cavity. Figure 11.11 shows that the intensity of the sidebands visibly increases relative to the cavity peak with increasing drive current. The idea was raised that the slow recombination rate of the quantum rings was limiting the emission intensity of the VCSEL. As the current increased, a growing proportion of the injected carriers were recombining spontaneously across the QR spectrum. Although this idea has now been disregarded (section 11.3.4) it was proposed that a device with an increased number of quantum ring layers would avoid this saturation of the output intensity at the cavity resonance.

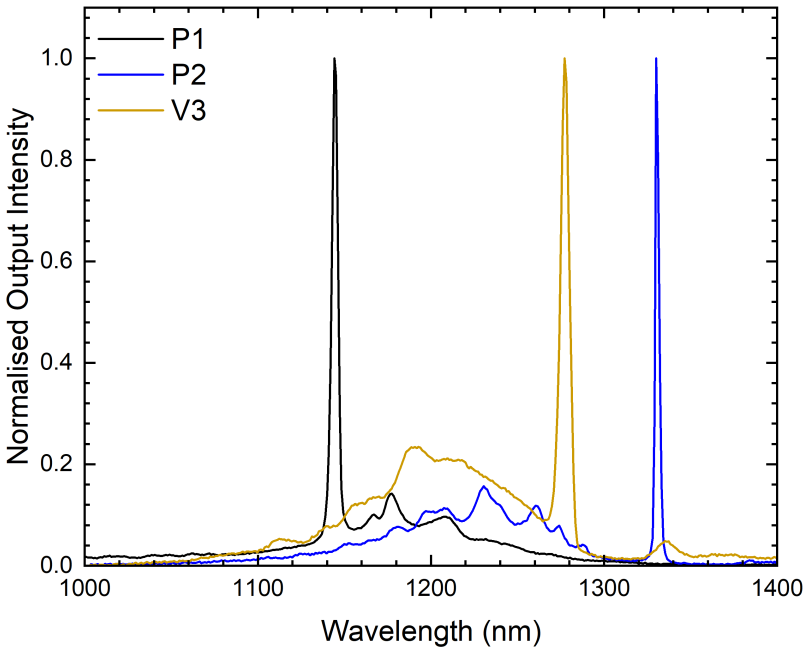

Figure 11.10: Normalised room-temperature electroluminescence spectra of QR-VCSEL samples V3, P1 and P2.

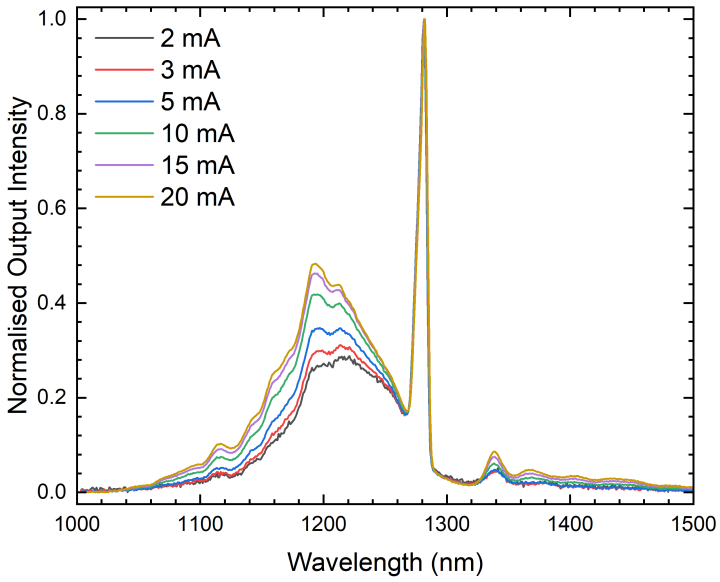

Figure 11.11: Normalised electroluminescence spectra of the $\lambda/2$ stepped-DBR VCSEL structure at various drive currents. The intensity of the sidebands visibly increases relative to the cavity peak as drive current increases.

11.3.3 Third-Generation Stepped-Interface VCSEL - V4

It is necessary to increase the peak output intensity of the QR VCSEL devices and reduce the background emission intensity. In an attempt to achieve this, a structure (sample V4) was designed with a $3\lambda/2$ cavity and a three times increase in the number of quantum ring layers when compared to the $\lambda/2$ structure. The structure, hereafter referred to as the $3\lambda/2$ structure, can be seen in Table 11.6 and incorporates a 30 nm $Al_{0.98}Ga_{0.02}As$ oxidation layer.

The structure was designed to emit at 1270 nm and it is clear from the reflectance spectrum (Figure 11.12) that the cavity resonance does not align with the target wavelength. TEM was used to measure the as-grown layer thickness in the cavity and for the first DBR repeats adjacent to the cavity on a small sample of the full wafer. During the growth of each DBR the growth rates of the III-V materials drift, meaning that the extracted layer thicknesses are not applicable to every layer in the VCSEL. Nevertheless, simulating the reflectance based on the layer thickness measurements provides a good approximation for the expected spectrum. It is clear from Figure 11.12 that the position of the cavity resonance and stopband are in reasonable agreement for the new simulation and the measured reflectance spectrum. In this case the DBRs had shifted to shorter-wavelengths and the cavity emission towards the longer-wavelength side of the stopband, resulting in a reduced reflectivity of the mirrors at the resonant wavelength. Full device processing was performed on the material despite the discrepancy between the design and the grown structure because a clear cavity resonance was present and the sample represented one of the best VCSEL growths to date. Following device processing it immediately became clear that there was no significant reduction in intensity of the background emission (Figure 11.13). Due to the lack of reduction in background emission it was not appropriate to incur the additional time and complexity of the oxide aperture incorporation with external collaborators. This will be reserved for future work when the background emission has been reduced significantly. Much of the analysis in this work is presented for $3\lambda/2$ cavity VCSELs due to their superior growth quality.

Emission Spectrum

The temperature dependence of the VCSELs is shown in Figure 11.14. A temperature sweep from 20 °C (room temperature) to 60 °C exhibits the characteristic redshift of emission wavelength which is well known for VCSELs. In this instance the redshift has an associated coefficient of (0.09 ± 0.01) nm/K which is comparable to other GaAs-cavity VCSELs operating around 1300 nm [20]. The redshift is due to changes in the refractive index and consequently the cavity resonance. In this instance, it is notable that the background emission across the quantum ring spectrum appears to be suppressed compared to the cavity peak at higher temperatures, this trend is more obvious when plotted on a normalised scale (Figure 11.14a). It is suspected that the reduction in background emission as temperature increases is due to non-radiative carrier recombination being favoured over the slow spontaneous recombination, whereas the cavity enhanced peak emission wavelength, which has a significantly reduced recombination time (chapter 10), is less affected. At 77 K the emission of the VCSEL displays the characteristic blue shift relative to room temperature (Figure 11.14b). The background emission is also blue-shifted, as expected due to an increase in bandgap, and more intense relative to the room temperature data [159]. The explanation for the increased intensity of the background is analogous to the explanation given for the room-temperature to 60 °C sweep, i.e. at

lower temperatures the non-radiative recombination is reduced and therefore does not suppress the slower spontaneous radiative recombination.

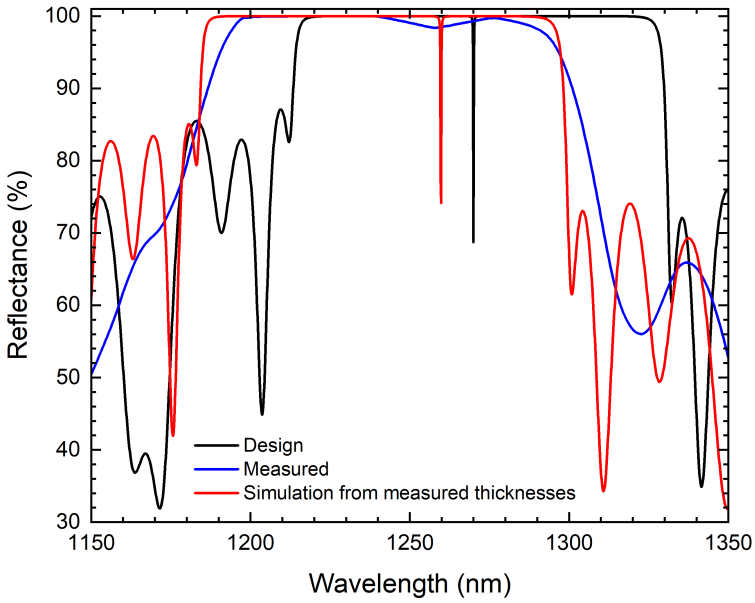

Figure 11.12: Reflectance spectra for the $3\lambda/2$ VCSEL including the measured spectrum, and models for the original design and model based on layer thickness measured using TEM.

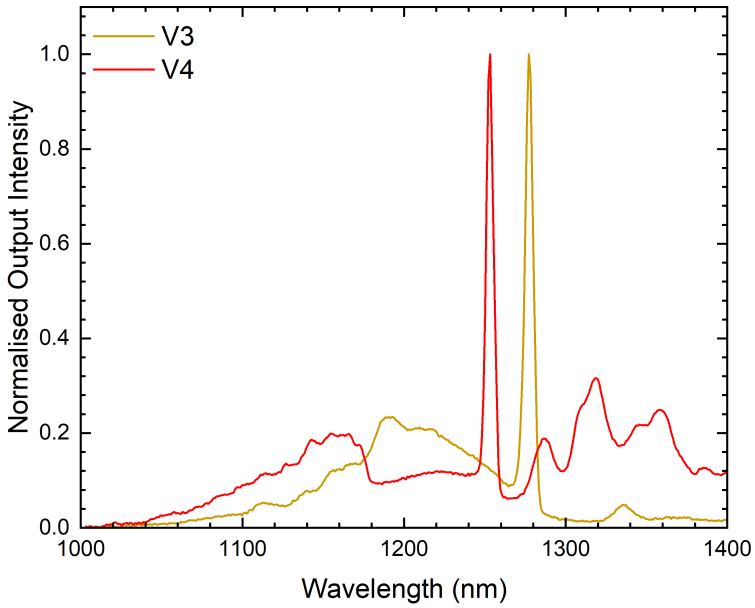

Figure 11.13: Normalised electroluminescence spectra of the $\lambda/2$ (V3) and $3\lambda/2$ (V4) stepped-DBR VCSEL structures.

		V4			
		Material	**Dopant**	**Concentration (cm^{-3})**	**Thickness (nm)**
	Contact Layer	GaAs	p-type (Be)	5×10^{18} to 1×10^{19}	82.2
	Upper DBR x21	$Al_{0.6}Ga_{0.4}As$	p-type (Be)	5×10^{18}	15
		$Al_{0.9}Ga_{0.1}As$	p-type (Be)	5×10^{18}	87.3
		$Al_{0.6}Ga_{0.4}As$	p-type (Be)	5×10^{18}	15
		GaAs	p-type (Be)	5×10^{18}	82.2
	Oxidation Layer	$Al_{0.98}Ga_{0.02}As$	p	5×10^{18}	30
	Spacer	$Al_{0.6}Ga_{0.4}As$	i	-	21.3
	GaSb QR x5	GaAs	i	-	10
		GaAs (cold)	i	-	5
		GaSb	i	-	2.1 ML
	Cavity	GaAs	i	-	106.0
2x	GaSb QR x5	GaAs	i	-	10
		GaAs (cold)	i	-	5
		GaSb	i	-	2.1 ML
	Cavity	GaAs	i	-	15
	Spacer	$Al_{0.6}Ga_{0.4}As$	i	-	57.9
	Lower DBR x34	GaAs	n-type (Si)	5×10^{18}	82.2
		$Al_{0.6}Ga_{0.4}As$	n-type (Si)	5×10^{18}	15
		$Al_{0.6}Ga_{0.4}As$	n-type (Si)	5×10^{18}	87.3
		$Al_{0.6}Ga_{0.4}As$	n-type (Si)	5×10^{18}	15
	Buffer	GaAs	n-type (Si)	5×10^{18}	170
	Substrate	GaAs	n-type (Si)	1×10^{18} to 5×10^{18}	0.35 mm

Table 11.6: Epitaxial design of the third-generation stepped-interface QR VCSEL (V4).

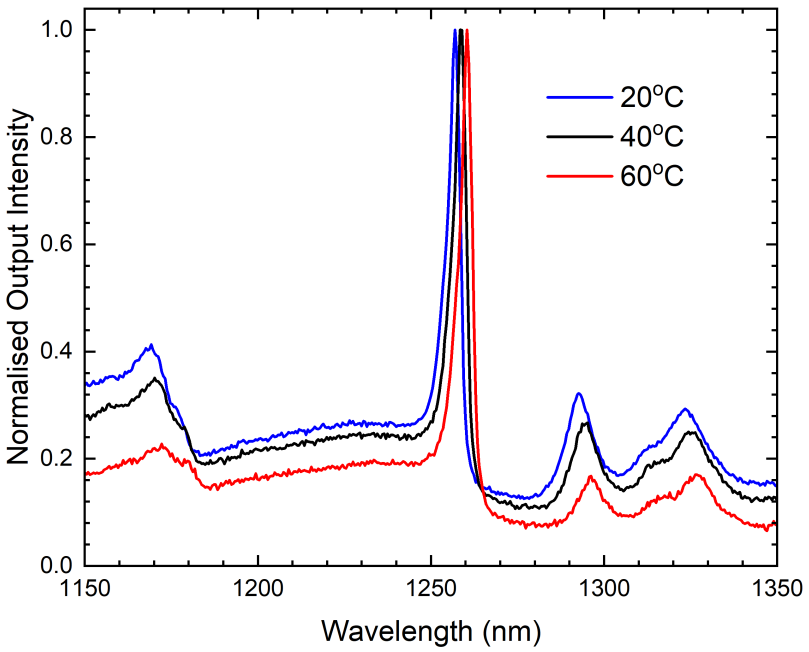

(a)

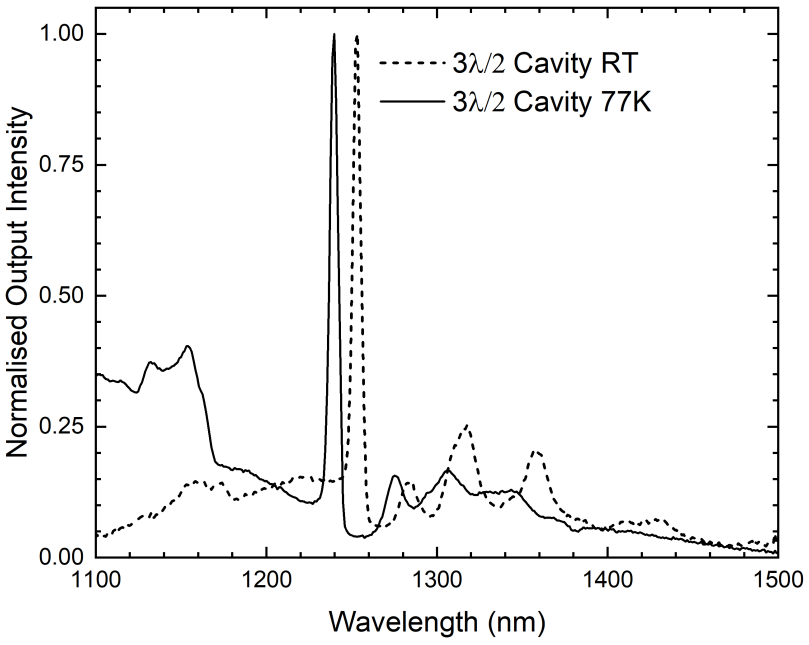

(b)

Figure 11.14: a) Temperature-dependent spectra of a $3\lambda/2$ cavity VCSEL with 10 µm mesa and a temperature coefficient of (0.09 ± 0.01) nm/K. b) Room-temperature and 77K spectra of a $3\lambda/2$ cavity VCSEL with 30 µm mesa.

Emission Intensity

Voltage-current and intensity-current measurements at the cavity resonance (1257 nm for this sample) are shown for continuous operation of a $3\lambda/2$ cavity VCSEL with 10 µm mesa (Figure 11.15a). A clear laser-like threshold is visible in the intensity-current characteristic at the peak wavelength of the device, and is identified to be in the region of 0.115 mA by taking the second derivative of the normalised light intensity with respect to the current (Figure 11.15b). This threshold corresponds to a very low threshold current density of approximately 0.15 kA/cm^2 for the 10 µm mesa under the assumption that the full area of the mesa is active. Typical threshold current densities range from 0.5 kA/cm^2 to a few kA/cm^2 [160, 161, 162, 163]. This figure should be taken with caution as lasing has not been explicitly proven, nor has the possibility that emission is present at lower currents and simply masked by the noise floor of the detector. In addition, it is unlikely that the full device area is active.

Low temperature (77 K) measurements reveal a non-trivial behaviour of the output intensity with increasing drive current. Intensity-current measurements at 77 K exhibit a sharp drop in output intensity of the peak emission between 5 mA to 6 mA (Figure 11.16). In this range the voltage, as shown in Figure 11.16, is in excess of 10 V. It is believed that at this point the electric field is large enough for carriers to overcome the potential barriers present at the cavity edge and are swept out of the active region. Loss of carrier containment results in recombination elsewhere in the structure, reducing radiative contributions from the QRs themselves. The recombination may occur through non-radiative means or radiative recombination at wavelengths outside of the measured spectrum. The reduction in intensity is visible across the full spectrum when comparing the 5 mA and 8 mA sweeps (Figure 11.17a). In particular, the reduction in intensity is much more significant for emission at the resonant cavity wavelength, which is made clear by the large quenching ratio shown in Figure 11.17b. The quenching ratio, R_q, at a wavelength is defined in this instance as

$$R_q = \frac{L_{5\,\mathrm{mA}}}{L_{8\,\mathrm{mA}}}, \tag{11.1}$$

where $L_{5\,\mathrm{mA}}$ and $L_{5\,\mathrm{mA}}$ are the emission intensities at 5 mA and 8 mA. At this time it is unclear what mechanism causes such quenching of the cavity enhancement, but since the cavity peak is quenched more than the background spontaneous emission, it seems that the amplification within the device is suppressed.

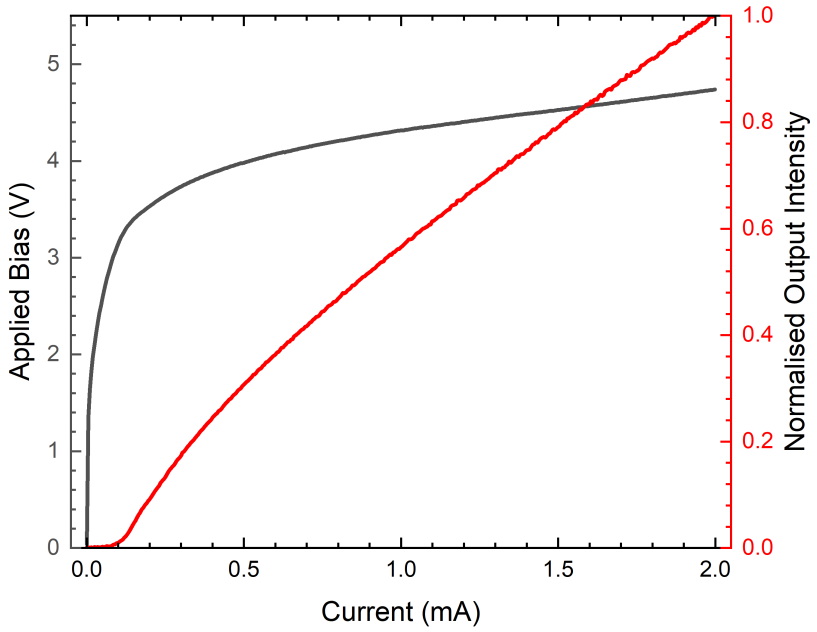

(a)

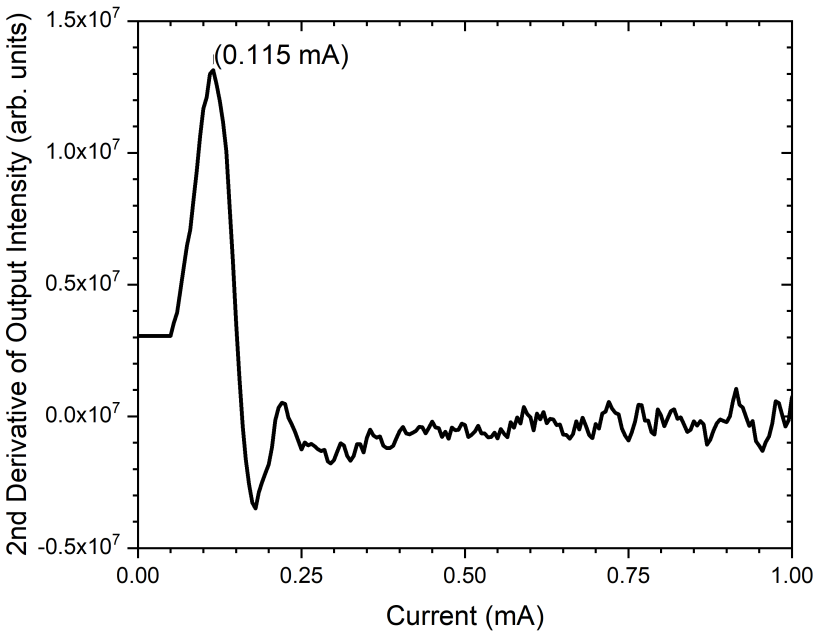

(b)

Figure 11.15: a) Room-temperature (20 °C) voltage-current and intensity-current measurements for continuous operation of a $3\lambda/2$ cavity VCSEL with 10 µm mesa. b) Threshold current for continuous room-temperature (20 °C) operation of a $3\lambda/2$ cavity VCSEL with 10 µm mesa indicated at the maximum of the second derivative of the output intensity with respect to current.

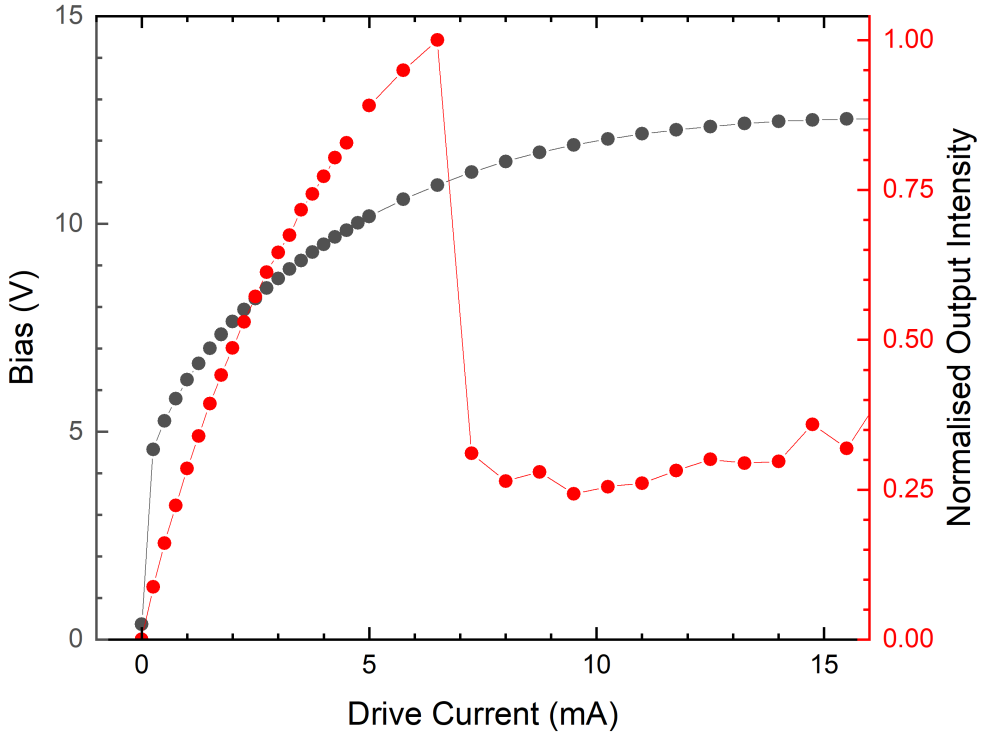

Figure 11.16: Low temperature (77 K) voltage-current and intensity-current measurements for continuous operation of a $3\lambda/2$ cavity VCSEL.

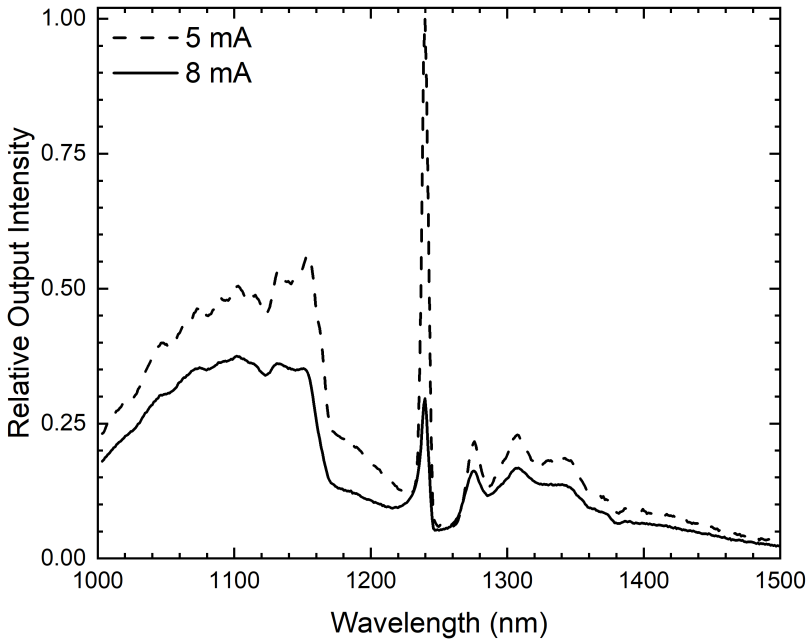

(a)

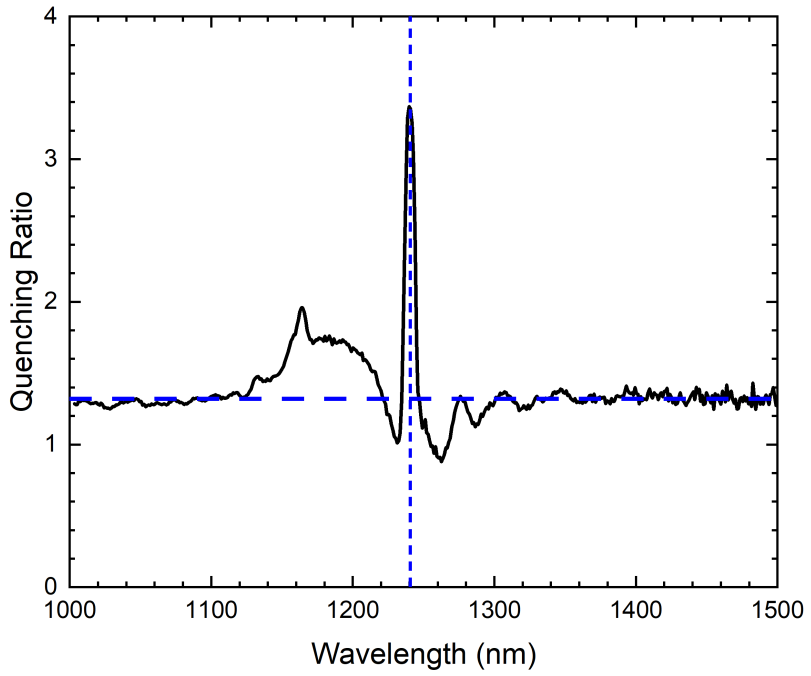

(b)

Figure 11.17: a) Normalised emission spectra for a $3\lambda/2$ cavity VCSEL with 30 µm mesa operating at 77 K for 5 mA and 8 mA. b) The ratio of 5 mA to 8 mA drive current intensity shows a stark quenching of the cavity enhanced emission. Horizontal and vertical dashed lines have been added to guide the eye.

11.3.4 Discussion of $\lambda/2$ and $3\lambda/2$ Cavity VCSELs

A general overview of the GaSb QR VCSEL characteristics is given here through comparison of the $\lambda/2$ and $3\lambda/2$ cavity devices. Comparison of the cavity lengths is the foundation of the latest understanding of QR VCSEL devices.

The motivation behind the increase in quantum ring layers from 5× to 15× layers was twofold. Primarily, the intention was to reduce the background emission intensity by avoiding presumed saturation of the quantum rings at the cavity resonance; however, there was no reduction in the relative intensity of the sidebands with the increased number of ring layers. The second motivation was an increase in the overall output intensity of the devices. A visible increase in overall intensity is apparent in Figure 11.18a. The area-scaled intensity as a function of current density has increased by more than a factor of three. A small portion of the intensity increase may be attributed to improved quality of the quantum ring growths and variations in device to device performance due to the different geometry of 150 µm ($\lambda/2$) and 30 µm ($3\lambda/2$) devices, but this is a distinct improvement that is attributed to the increase in number of QR layers.

As shown in Figure 11.11, the sidebands of the latest QR VCSELs increase relative to the cavity resonance with increasing drive current. The nature of the increase in background intensity is shown in Figure 11.18b, where the sideband intensity represents the first peak intensity on the long-wavelength side of the cavity (Figure 11.13). For both cavity lengths, the cavity emission weakens with respect to the sidebands as the current density increases. The reduction in sideband intensity for a greater number of ring layers is disproven here and requires an alternative approach to a reduction in background emission. The fraction of light emitted at the cavity resonance remains broadly similar for both cavity lengths (Figure 11.18b). From this it is inferred that a similar proportion of the carriers in each structure recombine in a spontaneous versus stimulated fashion.

It is possible that the spontaneous emission contribution is dominated by the quantum rings located further from the antinodes of the electric field (Figure 11.19). QR VCSEL devices with multiple ring layers centred on each antinode will inherently have rings located away from antinodes due to the requirement for the thin GaAs caps required for ring formation, with a correspondingly low confinement factor (equation 2.75). In the $3\lambda/2$ structure all sets of five quantum ring layers are equally distributed around the antinodes of the electric field. The equivalent distribution is seen at the single antinode in the $\lambda/2$ design (Figure 11.1). From this, it is reasonable to think that the proportion of injected carriers recombining in a spontaneous versus stimulated fashion should in fact remain broadly similar. In light of this, it is now believed that the spontaneous emission may be reduced by concentrating the quantum ring growth around the antinodes of the electric field, in favour of multiple layers centred around the antinodes.

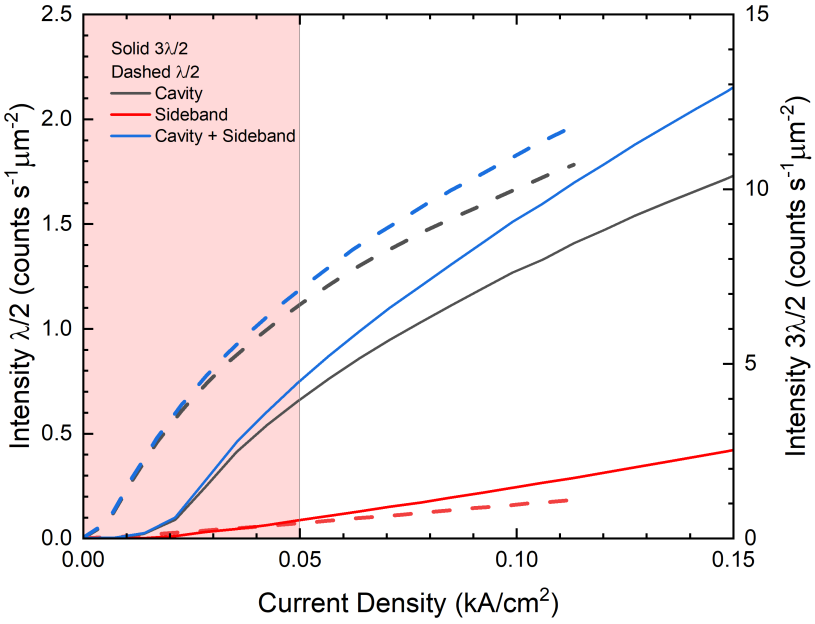

(a)

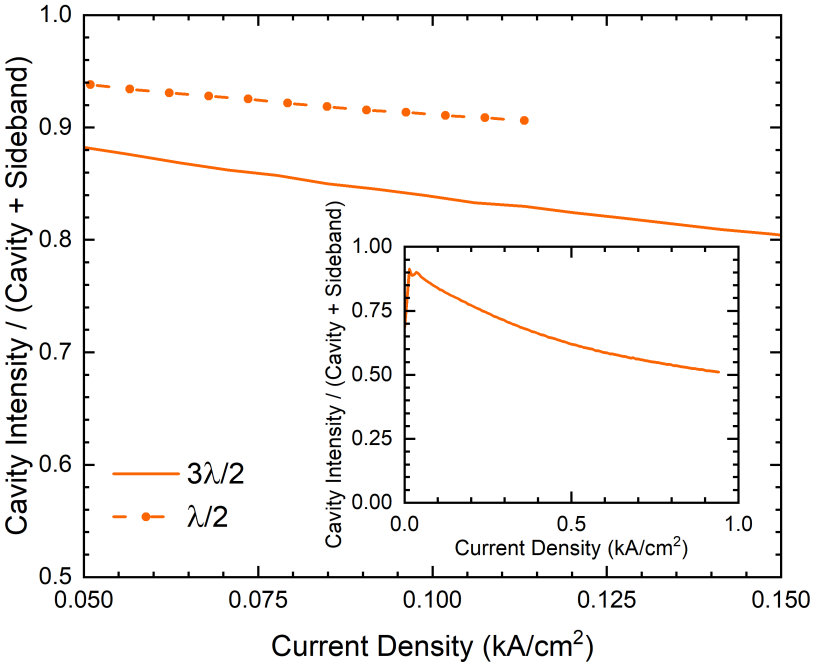

(b)

Figure 11.18: a) Area-scaled output intensity as a function of current density for a $3\lambda/2$ cavity device (V4) and $\lambda/2$ cavity (V3). b) The output intensity at the cavity resonance is given relative to the sum of the cavity resonance intensity and the maximum intensity at the first sideband on the long wavelength side of the cavity. The inset shows the ratio over a larger range for the $3\lambda/2$ structure. Intensity and current density below 5×10^{-4} mA/µm^2 should be taken with caution for the $3\lambda/2$ structure due to overall low intensity of light incident on the detector due to the small size of the device, this region is indicated by the shaded background.

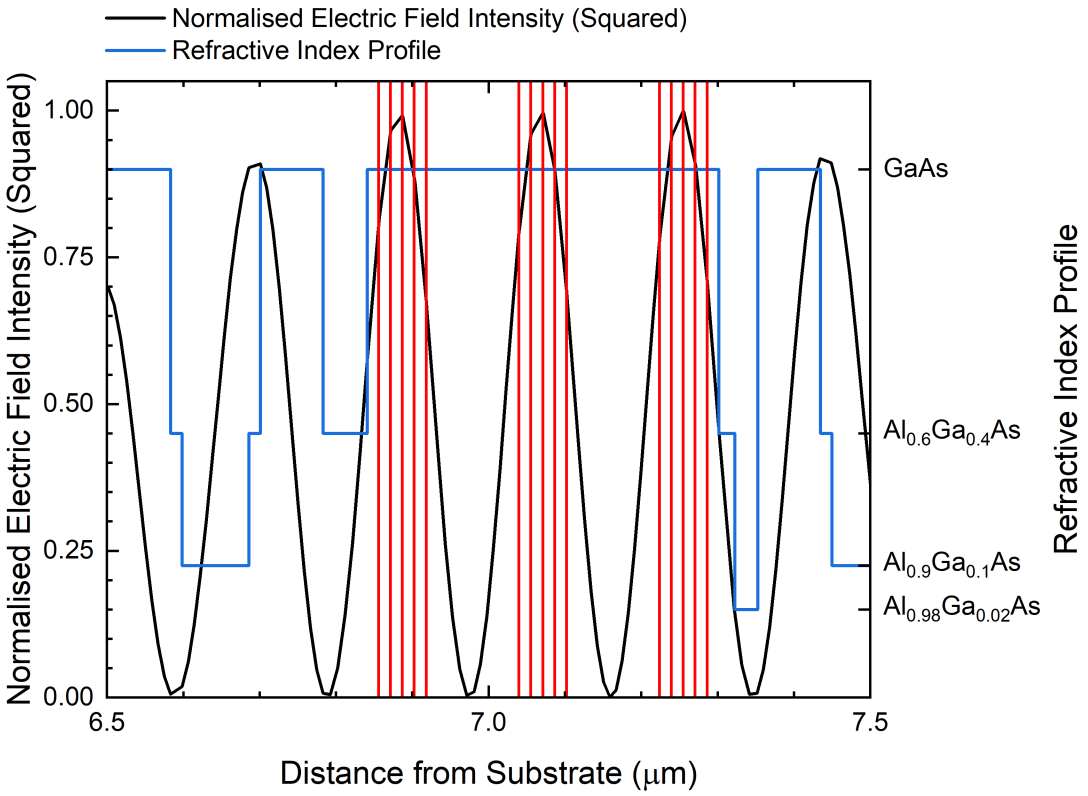

Figure 11.19: The electric field and refractive index profiles within the $3\lambda/2$ VCSEL are given as a function of position. The positions of the quantum ring layers are indicated by the vertical red lines.

11.3.5 Future Work

It would be prudent to ascertain whether the quantum ring background emission is related to the spatial overlap between the quantum rings and the electric field intensity in the cavity. An experiment may be designed to investigate this through the use of two contrasting structures. The cavity of a $3\lambda/2$ structure contains three antinodes and two nodes at positions compatible with quantum ring growth. A single layer of rings may be grown at two of the antinodes, and the same for a device with rings at nodes of the electric field. If the hypothesis that the spatial overlap is fundamental to the background emission then the first instance should show the purest spectral emission of any QR VCSEL grown to date. In contrast, the second design should exhibit poor spectral purity.

In addition to the investigation into quantum ring positioning, the QR VCSEL fabrication flow should be improved by the removal of the bridge between the device mesa and bondpad. As discussed in section 6.7, the potential for current to leak underneath the bondpad enables pumping of a larger area than desired. Pumping of quantum rings under the bondpad may contribute to a lower total output intensity, higher threshold currents and spontaneous recombination contributing to the background spectrum. The use of planarising resists and processes would enable complete electrical isolation of the cylindrical device mesas without the need for a bridge. Alternatively, the area under the bondpad may be isolated through the use of a quick fabrication flow developed at Cardiff University [164].

Long-term, the output intensity of quantum ring VCSELs must be increased. The output power and overall power conversion efficiency of the devices may be increased through a number of approaches including the introduction of a longer cavity with more quantum ring layers and the formation of an oxide aperture for current and optical mode guiding.

Chapter 12

Conclusions and Future Work

A study of Au/Ni/Au contacts to p-type GaAs, growth-rate determination in MBE using reflectance monitoring, studies of the optical and electrical properties of $Al_xGa_{1-x}As$-based DBRs around 1300 nm and time-resolved measurements of carrier recombination lifetimes were carried out within the context of GaSb QR VCSEL research. The results of these investigations informed the design, growth and fabrication of devices which demonstrated emission in the region of ∼1250 nm and ∼1300 nm.

Rapid thermal annealing of evaporated Au/Ni/Au contacts was performed and shown to produce ohmic contacts to p-type GaAs. The contact resistance achieved through this process was as low as $(1.6 \pm 0.2) \times 10^{-5}\,\Omega\,cm^2$. This alternative contact scheme was comparable to Au/Zn/Au contacts deposited in the same fabrication environment. In conclusion, annealed Au/Ni/Au forms an ohmic contact to p-type GaAs with similar doping concentrations to GaSb QR VCSEL contact layers and may be incorporated into the fabrication flow of GaSb QR VCSELs.

The growth of a six-layer GaAs/AlAs structure by MBE was tracked using in-situ reflectance monitoring. Group-III element growth rates and the thicknesses of each layer were calculated from the reflectance monitoring measurements and agreed, within error, with measurements from SEM. In conclusion, the home-built in-situ reflectance monitoring system is shown to be an effective tool for determining the growth rates of group-III elements and may be used prior to growth of VCSELs to improve the accuracy of calibrations for future growth runs.

The investigation into $Al_xGa_{1-x}As$-based DBRs at 1300 nm was driven by the desire for low-resistance DBRs for use in GaSb QR VCSELs and consisted of three independent studies. First, a study into structures readily compatible with MBE growth was conducted in order to find a DBR that could be incorporated into the material grown as a part of this project. The inclusion of a thin 15 nm $Al_{0.6}Ga_{0.4}As$ layer between alternating layers of GaAs and $Al_{0.9}Ga_{0.1}As$ exhibited the lowest resistance of the structures investigated. Next, a study surrounding the impact of beryllium doping concentrations on the optical absorption of DBRs was conducted in order to determine if higher doping concentrations would have significant implications for the performance of the DBRs in GaSb QR VCSELs. Doping concentrations ranging from nominally-undoped to $5 \times 10^{18}\,cm^{-3}$ were not found to have any impact on the absorption of the DBRs. A series of MOCVD-grown conventional and spiky DBRs were grown in parallel to the studies carried out on MBE-grown material. It was found that spiky structures exhibited high reflectance at their target wavelength, but a narrow stopband. The electrical performance of spiky structures was equivalent to their standard-DBR counterparts within the scope of this investigation. In conclusion, stepped-interface $GaAs/Al_{0.9}Ga_{0.1}As$ DBRs exhibited the best performance of the MBE-grown structures and are selected for use in GaSb QR VCSELs. Such DBRs may be beryllium doped to concentrations as high as $5 \times 10^{18}\,cm^{-3}$ with no detrimental effects to the optical performance of the DBRs, as observed in this work. The spiky DBRs exhibited reasonable performance but are inferior to conventional DBRs in conventional use cases.

TRPL measurements provided evidence of reduced carrier recombination lifetimes for QR devices in the presence of an optical cavity but revealed little about the interaction of the different carrier recombination mechanisms at work. Further investigation into the carrier lifetimes for QRs in the presence of an optical cavity is required.

Finally, several VCSEL structures were characterised over the duration of this work. All of the devices exhibited a similarly large background emission intensity relative to the peak emission with emission observed across the telecoms 'O'-band. Low temperature

(77K) measurements revealed a non-trivial quenching of the output intensity at large applied biases which was non-linear across the emission spectrum. Greater quenching at the position of the resonant cavity may be indicative of amplification within the device. A laser-like threshold of 0.15 kA/cm^2 was determined for a 10 µm diameter device with a $3\lambda/2$ cavity length. Lasing has not been explicitly proven, nor has the possibility that emission is present at lower currents and is simply masked by the noise floor of the detector. In conclusion, GaSb QR VCSELs show emission at telecoms wavelengths but are hampered by low output powers and large background emission. Further study and development are required in order to determine the origin of the background emission, assess the prospect of lasing and improve the device performance.

The scope for future work is broad and may be categorised into further investigation of the fundamental device physics, further characterisation of existing devices and improvements to device fabrication.

In the first instance, the relationship between the background emission profile of QR VCSELs and the spatial overlap of the quantum ring layers with the electric field in the cavity should be explored, as discussed in section 11.3.5. It is of interest to explore QR carrier recombination in greater depth to provide a more comprehensive understanding of the carrier recombination lifetimes both in bulk, and in a cavity. Previously, Hodgson et al. studied the energy-dependent recombination lifetime of QRs [21]. In principle, this may be extended to a study in the presence of a cavity to quantify the radiative lifetime of quantum rings in a cavity both at and away from the resonant wavelength.

To date, the linewidth of QR VCSEL spectra has been limited by the configuration of the spectrometer during measurements. Device output powers have been low with relatively strong background emission. As such, no great effort has been made to quantify the device output power. Further characterisation of the device output power, emission linewidth and polarisation of light from QR VCSELs is necessary to explore the prospect of lasing.

The device fabrication techniques used in this work were appropriate for the studies and proof-of-concept devices presented. However, improvements to the process will be required to understand the true performance of the devices. It would be preferable to include an oxide aperture which is standard practice in VCSEL processing; however, this equipment is not available in the Lancaster QTC labs at the time of this work. In addition, it would be beneficial to eliminate current paths which could lead to current under the bondpad and bridge. Both of these may be achieved through use of a simple quick fabrication flow developed at Cardiff University [164].

Alternatively, the bridge which is present between the bondpad and mesa for devices in this work may also be etched and bisbenzocyclobutene-based (BCB) resins used to planarise the surface. Conventionally, BCB spin-on dielectrics such as cyclotene 3000 are used to passivate and planarise devices for high speed operation [10]. However, these were not available during the course of this work and the cost of obtaining the chemicals was prohibitively expensive.

Finally, it is hoped that the future work outlined in this thesis will steer subsequent research in a direction towards the fabrication and testing of QR VCSELs with improved performance, the results of which will determine whether this material system is suitable for commercial applications.

This work presents a strong foundation for future QR VCSEL and telecoms-wavelength VCSEL research. A new Au/Ni/Au contact scheme for p-type GaAs has been demonstrated which exhibits a low specific contact resistance. Experiments show that $Al_xGa_{1-x}As$-

based DBRs operating in the region of 1300 nm may be p-doped using beryllium without detriment to their optical performance. Further experiments provided the first electro-optical study of a novel, continuously-graded DBR concept. Direct measurements of carrier lifetime were performed for GaSb QRs in an optical cavity providing experimental evidence for the enhancement of the recombination rate by the optical cavity. Finally, a series of devices were produced which exhibited emission within the telecoms range and provide the first measurements of the temperature dependence for the QR VCSEL peak emission wavelength and the first evidence of bias-induced emission quenching in such devices.

Bibliography

[1] H. Soda, K. Iga, C. Kitahara, and Y. Suematsu. GaInAsP/InP Surface Emitting Injection Lasers. *Japanese Journal of Applied Physics*, 18(12):2329, 1979.

[2] A. Liu, P. Wolf, J. A. Lott, and D. Bimberg. Vertical-Cavity Surface-Emitting Lasers for Data Communication and Sensing. *Photonics Research*, 7(2):121–136, 2019.

[3] Yadav Preeti, W. S. Vertical-Cavity Surface-Emitting Lasers (Vcsel) Market Size, by Type (Single Mode, Multi-Mode), by Material Type (Gallium Arsenide (Gaas), Indium Phosphide (Inp), Gallium Nitride), by Wavelength (<850 nm, 850 - 940 nm, 940 - 1,050 nm, > 1,050 nm), by Application (Sensing, Data Communication, Industrial Heating & Laser Printing), by Industry Verticals (Consumer Electronics, It & Telecom, Automotive, Industrial, Healthcare, Aerospace & Defense), Industry Analysis Report, Regional Outlook, Growth Potential, Price Trends, Competitive Market Share & Forecast, 2021 - 2027. Report, 2020.

[4] I. Melngailis. Longitudinal Injection-Plasma Laser of InSb. *Applied Physics Letters*, 6(3):59–60, 1965.

[5] T. E. Sale. *Vertical Cavity Surface Emitting Lasers*. Phd, 1993.

[6] T. E. Sale. *Vertical Cavity Surface Emitting Lasers*. Electronic & Electrical Engineering Research Studies: Optoelectronics Series. Research Studies Press, 1995.

[7] R. Michalzik. *VCSELs: Fundamentals, Technology and Applications of Vertical-Cavity Surface-Emitting Lasers*. Springer Series in Optical Sciences. Springer Berlin Heidelberg, 2014.

[8] R. Michalzik and K. J. Ebeling. *Operating Principles of VCSELs*, pages 53–98. Springer Berlin Heidelberg, 2003.

[9] K. Iga and H. Li. *Vertical-Cavity Surface-Emitting Laser Devices*. Springer, 2003.

[10] P. Moser. *Energy Efficient Oxide Confined VCSELs for Optical Interconnects in Data Centers and Supercomputers*. Doctoral thesis, 2015.

[11] A. Babichev, S. Blokhin, E. Kolodeznyi, L. Karachinsky, I. Novikov, A. Egorov, S.-C. Tian, and D. Bimberg. Long-Wavelength VCSELs: Status and Prospects. *Photonics*, 10(3), 2023.

[12] Klein Johnson, Mary Hibbs-Brenner, William Hogan, and Matthew Dummer. Advances in Red VCSEL Technology. *Advances in Optical Technologies*, 2012(1):569379, 2012.

[13] T. Sarmiento, L. Zhao, P. Moser, T. Li, Y. Huo, and J. S. Harris. Continuous-Wave Operation of GaAs-Based 1.5 μm GaInNAsSb VCSELs. *IEEE Photonics Technology Letters*, 31(20):1607–1610, 2019.

[14] James K. Franks. What is Eye Safe? In Anthony M. Johnson, editor, *Eyesafe Lasers: Components, Systems, and Applications*, volume 1419, pages 2 – 8. International Society for Optics and Photonics, SPIE, 1991.

[15] Jaffal Ali. VCSELs: Driving Innovations in 3D Sensing and Data Communication. In *Proc.SPIE*, number 12 in 12904. SPIE Photonics West, 2024.

[16] S. A. Blokhin, M. A. Bobrov, N. A. Maleev, A. A. Blokhin, A. P. Vasyl'ev, A. G. Kuzmenkov, S. I. Troshkov, V. M. Ustinov, S. S. Rochas, A. G. Gladyshev, I. I. Novikov, L. Y. Karachinsky, K. O. Voropaev, A. S. Ionov, and A. Y. Egorov. Vertical Cavity Surface Emitting Laser of 1.55 μm Spectral Range, Manufactured by Molecular Beam Epitaxy and Wafer Fusion Technique. *Journal of Physics: Conference Series*, 1697:012178, 2020.

[17] S. A. Blokhin, M. A. Bobrov, N. A. Maleev, A. A. Blokhin, A. G. Kuz'Menkov, A. P. Vasil'Ev, S. S. Rochas, A. G. Gladyshev, A. V. Babichev, I. I. Novikov, L. Y. Karachinsky, D. V. Denisov, K. O. Voropaev, A. S. Ionov, A. Y. Egorov, and V. M. Ustinov. A Vertical-Cavity Surface-Emitting Laser for the 1.55-μm Spectral Range with Tunnel Junction Based on n++-InGaAs/p++-InGaAs/p++-InAlGaAs Layers. *Technical Physics Letters*, 46(9):854–858, 2020.

[18] KO Voropaev, BI Seleznev, A Yu Prokhorov, AS Ionov, and SA Blokhin. The Fabrication Technology of VCSELs Emitting in the 1.55 μm Waveband. In *Journal of Physics: Conference Series*, volume 1658, page 012069. IOP Publishing, 2020.

[19] S. Spiga, W. Soenen, A. Andrejew, D. M. Schoke, X. Yin, J. Bauwelinck, G. Boehm, and M.-C. Amann. Single-Mode High-Speed 1.5-μm Vcsels. *Journal of Lightwave Technology*, 35(4):727–733, 2016.

[20] M. Gębski, D. Dontsova, N. Haghighi, K. Nunna, R. Yanka, A. Johnson, R. Pelzel, and J. A. Lott. Baseline 1300nm Dilute Nitride VCSELs. *OSA Continuum*, 3(7):1952–1957, 2020.

[21] P. D. Hodgson, M. Hayne, A. J. Robson, Q. D. Zhuang, and L. Danos. GaSb Quantum Rings in GaAs/Al_XGa_{1-X}As Quantum Wells. *Journal of Applied Physics*, 119(4), 2016.

[22] D. J. Griffiths. *Introduction to Electrodynamics*. Cambridge University Press, Cambridge, fourth edition, 2017.

[23] W. A. Harrison. *Electronic Structure and the Properties of Solids: The Physics of the Chemical Bond*. Courier Corporation, 2012.

[24] S. L. Chuang. *Physics of Photonic Devices*. John Wiley & Sons, second edition, 2009.

[25] S. H. Simon. *The Oxford Solid State Basics*. Oxford University Press Oxford, 2013.

[26] Prasanta Misra. *Physics of Condensed Matter*. Academic Press, 2011.

[27] C. Kittel. *Introduction to Solid State Physics*. Wiley, eigth edition, 2005.

[28] R. Ludeke. Chapter 11 - The Metal-Semiconductor Interface. In K. Horn and M. Scheffler, editors, *Electronic Structure*, volume 2 of *Handbook of Surface Science*, pages 749–862. North-Holland, 2000.

[29] A. F. J. Levi. *Applied Quantum Mechanics*. Cambridge University Press, Cambridge ; New York, third edition, 2024.

[30] Larry A Coldren and Eric R Hegblom. *Fundamental Issues in VCSEL Design*. Cambridge University Press, 1999.

[31] Fahrettin Sarcan, MS Nordin, F Kuruoğlu, Ayşe Erol, and AJ Vickers. Characterization of Temperature Dependent Operation of a GaInNAs-Based RCEPD Designed for 1.3 μm. *Superlattices and Microstructures*, 102:27–34, 2017.

[32] R. E. Fern and A. Onton. Refractive Index of AlAs. *Journal of Applied Physics*, 42(9):3499–3500, 1971.

[33] S. Adachi. GaAs, AlAs, and $Al_XGa_{1-X}As$: Material Parameters for Use in Research and Device Applications. *Journal of Applied Physics*, 58(3):R1–R29, 1985.

[34] K. Asakawa. Indium Phosphide and Related Materials, Processing, Technology and Devices. *Advanced Materials*, 5(3):228–229, 1993.

[35] T. W. Nee and A. K. Green. Optical Properties of InGaAs Lattice-Matched to InP. *Journal of Applied Physics*, 68(10):5314–5317, 1990.

[36] M. Levinshtein, S. L. Rumyantsev, M. Shur, and W. Scientific. *Handbook Series on Semiconductor Parameters: Ternary and Quaternary III-V Compounds*. EBL-Schweitzer. World Scientific Publishing Company, 1999.

[37] S. Birner, T. Zibold, T. Andlauer, T. Kubis, M. Sabathil, A. Trellakis, and P. Vogl. Nextnano: General Purpose 3-D Simulations. *IEEE Transactions on Electron Devices*, 54(9):2137–2142, 2007.

[38] S. Birner. Modeling of Semiconductor Nanostructures and Semiconductor-Electrolyte Interfaces. 2011.

[39] M Hayne, R J Young, E P Smakman, T Nowozin, P Hodgson, J K Garleff, P Rambabu, P M Koenraad, A Marent, L Bonato, A Schliwa, and D Bimberg. The Structural, Electronic and Optical Properties of GaSb/GaAs Nanostructures for Charge-Based Memory. *Journal of Physics D: Applied Physics*, 46(26):264001, jun 2013.

[40] R. J. Young, E. P. Smakman, A. M. Sanchez, P. Hodgson, P. M. Koenraad, and M. Hayne. Optical Observation of Single-Carrier Charging in Type-II Quantum Ring Ensembles. *Applied Physics Letters*, 100(8):082104, 02 2012.

[41] E. P. Smakman, J. K. Garleff, R. J. Young, M. Hayne, P. Rambabu, and P. M. Koenraad. GaSb/GaAs Quantum Dot Formation and Demolition Studied with Cross-Sectional Scanning Tunneling Microscopy. *Applied Physics Letters*, 100(14):142116, 2012.

[42] P. D. Hodgson, R. J. Young, M. Ahmad Kamarudin, P. J. Carrington, A. Krier, Q. D. Zhuang, E. P. Smakman, P. M. Koenraad, and M. Hayne. Blueshifts of the Emission Energy in Type-II Quantum Dot and Quantum Ring Nanostructures. *Journal of Applied Physics*, 114(7):073519, 2013.

[43] Timm, R. and Eisele, H. and Lenz, A. and Becker, S. K. and Grabowski, J. and Kim, T. Y. and Müller-Kirsch, L. and Pötschke, K. and Pohl, U. W. and Bimberg, D. and Dähne, M. Structure and Intermixing of GaSb/GaAs Quantum Dots. *Applied Physics Letters*, 85(24):5890–5892, 2004.

[44] B. Liang, A. Lin, N. Pavarelli, C. Reyner, J. Tatebayashi, K. Nunna, J. He, T. J. Ochalski, G. Huyet, and D. L. Huffaker. GaSb/GaAs Type-II Quantum Dots Grown by Droplet Epitaxy. *Nanotechnology*, 20(45):455–604, 2009.

[45] R. J. Young, E. P. Smakman, A. M. Sanchez, P. Hodgson, P. M. Koenraad, and M. Hayne. Optical Observation of Single-Carrier Charging in Type-II Quantum Ring Ensembles. *Applied Physics Letters*, 100(8):082104, 2012.

[46] M. Gębski, P.-S. Wong, M. Riaziat, and J. A. Lott. 30 GHz Bandwidth Temperature Stable 980 nm Vertical-Cavity Surface-Emitting Lasers with AlAs/GaAs Bottom Distributed Bragg Reflectors for Optical Data Communication. *Journal of Physics: Photonics*, 2(3):035008, 2020.

[47] Elijah Thimsen, Bryce Sadtler, and Mikhail Y Berezin. Shortwave-Infrared (SWIR) Emitters for Biological Imaging: A Review of Challenges and Opportunities. *Nanophotonics*, 6(5):1043–1054, 2017.

[48] Laura A Sordillo, Lingyan Shi, Diana C Sordillo, Peter P Sordillo, and Robert R Alfano. Advances in Medical Applications using SWIR Light in the Wavelength Range from 1000 to 2500 nm. In *Optical Biopsy XVII: Toward Real-Time Spectroscopic Imaging and Diagnosis*, volume 10873, pages 91–95. SPIE, 2019.

[49] Mial E Warren. Automotive LIDAR technology. In *2019 Symposium on VLSI Circuits*, pages C254–C255. IEEE, 2019.

[50] J. Blakemore. Semiconducting and Other Major Properties of Gallium Arsenide. *Journal of Applied Physics*, 53(10):R123–R181, 1982.

[51] Jungho Kim, Christian Meuer, Dieter Bimberg, and Gadi Eisenstein. Effect of Inhomogeneous Broadening on Gain and Phase Recovery of Quantum-Dot Semiconductor Optical Amplifiers. *IEEE Journal of Quantum Electronics*, 46(11):1670–1680, 2010.

[52] Huan Wang, Jin-Chuan Zhang, Feng-Min Cheng, Zeng-Hui Gu, Ning Zhuo, Shen-Qiang Zhai, Feng-Qi Liu, Jun-Qi Liu, Shu-Man Liu, and Zhan-Guo Wang. Broad Gain, Continuous-Wave Operation of InP-Based Quantum Cascade Laser at $\lambda \sim 11.8$ μm. *Chinese Physics B*, 30(12):124202, 2021.

[53] R. Timm, H. Eisele, A. Lenz, S. K. Becker, J. Grabowski, T.-Y. Kim, L. Müller-Kirsch, K. Pötschke, U. W. Pohl, D. Bimberg, and M. Dähne. Structure and Intermixing of GaSb/GaAs Quantum Dots. *Applied Physics Letters*, 85(24):5890–5892, 12 2004.

[54] B. R. Bennett, R. A. Soref, and J. A. Del Alamo. Carrier-Induced Change in Refractive Index of InP, GaAs and InGaAsP. *IEEE Journal of Quantum Electronics*, 26(1):113–122, 1990.

[55] M. Cross and M. J. Adams. Effects of Doping and Free Carriers on the Refractive Index of Direct-Gap Semiconductors. *Opto-electronics*, 6:199–216, 1974.

[56] L. Chusseau, P. Martin, C. Brasseur, C. Alibert, P. Hervè, P. Arguel, F. Lozes-Dupuy, and E. V. K. Rao. Carrier-Induced Change Due to Doping in Refractive Index of InP: Measurements at 1.3 and 1.5 μm. *Applied Physics Letters*, 69(20):3054–3056, 1996.

[57] H. C. Huang, S. Yee, and M. Soma. The Carrier Effects on the Change of Refractive Index for N-Type GaAs at λ=1.06, 1.3, and 1.55 μm. *Journal of Applied Physics*, 67(3):1497–1503, 1990.

[58] K. J. Kuhn, G. U. Iyengar, and S. Yee. Free Carrier Induced Changes in the Absorption and Refractive Index for Intersubband Optical Transitions in $Al_xGa_{1-x}As/GaAs/Al_xGa_{1-x}As$ Quantum Wells. *Journal of Applied Physics*, 70(9):5010–5017, 1991.

[59] T. J. Wilson, P. D. Hodgson, A. J. Robson, C. Jackson, B. Grew, and M. Hayne. A Detailed Comparison of Measured and Simulated Optical Properties of a Short-Period $GaAs/Al_XGa_{1-X}As$ Distributed Bragg Reflector. *Semiconductor Science and Technology*, 35(5):055003, 2020.

[60] T. J. Wilson. *The Design, Optimisation, and Characterisation of GaSb/GaAs Quantum Ring-Based Vertical-Cavity Devices Emitting at Telecoms Wavelengths*. Lancaster University (United Kingdom), 2021.

[61] J. C. H. Spence. *High-Resolution Electron Microscopy*. Monographs on the Physics and Chemistry of Materials. Oxford University Press, New York, third edition, 2009.

[62] A. J. Robson, I. Grishin, R. J. Young, A. M. Sanchez, O. V. Kolosov, and M. Hayne. High-Accuracy Analysis of Nanoscale Semiconductor Layers Using Beam-Exit Ar-Ion Polishing and Scanning Probe Microscopy. *ACS Applied Materials & Interfaces*, 5(8):3241–3245, 2013.

[63] Yue Chen, Wenkai Wu, Sergio Gonzalez-Munoz, Leonardo Forcieri, Charlie Wells, Samuel P. Jarvis, Fangling Wu, Robert Young, Avishek Dey, Mark Isaacs, Mangayarkarasi Nagarathinam, Robert G. Palgrave, Nuria Tapia-Ruiz, and Oleg V. Kolosov. Nanoarchitecture Factors of Solid Electrolyte Interphase Formation via 3D Nano-Rheology Microscopy and Surface Force-Distance Spectroscopy. *Nature communications*, 14(1):1321–1321, 2023.

[64] U. Vohrer, C. Blomfield, S. Page, and A. Roberts. Quantitative XPS Imaging—New Possibilities with the Delay-Line Detector. *Applied Surface Science*, 252(1):61–65, 2005.

[65] E. F. Smith, J. D. P. Counsell, J. Bailey, J. S. Sharp, M. R. Alexander, A. G. Shard, and D. J. Scurr. Sample Rotation Improves Gas Cluster Sputter Depth Profiling of Polymers. *Surface and Interface Analysis*, 49(10):953–959, 2017.

[66] W Patrick McCray. MBE Deserves a Place in the History Books. *Nature nanotechnology*, 2(5):259–261, 2007.

[67] G. R. Booker and B. A. Joyce. A Study of Nucleation in Chemically Grown Epitaxial Silicon Films Using Molecular Beam Techniques. *The Philosophical Magazine: A Journal of Theoretical Experimental and Applied Physics*, 14(128):301–315, 1966.

[68] Michael J Manfra. Molecular Beam Epitaxy of Ultra-High-Quality AlGaAs/GaAs Heterostructures: Enabling Physics in Low-Dimensional Electronic Systems. *Annu. Rev. Condens. Matter Phys.*, 5(1):347–373, 2014.

[69] Kambiz Alavi. Molecular beam epitaxy. *Handbook of Compound Semiconductors: Growth, Processing, Characterization and Devices, GEM Paul H. Holloway*, pages 84–169, 1995.

[70] B A Joyce. Molecular Beam Epitaxy. *Reports on Progress in Physics*, 48(12):1637, Dec 1985.

[71] Mohamed Henini. *Molecular Beam Epitaxy: From Research to Mass Production*. Newnes, 2012.

[72] D Bullock. Growth Rate Calculations for Epitaxially Grown Thin Films. *Journal of the Arkansas Academy of Science*, 62(1):142–144, 2008.

[73] Yoshiji Horikoshi, Minoru Kawashima, and Hiroshi Yamaguchi. Migration-Enhanced Epitaxy of GaAs and AlGaAs. *Japanese Journal of Applied Physics*, 27(2R):169, 1988.

[74] Peter M Martin. *Handbook of Deposition Technologies for Films and Coatings: Science, Applications and Technology*. William Andrew, 2009.

[75] Tsunenori Sakamoto. *Rheed Oscillations in MBE and Their Applications to Precisely Controlled Crystal Growth*, pages 93–110. Springer US, Boston, MA, 1988.

[76] J. H. Neave, P. J. Dobson, B. A. Joyce, and Jing Zhang. Reflection High-Energy Electron Diffraction Oscillations from Vicinal Surfaces - A New Approach to Surface Diffusion Measurements. *Applied Physics Letters*, 47(2):100–102, 07 1985.

[77] Andrew W Jackson, Paul R Pinsukanjana, Arthur C Gossard, and Larry A Coldren. In Situ Monitoring and Control for MBE Growth of Optoelectronic Devices. *IEEE Journal of Selected Topics in Quantum Electronics*, 3(3):836–844, 1997.

[78] F. G. Celii, Y. C. Kao, III Beam, E. A., W. M. Duncan, and T. S. Moise. Molecular-Beam Epitaxy Flux Transient Monitoring and Correction Using In Situ Reflection Mass Spectrometry. *Journal of Vacuum Science & Technology B: Microelectronics and Nanometer Structures Processing, Measurement, and Phenomena*, 11(3):1018–1022, 05 1993.

[79] K Bacher, B Pezeshki, SM Lord, and JS Harris Jr. Molecular Beam Epitaxy Growth of Vertical Cavity Optical Devices with In-Situ Corrections. *Applied Physics Letters*, 61(12):1387–1389, 1992.

[80] JD Walker, K Malloy, S Wang, and JS Smith. Precision AlGaAs Bragg Reflectors Fabricated by Phase-Locked Epitaxy. *Applied physics letters*, 56(25):2493–2495, 1990.

[81] W Braun, H Möller, and Y-H Zhang. Phase-Locked Substrate Rotation: New Applications for RHEED in MBE Growth. *Journal of Crystal Growth*, 201:50–55, 1999.

[82] N. K. Cho, S. P. Ryu, J. D. Song, W. J. Choi, J. I. Lee, and Heonsu Jeon. Comparison of Structural and Optical Properties of InAs Quantum Dots Grown by Migration-Enhanced Molecular-Beam Epitaxy and Conventional Molecular-Beam Epitaxy. *Applied Physics Letters*, 88(13):133104, 03 2006.

[83] FG Böbel, H Möller, A Wowchak, B Hertl, J Van Hove, LA Chow, and PP Chow. Pyrometric Interferometry for Real Time Molecular Beam Epitaxy Process Monitoring. *Journal of Vacuum Science & Technology B: Microelectronics and Nanometer Structures Processing, Measurement, and Phenomena*, 12(2):1207–1210, 1994.

[84] Y.M. Houng and M.R.T. Tan. MBE Growth of Highly Reproducible VCSELs. *Journal of Crystal Growth*, 175-176:352–358, 1997.

[85] J Iwan Davies, Andrew D Johnson, Rodney I Pelzel, Matthew D Geen, Andrew M Joel, and Sung Wook Lim. MOVPE and its Future Production Challenges. *Journal of Crystal Growth*, 605:127031, 2023.

[86] Manijeh Razeghi. *The MOCVD Challenge: A survey of GaInAsP-InP and GaInAsP-GaAs for Photonic and Electronic Device Applications*. CRC Press, 2010.

[87] H Juergensen. MOCVD Technology in Research, Development and Mass Production. *Materials Science in Semiconductor Processing*, 4(6):467–474, 2001.

[88] J Iwan Davies. *Studies in Metal Organic Vapour Phase Epitaxy (MOVPE) of Semiconductors*. The University of Manchester (United Kingdom), 1985.

[89] Wolfgang Decker, Rob Belan, Volker D. Heydemann, Sean Armstrong, and Tim Fisher. Novel Low Pressure Sputtering Source and Improved Vacuum Deposition of Small Patterned Features Using Precision Shadow Masks. In *59th Annual Technical Conference Proceedings*. Society of Vacuum Coaters, 2016.

[90] Alex Robinson and Richard Lawson. Materials and Processes for Next Generation Lithography , 2016.

[91] Yifang Chen. Nanofabrication by Electron Beam Lithography and its Applications: A review. *Microelectronic Engineering*, 135:57–72, 2015.

[92] Jiashi Shen, Ferhat Aydinoglu, Mohammad Soltani, and Bo Cui. E-Beam Lithography Using Dry Powder Resist of Hydrogen Silsesquioxane Having Long Shelf Life. *Journal of Vacuum Science & Technology B*, 37(2):021601, 02 2019.

[93] F. Lévy. Film Growth and Epitaxy: Methods. In *Reference Module in Materials Science and Materials Engineering*. Elsevier, 2016.

[94] K. J. L. Company. https://www.lesker.com/newweb/deposition_materials/depositionmaterials_evaporationmaterials_1.cfm?pgid=pt1 (accessed 11/07/24).

[95] S. M. Rossnagel. Thin Film Deposition with Physical Vapor Deposition and Related Technologies. *Journal of Vacuum Science & Technology A*, 21(5):S74–S87, 09 2003.

[96] John. E. Mahan. *Physical Vapor Deposition of Thin Films*. Wiley, 2000.

[97] Mikko Ritala, Harish Parala, Ravi Kanjolia, Russell D Dupuis, SE Alexandrov, Stuart JC Irvine, Robert Palgrave, Ivan P Parkin, Jaako Niinisto, Susan Krumdieck, et al. *Chemical Vapour Deposition: Precursors, Processes and Applications*. Royal Society of Chemistry, 2008.

[98] Ludvik Martinu, O Zabeida, and JE Klemberg-Sapieha. Plasma-Enhanced Chemical Vapor Deposition of Functional Coatings. *Handbook of deposition technologies for films and coatings*, pages 392–465, 2010.

[99] Jeffery P. Langer. *Plasma Etching of Antimonide Based III-V Semiconductor Materials and Device Structures*. PhD thesis, 2005.

[100] S O Jones, E Bancroft, S P Jarvis, and M Hayne. Au/Ni/Au as a Contact for p-Type GaAs. *Semiconductor Science and Technology*, 39(12):125011, Nov 2024.

[101] Pranav Kumar Asthana, Bahniman Ghosh, Yogesh Goswami, and Ball Mukund Mani Tripathi. High-Speed and Low-Power Ultradeep-Submicrometer III-V Heterojunctionless Tunnel Field-Effect Transistor. *IEEE Transactions on Electron Devices*, 61(2):479–486, 2014.

[102] Jae-Phil Shim, Seong Kwang Kim, Hansung Kim, Gunwu Ju, Heejeong Lim, SangHyeon Kim, and Hyung-jun Kim. Double-Gated Ultra-Thin-Body GaAs-on-Insulator p-FETs on Si. *APL Materials*, 6(1):016103, 01 2018.

[103] Nikola Papež, Rashid Dallaev, Ştefan Ţălu, and Jaroslav Kaštyl. Overview of the Current State of Gallium Arsenide-Based Solar Cells. *Materials*, 14(11), 2021.

[104] D. Ban, H. Luo, H. C. Liu, Z. R. Wasilewski, A. J. SpringThorpe, R. Glew, and M. Buchanan. Optimized GaAs/AlGaAs Light-Emitting Diodes and High Efficiency Wafer-Fused Optical Up-Conversion Devices. *Journal of Applied Physics*, 96(9):5243–5248, 11 2004.

[105] M. Premkumar, M. Arun, S. Sathiya Priya, D. Kalaiarasi, and R. Prathipa. Characteristics of Gallium Arsenide (GaAs) Light Emitting Diode for Wireless Systems. *Materials Today: Proceedings*, 80:1932–1935, 2023.

[106] Pallavi Kisan Patil, Esperanza Luna, Teruyoshi Matsuda, Kohki Yamada, Keisuke Kamiya, Fumitaro Ishikawa, and Satoshi Shimomura. GaAsBi/GaAs Multi-Quantum Well LED Grown by Molecular Beam Epitaxy Using a Two-Substrate-Temperature Technique. *Nanotechnology*, 28(10):105702, Feb 2017.

[107] Siming Chen, Mingchu Tang, Qi Jiang, Jiang Wu, Vitaliy G. Dorogan, Mourad Benamara, Yuriy I. Mazur, Gregory J. Salamo, Peter Smowton, Alwyn Seeds, and Huiyun Liu. InAs/GaAs Quantum-Dot Superluminescent Light-Emitting Diode Monolithically Grown on a Si Substrate. *ACS Photonics*, 1(7):638–642, 2014.

[108] T. Takagi, H. Imamoto, F. Sato, K. Imanaka, and M. Shimura. High-Power Broad Mesa Structure AlGaAs/GaAs Single-Quantum-Well Edge-Emitting LED. *IEEE Photonics Technology Letters*, 1(1):14–15, 1989.

[109] D. R. Lovell, T. Yamamoto, M. Inai, T. Takebe, and K. Kobayashi. Titanium/Gold Schottky Contacts on p-Type GaAs Grown on (111)a and (100) GaAs Substrates Using Molecular Beam Epitaxy. *Japanese Journal of Applied Physics*, 31(Part 2, No. 7B):L924–L927, 1992.

[110] A. G. Baca, F. Ren, J. C. Zolper, R. D. Briggs, and S. J. Pearton. A Survey of Ohmic Contacts to III-V Compound Semiconductors. *Thin Solid Films*, 308-309:599–606, 1997.

[111] T. Lin, J.-n. Xie, S.-h. Ning, Q.-m. Li, and B. Li. Study on the p-Type Ohmic Contact in GaAs-Based Laser Diode. *Materials Science in Semiconductor Processing*, 124:105622, 2021.

[112] D. K. Schroder. *Semiconductor Material and Device Characterization*. Wiley-Blackwell, 2006.

[113] H. J. Gopen and A. Y. C. Yu. Ohmic Contacts to Epitaxial p-GaAs. *Solid-State Electronics*, 14(6):515–517, 1971.

[114] Y. Lu, T. S. Kalkur, and C. A. Paz De Araujo. Rapid Thermal Alloyed Ohmic Contacts to p-Type GaAs. *Journal of The Electrochemical Society*, 136(10):3123–3129, 1989.

[115] Yen-Tang Lyu, Kuo-Liang Jaw, Ching-Ting Lee, Chang-Da Tsai, Yow-Jon Lin, and Ya-Tung Cherng. Ohmic Performance Comparison for Ti/Ni/Au and Ti/Pt/Au on InAs/Graded InGaAs/GaAs Layers. *Materials Chemistry and Physics*, 63(2):122–126, 2000.

[116] C. C. Han, X. Z. Wang, S. S. Lau, R. M. Potemski, M. A. Tischler, and T. F. Kuech. The Temperature Dependence of the Contact Resistivity of the Si/Ni(Mg) Nonspiking Contact Scheme on p-GaAs. *Journal of Applied Physics*, 69(5):3124–3129, 03 1991.

[117] A. Katz, C. R. Abernathy, and S. J. Pearton. Pt/Ti Ohmic Contacts to Ultrahigh Carbon-Doped p-GaAs Formed by Rapid Thermal Processing. *Applied Physics Letters*, 56(11):1028–1030, 03 1990.

[118] T. Sanada and O. Wada. Ohmic Contacts to p-GaAs with Au/Zn/Au Structure. *Japanese Journal of Applied Physics*, 19(8):L491–L494, 1980.

[119] K. J. L. Company. `https://www.lesker.com/newweb/deposition_materials/depositionmaterials_evaporationmaterials_1.cfm?pgid=zn1` (accessed 09/10/23).

[120] C.H. Wu, S.M. Liao, and K.C. Chang. Ni/Pd/Au Ohmic Contact for p-GaAs and its Application in Red RCLED. *Materials Science and Engineering: B*, 117(2):205–209, 2005.

[121] V. V. Filippov, S. E. Luzyanin, and K. A. Bogonosov. Features of the Formation of Ni–GaAs Contacts Obtained by Electrolysis and Their Electrophysical Properties. *Technical Physics*, 68(2):27–34, 2023.

[122] S. O. Jones, P. D. Hodgson, and M. Hayne. Electrical Properties of GaAs/AlGaAs DBRs and Ohmic Contacts for Gasb/GaAs Quantum-Ring VCSELs. 2022.

[123] showtheplanet inc. `https://www.dailymetalprice.com` (accessed 29/07/24).

[124] R. L. Van Meirhaeghe, W. H. Laflere, and F. Cardon. Influence of Defect Passivation by Hydrogen on the Schottky Barrier Height of GaAs and InP Contacts. *Journal of Applied Physics*, 76(1):403–406, 07 1994.

[125] Alessio Quadrelli and Samuel Jarvis. Chemical Analysis of Materials with X-Ray Photoelectron Spectroscopy. *Surface Coatings International*, 105.5:382–383, October 2022.

[126] U. Vohrer, C. Blomfield, S. Page, and A. Roberts. Quantitative XPS Imaging—New Possibilities with the Delay-Line Detector. *Applied Surface Science*, 252(1):61–65, 2005.

[127] Emily F. Smith, Jonathan D. P. Counsell, James Bailey, James S. Sharp, Morgan R. Alexander, Alexander G. Shard, and David J. Scurr. Sample Rotation Improves Gas Cluster Sputter Depth Profiling of Polymers. *Surface and Interface Analysis*, 49(10):953–959, 2017.

[128] Hiroji Kawai, Shunji Imanaga, Kunio Kaneko, and Naozo Watanabe. Complex Refractive Indices of AlGaAs at High Temperatures Measured by In Situ Reflectometry During Growth by Metalorganic Chemical Vapor Deposition. *Journal of Applied Physics*, 61(1):328–332, 01 1987.

[129] W. D. Charles, H. M. John, A. G. Kevin, and E. V. Thomas. Determination of Optical Constants of n- and p-Type GaAs as a Function of Carrier Concentration. In *Proc.SPIE*, volume 12882, 2024.

[130] C. H. Kuo, S. Anand, R. Droopad, K. Y. Choi, and G. N. Maracas. Measurement of GaAs Temperature-Dependent Optical Constants by Spectroscopic Ellipsometry. *Journal of Vacuum Science & Technology B: Microelectronics and Nanometer Structures Processing, Measurement, and Phenomena*, 12(2):1214–1216, 03 1994.

[131] JO Akinlami and AO Ashamu. Optical Properties of GaAs. *Journal of Semiconductors*, 34(3):032002, 2013.

[132] BY Zhang, G Solomon, G Weihs, and Y Yamamoto. Experimental Extract and Empirical Formulas of Refractive Indices of GaAs and AlAs at High Temperature by HRXRD and Optical Reflectivity Measurement. *Journal of Crystal Growth*, 251(1-4):777–781, 2003.

[133] Leonard I Kamlet, Fred L Terry, and George N Maracas. A Temperature-Dependent Model for the Complex Dielectric Function of GaAs. *Journal of Electronic Materials*, 26:1409–1416, 1997.

[134] Juan A Gonzalez-Cuevas, Tamer F Refaat, M Nurul Abedin, and Hani E Elsayed-Ali. Calculations of the Temperature and Alloy Composition Effects on the Optical Properties of $Al_xGa_{1-x}As_ySb_{1-y}$ and $Ga_xIn_{1-x}As_ySb_{1-y}$ in the Spectral Range 0.5-6 eV. *Journal of Applied Physics*, 102(1), 2007.

[135] F. A. I. Chaqmaqchee, S. Mazzucato, Y. Sun, N. Balkan, E. Tiras, M. Hugues, and M. Hopkinson. Electrical Characterisation of p-Doped Distributed Bragg Reflectors in Electrically Pumped GaInNAs VCSOAs for 1.3μm Operation. *Materials Science and Engineering: B*, 177(10):739–743, 2012.

[136] M. O. Watanabe and H. Maeda. Electron Activation Energy in Si-Doped AlGaAs Grown by MBE. *Japanese Journal of Applied Physics*, 23:L734, 1984.

[137] N. Chand, R. Fischer, J. Klem, T. Henderson, P. Pearah, W. T. Masselink, Y. C. Chang, and H. Morkoç. Beryllium and Silicon Doping Studies in $Al_xGa_{1-x}As$ and New Results on Persistent Photoconductivity. *Journal of Vacuum Science & Technology B: Microelectronics Processing and Phenomena*, 3(2):644–648, 1985.

[138] DL Miller and PM Asbeck. Be Redistribution During Growth of GaAs and AlGaAs by Molecular Beam Epitaxy. *Journal of Applied Physics*, 57(6):1816–1822, 1985.

[139] WC Liu. Investigation of Electrical and Photoluminescent Properties of MBE-Grown $Al_xGa_{1-x}As$ Layers. *Journal of Materials Science*, 25:1765–1772, 1990.

[140] C Asplund, S Mogg, G Plaine, F Salomonsson, N Chitica, and Mattias Hammar. Doping-Induced Losses in AlAs/GaAs Distributed Bragg Reflectors. *Journal of Applied Physics*, 90(2):794–800, 2001.

[141] Chao-Kun Lin, David P Bour, Jintian Zhu, William H Perez, Michael H Leary, Ashish Tandon, Scott W Corzine, and Michael RT Tan. High Temperature Continuous-Wave Operation of 1.3-and 1.55-μm VCSELs with InP/Air-Gap DBRs. *IEEE Journal of Selected Topics in Quantum Electronics*, 9(5):1415–1421, 2003.

[142] E. C. Larkins, E. S. Hellman, D. G. Schlom, Jr. Harris, J. S., M. H. Kim, and G. E. Stillman. Reduction of the Acceptor Impurity Background in GaAs Grown by Molecular Beam Epitaxy. *Applied Physics Letters*, 49(7):391–393, 1986.

[143] Ivica Cale, Aida Salihovic, and Matija Ivekovic. Gigabit Passive Optical Network-GPON. In *2007 29th International conference on information technology interfaces*, pages 679–684. IEEE, 2007.

[144] P. D. Hodgson, M. Hayne, M. Ahmad Kamarudin, Q. D. Zhuang, S. Birindelli, and M. Capizzi. Hydrogenation of GaSb/GaAs Quantum Rings. *Applied Physics Letters*, 105(8):081907, 08 2014.

[145] K. Gradkowski, T. J. Ochalski, N. Pavarelli, H. Y. Liu, J. Tatebayashi, D. P. Williams, D. J. Mowbray, G. Huyet, and D. L. Huffaker. Coulomb-Induced Emission Dynamics and Self-Consistent Calculations of Type-II Sb-Containing Quantum Dot Systems. *Phys. Rev. B*, 85:035432, Jan 2012.

[146] Kamil Gradkowski, Nicola Pavarelli, Tomasz J. Ochalski, David P. Williams, Jun Tatebayashi, Guillaume Huyet, Eoin P. O'Reilly, and Diana L. Huffaker. Complex Emission Dynamics of Type-II GaSb/GaAs Quantum Dots. *Applied Physics Letters*, 95(6):061102, 08 2009.

[147] C.-K. Sun, G. Wang, J. E. Bowers, B. Brar, H.-R. Blank, H. Kroemer, and M. H. Pilkuhn. Optical Investigations of the Dynamic Behavior of GaSb/GaAs Quantum Dots. *Applied Physics Letters*, 68(11):1543–1545, 03 1996.

[148] F. Hatami, M. Grundmann, N. N. Ledentsov, F. Heinrichsdorff, R. Heitz, J. Böhrer, D. Bimberg, S. S. Ruvimov, P. Werner, V. M. Ustinov, P. S. Kop'ev, and Zh. I. Alferov. Carrier Dynamics in Type-II GaSb/GaAs Quantum Dots. *Phys. Rev. B*, 57:4635–4641, Feb 1998.

[149] M. Ahmad Kamarudin, M. Hayne, R. J. Young, Q. D. Zhuang, T. Ben, and S. I. Molina. Tuning the Properties of Exciton Complexes in Self-Assembled GaSb/GaAs Quantum Rings. *Phys. Rev. B*, 83:115311, Mar 2011.

[150] Hee Yeon Kim, Mee-Yi Ryu, and Jin Soo Kim. Luminescence Properties of InAs Quantum Dots Formed by a Modified Self-Assembled Method. *Journal of Luminescence*, 132(7):1759–1763, 2012.

[151] R. Heitz, M. Veit, N. N. Ledentsov, A. Hoffmann, D. Bimberg, V. M. Ustinov, P. S. Kop'ev, and Zh. I. Alferov. Energy Relaxation by Multiphonon Processes in InAs/GaAs Quantum Dots. *Phys. Rev. B*, 56:10435–10445, Oct 1997.

[152] Edmund Harbord, S. Iwamoto, Y. Arakawa, P. Spencer, E. Clarke, and R. Murray. Influence of P-Doping on the Temperature Dependence of InAs/GaAs Quantum Dot Excited State Radiative Lifetime. *Applied Physics Letters*, 101(18):183108, 11 2012.

[153] J.-M. Gerard and B. Gayral. Strong Purcell Effect for InAs Quantum Boxes in Three-Dimensional Solid-State Microcavities. *Journal of Lightwave Technology*, 17(11):2089–2095, 1999.

[154] Hsiang-Ting Lin, Kung-Shu Hsu, Chih-Chi Chang, Wei-Hsun Lin, Shih-Yen Lin, Shu-Wei Chang, Yia-Chung Chang, and Min-Hsiung Shih. Photonic Crystal Circular Nanobeam Cavity Laser with Type-II GaSb/GaAs Quantum Rings as Gain Material. *Scientific reports*, 10(1):4757, 2020.

[155] Kung-Shu Hsu, Wei-Chun Hung, Chih-Chi Chang, Wei-Hsun Lin, Min-Hsiung Shih, Po-Tsung Lee, Shih-Yen Lin, Shu-Wei Chang, and Yia-Chung Chang. Lasing Action and Extraordinary Reduction in Long Radiative Lifetime of Type-II GaSb/GaAs Quantum Dots using Circular Photonic Crystal Nanocavity. *Applied Physics Letters*, 107(9):091113, 09 2015.

[156] K. S. Hsu, T. T. Chiu, Wei-Hsun Lin, K. L. Chen, M. H. Shih, Shih-Yen Lin, and Yia-Chung Chang. Compact Microdisk Cavity Laser with type-II GaSb/GaAs Quantum Dots. *Applied Physics Letters*, 98(5):051105, 02 2011.

[157] J. Tatebayashi, A. Khoshakhlagh, S. H. Huang, G. Balakrishnan, L. R. Dawson, D. L. Huffaker, D. A. Bussian, H. Htoon, and V. Klimov. Lasing Characteristics of GaSb/GaAs Self-Assembled Quantum Dots Embedded in an InGaAs Quantum Well. *Applied Physics Letters*, 90(26):261115, 06 2007.

[158] Derek Nesset. PON Roadmap. *Journal of Optical Communications and Networking*, 9(1):A71–A76, 2017.

[159] S. O. Jones, P. D. Hodgson, and M. Hayne. GaSb Quantum-Rings for Vertical-Cavity Surface-Emitting Lasers Emitting at Telecommunications and Mobile Sensing Wavelengths. In *Proc.SPIE*, volume 12904, 2024.

[160] C Hentschel, C P Allford, S-J Gillgrass, J Travers-Nabialek, R Forrest, J Baker, J Meiklejohn, D Powell, W Meredith, M Haji, J I Davies, S Shutts, and P M Smowton. Gain Measurements on VCSEL Material Using Segmented Contact Technique. *Journal of Physics D: Applied Physics*, 56(7):074003, Jan 2023.

[161] Y Ding, WJ Fan, DW Xu, CZ Tong, Y Liu, and LJ Zhao. Low Threshold Current Density, Low Resistance Oxide-Confined VCSEL Fabricated by a Dielectric-Free Approach. *Applied Physics B*, 98:773–778, 2010.

[162] Petter Westbergh, Johan S. Gustavsson, Åsa Haglund, Mats Skold, Andrew Joel, and Anders Larsson. High-Speed, Low-Current-Density 850 nm VCSELs. *IEEE Journal of Selected Topics in Quantum Electronics*, 15(3):694–703, 2009.

[163] Aiwen Yue, Kun Shen, Renfan Wang, and Jing Shi. Low Threshold Current 1.3-μm GaInNAs VCSELs Grown by MOVPE. *IEEE Photonics Technology Letters*, 16(3):717–719, 2004.

[164] Jack Baker, Sara Gillgrass, Craig P Allford, Tomas Peach, Curtis Hentschel, Tracy Sweet, J Iwan Davies, Samuel Shutts, and Peter M Smowton. VCSEL Quick Fabrication for Assessment of Large Diameter Epitaxial Wafers. *IEEE Photonics Journal*, 14(3):1–10, 2022.

Appendix A

Recipes

This chapter contains the recipes used in the plasma-enhanced deposition and etch processes presented in chapter 6. The recipes are included for the interest of the reader; however, a detailed discussion of the etch and deposition processes is not provided.

A.1 SiNx Deposition by ICP-PECVD

Step - Pump		
	Duration	1 hour
	Strike Pressure (mTorr)	0.0
	Set Chamber Pressure (mTorr)	0.0
	Ramp Rate (mTorr/s)	0
	DC Bias Minimum (V)	0
	Forward Power (W)	0
HF Generator	Lower Magnitude (%)	0
	Lower Phase (%)	0
	Forward Power (W)	0
ICP Coil	Upper Magnitude (%)	0
	Upper Phase (%)	0
	Table Temperature (°C)	110
	Helium Backing Pressure (Torr)	0
	NH_3	0
	SiH_4	0
Gas Flow (sccm)	N_2O	0
	N_2	0
	SF_6	0
Step - Gas Stabilise		
	Duration	15 seconds
	Strike Pressure (mTorr)	0.0

	Set Chamber Pressure (mTorr)	25.0
	Ramp Rate (mTorr/s)	0
	DC Bias Minimum (V)	0
	Forward Power (W)	0
HF Generator	Lower Magnitude (%)	0
	Lower Phase (%)	0
	Forward Power (W)	0
ICP Coil	Upper Magnitude (%)	0
	Upper Phase (%)	0
	Table Temperature (°C)	100
	Helium Backing Pressure (Torr)	0
	NH_3	0
	SiH_4	5.3
Gas Flow (sccm)	N_2O	0
	N_2	4.5
	SF_6	0
Step - Strike		
	Duration	20 seconds
	Strike Pressure (mTorr)	0.0
	Set Chamber Pressure (mTorr)	25.0
	Ramp Rate (mTorr/s)	0
	DC Bias Minimum (V)	0
	Forward Power (W)	50
HF Generator	Lower Magnitude (%)	0
	Lower Phase (%)	0
	Forward Power (W)	250
ICP Coil	Upper Magnitude (%)	0
	Upper Phase (%)	0
	Table Temperature (°C)	100
	Helium Backing Pressure (Torr)	0
	NH_3	0
	SiH_4	5.3
Gas Flow (sccm)	N_2O	0
	N_2	4.5
	SF_6	0
Step - Pressure Set 1 - Switch off HF coil		
	Duration	15 seconds
	Strike Pressure (mTorr)	0.0

	Set Chamber Pressure (mTorr)	17.0
	Ramp Rate (mTorr/s)	0
	DC Bias Minimum (V)	0
	Forward Power (W)	0
HF Generator	Lower Magnitude (%)	0
	Lower Phase (%)	0
	Forward Power (W)	250
ICP Coil	Upper Magnitude (%)	0
	Upper Phase (%)	0
	Table Temperature (°C)	100
	Helium Backing Pressure (Torr)	0
	NH_3	0
	SiH_4	5.3
Gas Flow (sccm)	N_2O	0
	N_2	4.5
	SF_6	0
Step - Pressure Step 2		
	Duration	20 seconds
	Strike Pressure (mTorr)	0.0
	Set Chamber Pressure (mTorr)	10.0
	Ramp Rate (mTorr/s)	0
	DC Bias Minimum (V)	0
	Forward Power (W)	0
HF Generator	Lower Magnitude (%)	0
	Lower Phase (%)	0
	Forward Power (W)	250
ICP Coil	Upper Magnitude (%)	0
	Upper Phase (%)	0
	Table Temperature (°C)	100
	Helium Backing Pressure (Torr)	0
	NH_3	0
	SiH_4	5.3
Gas Flow (sccm)	N_2O	0
	N_2	4.5
	SF_6	0

Step - Deposition		
	Duration	3 minutes
	Strike Pressure (mTorr)	0.0
	Set Chamber Pressure (mTorr)	10.0
	Ramp Rate (mTorr/s)	0
	DC Bias Minimum (V)	0
	Forward Power (W)	0
HF Generator	Lower Magnitude (%)	0
	Lower Phase (%)	0
	Forward Power (W)	250
ICP Coil	Upper Magnitude (%)	0
	Upper Phase (%)	0
	Table Temperature (°C)	100
	Helium Backing Pressure (Torr)	0
	NH_3	0
	SiH_4	5.3
Gas Flow (sccm)	N_2O	0
	N_2	4.5
	SF_6	0

Step - Pump		
	Duration	2 minutes
	Strike Pressure (mTorr)	0.0
	Set Chamber Pressure (mTorr)	0.0
	Ramp Rate (mTorr/s)	0
	DC Bias Minimum (V)	0
	Forward Power (W)	0
HF Generator	Lower Magnitude (%)	0
	Lower Phase (%)	0
	Forward Power (W)	0
ICP Coil	Upper Magnitude (%)	0
	Upper Phase (%)	0
	Table Temperature (°C)	25
	Helium Backing Pressure (Torr)	0
	NH_3	0
	SiH_4	0
Gas Flow (sccm)	N_2O	0
	N_2	0
	SF_6	0

Table A.1: The deposition recipe for SiNx used over the course of this work.

A.2 SiNx Etch by RIE

Step - Pump		
	Duration	2 minutes
	Strike Pressure (mTorr)	0.0
	Set Chamber Pressure (mTorr)	0.0
	Ramp Rate (mTorr/s)	0
	DC Bias Minimum (V)	0
	Forward Power (W)	0
RF Generator	Lower Magnitude (%)	0
	Lower Phase (%)	0
	Table Temperature (°C)	25
	Helium Backing Pressure (Torr)	0
	CHF_3	0
	CF_4	0
Gas Flow (sccm)	O_2	0
	Ar	0
	SF_6	0
Step - Gas Stabilise		
	Duration	15 seconds
	Strike Pressure (mTorr)	0.0
	Set Chamber Pressure (mTorr)	55.0
	Ramp Rate (mTorr/s)	0
	DC Bias Minimum (V)	0
	Forward Power (W)	0
RF Generator	Lower Magnitude (%)	0
	Lower Phase (%)	0
	Table Temperature (°C)	25
	Helium Backing Pressure (Torr)	0
	CHF_3	50
	CF_4	0
Gas Flow (sccm)	O_2	5
	Ar	0
	SF_6	0
Step - Etch		
	Duration	3 minutes 30 seconds
	Strike Pressure (mTorr)	0.0
	Set Chamber Pressure (mTorr)	55.0

	Ramp Rate (mTorr/s)	0
	DC Bias Minimum (V)	0
	Forward Power (W)	150
RF Generator	Lower Magnitude (%)	0
	Lower Phase (%)	0
	Table Temperature (°C)	25
	Helium Backing Pressure (Torr)	0
	CHF_3	50
	CF_4	0
Gas Flow (sccm)	O_2	5
	Ar	0
	SF_6	0
Step - Pump		
	Duration	2 minutes
	Strike Pressure (mTorr)	0.0
	Set Chamber Pressure (mTorr)	0.0
	Ramp Rate (mTorr/s)	0
	DC Bias Minimum (V)	0
	Forward Power (W)	0
RF Generator	Lower Magnitude (%)	0
	Lower Phase (%)	0
	Table Temperature (°C)	25
	Helium Backing Pressure (Torr)	0
	CHF_3	0
	CF_4	0
Gas Flow (sccm)	O_2	0
	Ar	0
	SF_6	0

Table A.2: The etch recipe for SiNx used over the course of this work.

A.3 Mesa-Etch by ICP

Step - Pump		
	Duration	1 minute
	Base Pressure Setpoint (mTorr) - Never reached	7.50×10^{-9}
	Strike Pressure (mTorr)	0.0
	Set Chamber Pressure (mTorr)	0.0
	Ramp Rate (mTorr/s)	0
	DC Bias Minimum (V)	0
RF Generator	Forward Power (W)	0
	Load Matching Capacitor 1	0
	Load Matching Capacitor 2	0
ICP Coil	Forward Power (W)	0
	Load Matching Capacitor 1	0
	Load Matching Capacitor 2	0
	Table Temperature Mode	Heated
	Heated Table Temperature (°C)	10
	Chilled Table Temperature (°C)	10
	Helium Backing Pressure (Torr)	0
Gas Flow (sccm)	BCl_3	0
	Cl_2	0
	CH_4	0
	H_2	0
	Ar	0
	O_2	0
	SF_6	0
Step - Gas Stabilisation		
	Duration	1 minute
	Base Pressure Setpoint (mTorr) - Never reached	7.50×10^{-9}
	Strike Pressure (mTorr)	0.0
	Set Chamber Pressure (mTorr)	25.0
	Ramp Rate (mTorr/s)	0
	DC Bias Minimum (V)	0
RF Generator	Forward Power (W)	0
	Load Matching Capacitor 1	0
	Load Matching Capacitor 2	0
ICP Coil	Forward Power (W)	0

	Load Matching Capacitor 1	0
	Load Matching Capacitor 2	0
	Table Temperature Mode	Heated
	Heated Table Temperature (°C)	10
	Chilled Table Temperature (°C)	10
	Helium Backing Pressure (Torr)	0
	BCl_3	7.5
	Cl_2	2.5
Gas Flow (sccm)	CH_4	0
	H_2	0
	Ar	5.0
	O_2	0
	SF_6	0
Step - Etch		
	Duration	-
	Base Pressure Setpoint (mTorr) - Never reached	7.50×10^{-9}
	Strike Pressure (mTorr)	25.0
	Set Chamber Pressure (mTorr)	4.0
	Ramp Rate (mTorr/s)	5
	DC Bias Minimum (V)	50
	Forward Power (W)	18
RF Generator	Load Matching Capacitor 1	0
	Load Matching Capacitor 2	0
	Forward Power (W)	120
ICP Coil	Load Matching Capacitor 1	0
	Load Matching Capacitor 2	0
	Table Temperature Mode	Heated
	Heated Table Temperature (°C)	10
	Chilled Table Temperature (°C)	10
	Helium Backing Pressure (Torr)	0
	BCl_3	7.5
	Cl_2	2.5
Gas Flow (sccm)	CH_4	0
	H_2	0
	Ar	5.0
	O_2	0
	SF_6	0
Step - Pump		
	Duration	1 minute

	Base Pressure Setpoint (mTorr) - Never reached	7.50×10^{-9}
	Strike Pressure (mTorr)	0.0
	Set Chamber Pressure (mTorr)	0.0
	Ramp Rate (mTorr/s)	0
	DC Bias Minimum (V)	0
	Forward Power (W)	0
RF Generator	Load Matching Capacitor 1	0
	Load Matching Capacitor 2	0
	Forward Power (W)	0
ICP Coil	Load Matching Capacitor 1	0
	Load Matching Capacitor 2	0
	Table Temperature Mode	Heated
	Heated Table Temperature (°C)	10
	Chilled Table Temperature (°C)	10
	Helium Backing Pressure (Torr)	0
	BCl_3	0
	Cl_2	0
Gas Flow (sccm)	CH_4	0
	H_2	0
	Ar	0
	O_2	0
	SF_6	0

Table A.3: The mesa-etch recipe used to etch VCSELs and DBRs over the course of this work.

A.4 Ti-Etch by ICP for Mask Fabrication

Step - Pump		
	Duration	1 minute
	Base Pressure Setpoint (mTorr) - Never reached	7.50×10^{-9}
	Strike Pressure (mTorr)	0.0
	Set Chamber Pressure (mTorr)	0.0
	Ramp Rate (mTorr/s)	0
	DC Bias Minimum (V)	0
RF Generator	Forward Power (W)	0
	Load Matching Capacitor 1	0
	Load Matching Capacitor 2	0
ICP Coil	Forward Power (W)	0
	Load Matching Capacitor 1	0
	Load Matching Capacitor 2	0
	Table Temperature Mode	Heated
	Heated Table Temperature (°C)	10
	Chilled Table Temperature (°C)	10
	Helium Backing Pressure (Torr)	0
Gas Flow (sccm)	BCl_3	0
	Cl_2	0
	CH_4	0
	H_2	0
	Ar	0
	O_2	0
	SF_6	0
Step - Gas Stabilisation		
	Duration	1 minute
	Base Pressure Setpoint (mTorr) - Never reached	7.50×10^{-9}
	Strike Pressure (mTorr)	0.0
	Set Chamber Pressure (mTorr)	50.0
	Ramp Rate (mTorr/s)	0
	DC Bias Minimum (V)	0
RF Generator	Forward Power (W)	0
	Load Matching Capacitor 1	0
	Load Matching Capacitor 2	0
ICP Coil	Forward Power (W)	0

	Load Matching Capacitor 1	0
	Load Matching Capacitor 2	0
	Table Temperature Mode	Heated
	Heated Table Temperature (°C)	10
	Chilled Table Temperature (°C)	10
	Helium Backing Pressure (Torr)	0
	BCl_3	7.5
	Cl_2	2.5
Gas Flow (sccm)	CH_4	0
	H_2	0
	Ar	5.0
	O_2	0
	SF_6	0
Step - Etch		
	Duration	-
	Base Pressure Setpoint (mTorr) - Never reached	7.50×10^{-9}
	Strike Pressure (mTorr)	50.0
	Set Chamber Pressure (mTorr)	7.0
	Ramp Rate (mTorr/s)	5
	DC Bias Minimum (V)	0
	Forward Power (W)	25
RF Generator	Load Matching Capacitor 1	0
	Load Matching Capacitor 2	0
	Forward Power (W)	250
ICP Coil	Load Matching Capacitor 1	0
	Load Matching Capacitor 2	0
	Table Temperature Mode	Heated
	Heated Table Temperature (°C)	10
	Chilled Table Temperature (°C)	10
	Helium Backing Pressure (Torr)	0
	BCl_3	7.5
	Cl_2	2.5
Gas Flow (sccm)	CH_4	0
	H_2	0
	Ar	5.0
	O_2	0
	SF_6	0
Step - Pump		
	Duration	1 minute

	Base Pressure Setpoint (mTorr) - Never reached	7.50×10^{-9}
	Strike Pressure (mTorr)	0.0
	Set Chamber Pressure (mTorr)	0.0
	Ramp Rate (mTorr/s)	0
	DC Bias Minimum (V)	0
	Forward Power (W)	0
RF Generator	Load Matching Capacitor 1	0
	Load Matching Capacitor 2	0
	Forward Power (W)	0
ICP Coil	Load Matching Capacitor 1	0
	Load Matching Capacitor 2	0
	Table Temperature Mode	Heated
	Heated Table Temperature (°C)	10
	Chilled Table Temperature (°C)	10
	Helium Backing Pressure (Torr)	0
	BCl_3	0
	Cl_2	0
Gas Flow (sccm)	CH_4	0
	H_2	0
	Ar	0
	O_2	0
	SF_6	0

Table A.4: The mesa-etch recipe used to etch VCSELs and DBRs over the course of this work.